Higgs boson and vacuum stability in models with extended scalar sector

Bogumiła Natalia Świeżewska

Doctoral dissertation prepared under the supervision of
prof. dr hab. Maria Krawczyk
at the Institute of Theoretical Physics, Faculty of Physics, University of Warsaw

February 2016

Acknowledgements

First and foremost, I would like to express my sincere gratitude to my supervisor, Prof. Maria Krawczyk. I am indebted to her for the help with finding interesting research problems, for her support during the research process, as well as for showing me that it is important to understand the structure of the problem and not only seek the answer. Moreover, I acknowledge her encouragement to participate in a number of conferences and schools, as it allowed me to widen my horizons, meet many interesting people and facilitated scientific interactions. I am also thankful for supporting me in presenting my results which helped me to become a better speaker. Finally, I would like to thank for her help and understanding showed during preparation of this dissertation.

I am also thankful to Dr Dorota Sokołowska, Paweł Swaczyna, Prof. Pedro Ferreira and Dr Marco Sampaio with whom I collaborated to obtain some of the results presented in this thesis. I learned a lot from working with them.

I am indebted to Prof. Piotr Chankowski and Grzegorz Gil for their patience in answering my questions regarding the effective potential and for sharing their knowledge, notes and other materials. I benefited a lot from talking with them and gained from their experience and knowledge.

Many thanks should go also to my fellow PhD students, Aqeel Ahmed, Olga Czerwińska, Grzegorz Gil, Mateusz Iskrzyński, Wojtek Kotlarski, Marek Lewicki, Paweł Olszewski and Arek Trawiński, who offered me their time for scientific discussions, explaining their work, helping with computer codes and other technical issues and of course for non-scientific conversations making everyday work more cheerful. I especially appreciate the company of Grzesiek and Arek who were the best office-mates.

Last but not least, I would like to thank my parents and the whole family for their constant support and the big dose of motivation passed to me at the final stage of preparing this work. I deeply appreciate the care and encouragement received from Jędrek which accompanied me all along the way.

This work was partially supported by the Polish National Science Centre grant PRELUDIUM under the decision number DEC-2013/11/N/ST2/04214.

Abstract

In this dissertation Two-Higgs-Doublet Models (2HDMs) with a $\mathbb{Z}_2$-symmetric scalar potential are studied from different perspectives. Two kinds of models, which differ by the choice of the vacuum state, are analysed. One of them is the so-called 2HDM (mixed) which breaks the symmetry of the potential by non-zero vacuum expectation values (VEVs) of the neutral components of the two scalar doublets. The other one, the exactly $\mathbb{Z}_2$-symmetric Inert Doublet Model (IDM) with only one non-vanishing VEV, is of central interest to this work. It contains a SM-like Higgs boson and a candidate for the dark matter (DM) particle.

The first part of this thesis is devoted to the analysis of the allowed parameter space of the studied 2HDMs. The models are subject to a number of constrains, such as: positivity of the potential, stability of the vacuum state, perturbative unitarity, electroweak precision tests and the LEP bounds. We also take into account the fact that the scalar discovered at the LHC is a SM-like Higgs boson with mass around 125 GeV. We present the allowed regions in the parameter space for the parameters of the potential and the physical masses. For the 2HDM (mixed), within a scenario where the lightest CP-even scalar plays a role of the SM-like Higgs particle, we find a strong bound on the parameter $\tan\beta$, which is independent of the type of Yukawa interactions. In the IDM we derive an upper bound on the mass parameter of the potential which is based on the condition for the stability of the vacuum and excludes a phenomenologically interesting part of the parameter space.

In the second part of the present dissertation, constraints on the properties of the new scalars of the IDM, based on the experimental results for the Higgs particle, are analysed. First of all, we study the Higgs diphoton decay. We show, that the additional scalars (in particular the charged scalar and the DM candidate) can affect the observed signal strength of this decay. From this fact, we infer strong upper and lower limits on the masses of these particles. Next, the decay of the Higgs to a Z boson and a photon is analysed. We demonstrate that the correlation between the diphoton and $Z\gamma$ signal strength is positive, which gives a possible experimental probe of the IDM. Furthermore, we study the invisible and total decay widths of

the Higgs boson and infer constraints on the DM particle and its coupling to the Higgs particle. In the following, the Higgs results are combined with the DM data. We derive constraints and exclusions for different possible DM scenarios, proving the idea of combining different sources of results very fruitful. Interestingly, the results of this combination, when translated to the parameters probed by the direct detection experiments, give constraints which are comparable or even stronger than the results of the dedicated searches.

In the final part of the present dissertation, the issue of vacuum stability is studied, in particular, the influence of the additional scalars on this problem. Two distinct approaches are adopted. First, the additional scalars of the IDM are assumed to be heavy, and thus they contribute to the effective potential only through loop corrections. We demonstrate that the heavy inert scalars can change the structure of the effective potential, introducing a new minimum which is deeper than the SM one and this way they can destabilise the vacuum state. In addition, the regions where destabilisation of the vacuum may occur are confronted with theoretical and experimental constraints, and we prove that the IDM, in the valid part of the parameter space, is free from the threat of vacuum instability. The other approach to the issue of vacuum stability adopted in this thesis admits all of the scalar fields in the effective potential, and thus allows the study of the coexistence of different minima. We show that the inert minimum can coexist with an inert-like one at one-loop level in a vaster region of the parameter space than at tree level. Moreover, we demonstrate that the loop corrections may invert the ordering of the minima, i.e. a tree-level global minimum may, in certain cases, become a local one at one-loop level. This shows the importance of beyond-tree-level analysis of the issue of vacuum stability.

Streszczenie

Niniejsza dysertacja poświęcona jest badaniu modeli z dwoma dubletami pól Higgsa (ang. *Two-Higgs-Doublet Model, 2HDM*) opisywanych potencjałem skalarnym z symetrią typu $\mathbb{Z}_2$. Analizowane są dwa rodzaje modeli 2HDM różniące się wyborem stanu próżni. Pierwszy z nich to tzw. 2HDM (mixed), który łamie symetrię potencjału, gdyż w stanie próżni neutralne składowe obu skalarnych dubletów uzyskują niezerową próżniową wartość oczekiwaną. Drugi, model z biernym dubletem pól skalarnych (ang. *Inert Doublet Model, IDM*) posiadający jedną niezerową próżniową wartość oczekiwaną i zachowujący tym samym symetrię potencjału, jest głównym przedmiotem niniejszej pracy. Zawiera on bozon Higgsa o własnościach zbliżonych do własności bozonu Higgsa z Modelu Standardowego (ang. *Standard Model, SM*) oraz kandydatkę na cząstkę ciemnej materii.

Pierwsza część niniejszej pracy jest poświęcona analizie przestrzeni parametrów badanych modeli 2HDM. Modele te są ograniczane przez rozmaite warunki i pomiary takie jak: dodatniość potencjału, stabilność stanu próżni, perturbacyjna unitarność, precyzyjne dane elektrosłabe oraz ograniczenia z akceleratora LEP. Ponadto bierzemy pod uwagę fakt, że cząstka skalarna odkryta w LHC ma własności standardowego bozonu Higgsa oraz masę około 125 GeV. Dozwolone obszary są przedstawione w przestrzeni parametrów potencjału oraz fizycznych mas cząstek. W modelu 2HDM (mixed), w przypadku gdy najlżejsza cząstka skalarna o dodatniej parzystości CP pełni rolę bozonu Higgsa, prezentujemy nowe silne ograniczenie na parametr $\tan\beta$, niezależnie od typu oddziaływań Yukawy. W modelu IDM, w oparciu o warunek stabilności próżni, wyprowadzamy ograniczenie na parametr masowy potencjału, które wyklucza interesujący z fenomenologicznego punktu widzenia obszar przestrzeni parametrów.

W drugiej części niniejszej dysertacji w oparciu o dane eksperymentalne dotyczące bozonu Higgsa, wyprowadzamy ograniczenia na możliwe własności nowych cząstek skalarnych w IDM. W pierwszej kolejności analizowany jest rozpad bozonu Higgsa na dwa fotony. Pokazujemy, że dodatkowe skalary, w szczególności cząstka naładowana oraz kandydatka na cząstkę ciemnej materii, mogą znacząco wpływać na

siłę sygnału dla tego rozpadu. Z tego faktu wyprowadzamy silne ograniczenia na masy tych cząstek. Następnie, analizowany jest rozpad bozonu Higgsa na bozon Z oraz foton. Pokazujemy, że korelacja między siłami sygnału w tym kanale oraz kanale dwufotonowym jest pozytywna, co stwarza możliwość poddania IDM eksperymentalnej weryfikacji. Ponadto, badamy stosunek rozgałęzień rozpadu bozonu Higgsa na cząstki niewidzialne oraz jego całkowitą szerokość rozpadu, co pozwala na wyprowadzenie ograniczeń na masę cząstki ciemnej materii oraz jej sprzężenie do bozonu Higgsa. W dalszej części wyniki dotyczące bozonu Higgsa są połączone z danymi dotyczącymi ciemnej materii. Wyprowadzamy istotne ograniczenia i wykluczenia dotyczące różnych możliwych scenariuszy istnienia ciemnej materii, pokazując tym samym, że łączenie różnych źródeł danych może być niezwykle owocne. Nasze ograniczenia wynikające z tej analizy przetłumaczone na ograniczenie parametrów próbkowanych przez eksperymenty bezpośredniej detekcji ciemnej materii okazują się być porównywalne lub nawet silniejsze od wyników tych dedykowanych poszukiwań ciemnej materii.

W ostatniej części niniejszej pracy analizowany jest problem stabilności stanu próżni, w szczególności wpływ jaki mają na niego dodatkowe cząstki skalarne. Badamy to zagadnienie na dwa różne sposoby. W ramach pierwszego podejścia zakładamy, że dodatkowe skalary są ciężkie i w związku z tym mogą dawać wkład do potencjału efektywnego jedynie poprzez efekty pętlowe. Pokazujemy, że dodatkowe skalary mogą zmodyfikować strukturę potencjału efektywnego i zdestabilizować stan próżni, wprowadzając dodatkowe głębsze minimum. Dodatkowo, konfrontując obszary parametrów, w których możliwa jest destabilizacja próżni z ograniczeniami teoretycznymi i doświadczalnymi, pokazujemy, że w IDM taki scenariusz nie jest możliwy. Drugie podejście do problemu stabilności próżni stosowane w niniejszej pracy pozwala na obecność wszystkich pól skalarnych w potencjale efektywnym, stwarzając tym samym możliwość zbadania współistnienia różnych typów minimów. Pokazujemy, że minima typu inert oraz inert-like mogą współistnieć na poziomie pętlowym, w szerszym zakresie parametrów niż na poziomie drzewowym. Co więcej, pokazujemy, że poprawki pętlowe mogą odwrócić uporządkowanie próżni, tzn. drzewowe minimum globalne może stać się na poziomie pętlowym minimum lokalnym. To pokazuje jak istotne może być wyjście poza poziom drzewowy w analizie stabilności próżni.

Contents

Preface

The work presented in the present dissertation is partially based on the following publications, see refs. [1–6],

1. Pedro M. Ferreira, Bogumiła Świeżewska, *One-loop contributions to neutral minima in the inert doublet model*, arXiv:1511.02879 [hep-ph],

2. Bogumiła Świeżewska, *Inert scalars and vacuum metastability around the electroweak scale*, JHEP 1507 (2015) 118,

3. Maria Krawczyk, Dorota Sokołowska, Paweł Swaczyna, Bogumiła Świeżewska, *Constraining Inert Dark Matter by $R_{\gamma\gamma}$ and WMAP data*, JHEP 1309 (2013) 055,

4. Bogumiła Świeżewska, Maria Krawczyk, *Diphoton rate in the inert doublet model with a 125 GeV Higgs boson*, Phys. Rev. D88 (2013) 3, 035019,

5. Bogumiła Świeżewska, *Yukawa independent constraints for 2HDMs with a 125 GeV Higgs boson*, Phys. Rev. D88 (2013) 055027,

6. Bogumiła Gorczyca, Maria Krawczyk, *Tree-Level Unitarity Constraints for the SM-like 2HDM*, arXiv:1112.5086 [hep-ph],

and conference proceedings [7–17],

1. Bogumiła Świeżewska, *Inert scalars and vacuum stability*, to appear in: Proceedings of The Toyama International Workshop on Higgs as a Probe of New Physics 2015 (HPNP2015),

2. Pedro M. Ferreira, Bogumiła Świeżewska, *One-loop inert and pseudo-inert minima*, to appear in: Proceedings of The Toyama International Workshop on Higgs as a Probe of New Physics 2015 (HPNP2015), arXiv:1506.00585 [hep-ph],

3. Maria Krawczyk, Małgorzata Matej, Dorota Sokołowska, Bogumiła Świeżewska, *The Universe in the light of LHC*, Acta Phys. Polon. B46 (2015) 169, arXiv:1501.04529 [hep-ph],

4. Maria Krawczyk, Dorota Sokołowska, Paweł Swaczyna, Bogumiła Świeżewska, *Implications of the 125 GeV Higgs for the inert Dark Matter*, Proceedings of the 49th Rencontres de Moriond on QCD and High Energy Interactions (2014),

5. Bogumiła Świeżewska, *Decay rates of the Higgs boson to two photons and Z plus photon in* $\mathbf{Z}_2$*-symmetric Two Higgs Doublet Models*, PoS (EPS-HEP 2013) 066, arXiv:1309.7343 [hep-ph],

6. Maria Krawczyk, Dorota Sokołowska, Paweł Swaczyna, Bogumiła Świeżewska, *Higgs* $\to \gamma\gamma$, $Z\gamma$ *in the Inert Doublet Model*, Acta Phys. Polon. B44 (2013) 2163–2170, arXiv:1309.7880 [hep-ph],

7. Bogumiła Świeżewska, Maria Krawczyk, *Two photon decay rate of the Higgs boson in the Inert Doublet Model*, PoS (Photon 2013) 078,

8. Bogumiła Świeżewska, Maria Krawczyk, *2-photon decay rate of the scalar boson in the Inert Doublet Model*, Proceedings of 48th Rencontres de Moriond on Electroweak Interactions and Unified Theories (2013), arXiv:1305.7356 [hep-ph],

9. Maria Krawczyk, Dorota Sokołowska, Bogumiła Świeżewska, *Inert Doublet Model with a 125 GeV Higgs*, Proceedings of The Toyama International Workshop on Higgs as a Probe of New Physics 2013 (HPNP2013) (2013), arXiv:1304.7757 [hep-ph],

10. Maria Krawczyk, Dorota Sokołowska, Bogumiła Świeżewska, *2HDM with* $\mathbf{Z}_2$ *symmetry in light of new LHC data*, J. Phys. Conf. Ser. 447 (2013), 012050, arXiv:1303.7102 [hep-ph],

11. Bogumiła Gorczyca, Maria Krawczyk, *New Results for the Inert Doublet Model*, Acta Phys. Polon. B42 (2011), 2229–2236, arXiv:1112.4356 [hep-ph].

Acronyms

Below we list the acronyms used throughout this dissertation.

2HDM Two-Higgs-Doublet Model

EWPT electroweak precision tests

BSM beyond the Standard Model

CW Coleman–Weinberg

DM dark matter

DRED dimensional reduction

DREG dimensional regularisation

EW electroweak

EWSB electroweak symmetry breaking

FCNC flavour-changing neutral current

IDM Inert Doublet Model

LHC Large Hadron Collider

MS minimal subtraction

OS on-shell

SM Standard Model

SSB spontaneous symmetry breaking

VEV vacuum expectation value

Chapter 1

Introduction

The work described in this dissertation was developed during extremely exciting times for particle physics — during the operation of the Large Hadron Collider (LHC) at CERN and in the era of the discovery of a new scalar particle in the ATLAS [18] and CMS [19] experiments. A scalar particle, the Higgs boson, was the only missing, not yet observed experimentally fundamental particle of the Standard Model (SM) of elementary interactions. It was predicted in the 1960' as an accompanying particle of spontaneous symmetry breaking (SSB) via the Brout–Englert–Higgs mechanism [20–23] which endows gauge bosons with mass. F. Englert and P. Higgs were awarded the Nobel prize in Physics in 2013 for proposing this mechanism of mass generation, R. Brout passed away in 2011 before the decision of the Nobel committee. The prevailing question was whether the discovered particle is the Higgs boson as predicted by the SM or maybe it shows some different features. In general, the experimental results converge towards the SM predictions [24], however some new physics effects could be hidden in the experimental uncertainties or in the processes that have not yet been observed. Furthermore, it still remains an open question what the upgraded run of the LHC, with the centre-of-mass energy equal to 13 TeV, will uncover. Some first exciting hints on the existence of a new resonance with mass around 750 GeV have been reported [25, 26] but we should probably wait with the wave of enthusiasm for more data.

The general excitement with which any discrepancy between the experimental results and the SM predictions is welcomed is caused by the fact that the SM faces certain theoretical and experimental problems and is believed not to be the final theory of fundamental interactions. Among these problems are the hierarchy

problem, metastability of the SM vacuum state, neutrino masses, existence of dark matter (DM) and domination of matter over antimatter. A large number of models describing new physics beyond the SM (BSM) has been devised to deal with these issues. Typically, they correspond to extensions of the SM with additional fields, which produce some new effects not present in the SM, as well as they modify the predictions for the SM processes. Any hint of disagreement between the SM and the observations may point towards a particular new physics model.

Among the simplest extensions of the SM, providing interesting phenomenology, are the models with an extended scalar sector which instead of one complex $SU(2)$ doublet of the SM contain more of the doublets or also scalar fields belonging to other representations of $SU(2)$. In the present thesis we will focus on the two-Higgs-doublet models (2HDM) which contain two scalar $SU(2)$ doublets and were first proposed by T. D. Lee in 1973 to provide an additional source of CP violation as compared to the SM (CKM matrix) [27]. Moreover, 2HDMs can offer a candidate for a DM particle, as well as some conditions for baryogenesis. In particular, the Inert Doublet Model (IDM), which is a special type of 2HDM with an exact $\mathbb{Z}_2$ symmetry, will be of main interest to us.

The Higgs boson is central to this dissertation. It will be studied here within the 2HDMs from different perspectives. First of all, we will study its properties via the analysis of the LHC results. We will focus on the decay of the Higgs boson to two photons, which was the first observational channel of the new particle and also at first showed some discrepancies from the SM expectations. We will also study the Higgs decays to a Z boson and a photon as well as to particles that are invisible for the detector, and the total decay width of the Higgs boson. In all of these studies our main goal will be to use the Higgs data to learn something about the new, yet unobserved particles present in the model. Therefore, one may say that the Higgs boson is treated in this thesis as a probe of new physics.

Moreover, we will study the interplay between the properties of the Higgs boson and the properties of the DM candidate present in the IDM. We will show that analysing the results related to the Higgs boson together with the DM data may lead to strong constraints, even stronger than results obtained by dedicated direct searches of DM. Therefore, the Higgs boson plays also a role of a portal to the DM sector.

On the other hand, the Higgs boson, interpreted as an excitation of the scalar field, will be studied from a theoretical perspective. The scalar field is a basic component of SSB, and the nature of its ground state determines the properties of the theory. In particular, it is crucial that the ground (vacuum) state is sufficiently stable, otherwise the theory cannot be predictive. In this thesis we study the impact

of additional scalar fields on the stability of the vacuum state.

Integrating these different ways of reasoning, a phenomenological approach with a more theoretical one, we develop a thorough analysis of the studied models.

This thesis is organised as follows. We start from introducing the studied models in chapter 2. We specify the lagrangian and its symmetries, discuss the potential and the possible vacuum states. Depending on the vacuum state chosen, different models are possible. For these models we specify the particle spectrum, giving expressions for masses and discussing the properties of the particles.

In chapter 3 we present the constraints on the parameter spaces of the discussed models. Among them are basic theoretical constraints: positivity of the potential, stability of the vacuum state and perturbative unitarity. Moreover, experimental bounds such as electroweak precision tests (EWPT), LEP and flavour physics constraints are presented. We show how these constraints affect parameter spaces of the studied models. Furthermore, we present the constraints to be studied in more detail in the following chapters: the results from the LHC as well as the DM constraints.

Chapter 4 is devoted to the study of the properties of the Higgs boson within the IDM. We start from the analysis of the Higgs diphoton decay. Providing both analytical and numerical analysis, we investigate what the influence of the new scalar particles on the diphoton signal strength is, and extract limits on the scalar masses from the observational data. Further on, we study the decay of the Higgs boson to a photon and a Z boson. We show that the mechanisms controlling the signal strength are very similar to the ones appearing in the case of the $h \to \gamma\gamma$ decay so also all the constraints derived in this case would be the same. An interesting observation is that the two signal strengths are positively correlated, which can serve as a potential experimental probe of the validity of the IDM. Next, we study the total decay width of the Higgs boson, as well as the branching rations of the decays to invisible particles. From these observables we are able to derive upper and lower bounds on the coupling between the Higgs boson and the DM candidate.

The next part of chapter 4 is devoted to the study of the interplay between the properties of the Higgs boson and the inert DM. We show that the same parameters, the mass of the DM particle and its coupling to the Higgs boson, are important for the computation of the diphoton signal strength and the DM relic abundance. Using this fact, we derive limits on different possible DM scenarios. Moreover, we interpret the obtained bounds so that it is possible to compare them with the results of the direct search experiments, and it appears that the bounds obtained by us are comparable with the results from the XENON100 and LUX experiments.

The following part of this dissertation is focused on the problem of vacuum stability. This issue gained a lot of attention after the discovery of the Higgs boson

and the measurement of its mass. The stability of the SM vacuum depends strongly on the values of the top quark and Higgs boson masses, and the most up-to-date analyses show that the SM vacuum is not absolutely stable [28–31]. This provokes questions about the influence of new physics on this result.

In chapter 5 we introduce the basic tool which allows the study of vacuum states — the effective potential. We show why it is well suited for our study and derive formulas for the one-loop contributions to the effective potential coming from different types of particles.

Next, in chapter 6, we study the stability of the vacuum state in the IDM using the effective potential formalism. The analysis is performed from two perspectives. First, we assume that the additional inert scalars are heavy and decoupled. This way they enter the effective potential only via loop corrections so only the Higgs field is dynamical and can develop a vacuum expectation value (VEV). This approach allows us to study the impact of the inert scalars on the SM-like inert vacuum state. It appears that in fact the new scalars can, in principle, destabilise the vacuum state. However, we show that this option is excluded in the IDM by the parameter space constraints.

Within the second approach all the scalar fields can acquire a VEV which allows us to study the coexistence of the inert and inert-like minima beyond tree level. We show that the loop corrections may have important consequences for the vacuum structure of the model — they can invert the hierarchy of coexisting minima such that the minimum which was global at tree level, at one-loop level becomes a local one.

In the closing part of chapter 6 we discuss a possible way of studying the vacuum structure of models with an extended scalar sector in full generality. We present a method of consistently using the effective potential in presence of many energy scales associated with the new scalar fields, and discuss possible problems with applying it in practice.

Chapter 7 contains a summary of the presented results, as well as a brief presentation of some open questions. There are also appendices, where additional information and derivations are collected. Appendix A contains a discussion of the appropriate choice for the range of the mixing angle α. Appendix B summarises the formulas for the decay widths of the Higgs boson, used in the computations presented in chapter 4. The details of dimensional regularisation of the one-loop contribution to the effective potential are described in appendix C. Derivation of and formulas for the one-loop self-energies of the scalar particles in the IDM, which were needed for the considerations presented in chapter 6, are given in appendix D.

Chapter 2

Models with extended scalar sector — Two-Higgs-Doublet Models

The present thesis is focused on studying the Higgs boson, its properties and relation to the issue of vacuum stability in models with extended scalar sector. In particular, the Inert Doublet Model (IDM), which is a special type of a Two-Higgs-Doublet Model (2HDM) is of main interest. In this chapter we will briefly introduce these models, specifying the lagrangian, its symmetries, and the possible vacuum states.

2.1 Lagrangian of 2HDM

2HDMs are extensions of the SM containing two, instead of one, scalar $SU(2)$ doublets, for a recent review see ref. [32]. Both doublets have weak hypercharge equal 1. The doublets will be denoted by ϕ_S and ϕ_D throughout this thesis.

In general, a 2HDM is described by the following lagrangian

$$\mathcal{L} = \mathcal{L}_{\text{SM}} + \mathcal{L}_H + \mathcal{L}_Y,$$

where $\mathcal{L}_{\text{SM}}$ denotes the SM part of the lagrangian, i.e. defines interactions of the fermions and gauge bosons with the gauge group $SU(3)_C \times SU(2)_L \times U(1)_Y$. The part of the lagrangian $\mathcal{L}_H$ describes the interactions of the scalar fields,

$$\mathcal{L}_H = (D_\mu \phi_S)^\dagger (D^\mu \phi_S) + (D_\mu \phi_D)^\dagger (D^\mu \phi_D) - V.$$

V is the scalar potential. The symbol D_μ denotes the covariant derivative, defined as follows

$$D_\mu = \partial_\mu + \frac{ig}{2}\tau_a W_\mu^a + \frac{ig'}{2} Y B_\mu,$$

where W_μ^a and B_μ are the gauge fields, and τ_a, and Y are the generators of the groups $SU(2)_L$, and $U(1)_Y$, respectively ($Y = \mathbb{I}_{2\times 2}$). The kinetic terms for the scalars introduce the gauge-scalar interactions, and these are the terms that generate the masses of the gauge bosons after SSB.

$\mathcal{L}_Y$ defines interactions between fermions and scalar fields, called the Yukawa interactions. In presence of two scalar doublets flavour-changing neutral currents (FCNC), which are strongly constrained experimentally, arise naturally. However, if all fermions with the same electric charge and helicity couple to the same scalar doublet, there is no possibility of mixing [33, 34]. To assure that, discrete symmetries (typically $\mathbb{Z}_2$) are imposed on the 2HDM lagrangian, and thus different types of Yukawa interactions arise. The two basic types, to be discussed in this work, are type I, and type II.

In type I all the quarks couple to a single scalar doublet, here it is ϕ_S, and the corresponding discrete symmetry is defined as $\phi_D \to -\phi_D$.

In type II the up-type right-handed quarks d_R couple to one of the doublets (ϕ_S), and the down-type right-handed quarks to the other (ϕ_D). The corresponding symmetry is $\phi_D \to -\phi_D$, $d_R \to -d_R$.

2.2 Potential

The most general potential of a 2HDM reads [35–38]

$$\begin{aligned} V = &-\frac{1}{2}\left[m_{11}^2 \phi_S^\dagger \phi_S + m_{22}^2 \phi_D^\dagger \phi_D + (m_{12}^2 \phi_D^\dagger \phi_S + \text{h.c.})\right] \\ &+ \frac{1}{2}\left[\lambda_1 (\phi_S^\dagger \phi_S)^2 + \lambda_2 (\phi_D^\dagger \phi_D)^2\right] + \lambda_3 (\phi_S^\dagger \phi_S)(\phi_D^\dagger \phi_D) + \lambda_4 (\phi_S^\dagger \phi_D)(\phi_D^\dagger \phi_S) \\ &+ \left[\frac{1}{2}\lambda_5 (\phi_S^\dagger \phi_D)^2 + \left(\lambda_6 \phi_D^\dagger \phi_D + \lambda_7 \phi_S^\dagger \phi_S\right)(\phi_D^\dagger \phi_S) + \text{h.c.}\right], \end{aligned}$$

where the parameters can, in principle, be complex. However, the requirement that V is a hermitean function forces that $\lambda_1, \ldots, \lambda_4$, m_{11}^2, m_{22}^2 are real numbers.

As was explained above, the most general 2HDM with no additional symmetries imposed, will in general lead to large FCNC. To avoid that, in this work we assume a $\mathbb{Z}_2$ symmetry of the potential. The most general $\mathbb{Z}_2$-symmetric 2HDM potential

reads

$$V = -\frac{1}{2}\left[m_{11}^2(\phi_S^\dagger\phi_S) + m_{22}^2(\phi_D^\dagger\phi_D)\right] + \frac{1}{2}\left[\lambda_1(\phi_S^\dagger\phi_S)^2 + \lambda_2(\phi_D^\dagger\phi_D)^2\right] + \lambda_3(\phi_S^\dagger\phi_S)(\phi_D^\dagger\phi_D) + \lambda_4(\phi_S^\dagger\phi_D)(\phi_D^\dagger\phi_S) + \frac{1}{2}\lambda_5\left[(\phi_S^\dagger\phi_D)^2 + (\phi_D^\dagger\phi_S)^2\right], \quad (2.1)$$

where $\lambda_6 = \lambda_7 = m_{12}^2 = 0$. Moreover, without loss of generality, the parameters can be chosen to be real, and we can assume that $\lambda_5 < 0$ (the choice $\lambda_5 > 0$ is equivalent from the physical point of view).

2.2.1 Symmetry of the potential

Saying that the potential (2.1) is $\mathbb{Z}_2$-symmetric is not enough, since in fact it possesses a "double" symmetry: $\mathbb{Z}_2 \times \mathbb{Z}_2$. The two transformations which are preserved are defined as follows

$$S : \phi_S \to -\phi_S, \quad \phi_D \to \phi_D, \qquad D : \phi_S \to \phi_S, \quad \phi_D \to -\phi_D. \quad (2.2)$$

At the level of the potential the S and D symmetries are absolutely equivalent — the roles of the doublets ϕ_S and ϕ_D can be easily exchanged with a global rephasing of the fields, which does not have any physical meaning. However, once Yukawa interactions are fixed the roles of the doublets are settled, and they can no longer be interchanged. In particular, lagrangians with Yukawa interaction of type I or II are only D-symmetric, and not S-symmetric. So with the choice of the Yukawa model, the initial $\mathbb{Z}_2 \times \mathbb{Z}_2$ symmetry of the potential is reduced to a single $\mathbb{Z}_2$.

2.2.2 Extrema of the potential

The theory should be built around the minimum of the potential, i.e. around a state with vacuum expectation values (VEV) fulfilling the extremum conditions (this is a necessary condition)

$$\left.\frac{\partial V}{\partial \phi_i}\right|_{\phi_i=\langle\phi_i\rangle} = 0, \qquad \left.\frac{\partial V}{\partial \phi_i^\dagger}\right|_{\phi_i=\langle\phi_i\rangle} = 0, \qquad i = D, S. \quad (2.3)$$

There are different possible patterns of symmetry breaking [39]. In general the VEVs can be written as follows

$$\langle\phi_S\rangle = \frac{1}{\sqrt{2}}\begin{pmatrix} 0 \\ v_S \end{pmatrix}, \quad \langle\phi_D\rangle = \frac{1}{\sqrt{2}}\begin{pmatrix} u \\ v_D e^{i\xi} \end{pmatrix}, \quad (2.4)$$

where $v_S^2 + v_D^2 + u^2 = v^2 = \frac{1}{\sqrt{2}G_F} \approx (246\,\mathrm{GeV})^2$. Depending on whether v_S, v_D and u are zero or not, different extrema of the potential are possible [39–42]. Below we discuss these types.

Electroweak symmetry conserving extremum. The EW symmetry conserving extremum is realised when both of the doublets have a zero VEV, as follows

$$\langle \phi_S \rangle = 0, \quad \langle \phi_D \rangle = 0.$$

With this vacuum state all the fermions and gauge bosons are massless, so definitely it is not the true vacuum state of the theory today. However it is expected that such a symmetric state was the ground state before EWSB.

Charge-breaking extremum. When the charged component of a scalar field acquires a non-zero VEV

$$\langle \phi_S \rangle = \frac{1}{\sqrt{2}} \begin{pmatrix} 0 \\ v_S \end{pmatrix}, \quad \langle \phi_D \rangle = \frac{1}{\sqrt{2}} \begin{pmatrix} u \\ v_D \end{pmatrix},$$

the electromagnetic $U(1)$ symmetry is spontaneously broken, and the photon gets a non-zero mass. This is of course unacceptable from the todays phenomenological point of view. However, in principle such a state could have been a vacuum during the evolution of the Universe.

CP violating extremum. CP violating extremum appears when there is a non-zero phase difference between the VEVs of the neutral components of the scalar doublets,

$$\langle \phi_S \rangle = \frac{1}{\sqrt{2}} \begin{pmatrix} 0 \\ v_S \end{pmatrix}, \quad \langle \phi_D \rangle = \frac{1}{\sqrt{2}} \begin{pmatrix} 0 \\ v_D e^{i\xi} \end{pmatrix}.$$

However, appearance of this phase does not necessarily mean that CP is spontaneously violated. For example, in the case of $\mathbb{Z}_2$-symmetric potential CP is conserved but a non-zero phase may appear. It has been shown using a transformation $\lambda_5 \to -\lambda_5$ that this case is equivalent to having two real VEVs [42].

Mixed (normal) extremum. The mixed or normal extremum is realised when both of the neutral components of the scalar doublets have non-zero VEVs

$$\langle \phi_S \rangle = \frac{1}{\sqrt{2}} \begin{pmatrix} 0 \\ v_S \end{pmatrix}, \quad \langle \phi_D \rangle = \frac{1}{\sqrt{2}} \begin{pmatrix} 0 \\ v_D \end{pmatrix}. \tag{2.5}$$

This vacuum violates the $\mathbb{Z}_2$ symmetry of the potential spontaneously. It is very well studied, as it forms the ground state of supersymmetric models, as well as general 2HDMs.

Inert extremum. The inert extremum is characterised by only ϕ_S having a non-zero VEV

$$\langle\phi_S\rangle = \frac{1}{\sqrt{2}}\begin{pmatrix}0\\ v\end{pmatrix}, \quad \langle\phi_D\rangle = \frac{1}{\sqrt{2}}\begin{pmatrix}0\\ 0\end{pmatrix}. \tag{2.6}$$

This vacuum state is symmetric under the D transformation, but violates the S symmetry of the potential.

Inert-like extremum. The inert-like extremum is an analog of the inert one, with the roles of ϕ_S and ϕ_D exchanged,

$$\langle\phi_S\rangle = \frac{1}{\sqrt{2}}\begin{pmatrix}0\\ 0\end{pmatrix}, \quad \langle\phi_D\rangle = \frac{1}{\sqrt{2}}\begin{pmatrix}0\\ v\end{pmatrix}. \tag{2.7}$$

This state violates the D, and preserves the S symmetry.

It should be underlined that the inert and inert-like states are not limiting cases of the mixed state. It can be shown as follows. When $u, \xi = 0$ is assumed in (2.4), the extremum conditions (2.3) take the following simple form [39]

$$v_S\left(\lambda_{345}v_D^2 + \lambda_1 v_S^2 - m_{11}^2\right) = 0, \tag{2.8}$$

$$v_D\left(\lambda_{345}v_S^2 + \lambda_2 v_D^2 - m_{22}^2\right) = 0. \tag{2.9}$$

The values of the VEVs in the mixed state are obtained with the assumption $v_S, v_D \neq 0$ so the expressions in brackets in the extremum conditions, eqs. (2.8), (2.9), must vanish. On the other hand, the solutions for the inert and inert-like states are obtained with the assumption $v_D = 0$ or $v_S = 0$, respectively, and thus only one of the expressions in brackets must vanish. Therefore, the relations between the parameters in the mixed and inert/inert-like extrema are different. In particular, the inert state could be considered a limiting case of the mixed one, only if together with the assumption $v_D \to 0$ one simultaneously requires that the expression in bracket in eq. (2.9) vanishes.

In principle, the potential for a given set of parameters can develop several minima with different properties (i.e. the minimisation conditions can have multiple solutions). It has been checked that if the mixed minimum exists it has to be a global one, and inert or inert-like minima cannot coexist with it [43–45]. On the other hand, the inert and inert-like minima can be developed simultaneously [41]. This coexistence is studied in detail in section 6.3.

Depending on which of the minima is the global one (i.e. which is the ground state of the theory) the resulting models will have different properties. We reserve the name 2HDM to refer to a general class of models with two scalar doublets. The

specific models studied in this thesis are the 2HDM (mixed), which has a mixed state as a vacuum state, and the IDM with the inert vacuum. Below we review the properties of these models. We also review the properties of the inert-like minimum which will be useful for the study of coexistence of inert and inert-like minima.

2.3 2HDM (mixed)

A version of the 2HDM with the potential (2.1) and a normal (mixed) vacuum state (i.e. where both of the doublets acquire non-zero VEVs) will be referred to as 2HDM (mixed).[1] The VEVs are given by eq. (2.5) and the vacuum state spontaneously breaks both the D and the S symmetry.

The doublets can be decomposed around the minimum as follows

$$\phi_S = \frac{1}{\sqrt{2}} \begin{pmatrix} \sqrt{2}\rho_S^+ \\ v_S + \rho_S + i\chi_S \end{pmatrix}, \quad \phi_D = \frac{1}{\sqrt{2}} \begin{pmatrix} \sqrt{2}\rho_D^+ \\ v_D + \rho_D + i\chi_D \end{pmatrix}, \tag{2.10}$$

where $v_S^2 + v_D^2 = v^2 = (246\,\mathrm{GeV}^2)$. The component fields appearing above are not mass-eigenstates. Mass-eigenstates are mixtures of the $\rho_K^\pm$, ρ_K and χ_K ($K = S,\ D$), namely

$$\begin{pmatrix} G^\pm \\ H^\pm \end{pmatrix} = R(\beta) \begin{pmatrix} \rho_S^\pm \\ \rho_D^\pm \end{pmatrix}, \quad \begin{pmatrix} G \\ A \end{pmatrix} = R(\beta) \begin{pmatrix} \chi_S \\ \chi_D \end{pmatrix}, \quad \begin{pmatrix} H \\ h \end{pmatrix} = R(\alpha) \begin{pmatrix} \rho_S \\ \rho_D \end{pmatrix},$$

where R denotes a rotation matrix of an angle α or β, $\alpha \in (-\pi/2,\ \pi/2)$, $\beta \in (0,\ \pi/2)$ and $\tan\beta = \frac{v_D}{v_S}$. R is defined as follows

$$R = \begin{pmatrix} \cos\alpha & \sin\alpha \\ -\sin\alpha & \cos\alpha \end{pmatrix}.$$

In the literature one may encounter some confusions about the appropriate range for the angle α. To clarify this point and justify our convention stated above we discuss this issue in detail in appendix A.

In the particle spectrum of the model there are two neutral CP-even scalars h and H, h being lighter than H. These are two possible candidates for the Higgs boson, both of the scenarios are possible. Moreover, there is a pseudoscalar A and

[1] In the literature it is most often called simply 2HDM, however here we need a clear distinction between a general class of models, and a model with the particular vacuum state, as explained before.

a charged Higgs boson $H^\pm$. The physical masses of the scalar particles read

$$\begin{aligned}
M_{H^\pm}^2 &= -\frac{1}{2}(\lambda_4+\lambda_5)v^2,\\
M_A^2 &= -\lambda_5 v^2,\\
M_H^2 &= \frac{1}{2}\Big(\lambda_1 v_S^2+\lambda_2 v_D^2+\sqrt{(\lambda_1 v_S^2-\lambda_2 v_D^2)^2+4\lambda_{345}^2 v_S^2 v_D^2}\Big),\\
&= \frac{v^2}{2}\frac{1}{1+\tan^2\beta}\Big(\lambda_1+\lambda_2\tan^2\beta+\sqrt{(\lambda_1-\lambda_2\tan^2\beta)^2+4\lambda_{345}^2\tan^2\beta}\Big),\\
M_h^2 &= \frac{1}{2}\Big(\lambda_1 v_S^2+\lambda_2 v_D^2-\sqrt{(\lambda_1 v_S^2-\lambda_2 v_D^2)^2+4\lambda_{345}^2 v_S^2 v_D^2}\Big).\\
&= \frac{v^2}{2}\frac{1}{1+\tan^2\beta}\Big(\lambda_1+\lambda_2\tan^2\beta-\sqrt{(\lambda_1-\lambda_2\tan^2\beta)^2+4\lambda_{345}^2\tan^2\beta}\Big).
\end{aligned} \tag{2.11}$$

It is convenient to study the model with the use of physical masses, and the mixing angles (most frequently $\tan\beta$ and $\sin\alpha$, or $\sin(\beta-\alpha)$). The parameters $\lambda_1,\dots,\lambda_5$ are expressed through these parameters as [38]

$$\begin{aligned}
\lambda_1 &= \frac{1}{v^2\cos^2\beta}(M_H^2\cos^2\alpha+M_h^2\sin^2\alpha),\\
\lambda_2 &= \frac{1}{v^2\sin^2\beta}(M_H^2\sin^2\alpha+M_h^2\cos^2\alpha),\\
\lambda_3 &= \frac{\sin 2\alpha}{v^2\sin 2\beta}(M_H^2-M_h^2)+\frac{2M_{H^\pm}^2}{v^2},\\
\lambda_4 &= \frac{1}{v^2}(M_A^2-2M_{H^\pm}^2),\\
\lambda_5 &= -\frac{1}{v^2}M_A^2.
\end{aligned} \tag{2.12}$$

2.4 Inert Doublet Model

The IDM [39, 46, 47] is a 2HDM with a scalar potential of the form of eq. (2.1), and the inert vacuum state of the form (2.6). Both the potential V, and the vacuum state are symmetric under the D symmetry defined in eq. (2.2) (with $\Psi\to\Psi$, where Ψ denotes the SM fields). In order to preserve this symmetry, Yukawa interactions are set to type I, i.e. only the ϕ_S doublet couples to fermions. This way the D symmetry is exact in the IDM.

The doublets can be decomposed around the minimum in the following way

$$\phi_S=\frac{1}{\sqrt{2}}\begin{pmatrix}\sqrt{2}G^+\\ v+h+iG\end{pmatrix},\quad \phi_D=\frac{1}{\sqrt{2}}\begin{pmatrix}\sqrt{2}H^+\\ H+iA\end{pmatrix}.$$

The second derivative of the potential, i.e. the mass matrix, is diagonal in the basis composed of the fields $G, G^\pm, h, H, A, H^\pm$ at the minimum so these are the mass-eigenstates. G and $G^\pm$ correspond to the massless Goldstone bosons, and the remaining fields correspond to physical scalar particles. Their tree-level masses read (we decompose $H^\pm$ and $G^\pm$ into real component fields as $H^\pm = H_1^\pm + iH_2^\pm$, $G^\pm = G_1^\pm + iG_2^\pm$)

$$\begin{aligned}
M_h^2 &= \left.\frac{\partial^2 V}{\partial h^2}\right|_I = -\frac{1}{2}m_{11}^2 + \frac{3}{2}\lambda_1 v^2 = \lambda_1 v^2 = m_{11}^2, \\
M_{H^\pm}^2 &= \left.\frac{\partial^2 V}{\partial H_1^{\pm 2}}\right|_I = \left.\frac{\partial^2 V}{\partial H_2^{\pm 2}}\right|_I = \frac{1}{2}\left(-m_{22}^2 + \lambda_3 v^2\right), \\
M_A^2 &= \left.\frac{\partial^2 V}{\partial A^2}\right|_I = \frac{1}{2}\left(-m_{22}^2 + \lambda_{345}^- v^2\right), \\
M_H^2 &= \left.\frac{\partial^2 V}{\partial H^2}\right|_I = \frac{1}{2}\left(-m_{22}^2 + \lambda_{345} v^2\right), \\
M_G^2 &= \left.\frac{\partial^2 V}{\partial G^2}\right|_I = \frac{1}{2}\left(-m_{11}^2 + \lambda_1 v^2\right) = 0, \\
M_{G^\pm}^2 &= \left.\frac{\partial^2 V}{\partial G_1^{\pm 2}}\right|_I = \left.\frac{\partial^2 V}{\partial G_2^{\pm 2}}\right|_I = \frac{1}{2}\left(-m_{11}^2 + \lambda_1 v^2\right) = 0,
\end{aligned} \tag{2.13}$$

where the subscript I indicates that the derivatives were computed in the inert vacuum state defined in eq. (2.6), and $\lambda_{345} = \lambda_3 + \lambda_4 + \lambda_5$, and $\lambda_{345}^- = \lambda_3 + \lambda_4 - \lambda_5$.

The boson h is a SM-like Higgs boson. It couples at tree level to fermions and gauge bosons just like the SM Higgs. The fields originating from the ϕ_D doublet are referred to as dark or inert scalars, as they do not couple to fermions. Their couplings to gauge bosons come from the covariant derivative. Due to the $\mathbb{Z}_2$ symmetry the dark scalars can appear in interaction vertices only in pairs. H and A are electrically neutral, and $H^\pm$ is a pair of charged scalar particles.

Due to exact conservation of the D symmetry, a new conserved quantum number can be introduced: D parity. The dark particles are odd under D, and all other are even. As a consequence of the conservation of D, the lightest D-odd particle is stable, and thus constitutes a dark matter (DM) candidate, provided that is electrically neutral. In the IDM the potential DM candidates are A and H. The two choices are equivalent, they differ only by the choice of the sign of λ_5. Here we choose $\lambda_5 < 0$, and thus $M_H < M_A$, and also $M_H < M_{H^\pm}$, which implies

$$\lambda_4 + \lambda_5 < 0. \tag{2.14}$$

The IDM can be parametrized by the original parameters appearing in the potential, i.e. m_{11}^2, m_{22}^2, $\lambda_1, \ldots, \lambda_5$ (where m_{11}^2 is fixed by the first line of eq. (2.13)). Alternatively, one may use sets of parameters containing the physical masses of the scalar particles. Two such sets used in this work are: $m_{22}^2, \lambda_2, M_h, M_H, M_A, M_{H^\pm}$, and

$\lambda_2, \lambda_{345}, M_h, M_H, M_A, M_{H^\pm}$. Useful relations inverse to those given in (2.13), which allow to switch between the parameter sets, read

$$\begin{aligned}
\lambda_1 &= \frac{M_h^2}{v^2}, \\
\lambda_3 &= \frac{1}{v^2}\left(2M_{H^\pm}^2 + m_{22}^2\right) = \frac{2}{v^2}\left(M_{H^\pm}^2 - M_H^2\right) + \lambda_{345}, \\
\lambda_4 &= \frac{1}{v^2}\left(M_H^2 + M_A^2 - 2M_{H^\pm}^2\right), \\
\lambda_5 &= \frac{1}{v^2}\left(M_H^2 - M_A^2\right), \\
m_{22}^2 &= -2M_H^2 + \lambda_{345}v^2.
\end{aligned} \tag{2.15}$$

2.5 Inert-like vacuum

The inert-like vacuum state, defined in eq. (2.7), is an analog of the inert state with the roles of ϕ_S and ϕ_D exchanged. A model with an inert-like vacuum state and Yukawa interactions defined such that only ϕ_D couples to fermions would be exactly equivalent to the IDM. However, if ordinary type I of Yukawa interactions is considered, then the fermions are massless in this minimum. Moreover, massive scalars from the ϕ_S doublet couple to the massless fermions and are thus very unstable. This is certainly an unphysical situation and should be avoided. This is particularly important when the IDM is considered — as was explained before the inert and inert-like minima can coexist in this model and we should make sure that the inert minimum is the proper ground state of the theory. This condition at tree level is discusses in section 3.1.2, and at one-loop level in section 6.3. To study the properties of this minimum the tree-level masses of the scalar particles will be needed.

In the inert-like minimum the scalar doublets can be decomposed as follows

$$\phi_S = \frac{1}{\sqrt{2}}\begin{pmatrix} \sqrt{2}H^+ \\ H + iA \end{pmatrix}, \quad \phi_D = \frac{1}{\sqrt{2}}\begin{pmatrix} \sqrt{2}G^+ \\ v + h + iG \end{pmatrix}.$$

The fields present in the above formula are all mass-eigenstates. G and $G^\pm$ are the Goldstone bosons, h is the Higgs boson, and H, A and $H^\pm$ are massive scalars. One should note that the field names are the same as in the case of the inert vacuum but they do not correspond to the same particles as the roles of ϕ_S and ϕ_D are exchanged.

The masses of the particles read

$$\begin{aligned}
M_h^2 &= \left.\frac{\partial^2 V}{\partial h^2}\right|_{IL} = -\frac{1}{2}m_{22}^2 + \frac{3}{2}\lambda_2 v^2 = \lambda_2 v^2 = m_{22}^2, \\
M_{H^\pm}^2 &= \left.\frac{\partial^2 V}{\partial H_1^{\pm 2}}\right|_{IL} = \left.\frac{\partial^2 V}{\partial H_2^{\pm 2}}\right|_{IL} = \frac{1}{2}\left(-m_{11}^2 + \lambda_3 v^2\right), \\
M_A^2 &= \left.\frac{\partial^2 V}{\partial A^2}\right|_{IL} = \frac{1}{2}\left(-m_{11}^2 + \lambda_{345}^- v^2\right), \\
M_H^2 &= \left.\frac{\partial^2 V}{\partial H^2}\right|_{IL} = \frac{1}{2}\left(-m_{11}^2 + \lambda_{345} v^2\right), \\
M_G^2 &= \left.\frac{\partial^2 V}{\partial G^2}\right|_{IL} = \frac{1}{2}\left(-m_{22}^2 + \lambda_2 v^2\right) = 0, \\
M_{G^\pm}^2 &= \left.\frac{\partial^2 V}{\partial G_1^{\pm 2}}\right|_{IL} = \left.\frac{\partial^2 V}{\partial G_2^{\pm 2}}\right|_{IL} = \frac{1}{2}\left(-m_{22}^2 + \lambda_2 v^2\right) = 0,
\end{aligned} \tag{2.16}$$

where the subscript IL indicates that the derivatives were computed in the inert-like minimum. These masses can be obtained from the masses in the inert minimum with an exchange $m_{11}^2 \to m_{22}^2$ and $\lambda_1 \to \lambda_2$ but one has to remember that the origin of respective particles is different in the inert-like minimum than in the inert one.

Chapter 3

Constraints on 2HDMs

Every model of new physics should be theoretically self-consistent and stay in agreement with the available experimental data. This poses diverse constraints on the parameter space of a given model. In this chapter we review the constraints that can be imposed on $\mathbb{Z}_2$-symmetric 2HDMs (the IDM and the 2HDM (mixed)). On the side of theory these include: positivity of the scalar potential, stability of the vacuum state and perturbative unitarity. Among the experimental constrains are the electroweak precision tests (EWPT) applied in terms of the oblique parameters S and T, constraints from the LEP experiment, flavour physics constraints, the bound from the LHC, and the DM related constraints. Since the presence of the DM candidate is an important feature of the IDM we review the issue of DM in more detail, giving motivation for the existence of DM, describing DM detection experiments, and the constraints from the measurements of the DM relic density.

In the next parts of this chapter we present the allowed parameter space for the IDM (section 3.5) and for the 2HDM (mixed) (section 3.4) resulting from imposition of the basic constraints (positivity of the potential, perturbative unitarity, EWPT, LEP constraints, Higgs mass). The results described here are mostly based on our work presented in ref. [5] (see also refs. [6, 17, 48]).

In the literature there exist several analyses of the parameter space of different types of 2HDMs, see e.g. [46, 49–65].[1] The features of our analysis presented here that distinguish it from other works are: careful treatment of the vacuum stability condition — we required that the vacuum state is not only a minimum, it should be a

[1] Here we mention only the references studying the basic constraints similarly to the analysis presented in this chapter. Subsequently, there appeared many papers studying various experimental constraints like the DM relic abundance and the LHC constraints.

global minimum, which gave us an important constraint on the mass parameter of the scalar potential; we considered the full scattering matrix of the scalar sector, including also doubly charged channels; our analysis for the 2HDM (mixed) is independent of the type of Yukawa interactions chosen, which makes the results very universal; we combined the information on the mass of the Higgs boson with perturbative unitarity constraints which gave stringent bounds on the parameter $\tan\beta$ which had not been known before.

3.1 Theoretical constraints

3.1.1 Positivity

In order to allow for a stable vacuum state (a global minimum of the potential), the scalar potential of the model should be bounded from below, i.e. it should not tend to minus infinity for any direction in the field space. Concrete bounds for the parameters of the potential are found by considering the potential along different directions, and demanding that the limit at infinity is positive. For potential (2.1), at tree level, this is assured by the following conditions [39, 66]

$$\lambda_1 > 0, \quad \lambda_2 > 0, \quad \lambda_3 + \sqrt{\lambda_1 \lambda_2} > 0, \quad \lambda_{345} + \sqrt{\lambda_1 \lambda_2} > 0. \tag{3.1}$$

These conditions are also often referred to as stability conditions (or vacuum stability conditions, even though they are only the necessary conditions, and not sufficient) or boundedness-from-below conditions. Second and third of these conditions are illustrated in figure 3.1 (it is only valid for the IDM since λ_1 is fixed to 0.26, as follows from eq. (2.13) with $M_h = 125\,\text{GeV}$, $v = 246\,\text{GeV}$.).

Discussion of positivity at loop level is more involved, since the effective potential has to be examined, and we postpone it to chapter 6.

3.1.2 Stability of the vacuum state

A model is always built around a vacuum state which should be stable. To be so, it has to correspond to a global minimum of the scalar potential. Therefore, the state playing the role of the vacuum has to be

(i) a stationary point, fulfilling eq. (2.3),

(ii) a minimum, i.e. the matrix of second derivatives of the potential in this state should be positive definite.

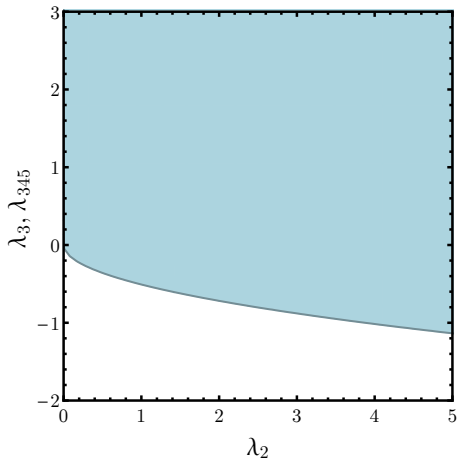

Figure 3.1: Region allowed by positivity constraints, eq. (3.1) (second and third condition) in the (λ_2, λ_3) and $(\lambda_2, \lambda_{345})$ planes. The value of λ_1 is fixed to 0.26, which is the value given in the IDM by the measurement of the Higgs boson mass (see eq. (2.13)).

This means that the masses squared of all the particles must be positive,

$$M_h^2,\, M_H^2,\, M_A^2,\, M_{H^\pm}^2 \geqslant 0. \tag{3.2}$$

In the case of the IDM this conditions give

$$m_{11}^2 > 0, \tag{3.3}$$

and a set of constraints for $\lambda_3, \lambda_{345}, \lambda_{345}^-$ and m_{22}^2, which can be easily obtained from the expressions for masses, eq. (2.13).

In the case of the 2HDM (mixed), conditions derived the same way can be simplified, and expressed as

$$\begin{aligned} &v_S^2 = \frac{m_{11}^2\lambda_2 - \lambda_{345}m_{22}^2}{\lambda_1\lambda_2 - \lambda_{345}^2} > 0, \quad v_D^2 = \frac{m_{22}^2\lambda_1 - \lambda_{345}m_{11}^2}{\lambda_1\lambda_2 - \lambda_{345}^2} > 0, \\ &\lambda_4 + \lambda_5 < 0, \quad \lambda_5 < 0, \quad \lambda_1\lambda_2 - \lambda_{345}^2 > 0. \end{aligned} \tag{3.4}$$

Moreover, the vacuum state should correspond to a minimum that is deeper than any other minimum (i.e. a global minimum).[2] It has been shown that once a mixed state (2.5) is a minimum, then it is a global one [41]. However, the inert minimum (2.6) can coexist with an inert-like one (2.7). In this case the energies (depths) of the minima should be compared. The inert one is deeper if [5, 41, 67]

$$\frac{m_{11}^2}{\sqrt{\lambda_1}} > \frac{m_{22}^2}{\sqrt{\lambda_2}}. \tag{3.5}$$

[2]Metastable states could also be allowed as vacua. However, we do not consider this case in this chapter, for a more detailed discussion see sections 6.1 and 6.2.

This condition can be translated to a constraint for m_{22}^2 if the parameters m_{11}^2 and λ_1 are expressed in terms of M_h and v (eq. (2.13))

$$m_{22}^2 < \sqrt{\lambda_2} M_h v. \tag{3.6}$$

In the next section we present an upper bound on λ_2, $\lambda_2 < 8.38$ (see eq. (3.13)). Anticipating this result and using the values $M_h = 125\,\mathrm{GeV}$ and $v = 246\,\mathrm{GeV}$ we obtain an upper bound on the value of the m_{22}^2 parameter [5]

$$m_{22}^2 \lesssim 9 \cdot 10^4\,\mathrm{GeV}^2. \tag{3.7}$$

As is shown in section 4.1, where the diphoton Higgs decay signal strength within the IDM is analysed, this constraint can have significant influence on the phenomenological predictions of the model.

3.1.3 Perturbative unitarity

The S matrix unitarity condition, $SS^\dagger = \mathbf{1}$, when translated into the language of partial wave amplitudes $a^j(s)$, gives for an elastic processes:

$$\left[\mathrm{Re}\left(a^j(s)\right)\right]^2 + \left[\mathrm{Im}\left(a^j(s)\right) + \frac{s}{2\sqrt{\lambda(s, m_1, m_2)}}\right]^2 = \frac{s^2}{4\lambda(s, m_1, m_2)} - A^2, \tag{3.8}$$

where A is a non-negative constant,[3] s is the center-of-mass energy of the process, m_1 and m_2 are masses of the particles involved in the scattering, and λ is defined as

$$\lambda(x, y, x) = x^2 + y^2 + z^2 - 2xy - 2xz - 2yz.$$

Equation (3.8) means that the partial wave amplitudes of elastic scattering processes lie on the so-called Argand circle, which is depicted schematically in fig. 3.2. From the properties of the circle it follows that:

$$\left|\mathrm{Re}\left(a^j(s)\right)\right| \leqslant \frac{s}{2\sqrt{\lambda(s, m_1, m_2)}},$$
$$\left|a^j(s)\right| \leqslant \frac{s}{\sqrt{\lambda(s, m_1, m_2)}},$$

which in the high energy limit ($s \gg m_i^2$) implies that the partial wave amplitudes are constrained as follows:

$$\left|\mathrm{Re}\left(a^j(s)\right)\right| \leqslant \frac{1}{2} \tag{3.9}$$
$$\left|a^j(s)\right| \leqslant 1. \tag{3.10}$$

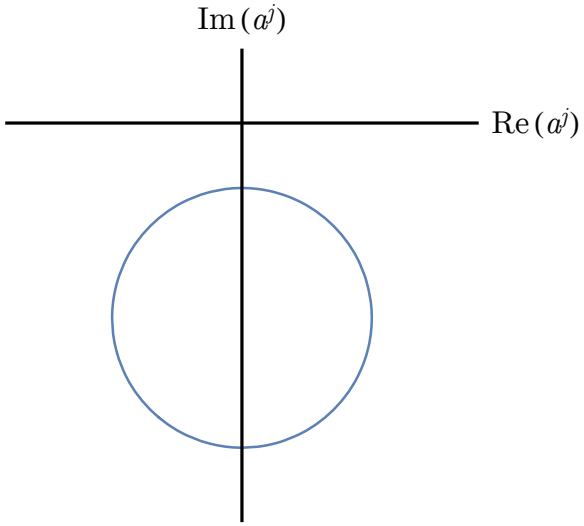

Figure 3.2: The Argand circle.

What should be underlined is that all above equations apply to the full amplitudes, i.e. to the solutions of the full theory, not its perturbative expansion.

When perturbation theory is concerned things cease to be that straightforward. All we know is that the full amplitudes lie on the circle (3.8). However, this does not necessarily apply to perturbative approximations. In particular, for the tree-level amplitude it is usually impossible to lie on the circle as it tends to be real. So the higher order corrections have to bring the full amplitude back to the circle. But if the theory is to be perturbative, the higher order corrections should be small compared to the zeroth order. Therefore for the theory to be perturbative and unitary it is necessary that the zeroth order amplitude lies "not too far" from the circle. Usually the condition of lying "not too far" is expressed by the requirement that the zeroth order amplitude fulfils either (3.9) or (3.10) (which means that the amplitude lies inside the circle). Here we will use the former one [54–56, 59]:

$$|\mathrm{Re}(a_0^{(0)}(s))| \leqslant \frac{1}{2}, \tag{3.11}$$

where $a_0^{(0)}(s)$ denotes the tree-level amplitude of the s wave. The choice of the perturbative unitarity condition is to some extent arbitrary; the following form $\left|a_0^{(0)}\right| \leqslant 1$ was also used in the literature [49–53, 57, 58, 68, 69].

A possible threat to unitarity is due to the scattering of the longitudinally polarised vector bosons, and the scalar particles are supposed to unitarise the scattering amplitudes. Because of the equivalence theorem [68–70], in the high-energy limit it is sufficient to take into account scattering of the Goldstone bosons instead of

[3]The exact value of A is not important for this reasoning, the definition of A can be found in ref. [48], on page 20.

the longitudinally polarized vector bosons, so only the scalar sector is of interest to us. Moreover, as the physical fields (mass eigenstates) are obtained from the original fields appearing in the basic Lagrangian by means of a unitary transformation and only the eigenvalues of the scattering matrix are important for the following analysis, it suffices to consider the scattering matrix between the original fields [54]. Therefore, using the high-energy formula for $a_0^{(0)}(s)$, the unitarity condition, eq. (3.11), can be re-expressed in terms of the eigenvalues Λ_i of the scattering matrix:

$$|\Lambda_i| \leqslant 8\pi. \tag{3.12}$$

The full scattering matrix of the scalar sector has dimension 25: there are 14 neutral channels [54], eight charged channels [55, 56] and three doubly charged channels [5, 6, 17, 48, 57, 58]. Diagonalisation of the scattering matrix leads to 12 distinct eigenvalues, being combinations of the quartic couplings λ_i,

$$\begin{aligned}
e_1 &= \lambda_3 + 2\lambda_4 - 3\lambda_5, \\
e_2 &= \lambda_3 - \lambda_5, \\
f_+ &= \lambda_3 + 2\lambda_4 + 3\lambda_5, \\
f_- &= \lambda_3 + \lambda_5, \\
f_1 &= \lambda_3 + \lambda_4, \\
a_\pm &= \frac{1}{2}\Big(3(\lambda_1+\lambda_2) \pm \sqrt{9(\lambda_1-\lambda_2)^2 + 4(2\lambda_3+\lambda_4)^2}\Big), \\
b_\pm &= \frac{1}{2}\Big(\lambda_1+\lambda_2 \pm \sqrt{(\lambda_1-\lambda_2)^2 + 4\lambda_4^2}\Big), \\
c_\pm &= \frac{1}{2}\Big(\lambda_1+\lambda_2 \pm \sqrt{(\lambda_1-\lambda_2)^2 + 4\lambda_5^2}\Big), \\
p_1 &= \lambda_3 - \lambda_4.
\end{aligned}$$

Applying eq. (3.12) to these eigenvalues gives a set o inequalities and leads to constraints for the parameter space of the model.

To obtain numerical bounds on the parameters $\lambda_1, \ldots, \lambda_5$, we solved these inequalities numerically by randomly scanning the parameter space of the model. In addition, we imposed also the positivity constraints, and the requirements $\lambda_5 < 0$ (see comment below eq. (2.1)), $\lambda_4 + \lambda_5 < 0$ (see eqs. (2.14) and (3.4)). The values of the parameters were chosen randomly from the following ranges: λ_1, $\lambda_2 \in (0, 35]$, $\lambda_5 \in [-20, 0)$, $\lambda_4 \in [-30, -\lambda_5)$, $\lambda_3 \in (-\sqrt{\lambda_1\lambda_2} - \lambda_4 - \lambda_5, 35]$. As a result we

obtained the overall bounds on the parameters λ_i which read

$$\begin{aligned} 0 \leqslant \lambda_1 &\leqslant 8.38, \\ 0 \leqslant \lambda_2 &\leqslant 8.38, \\ -6.05 \leqslant \lambda_3 &\leqslant 16.53, \\ -15.98 \leqslant \lambda_4 &\leqslant 5.93, \\ -8.34 \leqslant \lambda_5 &\leqslant 0. \end{aligned} \tag{3.13}$$

These bound are not very strong but comparing with the traditional bound from perturbativity $|\lambda_i| < 4\pi$ they present some improvement.

It should be underlined that the parameters $\lambda_1, \ldots, \lambda_5$ are interpreted here as parameters of the potential (2.1), with no reference to the vacuum state. This means that the constraints discussed here are universal for all 2HDMs with the same scalar potential. If some model-specific constraints are added to the analysis (such as conditions for stability of a particular vacuum state, or model-specific experimental constrains) more restrictive limits, which are valid only for a particular model, can be obtained. We present such limits for the 2HDM (mixed) and the IDM in sections 3.4 and 3.5, respectively.

The limits of eq. (3.13) do not give full information that can be derived from perturbative unitarity constraints, since in fact different parameters λ_i are correlated, and the allowed region is a complicated figure in a 5-dimensional space. To show some of the correlations we present some two-dimensional projections of the allowed regions in fig. 3.3.

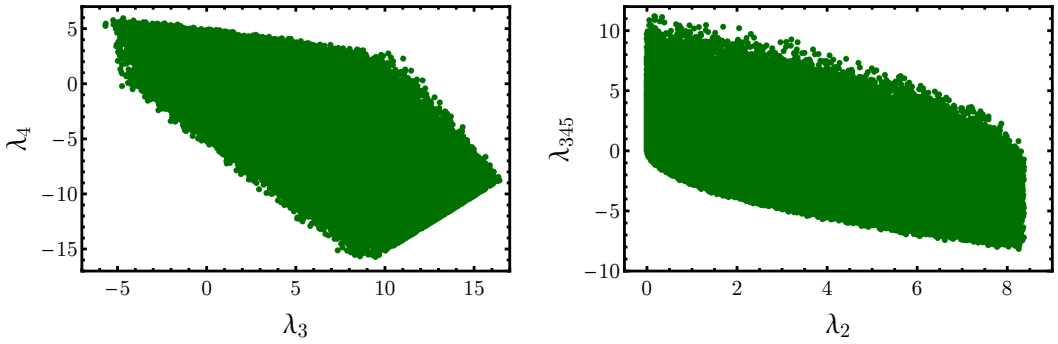

Figure 3.3: The allowed regions in the (λ_3, λ_4) and $(\lambda_2, \lambda_{345})$ planes.

Origin of some of the bounds visible in the plots can be easily identified, for example the sharp cutoff in the lower right part of the plot in fig. 3.3 (left panel) corresponds to the unitarity bound on the eigenvalue p_1 of the scattering matrix, which implies $\lambda_4 \geqslant \lambda_3 - 8\pi$ for $\lambda_3 \geqslant \lambda_4$. Similarly the upper bound on λ_2 visible in fig. 3.3 (right panel) originates from constraint on another eigenvalue: $|a_+| \leqslant$

8π, which for $\lambda_1 = \lambda_2$, $2\lambda_3 = -\lambda_4$ gives $\lambda_2 \leqslant \frac{8\pi}{3} \approx 8.38$. The lower border of the region in fig. 3.3 (right panel) corresponds to the positivity constraint, eq. (3.1), $\lambda_{345} + \sqrt{\lambda_1\lambda_2} > 0$ with maximal value of λ_1 inserted (see eq. (3.13)): $\lambda_1 = 8.38$.

3.2 Experimental constraints

3.2.1 Electroweak precision tests (EWPT)

With the use of the so-called oblique parameters [71] radiative contributions from new physics to the electroweak processes can be tracked. Then, precise measurements of these processes allow to constrain these parameters. We follow the definitions from [72, 73] (see also references therein). Namely

$$T = \frac{1}{\alpha}\left(\frac{A_{WW}(0)}{M_W^2} - \frac{A_{ZZ}(0)}{M_Z^2}\right),$$
$$S = \frac{4s_W^2 c_W^2}{\alpha}\left(\frac{A_{ZZ}(M_Z^2) - A_{ZZ}(0)}{M_Z^2} - \frac{\partial A_{\gamma\gamma}(q^2)}{\partial q^2}\bigg|_{q^2=0} + \frac{c_W^2 - s_W^2}{c_W s_W}\frac{\partial A_{\gamma Z}(q^2)}{\partial q^2}\bigg|_{q^2=0}\right),$$

where $\alpha = e^2/(4\pi)$ is the fine-structure constant, $s_W = \sin\theta_W$, $c_W = \cos\theta_W$ are the sine and cosine, respectively, of the weak mixing angle and $A_{VV'}$ is defined as follows:

$$\Pi^{\mu\nu}_{VV'} = g^{\mu\nu} A_{VV'}(q^2) + q^\mu q^\nu B_{VV'}(q^2).$$

Here $\Pi^{\mu\nu}_{VV'}$ is the vacuum-polarisation tensor and VV' denotes the divectors: $\gamma\gamma$, γZ, ZZ or WW. Moreover, one has to remember that $A_{VV'}(q^2)$ contains only contributions from the new physics, namely

$$A_{VV'}(q^2) = A^{\text{full}}_{VV'}(q^2) - A^{\text{SM}}_{VV'}(q^2),$$

where $A^{\text{full}}_{VV'}(q^2)$ denotes the quantity calculated in considered model (in this case 2HDM (mixed) or IDM) and $A^{\text{SM}}_{VV'}(q^2)$ denotes the same quantity computed in the SM.

The latest results for the S and T values come from the Gfitter group [74], with U fixed to 0 they read (the reference value of M_h is 125 GeV),

$$T = 0.10 \pm 0.07,$$
$$S = 0.06 \pm 0.09,$$

with the correlation between the parameters equal to 0.91. We will implement the constraints at 2σ level.

In fig. 3.4 the values of the S and T parameters for the IDM (for two values of m_{22}^2, points corresponding to $m_{22}^2 = 0$ are displayed in dark green, and to $m_{22}^2 =$

$-10^6\,\mathrm{GeV}^2$ in light green) and 2HDM (mixed) (for the analytical expressions for S and T see below) are shown together with the 2σ ellipses around the central values.[4] The masses of the scalar particles were randomly selected from the following intervals

- in the IDM: $M_A,\, M_{H^\pm} \in (0,\, 1010]\,\mathrm{GeV}$, $M_H \in (0,\, \min(M_A,\, M_{H^\pm})]$, $M_h = 125\,\mathrm{GeV}$;

- in the 2HDM (mixed): $M_{H^\pm},\, M_H,\, M_A \in (0, 800]\,\mathrm{GeV}$, $M_h \in (0,\, M_H]$, $\tan\beta \in [0,\, 60]$ and $\sin\alpha \in [-1,\, 1]$.

Then the theoretical constraints described in the preceding section and the LEP bound (see section 3.2.2 below) were imposed, and for the valid points the values of S and T were computed.

In general, in models with two scalar doublets the predicted value of S is within or close to the experimental bounds so the important constraints come from the T parameter. This is confirmed by the plot, with an exception for some of the points for 2HDM (mixed), where however still the parameter T is in general far more constraining.

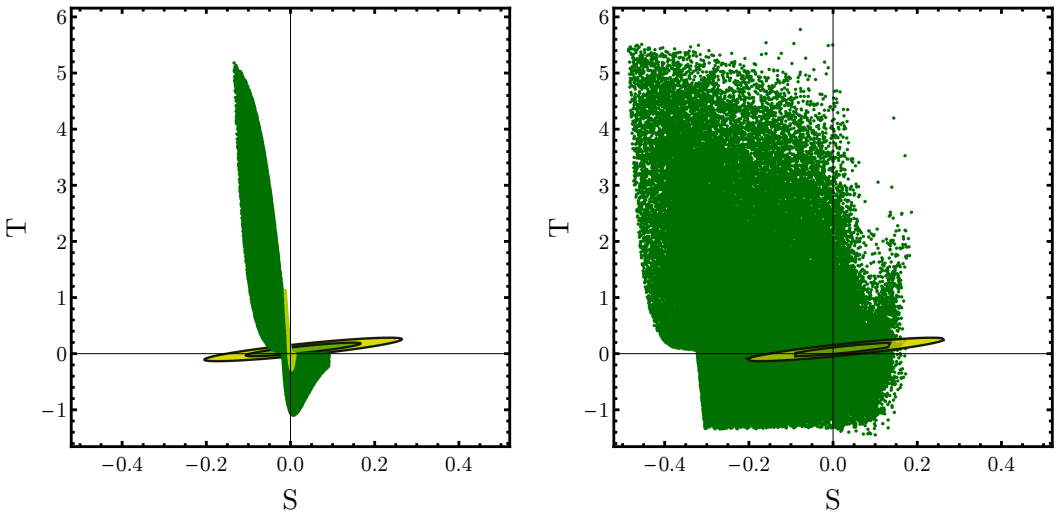

Figure 3.4: Values of the S and T parameters computed for the IDM (left panel, for two values of m_{22}^2: 0 (dark green), and $-10^6\,\mathrm{GeV}^2$ (light green)) and for the 2HDM (mixed) (right panel), for the values of masses fulfilling the theoretical constraints described previously, and the LEP bounds (see section 3.2.2).

[4]The central values used are based on older results from ref. [75], with $T = 0.07 \pm 0.08, S = 0.03 \pm 0.09$, but this does not effect the conclusions.

3.2.1.1 S and T parameters in the 2HDM (mixed)

For the 2HDM (mixed), using formulas from [72, 73] adapted for a two-doublet case, the following expressions for the S and T parameters are obtained (compare also with ref. [76]):

$$\begin{aligned}
T = \frac{1}{16\pi^2 v^2 \alpha}\Big\{ & F(M_{H^\pm}^2, M_A^2) + \sin^2(\beta-\alpha)\Big[F(M_{H^\pm}^2, M_H^2) - F(M_A^2, M_H^2)\Big] \\
& + \cos^2(\beta-\alpha)\Big[F(M_{H^\pm}^2, M_h^2) - F(M_A^2, M_h^2)\Big] \\
& + 3\cos^2(\beta-\alpha)\Big[F(M_Z^2, M_H^2) - F(M_W^2, M_H^2)\Big] \\
& + 3\sin^2(\beta-\alpha)\Big[F(M_Z^2, M_h^2) - F(M_W^2, M_h^2)\Big] \\
& - 3\Big[F(M_Z^2, M_{h_{\rm ref}}^2) - F(M_W^2, M_{h_{\rm ref}}^2)\Big]\Big\}, \\
S = \frac{1}{24\pi}\Big\{ & (2s_W^2-1)^2 G(M_{H^\pm}^2, M_{H^\pm}^2, M_Z^2) \\
& + \sin^2(\beta-\alpha)\Big[G(M_A^2, M_H^2, M_Z^2) + \hat{G}(M_h^2, M_Z^2)\Big] \\
& + \cos^2(\beta-\alpha)\Big[G(M_A^2, M_h^2, M_Z^2) + \hat{G}(M_H^2, M_Z^2)\Big] \\
& - 2\log M_{H^\pm}^2 + \log M_A^2 + \log M_H^2 + \log M_h^2 - \log M_{h_{\rm ref}}^2 - \hat{G}(M_{h_{\rm ref}}, M_Z^2)\Big\}.
\end{aligned}$$

The following definitions were used:

$$\begin{aligned}
G(x,y,z) = & -\frac{16}{3} + \frac{5(x+y)}{z} - \frac{2(x-y)^2}{z^2} \\
& + \frac{3}{z}\left(\frac{x^2+y^2}{x-y} - \frac{x^2-y^2}{z} + \frac{(x-y)^3}{3z^2}\right)\log\frac{x}{y} \\
& + \frac{z^2 - 2z(x+y) + (x-y)^2}{z^3} f\big(x+y-z, z^2 - 2z(x+y) + (x-y)^2\big),
\end{aligned}$$

$$f(x,y) = \begin{cases} \sqrt{y}\log\left|\frac{x-\sqrt{y}}{x+\sqrt{y}}\right| & \text{for} \quad y > 0, \\ 0 & \text{for} \quad y = 0, \\ 2\sqrt{-y}\arctan\frac{\sqrt{-y}}{x} & \text{for} \quad y < 0, \end{cases}$$

$$\begin{aligned}
\hat{G}(x,y) = & -\frac{79}{3} + 9\frac{x}{y} - 2\frac{x^2}{y^2} + \left(-10 + 18\frac{x}{y} - 6\frac{x^2}{y^2} + \frac{x^2}{y^3} - 9\frac{x+y}{x-y}\right)\log\frac{x}{y} \\
& + \left(12 - 4\frac{x}{y} + \frac{x^2}{y^2}\right)\frac{f(x, x^2-4xy)}{y}.
\end{aligned}$$

3.2.1.2 S and T parameters in the IDM

For the IDM the expressions for S and T were taken from [46] (see also [63, 73][5]):

[5]Note that in the formulas in [63, 72] terms containing M_h and $M_{h_{\rm ref}}$ do not appear. They are assumed to cancel, however it is not the case unless $M_h = M_{h_{\rm ref}}$, which is not always true.

$$T = \frac{1}{32\pi^2\alpha v^2}\left(F(M_{H^\pm}^2, M_A^2) + F(M_{H^\pm}^2, M_H^2) - F(M_A^2, M_H^2)\right) + \frac{3}{8\pi}\log\left(\frac{M_{h_{\text{ref}}}}{M_h}\right),$$

$$S = \frac{1}{2\pi}\left\{\frac{1}{6}\frac{M_A^4\left(M_A^2 - 3M_H^2\right)}{(M_A^2 - M_H^2)^3}\log\left(\frac{M_A^2}{M_H^2}\right) + \frac{1}{6}\log\left(\frac{M_H^2}{M_{H^\pm}^2}\right) - \frac{5}{36}\right.$$
$$\left. + \frac{M_H^2 M_A^2}{3\left(M_A^2 - M_H^2\right)^2} - \frac{1}{3}\log\left(\frac{M_{h_{\text{ref}}}}{M_h}\right)\right\}.$$

$M_{h_{\text{ref}}}$ denotes the reference value of the SM Higgs boson mass used in the fit of the experimental data. As was mentioned before in the latest fit the reference value of the Higgs boson mass was equal to the experimentally measured one, so the contributions from the physical Higgs mass M_h and $M_{h_{\text{ref}}}$ cancel, but we keep the reference terms for completeness, since in older data different values were assumed, e.g. $M_{h_{\text{ref}}} = 117\,\text{GeV}$ in [75]. Function F is defined as follows:

$$F(x,y) = \begin{cases} \frac{x+y}{2} - \frac{xy}{x-y}\log\frac{x}{y} & \text{for} \quad x \neq y, \\ 0 & \text{for} \quad x = y. \end{cases}$$

3.2.2 LEP bounds

The results obtained at LEP (Large Elctron–Positron collider) provide several sources of bounds on new physics, in particular on 2HDMs. First of all, the masses of additional scalars are constrained by precise measurements of the decay widths of the Z and W bosons. Secondly, there were also dedicated searches for the charged Higgs bosons of 2HDM (mixed) with type I and type II Yukawa interactions. Moreover, some constraints for the IDM have been rederived from neutralino searches.

Finally the bounds for the IDM read [67, 77, 78]

$$M_{H^\pm} + M_H > M_W, \quad M_{H^\pm} + M_A > M_W, \quad M_H + M_A > M_Z, \quad M_{H^\pm} > 70 - 90\,\text{GeV}. \tag{3.14}$$

Moreover, the region where simultaneously [77]:

$$M_H < 80\,\text{GeV}, \quad M_A < 100\,\text{GeV}, \quad M_A - M_H > 8\,\text{GeV} \tag{3.15}$$

is excluded.

For the 2HDM (mixed) there are bounds on the charged Higgs mass at 95% confidence level, from a combination of the results from all experiments at LEP [79]

$$\begin{aligned} &M_{H^\pm} > 80\,\text{GeV} \quad \text{(for type II)}, \\ &M_{H^\pm} > 72.5\,\text{GeV} \quad \text{(for type I and } M_A > 12\,\text{GeV}). \end{aligned} \tag{3.16}$$

3.2.3 Flavour physics constraints

Flavour physics observables provide some constraints on 2HDMs. The key feature of models with more scalar doublets is that they contain a charged scalar, different than the charged Goldstone boson, which can contribute to the flavour processes. There are many observables that can be analysed in the context of 2HDMs, for example $B \to \tau\nu$, $D \to \mu\nu$, $D_s \to \tau\nu$, $D_s \to \mu\nu$, $K \to \mu\nu$, $\pi \to \mu\nu$, $B_s^0 \to \mu^+\mu^-$, $B_d^0 \to \mu^+\mu^-$, $\tau \to K\nu$, $\tau \to \pi\nu$, $B \to X_s\gamma$, K–$\bar{K}$ mixing, B_d^0–$\bar{B}_d^0$ mixing, and B_s^0–$\bar{B}_s^0$ mixing [80], for analyses within the 2HDM framework see e.g. [32, 80–83]. Some of the observables, such as the branching ratio of $\bar{B} \to D^{(*)}\tau^-\bar{\nu}_\tau$ relative to $\bar{B} \to D^{(*)}\ell^-\bar{\nu}_\ell$ decays (measured by Belle [84–86], BaBar [87, 88] and LHCb [89] collaborations) were claimed to show deviation from the SM prediction [88–90]. In principle, this discrepancy could be explained within 2HDMs, however, the data seemed to disprove this scenario. With an improved measurement, the experimental values agree both with the SM and 2HDM (mixed) (Yukawa type II) [86].

A well known, stringent bound on the mass of the charged Higgs boson $H^\pm$ in a 2HDM (mixed) with the Yukawa interactions of type II comes from the $\bar{B} \to X_s\gamma$ process [91], it reads

$$M_{H^\pm} > 480\,\text{GeV} \quad \text{at } 95\% \text{ C.L.}$$

For $\tan\beta \lesssim 2$ the bound becomes even stronger.

As can be noticed from the short discussion above, flavour constrains depend on the model of Yukawa interactions considered. This makes them less universal and very model-specific. In section 3.4 we present parameter space constraints on 2HDMs with the mixed (normal) vacuum state and for the sake of generality we do not include flavour constraints so that the presented results are independent of the assumption on the Yukawa sector. Flavour physics does not introduce serious constraints in the case of the IDM so we do not consider flavour observables in this case either.

3.2.4 LHC bounds

The LHC up to now has shown that the discovered Higgs particle is SM-like. Nonetheless, it has provided numerous measurements which can be used to constrain various models of new physics. The ones to which we refer in the present thesis are

1. Measurement of the Higgs mass [92]: $M_h \approx 125\,\text{GeV}$.

2. Constraint on the width of the Higgs boson [93, 94]: $\Gamma_h < 22$ MeV ($\Gamma_h/\Gamma_h^{\text{SM}} < 5.4$).

3. Constraints on the invisible Higgs decay rates [95]: $\mathrm{Br}(h \to \mathrm{inv}) < 0.23$. A global fit to LHC and Tevatron data provides even stronger constraints [96]: $\mathrm{Br}(h \to \mathrm{inv}) < 0.2$.

4. Measurement of the Higgs decay width to two photons [24]: $R_{\gamma\gamma} = 1.16^{+0.20}_{-0.18}$.

These constraints are discussed in detail in the context of the IDM in chapter 4.

Of course, more data and more measurements are available, however in this thesis we focus on the measurements listed above because analysing them we can track the influence of the new scalar particles. This way not only do we obtain constrains on the parameter space, but also we develop some insight into the structure of the model.

3.3 Dark matter

As was mentioned in the introduction to this chapter, the DM candidate is an important feature of the IDM, and one of the main reasons to study this particular model. Therefore, in this section we review not only the bounds on the parameter space that can be obtained from the DM measurements but also the motivation to study DM and possible ways of DM searches.

3.3.1 Motivation for the postulate of dark matter

The question of the existence of DM is an unsolved problem of cosmology. There are several observations which can be interpreted as hints on the existence of some non-baryonic matter. For reviews on particle DM see e.g. refs. [97–99].

Rotation curves of galaxies. Orbital velocities of stars in galaxies are measured and it appears that the observed velocities do not coincide with the predictions based on the Kepler law, and the observed density of matter in the galaxy [100]. The discrepancy can be explained by the presence of a halo composed of non-luminous matter. Another possible explanation is modified theory of gravity.

Gravitational lensing. A massive object (such as a cluster of galaxies) placed on the way between a shining astronomical object (e.g. a quasar) and an observer can bend the light due to gravitational interactions. Based on the measurement of the light distortion the mass of the distorting object can be estimated. On the other hand, mass of luminous matter in this object can be computed based on the light it emits. Discrepancies between these two measurements indicate existence of some type of non-luminous matter [98].

Bullet cluster. A collision of two galaxy clusters has been observed. The measurements using light (X-rays) show that most of the light-emitting matter is placed around the centre of the system — the matter which interacts electromagnetically was bound together by these interactions around the collision point. However, the weak lensing measurements show that there is much matter that passed by, without interactions. This, supposedly, is the DM [101, 102].

Primordial nucleosynthesis. According to primordial nucleosynthesis, the observed ratio of the number density of hydrogen to other light elements indicates a baryon density which is too low to account for the observed expansion rate of the Universe. This suggests the necessity of existence of some other, non-baryonic matter.

Cosmic microwave background measurements. Analysis of the anisotropies of the cosmic microwave background radiation (CMB), measured by the WMAP and Planck experiments [103, 104], allows to estimate the density of matter in the Universe.[6] It appears, that the density of matter is by far greater than the density of the baryonic matter. This leads to a conjecture of the existence of non-baryonic matter — dark matter.

3.3.2 Dark matter detection experiments

There are many experiments aiming at detection of DM particles. The two main groups of experiments are direct detection experiments, which are based on the scattering of DM off nuclei, and indirect detection experiments, which look for the products of DM annihilation or decay. Moreover, the DM particles could be directly produced and detected in accelerator experiments at the LHC.

3.3.2.1 Direct detection experiments

The details of the experimental techniques used in the direct detection searches differ between experiments (ionisation, scintillation and nuclear recoil effects are used as well as the measurements of the yearly modulation of DM signal due to the variation of relative velocity of the Earth and DM). In general, the important parameters for these experiments are the mass of the DM particle and the cross section for its scattering off a nucleus, $\sigma_{\mathrm{DM,N}}$, and these are the ones that can be constrained by the direct detection experiments.

[6] The estimate relies on the standard cosmological model.

The DAMA/LIBRA [105], CoGeNT [106] and CRESST-II [107] experiments reported excesses of events that could not be explained by background, and claimed observation of DM signal. The highest significance, at the confidence level of 9.3σ was reported by the DAMA/LIBRA collaboration. The regions favoured by these experiments are shown in fig. 3.5 (left panel, taken from ref. [108]). It can be easily noted that these regions do not overlap, which causes tension. Moreover, the liquid xenon experiments, XENON100 [108] and LUX [109, 110] set upper bounds on $\sigma_{\mathrm{DM,N}}$ which exclude all the regions favoured by DAMA/LIBRA, CoGeNT and CRESST-II, see fig. 3.5, left and right panel (taken from ref. [110]). Recently, also the CRESST-II experiment, with an improved detector reported an upper bound on the DM-nucleon scattering cross section, which excludes the region favoured by its previous analysis, as well as the discovery regions of DAMA/LIBRA and CoGeNT [111]. It also provides the most stringent bounds for very light DM particles, with masses of the order of a few GeV [112].

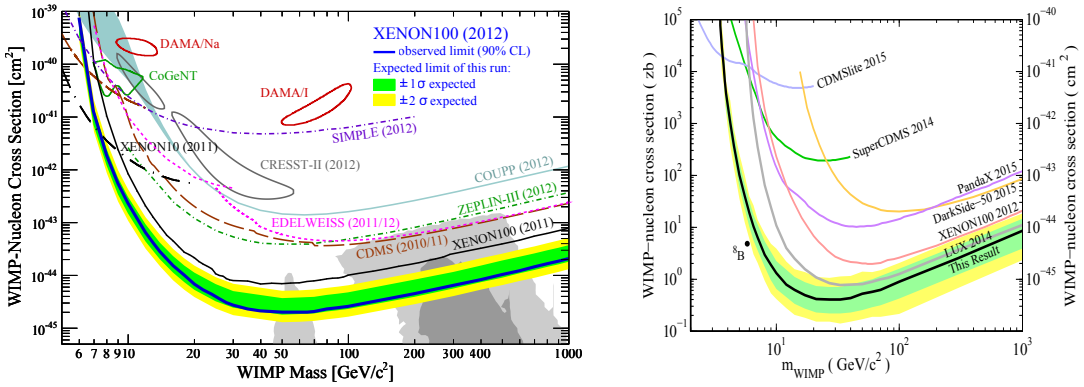

Figure 3.5: Results of direct detection searches for DM. Left panel: Regions favoured by the DAMA/LIBRA, CoGeNT and CRESST-II experiments confronted with the bounds from XENON100, plot taken from ref. [108]. Right panel: Bounds from the LUX experiment compared with the bounds from XENON100, and other experiments, plot taken from ref. [110].

Due to these, yet not understood, discrepancies we will not directly incorporate the direct detection limits/signals in the analysis presented in this dissertation. Nonetheless, in section 4.4.3 we present a comparison of our bounds on the DM-nucleon cross section with the ones from XENON100 and LUX.

3.3.2.2 Indirect detection experiments

In the indirect detection experiments products of DM annihilation or decay in the regions of high DM density, such as the galactic centre, are searched for. These products are SM particles such as antiprotons, positrons, neutrinos and photons.

The biggest problem with the interpretation of such searches is that it strongly depends on the distribution of DM in the Universe, which is unknown [113]. Thus uncertainties related to such observations are rather big.

Among the indirect detection experiments are PAMELA, INTEGRAL, AMS and Fermi-LAT [114–119]. Most of them reported certain excesses of the measured events over the expected background, however, it is not proven that the source of these signals is indeed DM annihilation. Due to these uncertainties we will not include the indirect DM signals in our analysis.

In the future a new experiment is planned, the Cherenkov Telescope Array (CTA) which should improve the gamma-ray observations [120, 121]. It has recently been demonstrated in refs. [122, 123] that the IDM parameter space will be within the reach of this experiment, and that the heavy DM mass region could be significantly constrained.

3.3.2.3 Collider experiments

Since DM particles interact with the SM particles weakly, in collider experiments they can be observed through a measurement of missing energy. Important signatures for DM production processes are the ones with a single photon or a single jet and missing energy [124]. It has been argued that these searches may provide stronger bounds than the direct detection experiments [124]. Within the IDM, processes with two [125–127] or more leptons [64, 128], as well as a monojet [129] and missing energy were also analysed, providing some constraints on the parameter space.

Moreover, within the IDM the invisible decays of the Higgs boson can be interpreted as decays to DM particles (or the other neutral scalars A). Thus, the measurements of the Higgs invisible decay width provide constraints on DM mass and coupling, see sections 3.2.4 and 4.3.

3.3.3 Dark matter relic density

The density of matter in the Universe was estimated based on the measurements of the anisotropies of the cosmic microwave background radiation made by the astrophysical experiments WMAP [103], and more recently Planck [104]. The density of matter is greater than the density of baryonic matter, and the difference between these two quantities is attributed to DM. The current value of the DM relic abundance reads [104]

$$0.1118 < \Omega_{\rm DM} h^2 < 0.1280 \quad (\text{at } 3\sigma), \tag{3.17}$$

where h denotes Hubble constant in the units 100 km/Mpc/s. If the density predicted by a model is below the lower bound, the model can be either rejected or an additional source of DM has to be invoked. Too high relic density, above the upper limit, means that the Universe is overclosed in the discussed model, and thus it has to be rejected.

The relic density of DM is determined by the production and annihilation processes of the DM in the early Universe, which in turn depend on the possible interactions and couplings of the DM matter candidate. This way the relic density measurement can constrain parameters of a given model. A common tool for computation of DM relic density predictions is `MicrOMEGAs` [130–132], which allows to effectively compare the predictions of the model with the value obtained experimentally.

There were numerous studies treating the potential of the inert DM to account for the observed relic density [64, 65, 125, 129, 133–140]. In general, it has been shown that there are three viable regions where the inert DM can account for all the observed relic density. These are

Light DM with mass below 10 GeV, and the coupling to the Higgs boson $|\lambda_{345}| \sim \mathcal{O}(0.5)$,

Intermediate DM with mass $40\,\text{GeV} \lesssim M_H \lesssim 80\,\text{GeV}$ and $|\lambda_{345}| \sim \mathcal{O}(0.05)$,

Heavy DM with mass above 500 GeV and $|\lambda_{345}| \sim \mathcal{O}(0.1)$.

A more detailed discussion of the DM relic abundance constraints, in combination with the LHC data, is presented in section 4.4.

3.4 Parameter space of the 2HDM (mixed)

In this section the constrained parameter space of the 2HDM (mixed) is presented. The basic constraints described previously in this chapter are imposed, namely: positivity constraints, eq. (3.1), condition for the mixed minimum, eq. (3.4), perturbative unitarity, eq. (3.12), EWPT constraints, and the LEP bounds (since the two bounds of eq. (3.16) are close it does not make a big difference which one is used, thus we use a common bound $M_{H^\pm} < 78\,\text{GeV}$ which was an older value of this constraint). The results are obtained using a random scan of the parameter space, with the ranges of parameters described in section 3.1.3 (for λ_i) and in section 3.2.1 (for the scalar masses). We do not impose the flavour constraints so the obtained results are independent of the type of Yukawa interactions chosen. The results are based on refs. [5, 6, 48].

3.4.1 Limits on couplings

As was already discussed in section 3.1.3, the constraints on the parameters λ_i, when they are treated as parameters of a 2HDM with a fixed vacuum state are different then the constraints for parameters of the general potential (2.1). The numerical limits for the parameters $\lambda_1, \ldots, \lambda_5$ within the 2HDM (mixed) read

$$\begin{aligned} 0 \leqslant \lambda_1 &\leqslant 8.38, \\ 0 \leqslant \lambda_2 &\leqslant 8.38, \\ -4.92 \leqslant \lambda_3 &\leqslant 15.95, \\ -13.49 \leqslant \lambda_4 &\leqslant 5.50, \\ -8.06 \leqslant \lambda_5 &\leqslant 0. \end{aligned} \tag{3.18}$$

The correlations between some of the parameters are presented in fig. 3.6 (light green). For comparison they are shown together with the correlations obtained for general 2HDMs (dark green). It should be noted that the regions allowed within 2HDM (mixed) differ significantly form the generally allowed regions. This shows that the constraints related to the type of vacuum are important.

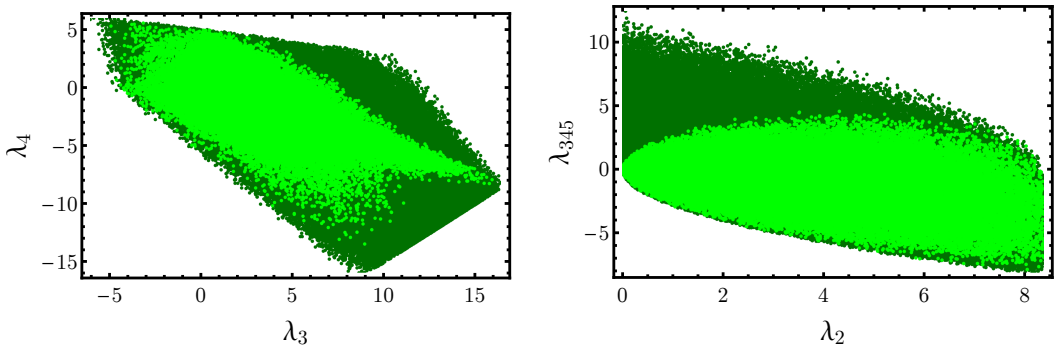

Figure 3.6: Correlations between parameters in the 2HDM (mixed) caused by imposing the basic theoretical and experimental bounds (see the text). Dark green regions are allowed for an arbitrary 2HDM with the potential (2.1), the light green regions are obtained by applying also specific bounds for the 2HDM (mixed).

3.4.2 Constraints on masses

The overall bounds on the masses of the scalar particles within the 2HDM (mixed) read

$$\begin{aligned} M_H &\leqslant 697\,\mathrm{GeV}, \\ M_{H^\pm} &\leqslant 707\,\mathrm{GeV}, \\ M_A &\leqslant 706\,\mathrm{GeV}, \\ M_h &\leqslant 446\,\mathrm{GeV}. \end{aligned} \tag{3.19}$$

Here both h and H can play a role of the Higgs boson so we did not fix any of the masses to 125 GeV. The obtained bounds are in good agreement with the most precise analytical results derived from perturbative unitarity constraints of ref. [59].[7] The allowed regions of masses are presented in fig. 3.7. The EWPT constraints were imposed in the second step (light green) to see what is their significance. It can be concluded that in the 2HDM (mixed) EWPT do not constrain the space of allowed masses strongly.

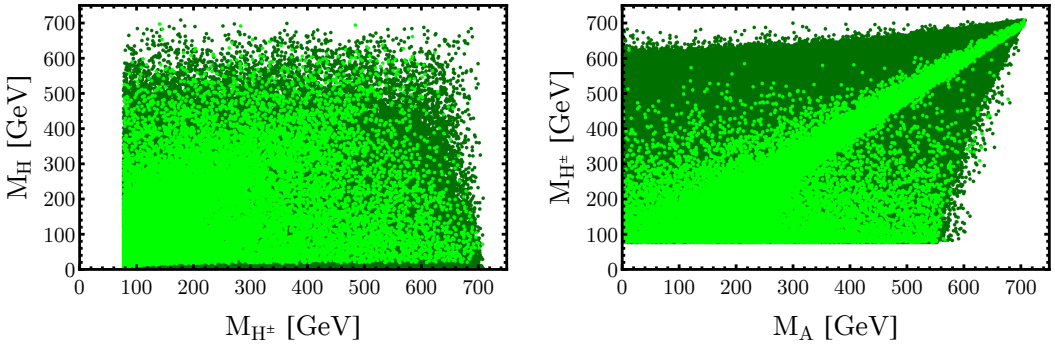

Figure 3.7: Regions of masses allowed in the Mixed Model with/without EWPT included (ligh/dark green).

3.4.3 Constraint on the parameter $\tan\beta$

We also investigated correlations between the values of scalars' masses and $\tan\beta$ allowed by the analysed constraints, see also [6]. M_h exhibits interesting dependence on $\tan\beta$, the results are presented in fig. 3.8.[8] It shows maximal allowed values of M_h as a function of $\tan\beta$, $M_h^{\max}(\tan\beta)$. We have checked that for any value of $\sin(\beta-\alpha)$ only the area below that curve $M_h^{\max}(\tan\beta)$ is allowed. From fig. 3.8 it follows that if we consider a particular value of the mass of h (or at least set a lower bound on it), then $\tan\beta$ is constrained, both from above and below. For $M_h = 125\,\text{GeV}$ the following bound is obtained:[9]

$$0.18 \lesssim \tan\beta \lesssim 5.59. \tag{3.20}$$

It should be underlined that this bound is obtained without any assumptions on the Yukawa couplings.

The correlations between M_H and $\tan\beta$ are more complicated. For different values of $\sin(\beta-\alpha)$ we obtained different curves $M_H^{\max}(\tan\beta)$. In particular for

[7] Small discrepancies are due to the uncertainty of the numerical method applied in our analysis.

[8] EWPT were not included in the analysis leading to this plot, however, they would hardly change the picture.

[9] Here also EWPT are included.

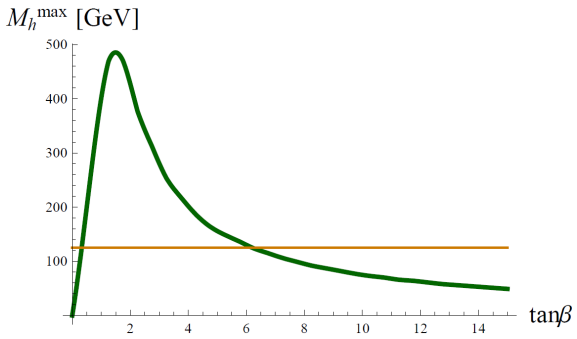

Figure 3.8: Correlation between maximal values of the mass of h and $\tan\beta$ in the Mixed Model allowed by the analysed constraints. For any value of $\sin(\beta-\alpha)$ only the points lying below the curve are allowed. The horizontal line corresponds to the mass of 125 GeV.

the case with $\sin(\beta-\alpha)=0$ (SM-like scenario) the corresponding curve is just a straight line at $M_H \approx 700\,\text{GeV}$. This means that fixing M_H cannot introduce any bounds on $\tan\beta$ unless we fix $\sin(\beta-\alpha)$ to a non-zero value.

To understand why there is a bound on $\tan\beta$ if we assume $M_h = 125\,\text{GeV}$, while there is no bound in the $M_H = 125\,\text{GeV}$ case, one should go back to the expressions for masses of the scalars, eq. (2.11) [6]. It can be easily checked that $M_h \to 0$ as $\tan\beta \to 0$ or $\tan\beta \to \infty$ for any fixed values of λ_1, λ_2, λ_{345}. Thus the curve in fig. 3.8 was bound to tend to zero for $\tan\beta \to 0$ and $\tan\beta \to \infty$, and so fixing M_h must introduce an upper and a lower bound on $\tan\beta$. On the contrary, this does not apply to M_H and therefore no bound on $\tan\beta$ follows from the assumption $M_H = 125\,\text{GeV}$ (independently of $\sin(\beta-\alpha)$).

3.5 Parameter space of the IDM

In this section we present the results of applying to the IDM the basic constraints described in previous sections, namely: positivity of the potential, eq. (3.1), condition for existence of an inert minimum, eq. (3.2), and for that minimum being a global one, eq. (3.5), perturbative unitarity, eq. (3.12), EWPT (with the values taken from ref. [75]) at 2σ level, LEP bounds, eqs. (3.14), (3.15), and the mass of the Higgs mass, $M_h = 125\,\text{GeV}$ (which fixes λ_1 to a value of 0.26). We will start from the constraints on the couplings, and then also present constraints on the masses of the scalar particles. The results are based on our work described in ref. [5] (see also [17, 48]).

The results were obtained by randomly scanning the parameter space of the model and imposing the constraints listed above. The ranges of the parameters are the same as those described in section 3.1.3 (for the parameters λ_i) and in section 3.2.1

(for the scalar masses).

3.5.1 Limits on couplings

As explained in the case of the 2HDM (mixed), the parameters $\lambda_1, \ldots, \lambda_5$ when interpreted within the IDM are subject to more stringent limits than in the general case (eq. (3.13)). Moreover, the scalar couplings in the IDM are simple combinations of the parameters of the potential so they are mostly constrained by unitarity. The overall bounds on the couplings within the IDM read

$$\begin{aligned}
0 \leqslant\ & \lambda_2 \leqslant 8.38, \\
-1.32 \leqslant\ & \lambda_3 \leqslant 16.53, \\
-8.95 \leqslant\ & \lambda_4 \leqslant 5.08, \\
-8.22 \leqslant\ & \lambda_5 \leqslant 0, \\
-1.45 \leqslant\ & \lambda_{345} \leqslant 11.94, \\
-1.15 \leqslant\ & \lambda^-_{345} \leqslant 16.40, \\
-8.33 \leqslant\ & \tfrac{1}{2}\lambda_{45} \leqslant 0, \\
-2.64 \leqslant\ & \tfrac{1}{2}\lambda^-_{45} \leqslant 5.08, \\
-1.22 \leqslant\ & \lambda_{34} \leqslant 13.34,
\end{aligned} \tag{3.21}$$

where $\lambda_{ij} = \lambda_i + \lambda_j$, $\lambda^-_{ij} = \lambda_i - \lambda_j$, and the value of λ_1 is fixed to 0.26 by the measured value of the Higgs boson mass. Later on the most important of these couplings will be λ_2 as the quadratic DM couplings (corresponding e.g. to the vertex $HHHH$), and λ_{345} which is proportional to the hHH vertex. The bounds on the parameters $\lambda_1, \ldots, \lambda_5$ can be compared with eq. (3.13) where bounds on the same parameters, but without inclusion of any assumptions about the vacuum state are presented. It is clear that the constraints imposed on IDM strengthen some of the bounds. To better compare the bounds imposed on a general 2HDM with scalar potential of the form (2.1), and the bounds relevant for the model with definite vacuum state, in fig. 3.9 the correlations between some of the couplings are shown (dark green corresponds to the general 2HDM, and light green to the IDM). It can be interesting to compare this figure with fig. 3.6, where analogous plots for the 2HDM (mixed) are presented. It can be noticed, that the bounds significantly differ between the two models.

3.5.2 Constraints on masses

Using the relations (2.13) the constraints from positivity and perturbative unitarity on the parameters appearing in the lagrangian can be translated to constraints

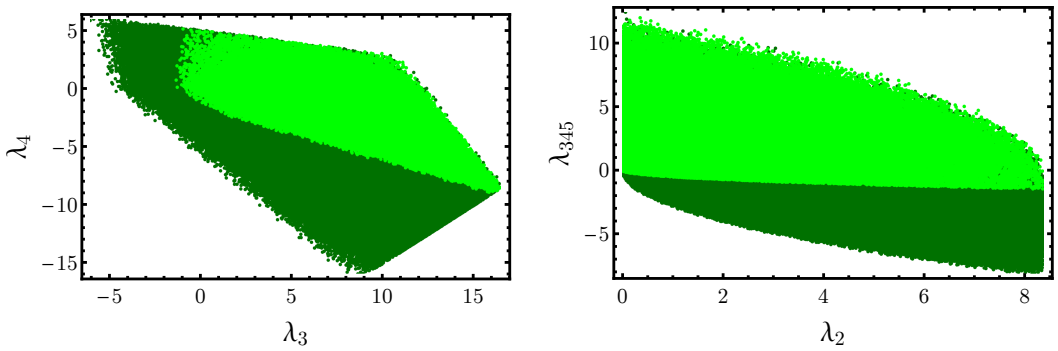

Figure 3.9: Correlations between parameters in the IDM caused by imposing the basic theoretical and experimental bounds (light green, see the text). Dark green regions are allowed for an arbitrary model with the potential (2.1).

on masses of the scalar particles. The parameter m_{22}^2 enters the expressions for the masses of the dark scalars (eq. (2.13)), but does not enter the unitarity (eq. (3.12)) or positivity conditions (eq. (3.1)). Thus, the bounds on masses depend on its value. For the case with $m_{22}^2 = 0$ the bounds on the masses of the scalars following from the constraints listed in the beginning of this section read

$$\begin{aligned} M_H &\leqslant 602\,\text{GeV}, \\ M_{H^\pm} &\leqslant 708\,\text{GeV}, \\ M_A &\leqslant 708\,\text{GeV}. \end{aligned} \tag{3.22}$$

As was mentioned before in the IDM h plays the role of the SM Higgs boson so we fixed its mass to $M_h = 125\,\text{GeV}$ (so $m_{11}^2 = (125\,\text{GeV})^2$ and $\lambda_1 = 0.26$).

We have checked that in a large range of m_{22}^2, for $|m_{22}^2| \lesssim 10^4\,\text{GeV}^2$, the results hardly change with respect to the case with $m_{22}^2 = 0$. However, when m_{22}^2 is extremely big and negative, the allowed regions of masses are changed and also lower bounds on masses develop. The allowed regions of dark scalars' masses for both of the cases ($m_{22}^2 = 0$, $m_{22}^2 = -10^6\,\text{GeV}^2$) are presented in fig. 3.10 in the $(M_{H^\pm}, M_A)$ and $(M_{H^\pm}, M_H)$ planes. The plot representing correlations in the (M_A, M_H) plane is not displayed as it is very similar to the one for $(M_{H^\pm}, M_H)$. Note that the regions of masses allowed for the cases with $m_{22}^2 = 0$ and $m_{22}^2 = -10^6\,\text{GeV}^2$ have empty intersection (see fig. 3.10, right panel). It can be seen that EWPT strongly constrain the available parameter space.

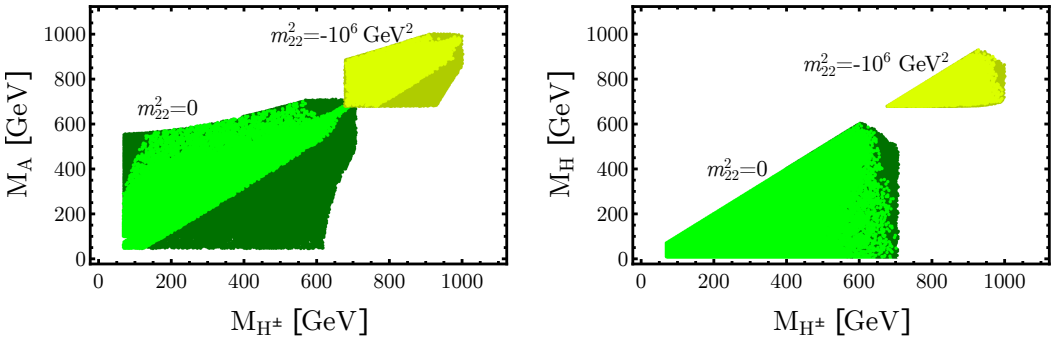

Figure 3.10: Regions of masses allowed in the IDM. The darker, wider regions correspond to applying constraints without the EWPT, while the lighter ones to all of the constraints applied. In both of the plots the figures in the lower left corner correspond to the case with $m_{22}^2 = 0$, while the figures in the upper right corner (pale colors) correspond to $m_{22}^2 = -10^6\,\mathrm{GeV}^2$.

Chapter 4

Properties of the Higgs boson in the Inert Doublet Model

A new scalar particle with mass around 125 GeV was discovered by the ATLAS and CMS collaborations at the LHC in 2012 [18, 19, 92]. A crucial question arose: is it the missing piece of the SM of electroweak interactions — the Higgs boson? To answer it many measurements have been performed, studying the properties of the new particle, its production and decay modes. The results obtained to date are fully consistent with the SM hypothesis [24]. However, the experimental uncertainties leave some space for effects of new BSM physics.

The IDM contains a SM-like Higgs boson which has all tree-level couplings to fermions and gauge bosons identical as the SM Higgs particle. Therefore it fits well the current experimental status. Nonetheless, it contains also the new dark scalars which affect the Higgs phenomenology.

In this chapter a study of the properties of the Higgs boson within the IDM is presented. Using the Higgs data we aim at constraining the properties of the inert, yet unobserved scalars. We start from the analysis of the decay of the Higgs boson to two photons, which gave the first experimental hint on the existence of the Higgs particle. This analysis gives us some information about the properties of the neutral and charged scalar particles. Then, an analysis of the $h \to Z\gamma$ decay follows, in particular we study a correlation between signal strength of this and the diphoton decay. Another element is a study of the total and invisible decay widths of the Higgs, which also sheds some light on the possible values of the additional scalars' masses and couplings. In the next part of this chapter we present results

which follow from combining the information on the Higgs diphoton decay, and the measurements of the DM relic density. It appears that this two seemingly disjoint sources of information can be considered as complementary, and the combination provides important new predictions about the DM properties.

Of course, the analyses presented in the present chapter do not make use of all the available data provided by the LHC experiments. This is because our aim was to understand the relations between different particles present in the IDM, the impact of the new particles on the LHC phenomenology, and the interplay between the LHC searches and the DM studies, and this becomes extremely involved when too many results are included. On the one hand, this approach does not provide the most stringent constrains possible, but on the other it allows deeper understanding of the studied model. There exist publicly available numerical tools allowing to study a wide spectrum of the experimental constrains. Most of the available constraints are implemented for example in the programs `HiggsBounds` (contains bounds also from LEP and Tevatron) [141–143] and `HiggsSignals` [144] which have been used in the recent thorough analysis of ref. [145]. Other phenomenological analyses of the IDM can be found in refs. [64, 129, 139].

4.1 Decay of the Higgs boson to two photons

The $h \to \gamma\gamma$ decay is one of the most important observational channels of the Higgs boson at the LHC. It gained much interest when some deviations from the SM prediction for its rate have been reported. The current experimental results for the $h \to \gamma\gamma$ decay signal strength read [24]: $R_{\gamma\gamma} = 1.16^{+0.20}_{-0.18}$. This measurement is fully consistent with the SM expectation, however, the experimental uncertainties leave some space for new physics effects.

The $\gamma\gamma$ signal strength is interesting, because it is sensitive to new physics — in particular to the existence of new charged particles coupling to the Higgs boson. By this means it is well suited to study 2HDMs, distinctive feature of which is the existence of a charged scalar. Precise measurement of the decay rate of the $h \to \gamma\gamma$ channel can also constrain the invisible decays branching ratios, which would bring information about the masses of extra scalars present in in the IDM.

The diphoton decay rate in the IDM was studied in refs. [47, 63, 146, 147]. In the parameter region studied in ref. [47] no enhancement of the signal was found, while in ref. [146] the possibility of modifying the total decay width of the Higgs boson due to the invisible decays into DM particles was not taken into account. In refs. [63, 147] the entire parameter space was not investigated; as the mass parameter of the

potential was taken with only one sign, the DM particle was assumed to be lighter than the Higgs boson and the mass of DM was constrained ($M_H < 150\,\text{GeV}$). The diphoton decay rate was also considered in the context of the electroweak phase transition in ref. [148]. Below we present an independent thorough analysis of the diphoton Higgs decay mode in the IDM which improves the points mentioned above, it is based on the results presented in ref. [4] (see also refs. [11–16]). Subsequently, the diphoton decay rate was included in many analyses of the IDM, see e.g. refs. [3, 129, 139, 149, 150].

4.1.1 General analysis

The diphoton signal strength $R_{\gamma\gamma}$ (often denoted also as $\mu_{\gamma\gamma}$) is measured at the LHC and is defined as follows [4, 63]:

$$\begin{aligned} R_{\gamma\gamma} &= \frac{\sigma(pp \to h \to \gamma\gamma)^{\text{IDM}}}{\sigma(pp \to h \to \gamma\gamma)^{\text{SM}}} \approx \frac{[\sigma(gg \to h)\text{Br}(h \to \gamma\gamma)]^{\text{IDM}}}{[\sigma(gg \to h)\text{Br}(h \to \gamma\gamma)]^{\text{SM}}} \\ &= \frac{\text{Br}(h \to \gamma\gamma)^{\text{IDM}}}{\text{Br}(h \to \gamma\gamma)^{\text{SM}}} = \frac{\Gamma(h \to \gamma\gamma)^{\text{IDM}}}{\Gamma(h \to \gamma\gamma)^{\text{SM}}} \frac{\Gamma(h)^{\text{SM}}}{\Gamma(h)^{\text{IDM}}}. \end{aligned} \tag{4.1}$$

Above we used the narrow width approximation and the fact that the gluon fusion is the dominant channel of Higgs production. Moreover, in the IDM $\sigma(gg \to h)^{\text{IDM}} = \sigma(gg \to h)^{\text{SM}}$, so $R_{\gamma\gamma}$ reduces to the ratio of the $h \to \gamma\gamma$ branching ratios.

As can be seen, both the partial decay width of the Higgs boson to two photons, $\Gamma(h \to \gamma\gamma)^{\text{IDM}}$, and the total decay width of the Higgs, $\Gamma(h)^{\text{IDM}}$, contribute to $R_{\gamma\gamma}$. There are two possible origins of deviation from $R_{\gamma\gamma} = 1$, which is the SM prediction: the charged scalar loop contributing to $\Gamma(h \to \gamma\gamma)^{\text{IDM}}$ and the invisible decays augmenting $\Gamma(h)^{\text{IDM}}$. In different regions of the parameter space, different effects dominate.

4.1.1.1 Total decay width of the Higgs boson

Many channels contribute to the total decay width of the Higgs boson h. The most important ones for the mass $M_h = 125\,\text{GeV}$ are $b\bar{b}$, $c\bar{c}$, $\tau^+\tau^-$, ZZ^*, WW^*, gg, $\gamma\gamma$, $Z\gamma$, HH, and AA. To compute the decay widths we used the formulas from refs. [151–155]. For completeness they are summarised in Appendix B. The partial widths of the tree-level h decays into SM particles, and the loop-mediated decay into gg in the IDM are equal to the corresponding ones in the SM. The $\gamma\gamma$ and $Z\gamma$ partial decay widths are modified with respect to the SM by the presence of the charged scalar loop. However, the $\gamma\gamma$ and $Z\gamma$ branching ratios are of the order of 10^{-2}–10^{-3} so their contributions to the total decay width are negligible. Thus the total decay width can deviate from the SM prediction only due to the invisible decay channels.

The branching ratios of the Higgs boson as functions of λ_{345} are shown in Fig. 4.1 [4, 156]. Three different cases are considered: decay channels $h \to AA$ and $h \to HH$ are open (with $M_H = 50\,\text{GeV}$, $M_A = 58\,\text{GeV}$, left panel), $h \to AA$ is closed and $h \to HH$ is open ($M_H = 60\,\text{GeV}$, $M_A > 63\,\text{GeV}$, middle panel), and both $h \to AA$ and $h \to HH$ are closed ($M_H = 75\,\text{GeV}$, $M_A > M_H$, right panel). It can be seen, that the invisible decay channels dominate over the SM decays if they are kinematically allowed. Within the detailed numerical analysis it will be shown, that in these cases the total decay width of the Higgs boson is so big that $\text{Br}(h \to \gamma\gamma)^{\text{IDM}} < \text{Br}(h \to \gamma\gamma)^{\text{SM}}$. If the invisible channels are closed, the $H^\pm$ loop impact on $h \to \gamma\gamma$ and $h \to Z\gamma$ becomes clearly visible.

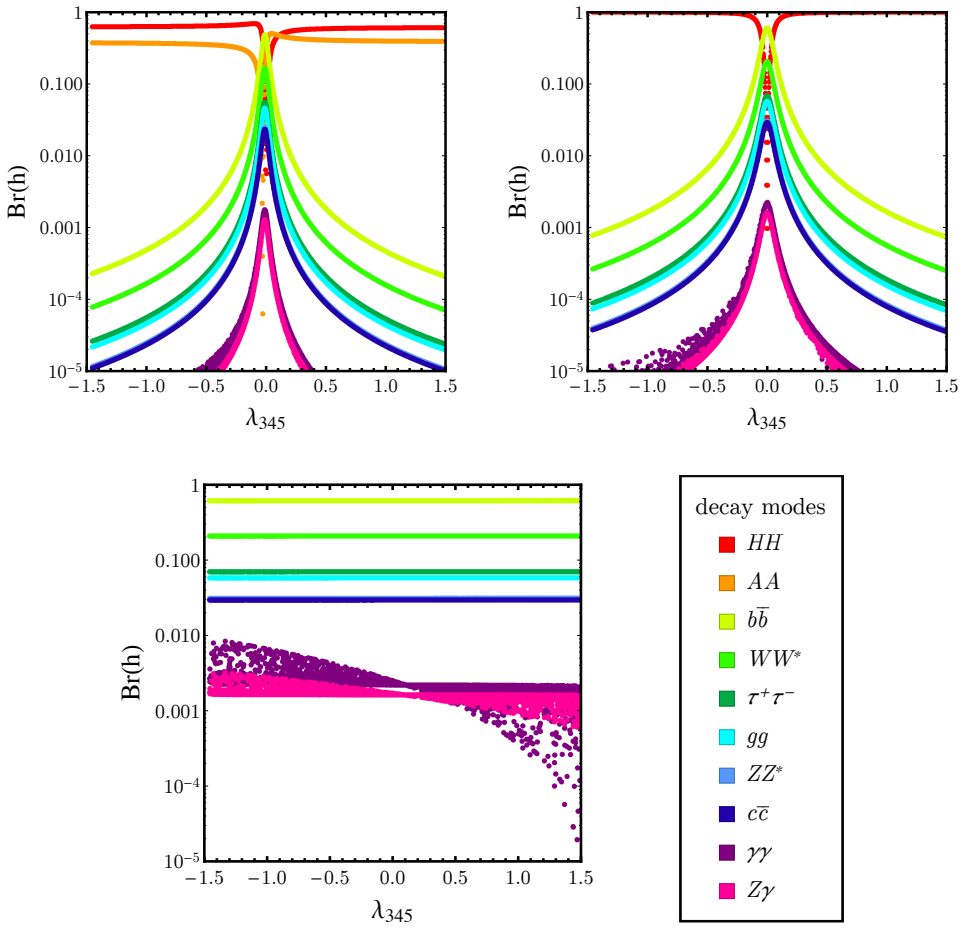

Figure 4.1: Branching ratios for h with mass equal to 125 GeV as functions of λ_{345}. Upper panel, left: decay channels $h \to HH$ and $h \to AA$ are open ($M_H = 50\,\text{GeV}$, $M_A = 58\,\text{GeV}$); upper panel, right: $h \to HH$ open ($M_H = 60\,\text{GeV}, M_A > 63\,\text{GeV}$); lower panel: no invisible h decay channels allowed ($M_H = 75\,\text{GeV}, M_A > M_H$). The legend is common for all the plots, the decay channels are listed in the same order in which they appear in the plots. Note that the curves corresponding to the $h \to c\bar{c}$ decay almost entirely overlap the ones for $h \to ZZ^*$, and thus the latter ones can barely be seen.

4.1.1.2 Partial diphoton decay width of the Higgs boson

As was explained above, if the decay channels $h \to HH$ and $h \to AA$ are kinematically closed, the total width of h is barely modified with respect to the SM case. Thus in this case $R_{\gamma\gamma}$ (eq. (4.1)) reduces to the ratio of the partial widths in the IDM and in the SM, namely

$$\widetilde{R}_{\gamma\gamma} = \frac{\Gamma(h \to \gamma\gamma)^{\rm IDM}}{\Gamma(h \to \gamma\gamma)^{\rm SM}}. \tag{4.2}$$

In the IDM, the partial decay width of the Higgs boson to $\gamma\gamma$ is (approximately) given by [47, 63, 146, 151, 152]

$$\Gamma(h \to \gamma\gamma)^{\rm IDM} = \frac{G_F \alpha^2 M_h^3}{128\sqrt{2}\pi^3} \Bigg| \underbrace{\frac{4}{3} A_{1/2}\left(\frac{4M_t^2}{M_h^2}\right) + A_1\left(\frac{4M_W^2}{M_h^2}\right)}_{\mathcal{M}^{\rm SM}} + \underbrace{\frac{2M_{H^\pm}^2 + m_{22}^2}{2M_{H^\pm}^2} A_0\left(\frac{4M_{H^\pm}^2}{M_h^2}\right)}_{\delta\mathcal{M}^{\rm IDM}} \Bigg|^2, \tag{4.3}$$

where $\mathcal{M}^{\rm SM}$ denotes the contribution from the SM and $\delta\mathcal{M}^{\rm IDM}$ is the extra contribution present in the IDM, $\mathcal{M}^{\rm IDM} = \mathcal{M}^{\rm SM} + \delta\mathcal{M}^{\rm IDM}$.[1] The form factors in eq. (4.3) are defined as follows [157]:

$$\begin{aligned} A_0(\tau) &= -\tau[1 - \tau f(\tau)], \\ A_{1/2}(\tau) &= 2\tau[1 + (1-\tau) f(\tau)], \\ A_1(\tau) &= -[2 + 3\tau + 3\tau(2-\tau) f(\tau)] \end{aligned}$$

and

$$f(\tau) = \begin{cases} \arcsin^2\left(\frac{1}{\sqrt{\tau}}\right) & \text{for } \tau \geqslant 1, \\ -\frac{1}{4}\left[\log\left(\frac{1+\sqrt{1-\tau}}{1-\sqrt{1-\tau}}\right) - i\pi\right]^2 & \text{for } \tau < 1. \end{cases}$$

The important contribution to $R_{\gamma\gamma}$ comes from the charged scalar loop, which can interfere either constructively or destructively with the SM part. Furthermore, in eq. (4.3) $2M_{H^\pm}^2 + m_{22}^2 = \lambda_3 v^2$, where λ_3 is proportional to the hH^+H^- coupling, so one of the following sets of parameters λ_3, $M_{H^\pm}$ or m_{22}^2, $M_{H^\pm}$ can be chosen to determine $\Gamma(h \to \gamma\gamma)^{\rm IDM}$.

We are interested in the possible modifications of $R_{\gamma\gamma}$ with respect to the SM case, so we consider the inequality $\widetilde{R}_{\gamma\gamma} > 1$, which corresponds to:

$$\left|\mathcal{M}^{\rm SM} + \delta\mathcal{M}^{\rm IDM}\right|^2 > \left|\mathcal{M}^{\rm SM}\right|^2, \tag{4.4}$$

[1] Above we do not include the contributions from the bottom- and charm-quark loops as well as from the τ loop, as we have checked that they are negligible. We take $M_W = 80.399\,\text{GeV}$ and $M_t = 173\,\text{GeV}$ from the Particle Data Group analysis [154].

where $\mathcal{M}^{\mathrm{SM}}$ is fixed for $M_h = 125\,\mathrm{GeV}$.[2] The inequality (4.4) can be solved analytically. We will discuss the results first, and the derivation is presented below, in the next section. There are two possible cases for which $\widetilde{R}_{\gamma\gamma} > 1$, in each case the analytical bounds can be be translated to numerical constraints on m_{22}^2 using the LEPII bound on the mass of the charged scalar, $M_{H^\pm} \leqslant 70\,\mathrm{GeV}$. The two cases correspond to:

Constructive interference In the case of constructive interference the charged scalar loop contributes to $\Gamma(h \to \gamma\gamma)$ with the same sign as the SM terms. The upper bound on m_{22}^2 reads

$$m_{22}^2 < -2M_{H^\pm}^2 \leqslant -9.8 \cdot 10^3\,\mathrm{GeV}^2. \tag{4.5}$$

This bound can be translated to a constraint on λ_3, and gives $\lambda_3 < 0$ [4, 63].

Destructive interference In the case of destructive interference the contribution from the charged scalar has to be at least twice as big as the SM term [146]. The obtained bound on m_{22}^2 reads

$$m_{22}^2 > \frac{M_h^2\,\mathrm{Re}\left(\mathcal{M}^{\mathrm{SM}}\right)}{1 - \left(\frac{2M_{H^\pm}}{M_h}\right)^2 \arcsin^2\left(\frac{M_h}{2M_{H^\pm}}\right)} - 2M_{H^\pm}^2 \gtrsim 1.8 \cdot 10^5\,\mathrm{GeV}^2. \tag{4.6}$$

If this bound is compared with the constraint following from the requirement of the existence of the inert vacuum, eq. (3.7) it is clear that this solution is excluded.

Thus it can be concluded that enhancing $\widetilde{R}_{\gamma\gamma}$ is only possible if the charged scalar loop interferes constructively with the SM contribution.

4.1.1.3 Analytical solution for the enhancement of the $h \to \gamma\gamma$ signal strength

We need to solve the following inequality

$$\left|\mathcal{M}^{\mathrm{SM}} + \delta\mathcal{M}^{\mathrm{IDM}}\right|^2 > \left|\mathcal{M}^{\mathrm{SM}}\right|^2, \tag{4.7}$$

while $\mathcal{M}^{\mathrm{SM}}$ is fixed, and we assume that the invisible decay channels are closed, i.e. $M_H > M_h/2$. Let us use the following definitions

$$\begin{aligned} a &= \mathrm{Re}\mathcal{M}^{\mathrm{SM}}, \\ b &= \mathrm{Im}\mathcal{M}^{\mathrm{SM}}, \\ c &= \delta\mathcal{M}^{\mathrm{IDM}} = \frac{2M_{H^\pm}^2 + m_{22}^2}{2M_{H^\pm}^2} A_0(\tau), \end{aligned}$$

[2] If the contributions from light quarks are neglected, $\mathcal{M}^{\mathrm{SM}}$ is real, but we treat it as a complex number to keep the reasoning general.

where $\tau = \frac{4M_{H^\pm}^2}{M_h^2}$, $\tau > 1$. The parameter c is a real number, because $f\left(\frac{4M_{H^\pm}^2}{M_h^2}\right) = \arcsin^2\left(\frac{M_h}{2M_H}\right)$ for $M_H > M_h/2$. Hence the inequality (4.7) can be written as

$$|a + ib + c|^2 > |a + ib|^2$$

and is equivalent to

$$c(c + 2a) > 0.$$

There are two possibilities:

$$c > 0 \text{ and } c + 2a > 0 \quad \text{or} \quad c < 0 \text{ and } c + 2a < 0.$$

One can compute that $a \approx -6.53 < 0$, so these two cases reduce to

$$c > -2a \quad \text{or} \quad c < 0.$$

The first case is realised if and only if $\frac{2M_{H^\pm}^2 + m_{22}^2}{2M_{H^\pm}^2} A_0(\tau) > -2a$. Since$A_0(\tau) = -\tau + \tau^2 \arcsin^2(1/\tau)$, then $A_0(\tau) > 0$ for $\tau > 1$. Therefore this condition is translated to

$$m_{22}^2 > \frac{aM_h^2}{1 - \left(\frac{2M_{H^\pm}}{M_h}\right)^2 \arcsin^2\left(\frac{M_h}{2M_{H^\pm}}\right)} - 2M_{H^\pm}^2.$$

The other case, $c > 0$, can be realised either if $2M_{H^\pm}^2 + m_{22}^2 > 0$ and $A_0(\tau) < 0$, or if $2M_{H^\pm}^2 + m_{22}^2 < 0$ and $A_0(\tau) > 0$. As $A_0(\tau) > 0$, the first option is excluded and the other reduces to $m_{22}^2 < -2M_{H^\pm}^2$.

Summing up, there are two regions where enhancement in the $h \to \gamma\gamma$ channel is possible:

$$m_{22}^2 < -2M_{H^\pm}^2 \quad \text{or}$$
$$m_{22}^2 > \frac{aM_h^2}{1 - \left(\frac{2M_{H^\pm}}{M_h}\right)^2 \arcsin^2\left(\frac{M_h}{2M_{H^\pm}}\right)} - 2M_{H^\pm}^2,$$

which correspond to constructive and destructive interference between the SM and the IDM contributions, as discussed in the previous section.

4.1.2 Numerical results

4.1.2.1 Method of analysis

We randomly scanned the parameter space of the IDM, taking into account the following constraints: positivity, existence of the inert vacuum, perturbative unitarity, EWPT, LEP bound (the details can be found in chapter 3.5). We also assume

$M_H < M_A, M_{H^\pm}$, for H to be the DM candidate. The parameters were varied in the following regimes:

$$\begin{aligned} M_h &= 125\,\text{GeV}, \\ 70\,\text{GeV} \leqslant M_{H^\pm} &\leqslant 800\ (1400)\,\text{GeV}, \\ 0 < M_A &\leqslant 800\ (1400)\,\text{GeV}, \\ 0 < M_H &< M_A, M_{H^\pm}, \\ -25 \cdot 10^4\ (-2 \cdot 10^6)\,\text{GeV}^2 \leqslant m_{22}^2 &\leqslant 9 \cdot 10^4\,\text{GeV}^2, \\ 0 < \lambda_2 &\leqslant 10. \end{aligned}$$

The allowed region in the parameter space depends on the choice of the minimal value of m_{22}^2, which is not constrained by perturbative unitarity, as was discussed in section 3.5. We considered two regimes for m_{22}^2, narrow and wide. For the wider of the two, larger masses of dark scalars were allowed, up to 1400 GeV (values in brackets). In the parameter space fulfilling the constraints we analysed the possible values of $R_{\gamma\gamma}$.

4.1.2.2 $R_{\gamma\gamma}$ and the masses of the scalar particles

In fig. 4.2 (upper panel) the regions of masses allowed in the IDM by the constraints for the narrow m_{22}^2 range are presented. The regions where the enhancement in the $h \to \gamma\gamma$ channel occurs are displayed in light green. It can be seen that the $R_{\gamma\gamma}$ enhancement is only possible when $M_H > M_h/2$ and $M_A > M_h/2$. This means that the partial widths of invisible decays increase the total width of the Higgs boson so much that the enhancement of $R_{\gamma\gamma}$ with respect to the SM case is impossible (this is in agreement with the results of ref. [63]). The plots in fig. 4.2 (upper panel) seem to suggest that $R_{\gamma\gamma} > 1$ can only be realised if $M_{H^\pm} \lesssim 350\,\text{GeV}$ (see also the analysis of ref. [63]). However, it is only an artefact of the choice of the range for the m_{22}^2 parameter, which can be understood by comparing the upper and the lower panel of fig. 4.2. In fact, as we will shortly show, the Higgs diphoton signal strength can be enhanced for any value of the charged scalar mass.

Now we turn to the possible values that $R_{\gamma\gamma}$ can assume in the IDM. In fig. 4.3 $R_{\gamma\gamma}$ as a function of scalar masses is displayed together with the experimental bounds on $R_{\gamma\gamma}$. The solid purple line corresponds to the current experimentally measured value, $R_{\gamma\gamma} = 1.16$, and the dashed lines to 1σ, 2σ and 3σ limits. The upper panel corresponds to the narrow, and the lower panel to the wide range of the m_{22}^2 parameter. Clearly, both enhanced and suppressed signal is allowed by the data. It can be read off from the plot that in the IDM $R_{\gamma\gamma}$ can be enhanced with respect to the SM up to about 3.4 times. It can also be noted that substantial enhancement

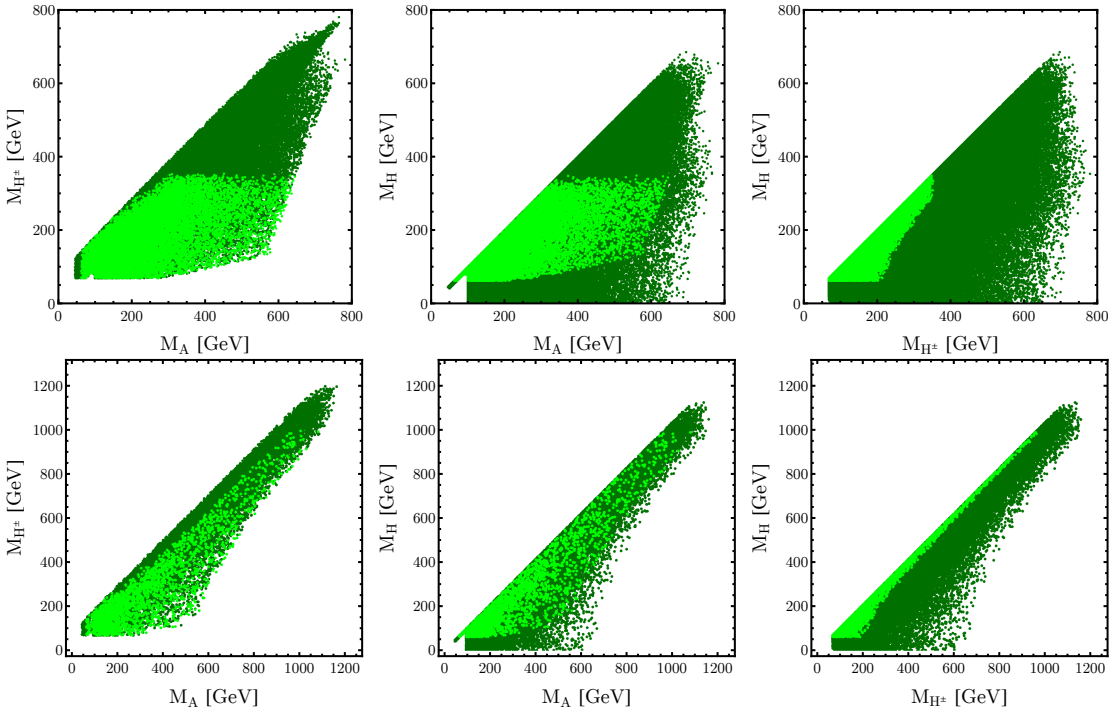

Figure 4.2: The regions in the parameter space allowed by the constraints. In light green the points for which $R_{\gamma\gamma} > 1$ are displayed. The plots in the upper panel correspond to the scan in the narrow m_{22}^2 range ($25 \cdot 10^4\,\mathrm{GeV}^2 \leqslant m_{22}^2 \leqslant 9 \cdot 10^4\,\mathrm{GeV}^2$), and the lower panel to the scan in the wide range $-2 \cdot 10^6\,\mathrm{GeV}^2 \leqslant m_{22}^2 \leqslant 9 \cdot 10^4\,\mathrm{GeV}^2$.

of $R_{\gamma\gamma}$ is only possible for rather light charged scalar (and consequently also light DM candidate). This bound is independent of the range of m_{22}^2.

To clarify the issue of the dependence of the bounds on masses on the m_{22}^2 range we analyse the allowed region in the $(m_{22}^2, M_{H^\pm})$ plane, see fig. 4.4. The points for which $R_{\gamma\gamma} > 1$ are displayed in light green. The purple lines correspond to fixed values of $\widetilde{R}_{\gamma\gamma}$. We use here $\widetilde{R}_{\gamma\gamma}$ (eq. (4.2)) instead of the full $R_{\gamma\gamma}$ (eq. (4.1)) because we are interested in the enhanced $R_{\gamma\gamma}$ rate, which, as we have already shown, is only realised in the case when the invisible Higgs decay channels are closed. In this case $R_{\gamma\gamma}$ reduces to $\widetilde{R}_{\gamma\gamma}$.

As can be seen from the right panel of fig. 4.4 values of $R_{\gamma\gamma}$ equal to or slightly greater than one can be achieved for arbitrarily big values of $M_{H^\pm}$, up to a few GeV. However, since the $H^\pm$ loop contribution to $\Gamma(h \to \gamma\gamma)$ is controlled by $\frac{\lambda_3 v^2}{2M_{H^\pm}^2}$ (see eq. (4.3) and comments below), and λ_3 is constrained by unitarity, for big values of $M_{H^\pm}$ the contribution of the charged scalar will become less and less important. This could be expected, it means that the heavy $H^\pm$ particle decouples. It confirms the conclusion formulated before, that by requiring $R_{\gamma\gamma} > 1$ we cannot constrain $M_{H^\pm}$. The apparent constraints on masses, visible in fig. 4.2 are coming solely from

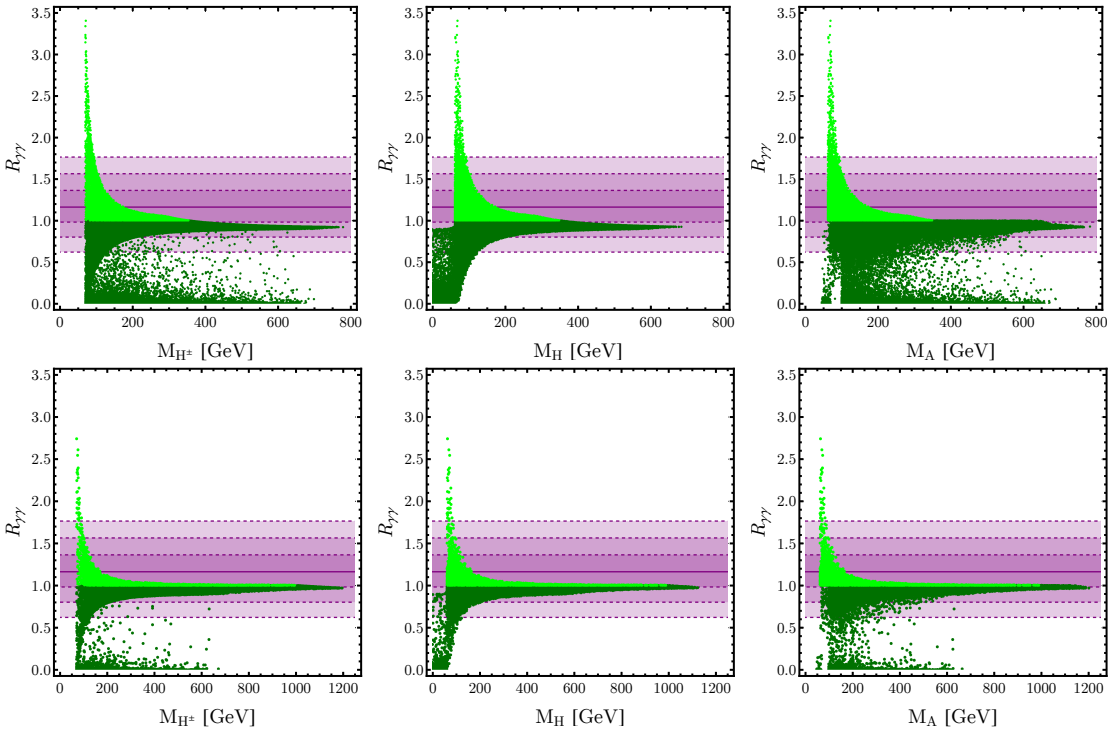

Figure 4.3: Allowed values of $R_{\gamma\gamma}$ as a function of the scalar masses. Points with $R_{\gamma\gamma} > 1$ are displayed in light green. The solid purple line corresponds to the current experimentally measured value, $R_{\gamma\gamma} = 1.16$, and the dashed lines to 1σ, 2σ and 3σ limits. The plots in the upper panel correspond to the scan in the narrow m_{22}^2 range ($25 \cdot 10^4\,\mathrm{GeV}^2 \leqslant m_{22}^2 \leqslant 9 \cdot 10^4\,\mathrm{GeV}^2$), and the lower panel to the scan in the wide range $-2 \cdot 10^6\,\mathrm{GeV}^2 \leqslant m_{22}^2 \leqslant 9 \cdot 10^4\,\mathrm{GeV}^2$.

the constraint imposed on the range of the m_{22}^2 parameter, since big scalar masses are associated with big negative values of m_{22}^2.

On the other hand, if we look at the contours of $\widetilde{R}_{\gamma\gamma} = 1.1, 1.2$, we see that substantial enhancement of $R_{\gamma\gamma}$ is only possible for a constrained range of $M_{H^\pm}$, and thus these constraints do not depend on on the range of m_{22}^2. For example, for $R_{\gamma\gamma} > 1.2$ we have $M_{H^\pm} \lesssim 154\,\mathrm{GeV}$. This implies also $M_H \lesssim 154\,\mathrm{GeV}$. Of course, for $R_{\gamma\gamma}$ enhancement to occur the invisible channels have to be closed. Combining these constraints with the LEP bounds on the charged scalar mass, we can conclude that if $R_{\gamma\gamma} > 1.2$ is measured, then

$$62.5\,\mathrm{GeV} < M_H \lesssim 154\,\mathrm{GeV}, \qquad 70\,\mathrm{GeV} < M_{H^\pm} \lesssim 154\,\mathrm{GeV}. \tag{4.8}$$

This means that in case of substantial $R_{\gamma\gamma}$ enhancement the additional scalars (at least H and A) have to be fairly light, with masses that allow to potentially observe them at colliders.

Looking at the parts of the plots in fig. 4.4 corresponding to positive values of m_{22}^2 we can see that the allowed points come very close to the curve $\widetilde{R}_{\gamma\gamma} = 1$, and they

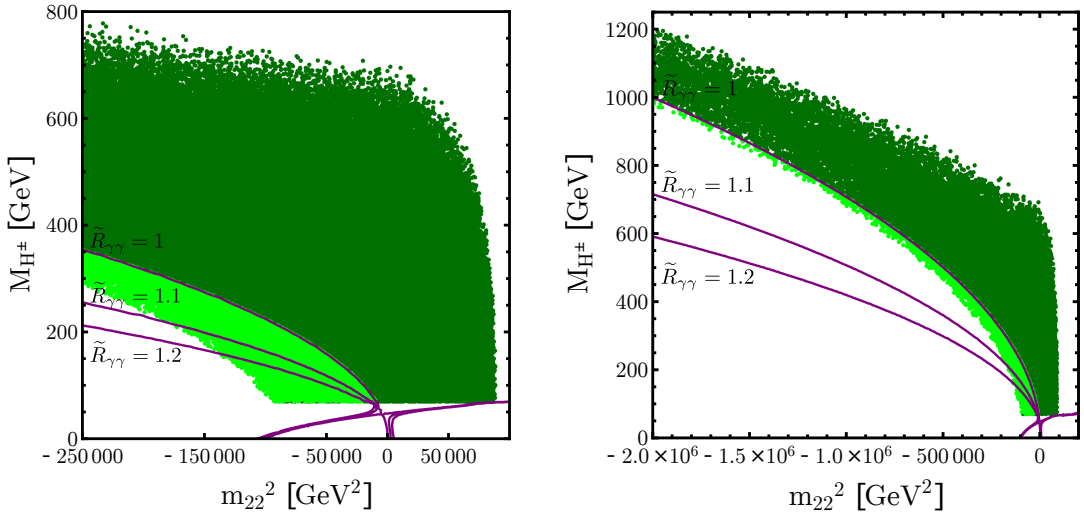

Figure 4.4: Allowed region in the $(m_{22}^2, M_{H^\pm})$ plane. Points with $R_{\gamma\gamma} > 1$ are displayed in light green. The solid purple lines corresponds to fixed values of $R_{\gamma\gamma}$. The plot in the left panel correspond to the scan in the narrow m_{22}^2 range ($25 \cdot 10^4\,\mathrm{GeV}^2 \leqslant m_{22}^2 \leqslant 9 \cdot 10^4\,\mathrm{GeV}^2$), and in the right panel to the scan in the wide range ($-2 \cdot 10^6\,\mathrm{GeV}^2 \leqslant m_{22}^2 \leqslant 9 \cdot 10^4\,\mathrm{GeV}^2$).

would go below this curve (thus yielding $R_{\gamma\gamma} > 1$) if bigger values of m_{22}^2 were allowed. These points would correspond to enhancement through destructive interference, see the discussion in section 4.1.1.2. This shows that a phenomenologically interesting region of the parameter space is excluded by the condition for the inert vacuum state, eq. (3.7), which is often not taken into account in the literature.

4.1.2.3 $R_{\gamma\gamma}$ and the scalar couplings

As discussed before, the mechanisms modifying $R_{\gamma\gamma}$ with respect to the SM are the invisible Higgs decays to the HH and AA pairs, and the propagation of the charged scalar in a loop. The first of these are controlled by the scalar couplings λ_{345} and λ_{345}^-, which are proportional to the hHH and hAA couplings (see also eq. (B.1)). The latter is controlled by the λ_3 parameter, see eq. (4.3) and discussion below. Thus λ_3, λ_{345} and λ_{345}^- are the parameters which should be analysed in the context of the study of $R_{\gamma\gamma}$ in the IDM. Dependence of $R_{\gamma\gamma}$ on these parameters is presented in fig. 4.5. First of all, looking at the left panel of fig. 4.5 we can see that enhanced $R_{\gamma\gamma}$ only appears for $\lambda_3 < 0$, which confirms the conclusion of our analytic computation presented in section 4.1.1.2. Second conclusion that can be read off from this figure, is that $R_{\gamma\gamma} > 1$ strongly constraints the couplings, namely it yields

$$-1.47 \lesssim \lambda_3, \lambda_{345} \lesssim 0. \tag{4.9}$$

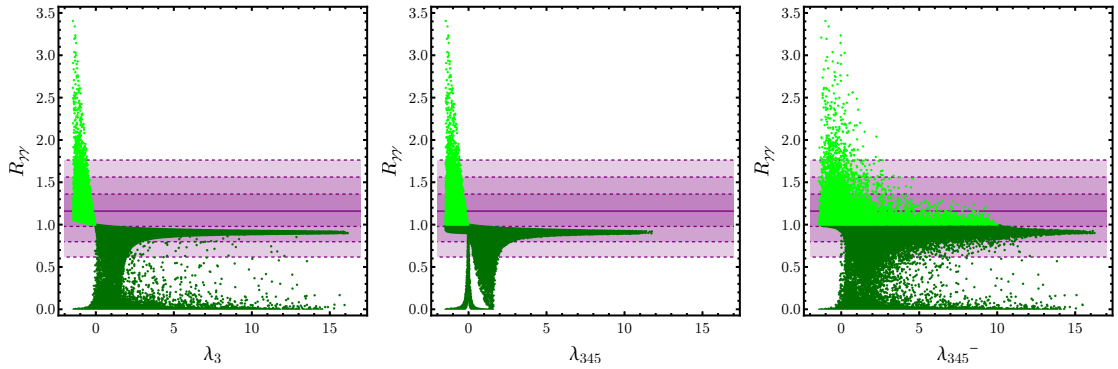

Figure 4.5: Allowed values of $R_{\gamma\gamma}$ as a function of the scalar couplings. Points with $R_{\gamma\gamma} > 1$ are displayed in light green. The solid purple line corresponds to the current experimentally measured value, $R_{\gamma\gamma} = 1.16$, and the dashed lines to 1σ, 2σ and 3σ limits. The plots correspond to the scan in the narrow m_{22}^2 range ($25 \cdot 10^4\,\mathrm{GeV}^2 \leqslant m_{22}^2 \leqslant 9 \cdot 10^4\,\mathrm{GeV}^2$). Results of the scan in the wide range are very similar to the ones presented here so we do not display them here.

If substantial enhancement is required, for concreteness let us set $R_{\gamma\gamma} > 1.2$, then

$$-1.46 \lesssim \lambda_3, \lambda_{345} \lesssim -0.24. \tag{4.10}$$

It can be also noted that the dependence of $R_{\gamma\gamma}$ on λ_{345} is sharp, the allowed region is well defined, whereas the regions in the $(\lambda_3, R_{\gamma\gamma})$ and $(\lambda_{345}^-, R_{\gamma\gamma})$ planes have many scattered points. It can by explained by the fact that it is the λ_{345} parameter that opens and closed the invisible decay channels of the Higgs boson. It is because the H particle is the lightest one among the inert scalars, so only if $h \to HH$ is allowed, also $h \to AA$ is possible.

4.2 Decay of the Higgs boson to a photon and a Z boson

The decay $h \to Z\gamma$ is another one, after $h \to \gamma\gamma$, that is purely loop-induced in the SM, and as such is sensitive to new-physics effects. This decay has not yet been observed at the LHC, there are only upper bounds on the signal strength, $R_{Z\gamma} < 9.5$ (CMS [158]), $R_{Z\gamma} < 11$ (ATLAS [159]). The results presented in this section are based on ref. [4].

The signal strength is defined the same way as for the diphoton decay

$$R_{Z\gamma} = \frac{\mathrm{Br}(h \to Z\gamma)^{\mathrm{IDM}}}{\mathrm{Br}(h \to Z\gamma)^{\mathrm{SM}}}.$$

Analogously to the $R_{\gamma\gamma}$ case, $R_{Z\gamma}$ can be modified with respect to the SM case ($R_{Z\gamma} = 1$) due to the charged scalar loop influencing the partial decay width and

the invisible decays augmenting the total decay width. Just like in the $h \to \gamma\gamma$ case if the invisible decays of h are open, $R_{Z\gamma} > 1$ is impossible.

The partial decay width $\Gamma(h \to Z\gamma)^{\mathrm{IDM}}$ is given by the following formulas,

$$\begin{aligned}\Gamma(h \to Z\gamma) = \frac{G_F^2 \alpha}{64\pi^4} M_W^2 M_h^3 \left(1 - \frac{M_Z^2}{M_h^2}\right)^3 \Bigg| 2\frac{1 - \frac{8}{3}\sin^2\theta_W}{\cos\theta_W} A_{1/2}^h\left(\frac{4m_t^2}{M_h^2}, \frac{4m_t^2}{M_Z^2}\right) \\ + A_1^h\left(\frac{4M_W^2}{M_h^2}, \frac{4M_W^2}{M_Z^2}\right) \\ - \frac{2M_{H^\pm}^2 + m_{22}^2}{2M_{H^\pm}^2} \frac{(1 - 2\sin^2\theta_W)}{\cos\theta_W} I_1\left(\frac{4M_{H^\pm}^2}{M_h^2}, \frac{4M_{H^\pm}^2}{M_Z^2}\right) \Bigg|^2, \end{aligned} \tag{4.11}$$

where

$$\begin{aligned} A_{1/2}^h(\tau, \lambda) &= I_1(\tau, \lambda) - I_2(\tau, \lambda), \\ A_1^h(\tau, \lambda) &= \cos\theta_W \left\{ 4\left(3 - \frac{\sin^2\theta_W}{\cos^2\theta_W}\right) I_2(\tau, \lambda) + \left[\left(1 + \frac{2}{\tau}\right)\frac{\sin^2\theta_W}{\cos^2\theta_W} - \left(5 + \frac{2}{\tau}\right)\right] I_1(\tau, \lambda) \right\}, \\ I_1(\tau, \lambda) &= \frac{\tau\lambda}{2(\tau - \lambda)} + \frac{\tau^2\lambda^2}{2(\tau - \lambda)^2}\big[f(\tau) - f(\lambda)\big] + \frac{\tau^2\lambda}{(\tau - \lambda)^2}\big[g(\tau^{-1}) - g(\lambda^{-1})\big], \\ I_2(\tau, \lambda) &= -\frac{\tau\lambda}{2(\tau - \lambda)}\big[f(\tau) - f(\lambda)\big], \end{aligned}$$

$$g(\tau) = \begin{cases} \sqrt{\frac{1}{\tau} - 1}\arcsin\sqrt{\tau} & \text{for } \tau \leqslant 1, \\ \frac{\sqrt{1-\frac{1}{\tau}}}{2}\left(\log\frac{1+\sqrt{1-\frac{1}{\tau}}}{1-\sqrt{1-\frac{1}{\tau}}} - i\pi\right) & \text{for } \tau > 1. \end{cases}$$

The charged scalar contribution is given by the third line of eq. (4.11), and is controlled by the hH^+H^- coupling λ_3 and the mass of the charged scalar (or equivalently m_{22}^2 and $M_{H^\pm}$) so by the same parameters that were crucial for $R_{\gamma\gamma}$.[3] To compare the impact of the charged scalar loop on the $h \to \gamma\gamma$ and $h \to Z\gamma$ partial decay widths in fig. 4.6 we present the region where $\widetilde{R}_{\gamma\gamma} > 1$ (shaded region) and the region where $\widetilde{R}_{Z\gamma} > 1$ (inside the dashed line). $\widetilde{R}_{Z\gamma}$ is defined analogously to $\widetilde{R}_{\gamma\gamma}$, namely

$$\widetilde{R}_{Z\gamma} = \frac{\Gamma(h \to Z\gamma)^{\mathrm{IDM}}}{\Gamma(h \to Z\gamma)^{\mathrm{SM}}}. \tag{4.12}$$

We analyse $\widetilde{R}_{\gamma\gamma}$ and $\widetilde{R}_{Z\gamma}$ instead of $R_{\gamma\gamma}$ and $R_{Z\gamma}$ to focus on the contribution from the charged scalar, not taking care of the invisible decays. In fig. 4.6 it can be seen that the two regions overlap almost ideally, with differences only present for $M_{H^\pm} < 70\,\mathrm{GeV}$ (the red line corresponds to $M_{H^\pm} = 70\,\mathrm{GeV}$), i.e., in the region excluded by the LEP constraints. Thus, in the IDM if $R_{\gamma\gamma} > 1$ than also $R_{Z\gamma} > 1$ and vice versa.[4]

[3] Note the minus sign of the charged scalar contribution [155], which is different than in some publications, e.g. ref. [151].

[4] Since $R_{\gamma\gamma}$ and $R_{Z\gamma}$ are so similar we will not present here analogs of the plots in figs. 4.2–4.5 because they would be very simmilar the ones already presented.

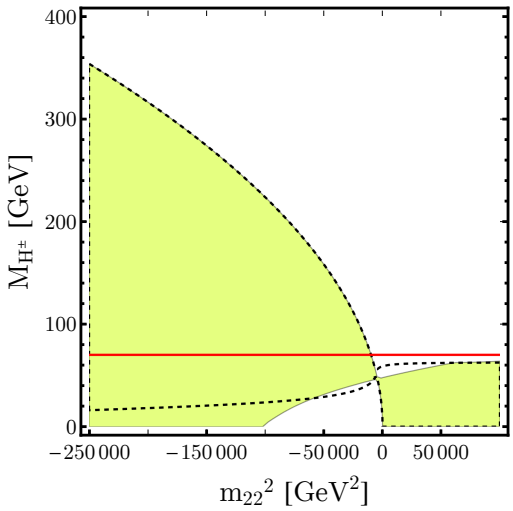

Figure 4.6: Region in the $(m_{22}^2,\ M_{H^\pm})$ plane where $\widetilde{R}_{\gamma\gamma} > 1$ (shaded region) and the region where $\widetilde{R}_{Z\gamma} > 1$ (inside the dashed line). Differences appear only below the $M_{H^\pm} = 70\,\text{GeV}$ line (red solid line), in the region excluded by the LEP constraints.

Another interesting question that one can address is about the correlation between $R_{\gamma\gamma}$ and $R_{Z\gamma}$. This correlation is presented in fig. 4.7. The correlation is positive, which could have already been inferred from fig. 4.6, and the curve passes through the point $(1, 1)$, which corresponds to the SM. The structure of a two-branch curve can be easily explained: the lower branch (straight line, for which $R_{\gamma\gamma} \approx R_{Z\gamma}$) represents the case of open invisible channels, where both $R_{\gamma\gamma}$ and $R_{Z\gamma}$ are damped by a big common constant (invisible decays widths), which dominates over the charged scalar contributions, leading to $R_{\gamma\gamma} \approx R_{Z\gamma} < 1$. The other branch describes the correlation following from the fact that both $H^\pm$ loops in $h \to \gamma\gamma$ and $h \to Z\gamma$ are controlled by the same parameters. The fact that in the IDM the correlation between $R_{\gamma\gamma}$ and $R_{Z\gamma}$ is positive can serve in the future as a good probe of the model since a measurement showing a negative correlation would exclude the IDM. The result shown in fig. 4.7 was confirmed by refs. [160, 161].

4.3 Total and invisible decay widths of the Higgs boson

So far the experiments at the LHC have managed to pose some constraints on the total width of the Higgs boson, as well as on its invisible decay width. The current constraints for the total decay width read [93, 94]

$$\Gamma_h < 22\ \text{MeV} \quad \text{or} \quad \Gamma_h/\Gamma_h^{\text{SM}} < 5.4, \tag{4.13}$$

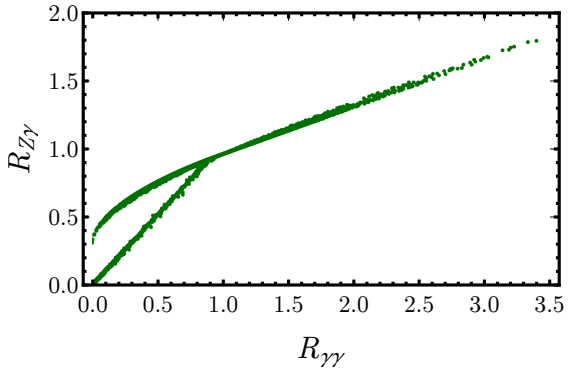

Figure 4.7: Correlation between $R_{\gamma\gamma}$ and $R_{Z\gamma}$.

and for the invisible branching ratios [95]

$$\mathrm{Br}(h \to \mathrm{inv}) < 0.23. \tag{4.14}$$

A global fit to the LHC and Tevatron data provides even stronger constraints [96]:

$$\mathrm{Br}(h \to \mathrm{inv}) < 0.2. \tag{4.15}$$

Remembering that the branching ratios of the $\gamma\gamma$ and $Z\gamma$ Higgs decays are of the order of 10^{-3}, the total decay width of the Higgs boson in the IDM can be approximated by

$$\Gamma(h)^{\mathrm{IDM}} \approx \Gamma(h)^{\mathrm{SM}} + \Gamma(h \to HH) + \Gamma(h \to AA).$$

The partial width of the decay to a pair of DM candidates is given by

$$\Gamma(h \to HH) = \frac{\lambda_{345}^2 v^2}{32\pi M_h}\sqrt{1 - \frac{4M_H^2}{M_h^2}}, \tag{4.16}$$

and for the $h \to AA$ decay λ_{345} should be exchanged to λ_{345}^-, and M_H to M_A. Therefore, the parameters that can be constrained by these measurements are the masses of the neutral dark scalars, M_H and M_A, and their couplings to the Higgs boson, λ_{345}, λ_{345}^-. To reduce the number of free parameters we will assume for now that the channel $h \to AA$ is kinematically closed (some results for the general case can be found in ref. [3]). In this case the constraints following from eqs. (4.13) and (4.14) can be represented in the (M_H, λ_{345}) plane. (Since the result in eq. (4.15) is very close to the bound of eq. (4.14) we will not include it in the analysis.) The results are presented in fig. 4.8, the region between the dashed curves is allowed by the constraint on invisible branching ratios, whereas the region between the solid lines is consistent with the bound given by the total width measurement. It is clear that

the measurement of the invisible branching ratios is by far more constraining than the bound on the total Higgs decay width. To be in agreement with the LHC results, for $M_H < 62.5\,\text{GeV}$ the parameter λ_{345} has to be less than about 0.1. In fact in most of the M_H range λ_{345} has to be less than 0.03.

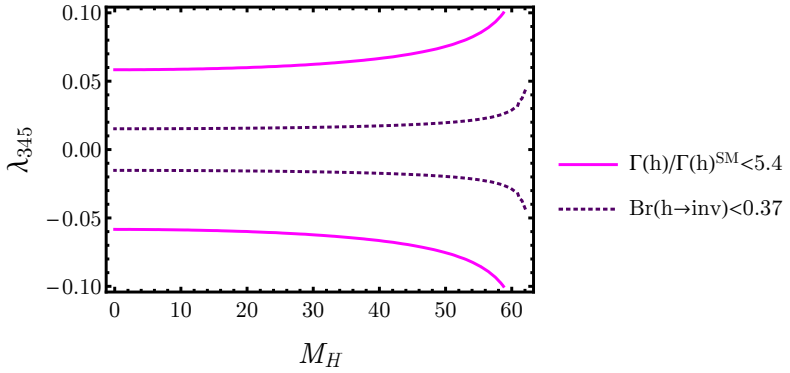

Figure 4.8: Region allowed by the constraints on the total decay of the Higgs boson (between the solid lines), and region allowed by the constraint on the invisible branching ratios (between the dashed lines).

4.4 Interplay between the properties of the Higgs boson and the inert DM

We have already discussed the consequences of observing an enhanced signal in the $h \to \gamma\gamma$ decay channel. In this section we will focus on the implications of setting a lower bound on $R_{\gamma\gamma}$. Moreover, these bounds will be combined with the constraints following from the measurements of the relic density of DM performed by the WMAP [103] and Planck [104] experiments.

4.4.1 Interplay between constraints from $R_{\gamma\gamma}$ and DM relic density

As was already explained in section 4.1, the diphoton signal strength depends on the DM mass, and its coupling to the Higgs boson through the total decay width of the Higgs particle. Thus the parameters M_H and λ_{345} are important for the value of $R_{\gamma\gamma}$. We can choose the scalar masses and the parameters λ_{345} and λ_2 as a set of independent variables describing the IDM (see section 2.4). The parameter λ_2 does not influence $R_{\gamma\gamma}$ in any way. Therefore, once the masses of the inert scalars are fixed, $R_{\gamma\gamma}$ is just a function of λ_{345}. Behaviour of $R_{\gamma\gamma}(\lambda_{345})$ for a certain choice

of masses ($M_H = 55\,\text{GeV}$, $M_A = 60\,\text{GeV}$, $M_{H^\pm} = 120\,\text{GeV}$) is presented in fig. 4.9. The $R_{\gamma\gamma}(\lambda_{345})$ curve is bell-shaped, so setting a lower limit on $R_{\gamma\gamma}$ will yield upper and lower bounds on the values of λ_{345}. These will of course depend on the masses of the inert scalars that have been chosen. In the case presented in fig. 4.9, requiring $R_{\gamma\gamma} > 0.7$ implies that λ_{345} has to be in the range $-0.023 \leqslant \lambda_{345} \leqslant 0.009$ so the bound is rather restrictive.

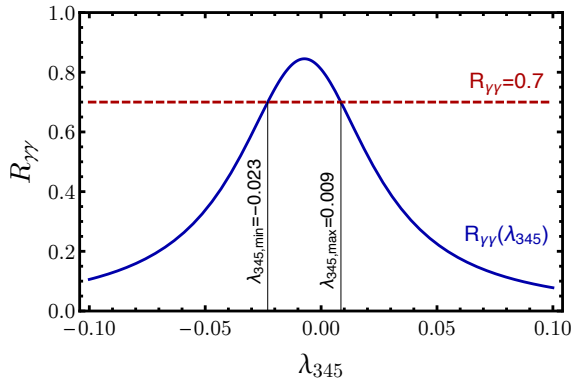

Figure 4.9: The diphoton signal strength, $R_{\gamma\gamma}$, as a function of λ_{345} for $M_H = 55\,\text{GeV}$, $M_A = 60\,\text{GeV}$, $M_{H^\pm} = 120\,\text{GeV}$. Constraints on λ_{345} following from the requirement that $R_{\gamma\gamma} > 0.7$ are shown. Figure taken from ref. [3].

In the case when the invisible decay channel $h \to AA$ is kinematically closed, $R_{\gamma\gamma}$ does not depend on M_A, and consequently neither do the discussed λ_{345} bounds. In this thesis we will focus on this case, for the clarity of presentation. The study of M_H-dependence of the λ_{345} constraints is enough to show relations between the parameters, and some tendencies while keeping the plots two-dimensional. A study of the case with both $h \to HH$, and $h \to AA$ open can be found in refs. [3, 126].

Since the H particle in the IDM plays also the role of a DM candidate, it is also constrained by the DM relic density measurements performed by the WMAP [103] and the Planck [104] experiments. The most currently precise 3σ bounds read

$$0.1118 < \Omega_{\text{DM}} h^2 < 0.1280. \tag{4.17}$$

The relic density of DM in the IDM is controlled by different annihilation processes, the most important among them are annihilation into a pair of fermions (with an intermediate h particle), or annihilation into a pair of gauge bosons, see fig. 4.10. The first is more important for lighter DM particles, whereas the latter for heavier ones. For very heavy DM also coannihilation with A is significant.

The annihilation process $HH \to h \to f\bar{f}$ is controlled by the hHH coupling, which is proportional to λ_{345}, and by the mass of H. Thus constraints on the relic density can be translated to constraints on λ_{345}, depending on the mass of H. These

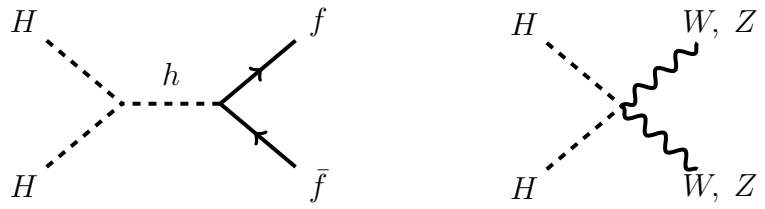

Figure 4.10: Most important processes controlling the DM relic density in the IDM.

constraints were discussed in ref. [137], and the dependence of the relic abundance of DM, $\Omega_{\rm DM}h^2$, on λ_{345} for different values of M_H is presented in fig. 4.11, which was taken from this reference. In the plot also the constraints from WMAP are marked (the allowed region lies between the black dashed lines), the numerical values differ slightly from those quoted in eq. (4.17) but it is not important for the qualitative discussion presented here. For the numerical bounds presented in the next section, the Planck constraints, eq. (4.17) will be used. It can be seen that imposing the relic density constraints results in upper and lower limits on λ_{345}. In general, the larger λ_{345} get, the more efficient the annihilation to fermionic pair becomes, thus yielding small DM relic density. On the other hand, for very small λ_{345} the annihilation is inefficient leading to overabundance of DM.

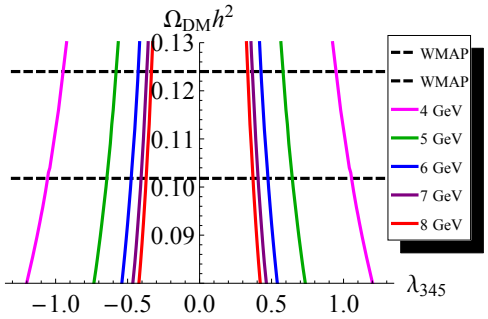

Figure 4.11: The dependence of the relic abundance of DM, $\Omega_{\rm DM}h^2$, as a function of λ_{345} for different values of the DM mass, in the low mass regime. The region between black dashed lines is allowed by WMAP. Plot taken from ref. [137].

Our aim is to combine the discussed constraints on λ_{345} and M_H following from lower bounds on $R_{\gamma\gamma}$, and the experimental bounds on $\Omega_{\rm DM}h^2$. The discussion of the results is presented in the next section.

4.4.2 Combined results

In this section the combination of the constraints on λ_{345} and M_H following from lower bounds on $R_{\gamma\gamma}$ with the bounds following from the relic density measurements is presented following ref. [3] (see also refs. [9, 10]).

4.4.2.1 Light DM

In fig. 4.12 the bounds on the λ_{345} parameter as a function of M_H are presented for $M_H < M_h/2$. The plots correspond to the requirement $R_{\gamma\gamma} > 0.7$ (left), $R_{\gamma\gamma} > 0.8$ (middle) and $R_{\gamma\gamma} > 0.9$ (right), different styles of curves correspond to different values of $M_{H^\pm}$. Since we assume $M_A > M_h/2$, the bounds do not depend on M_A. They are in general very stringent and yield

$$|\lambda_{345}| < 0.04 \quad \text{for} \quad M_H < M_h/2 \tag{4.18}$$

and they are stronger for lighter $M_{H^\pm}$. In the case of $R_{\gamma\gamma} > 0.9$ the whole region of very light DM with $M_H \lesssim 40 - 50\,\text{GeV}$ is excluded.

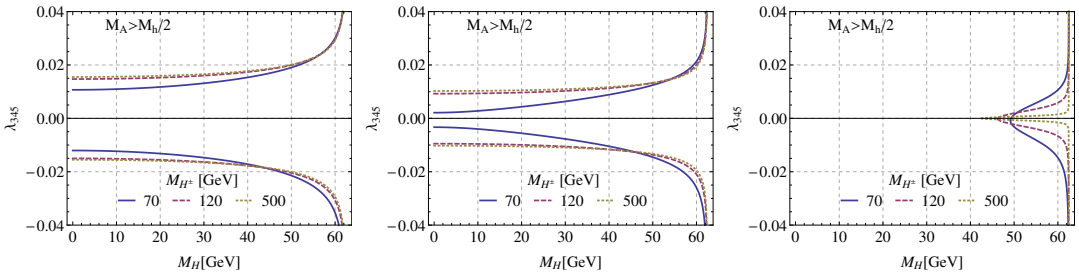

Figure 4.12: Constraints on the λ_{345} parameter following from the requirement that $R_{\gamma\gamma} > 0.7$ (left panel), $R_{\gamma\gamma} > 0.8$ (middle panel), $R_{\gamma\gamma} > 0.9$ (right panel). Different styles of curves correspond to different values of $M_{H^\pm}$. The regions between the curves are allowed. Plot taken from ref. [3].

On the other hand, the analyses of DM relic abundance [137] show that if light DM (with $M_H \lesssim 10\,\text{GeV}$) is to account for the total relic abundance of DM, its coupling to the Higgs boson has to fulfill (see also fig. 4.11)

$$|\lambda_{345}| \sim 0.4 - 1.2. \tag{4.19}$$

This is, however, in contradiction with eq. (4.18). Therefore, if the assumption $R_{\gamma\gamma} > 0.7$ is experimentally confirmed, the light DM region for $M_H \lesssim 10\,\text{GeV}$ can be excluded.

4.4.2.2 Intermediate DM

Another region in the parameter space where the inert H particle may account for the observed relic density is for intermediate masses of H, $40\,\text{GeV} \lesssim M_H \lesssim 80\,\text{GeV}$. From the point of view of the $R_{\gamma\gamma}$ analysis this region breaks into two sub-regions with different properties, depending whether the Higgs particle may or may not decay into DM pairs.

In fig. 4.13 plots combining information on the values of $R_{\gamma\gamma}$ and the relic abundance are shown for these two cases. The plots can be viewed as a combination of analogs of figs. 4.11 and 4.12 for the intermediate mass region. In fig. 4.13 different shades of blue indicate the values of $R_{\gamma\gamma}$. The grey shaded region is excluded by the Planck measurement, i.e. the relic density in this region is too big. The red region is in agreement with the relic density measurements, it fulfils eq. (4.17). In the remaining parameter space, the relic abundance of DM is too low, below the lower bound of eq. (4.17). It is excluded, if no other DM candidate is proposed. The masses of A and $H^\pm$ were fixed for concreteness. In the left panel $M_A = M_{H^\pm} = 120\,\text{GeV}$, in the right one $M_A = M_{H^\pm} = M_H + 50\,\text{GeV}$.

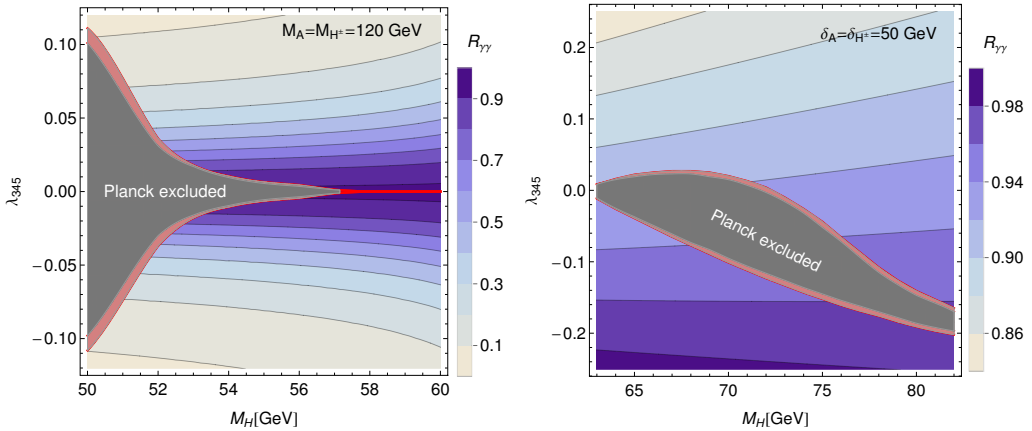

Figure 4.13: Map of the values of $R_{\gamma\gamma}$ in the (M_H, λ_{345}) plane for the intermediate DM masses. Superimposed are constraints from the relic density measurements: grey shaded region is excluded (DM relic density is too big), in the red region the relic density is in agreement with the Planck measurement, and in the remaining parameter space the relic density is too low. In the left panel $M_A = M_{H^\pm} = 120\,\text{GeV}$, in the right panel $M_A = M_{H^\pm} = M_H + 50\,\text{GeV}$ ($\delta_A = M_A - M_H$, $\delta_{H^\pm} = M_{H^\pm} - M_H$). Plot taken from ref. [10].

In the left panel of fig. 4.13 results for the case with $M_H < M_h/2$ are presented. It can be observed that due to the presence of invisible Higgs decays λ_{345} has to be very small to obtain high values of $R_{\gamma\gamma}$. Because of this, requiring $R_{\gamma\gamma} > 0.7$, and simultaneously demanding that the DM relic density produced within the IDM is

correct, we obtain a lower bound on the DM mass

$$M_H \gtrsim 53\,\mathrm{GeV}. \tag{4.20}$$

It should be also noted, that for bigger masses of H, close to the resonant $M_H = M_h/2$, both $R_{\gamma\gamma} > 0.7$, and correct relic density require very small, finely tuned values of λ_{345}.

In the right panel, results for the case of closed invisible decays are presented. Here in the whole considered parameter space $R_{\gamma\gamma} > 0.7$. However, if we require agreement with the Planck data, the $R_{\gamma\gamma}$ signal strength is always suppressed with respect to the SM.

4.4.2.3 Heavy DM

The correct relic density of DM can be obtained within the IDM also in the high DM mass region, for $M_H \gtrsim 500\,\mathrm{GeV}$. In this region all the inert particles have to be quasi-degenerate in mass because coannihilation effects are crucial to obtain correct relic density [162].

In fig. 4.14 a map of values of $R_{\gamma\gamma}$, together with the Planck constraints for heavy DM is presented, the colour coding is the same as in fig. 4.13. The masses of the inert scalars A and $H^{\pm}$ differ from the mass of H by 1 GeV. It is visible that in the whole region that is in agreement with the Planck measurements, $R_{\gamma\gamma}$ is very close to one. This behaviour is due to decoupling of the inert scalars — not only are they all heavy, but also due to small mass splittings, the couplings are relatively small. This scenario may be very hard to distinguish from the SM.

4.4.3 Comparison with the direct detection constraints

One of the main search strategies of DM is via direct detection — these experiments, such as LUX [109] or XENON [108], aim to measure recoil energy of the scattering of DM off heavy nuclei (see also section 3.3.2). The key parameter for these searches is the cross section for the scattering process, $\sigma_{\mathrm{DM,N}}$. In the case of inert DM (similarly as in other Higgs-portal DM models) it can only interact with the nucleon through an exchange of the Higgs boson. Thus, the tree-level cross section is proportional to the λ_{345} parameter squared and it reads

$$\sigma_{\mathrm{DM,N}} = \frac{\lambda_{345}^2}{4\pi M_h^4} \frac{m_N^4}{(m_N + M_H)^2} f_N^2, \tag{4.21}$$

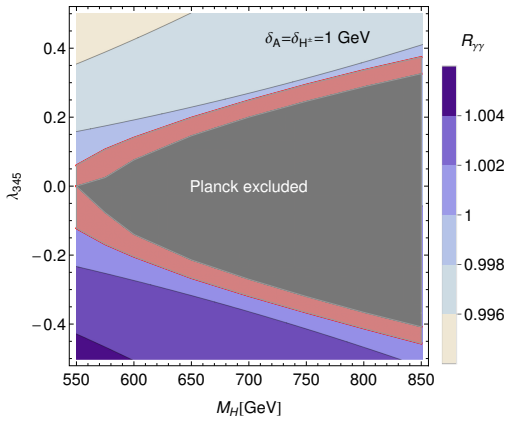

Figure 4.14: Map of the values of $R_{\gamma\gamma}$ in the (M_H, λ_{345}) plane for the heavy DM masses. Superimposed are constraints from relic density measurements: grey, shaded region is excluded (DM relic density is too big), in the red region the relic density is in agreement with the Planck measurement, and in the remaining parameter space the relic density is too low. We set $M_A = M_{H^\pm} = M_H + 1\,\text{GeV}$. Plot taken from ref. [10].

where m_N denotes the mass of the nucleon, and f_N is a universal Higgs-nucleon coupling.[5] There is no agreement on the value of the f_N coupling and various estimations exist in the literature because of uncertainty of the strange quarks contribution to the mass of the nucleon. Here, following our choice made in ref. [3], we consider the middle value of $0.14 < f_N < 0.66$ [165, 166], $f_N = 0.326$. For a recent discussion on the DM-nucleon interaction see e.g. ref. [167].

As can be seen from eq. (4.21) the only unknown parameters in $\sigma_{\text{DM,N}}$ are the Higgs-DM coupling, λ_{345}, and the DM mass. Thus, having upper bounds on λ_{345}, an upper bound on $\sigma_{\text{DM,N}}$ can be derived. To this end we used the constraints following from the requirement that $R_{\gamma\gamma} > 0.7$ ($R_{\gamma\gamma} > 0.8$) presented in fig. 4.12, the resulting bounds are shown in fig. 4.15. They bounds are computed for $M_{H^\pm} \approx 500\,\text{GeV}$ but the dependence on the mass of the charged scalar is slight. Only for very light charged scalar, on the verge of the LEP bounds, the bounds would be stronger (see also [3]). For comparison, we present also the bounds from the XENON100 [108] and the LUX [109] experiments.

The same reasoning can be used to derive bounds on $\sigma_{\text{DM,N}}$ from the measurement of invisible decay width of the Higgs boson (see section 4.3). Such studies were performed by the ATLAS collaboration [95]. These results are also presented in fig. 4.15.

[5] It has been shown that one-loop electroweak corrections to the DM-nucleon scattering cross section may be significant, especially in the case when λ_{345} is very small [163, 164]. However, the discussion of these corrections is beyond the scope of this work.

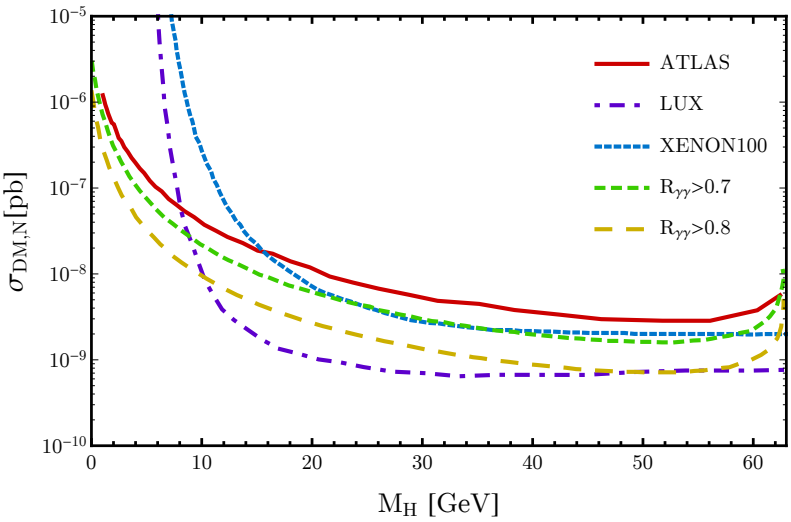

Figure 4.15: Bounds on the DM-nucleon scattering cross section, $\sigma_{\mathrm{DM,N}}$, as a function of DM mass derived from the requirement that $R_{\gamma\gamma} > 0.7$ ($R_{\gamma\gamma} > 0.8$). For comparison, also ATLAS results inferred from invisible decay width measurement [95], as well as XENON100 [108] and LUX [109] results are presented.

It can be seen that the bounds following from the collider measurements are far more sensitive in the low mass region, for $M_H \lesssim 10\,\mathrm{GeV}$, our results from $h \to \gamma\gamma$ being more constraining than the ones from invisible Higgs decays. In the rest of the parameter space considered, our results are stronger or comparable to the constraints from XENON100, and slightly weaker or comparable to the ones from LUX. It should be noted, however, that if stronger lower bounds on $R_{\gamma\gamma}$ are imposed, then $\sigma_{\mathrm{DM,N}}$ will be even more constrained. This shows how powerful are the collider searches, they can compete in predictions with the dedicated DM search experiments.

Chapter 5

One-loop effective potential

In the following part of this thesis we study the issue of stability of the vacuum state. A vacuum state is an extremely important element of any model of elementary interactions since it is the ground state around which the theory is built. It is crucial that the vacuum state is stable if the theory is to be predictive. At tree level the issue of vacuum stability is rather simple, however complications appear when loop corrections are included because they may significantly change the vacuum state (for example introducing symmetry breaking [168]).

A basic tool to study vacuum states is the effective potential. In the present chapter, before we move to the detailed analyses of the effective potential within the IDM, we introduce this notion, give arguments that indeed it is a well suited object for the study of vacuum stability, and show how to compute it in various models. This is a textbook material, it is presented here to keep this dissertation self-consistent and self-explanatory. In the presentation we follow the seminal paper by Coleman and Weinberg [168], the book of Li and Cheng [169], the notes by Coleman [170] and the textbook by Chankowski [171].

5.1 Definition of the effective potential

Let us start from the generating functional for the Green's functions for a simple theory with one scalar field ϕ (the generalisation the the case with more scalar fields is straightforward)

$$W[J] = \int \mathcal{D}\phi \exp\left\{ i \int d^4x \left[\mathcal{L}(\phi(x)) + J(x)\phi(x) \right] \right\}, \tag{5.1}$$

it can be thought of as a vacuum-to-vacuum transition amplitude in the presence of an external source $J(x)$

$$W[J] = \langle 0|0\rangle_J.$$

The coefficients of the expansion of $\log W$ in a functional Taylor series in $J(x)$ are the connected Green's functions

$$-i \log W[J] = \sum_n \frac{1}{n!} d^4x_1 \dots d^4x_n G^{(n)}(x_1, \dots, x_n) J(x_1) \dots J(x_n).$$

The classical field, denoted here by φ, is defined as the VEV of the quantum field operator ϕ in the presence of the source $J(x)$

$$\varphi \equiv -i \frac{\delta \log W}{\delta J(x)} = \left[\frac{\langle 0|\phi(x)|0\rangle}{\langle 0|0\rangle} \right]_J,$$

where the x-dependence of φ is not written explicitly for the sake of simplicity. Therefore, if $J = 0$, the classical field corresponds to the simple VEV of the field operator v_φ

$$v_\varphi = \frac{\langle 0|\phi(x)|0\rangle}{\langle 0|0\rangle},$$

and is constant in space and time due to translational invariance of the theory.

The effective action, which is a functional of φ, is a Legendre transform of $\log W[J]$,

$$\Gamma[\varphi] = -i \log W[J] - \int d^4x J(x)\varphi(x),$$

and hence

$$\frac{\delta \Gamma[\varphi]}{\delta \varphi} = -J(x).$$

For a constant classical field configuration this derivative vanishes

$$\left. \frac{\delta \Gamma[\varphi]}{\delta \varphi} \right|_{\varphi = v_f} = 0, \tag{5.2}$$

which shows that VEVs of the field operators correspond to the stationary points of the effective action. That is why the effective action is useful in the study of spontaneous symmetry breaking. $\Gamma[\varphi]$ contains the information about possible VEVs to all orders in perturbation theory, however, it is not straightforward to use in practice. That is why we need a simpler tool for practical calculations.

The effective action $\Gamma[\varphi]$ can be expanded in powers of φ

$$\Gamma[\varphi] = \sum_n \frac{1}{n!} \int d^4x_1 \dots d^4x_n \Gamma^{(n)}(x_1 \dots, x_n) \varphi(x_1) \dots \varphi(x_n), \tag{5.3}$$

where $\Gamma^{(n)}$ is a sum of all 1PI Feynman diagrams with n external legs. Alternatively we can expand Γ in powers of momenta

$$\Gamma[\varphi] = \int d^4x \left[-V(\varphi) + \frac{1}{2}(\partial_\mu \varphi)^2 Z(\varphi) + \dots \right]. \tag{5.4}$$

The term with zero power of momentum, $V(\varphi)$, is called the effective potential. It is clear that for constant classical fields, $\varphi = v_\varphi$ the effective action is proportional to the effective potential

$$\Gamma[v_\varphi] = -V(v_\varphi) \int d^4x.$$

Thus looking at eq. (5.2) it is clear that VEVs of field operators correspond to stationary points of the effective potential,

$$\left.\frac{\delta \Gamma[\varphi]}{\delta \varphi}\right|_{\varphi = v_f} = \left.\frac{\delta V(\varphi)}{\delta \varphi}\right|_{\varphi = v_f} \int d^4x = 0.$$

Since in the following we will use the effective potential to study the VEVs of the quantum fields, we limit ourselves to constant classical fields φ.

A physical interpretation of the effective potential given by Coleman (here we follow ref. [171], see also ref. [170]) is that $V(\varphi)$ corresponds to the minimum of the expectation values of the Hamiltonian density $\mathcal{H}$ calculated in a class of normalised states, such that the VEV of the field operator ϕ is equal to φ.[1] Namely,

$$V(\varphi) = \min \langle \Psi | \mathcal{H} | \Psi \rangle, \quad \text{for } \Psi \text{ such that } \quad \langle \Psi | \Psi \rangle = 1 \quad \text{and} \quad \langle \Psi | \phi | \Psi \rangle = \varphi.$$

This shows that the effective potential is a function which for a given VEV gives the minimal energy density. So a state that minimises V, minimises the energy density, i.e. corresponds to the ground state of a theory. This shows that indeed to find a ground state of a theory, i.e. the vacuum state, one has to minimise the effective potential.

To express $V(\varphi)$ in terms of Green's functions we will rewrite $\Gamma^{(n)}$ in the momentum space

$$\Gamma^{(n)}(x_1, \dots, x_n) = \int \frac{d^4k_1}{(2\pi)^4} \dots \frac{d^4k_n}{(2\pi)^4} (2\pi)^4 \delta^{(4)}(k_1 + \dots + k_n) e^{i(k_1 x_1 + \dots + k_n x_n)} \Gamma^{(n)}(k_1, \dots, k_n).$$

Substituting this to eq. (5.3), expanding in powers of momenta, and writing the δ function in a form of an integral we get

$$\begin{aligned} \Gamma[\varphi] = & \sum_n \frac{1}{n!} \int d^4x_1 \dots d^4x_n \int \frac{d^4k_1}{(2\pi)^4} \dots \frac{d^4k_n}{(2\pi)^4} \int d^4x e^{i(k_1 + \dots + k_n)x} e^{i(k_1 x_1 + \dots k_n x_n)} \\ & \times \left[\Gamma^{(n)}(0, \dots, 0) \varphi(x_1) \dots \varphi(x_n) + \dots \right] \\ = & \int d^4x \sum_n \frac{1}{n!} \left[\Gamma^{(n)}(0, \dots, 0) \varphi(x)^n + \dots \right]. \end{aligned} \tag{5.5}$$

[1] The argumentation showing that this interpretation is correct is rather involved, and therefore we do not show it here. It can be found in ref. [171].

We can now compare eq. (5.4) with eq. (5.5), and find out that the nth derivative of the effective potential is the sum of all 1PI diagrams with n external legs. Thus $V(\varphi)$ reads

$$V(\varphi) = -\sum_n \frac{1}{n!}\Gamma^{(n)}(0,\ldots,0)\varphi(x)^n. \tag{5.6}$$

V can be also expanded in subsequent loops, as an alternative to the perturbative expansion in coupling constant.[2] If we expand V from eq. (5.6) in loops, we can see that at tree level the effective potential coincides with the scalar potential appearing in the lagrangian treated as a function of the classical field. At the one-loop level, the contribution to the effective potential δV_{CW} is the sum of all one-loop diagrams with growing number of external legs, with the $\frac{1}{n!}$ coefficient, and vanishing external momenta,

$$\delta V_{\mathrm{CW}}(\varphi) = -\sum_n \frac{1}{n!}\Gamma^{(n)}_{\text{1-loop}}(0,\ldots,0)\varphi(x)^n, \tag{5.7}$$

where the subscript CW stands for the Coleman–Weinberg contribution. The renormalised one loop effective potential is the sum of the tree-level effective potential and the one-loop correction, as well some counterterms δV, necessary to obtain a finite result,

$$V^{(1)}_{\mathrm{eff}}(\varphi) = V^{(0)}_{\mathrm{eff}}(\varphi) + \delta V_{\mathrm{CW}}(\varphi) + \delta V.$$

As can be seen from eq. (5.7) the concrete form of the effective potential depends on a theory, and in particular on its particle content (different particles will give different loop contributions). In the following section we present a derivation of the effective potential in various simplified models, to show how the effective potential depends on particles of different spin. We use the straightforward method of diagrammatical calculations to get the results. For other possible methods see e.g. ref. [171].

5.2 Effective potential for $\lambda\phi^4$ theory of a single scalar field

Let us start from deriving the effective potential for a theory with a single, real scalar field with the self-interaction term of the $\lambda\phi^4$ form. The lagrangian for this model reads

$$\mathcal{L} = \frac{1}{2}(\partial_\mu\phi)(\partial^\mu\phi) - \frac{1}{2}m^2\phi^2 - \frac{\lambda}{4!}\phi^4.$$

[2]Here we skip the argumentation why it is a valid way of expanding the potential, it can be found for example in the book of Li and Cheng [169].

Then the scalar potential is given by

$$V = \frac{1}{2}m^2\phi^2 + \frac{\lambda}{4!}\phi^4. \tag{5.8}$$

Above ϕ denotes the quantum field, in the following φ will denote the corresponding classical field. Note that the tree-level effective potential is given by eq. (5.8) with ϕ exchanged by φ. This is a general property — to obtain the tree-level effective potential one has to replace the quantum scalar fields by the corresponding classical fields. Thus having the tree-level scalar potential we also have the tree-level effective potential.

The effective one-loop potential is given by the sum of all 1-loop diagrams with zero external momenta. In fact, due to the structure of the potential (no odd powers of ϕ) there is no way of generating diagrams with an odd number of external legs so we only need to sum the diagrams with an even number of legs. The computation differs depending on the sign of the mass parameter m^2, and we will consider different cases separately.

5.2.1 Case with $m^2 \geqslant 0$

When $m^2 \geqslant 0$, the term $\frac{1}{2}m^2\varphi^2$ is just a mass term for the scalar field. Feynman rules for this theory are as follows:

- interaction vertex $= -i\lambda$,
- scalar propagator $= \frac{i}{k^2-m^2+i\varepsilon}$.

Therefore the diagram with one pair of external legs (see fig. 5.1, left panel) gives the following contribution:

$$-i\lambda \int \frac{d^4k}{(2\pi)^4}\frac{i}{k^2-m^2+i\varepsilon}\frac{1}{2}\varphi^2 = \int \frac{d^4k}{(2\pi)^4}\frac{\frac{1}{2}\lambda\varphi^2}{k^2-m^2+i\varepsilon},$$

where $\frac{1}{2}$ comes from the symmetry factor accounting for the exchange of external legs, and external legs contribute a factor of φ. The diagram with two pairs of

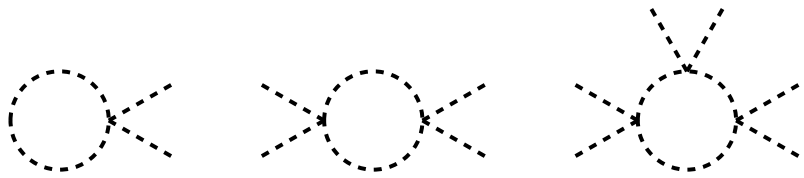

Figure 5.1: Diagrams with two (left), four (middle), and six (right) external legs contributing to the one-loop effective potential of the $\lambda\varphi^4$ model.

external legs with zero momentum (fig. 5.1, middle) gives the contribution

$$\frac{1}{2}\int \frac{d^4k}{(2\pi)^4}(-i\lambda)\frac{i}{k^2-m^2+i\varepsilon}(-i\lambda)\frac{i}{k^2-m^2+i\varepsilon}\left(\frac{1}{2}\varphi^2\right)^2 = \int \frac{d^4k}{(2\pi)^4}\frac{1}{2}\left(\frac{\frac{1}{2}\lambda\varphi^2}{k^2-m^2+i\varepsilon}\right)^2,$$

where the 1/2 factor at the beginning accounts for the possibility of exchanging the internal propagators.

Expressions for diagrams with bigger number of external legs are constructed analogously. Only the symmetry factors have to be assigned carefully. In each diagram the factor of $(1/2)^n$ will account for swapping external legs within the pairs. We can think of the interaction vertices as of the vertices of a regular polygon of n sites. For a given n, $n!$ polygons with different numberings of the vertices can be constructed. However, two configurations that differ by a rotation or a mirror symmetry are equivalent, and should not be counted twice. Therefore the right symmetry factor is $\frac{n!}{2n}$. We have to remember also about the $\frac{1}{n!}$ factor from eq. (5.7). Finally we get a $\frac{1}{2n}$ factor for a n-leg class of diagrams.

The contribution to the effective potential coming from all such diagrams reads:

$$\delta V_{\mathrm{CW}} = i\sum_{n=1}^{\infty}\int \frac{d^4k}{(2\pi)^4}\frac{1}{2n}\left(\frac{\frac{1}{2}\lambda\varphi^2}{k^2-m^2+i\varepsilon}\right)^n. \tag{5.9}$$

The overall factor of i comes from the expansion of the generating functional W. To compute δV_{CW} we perform the Wick rotation by setting $k_0 = ik_0^E$, where "E" stands for Euclidean, $\left(k^E\right)^2 = k_0^E k^{E0} + k_i^E k^{Ei}$. Then

$$\begin{aligned}\delta V_{\mathrm{CW}} &= i^2\sum_{n=1}^{\infty}\int \frac{d^4k^E}{(2\pi)^4}\frac{1}{2n}\left(\frac{\frac{1}{2}\lambda\varphi^2}{-(k^E)^2-m^2}\right)^n \\ &= \sum_{n=1}^{\infty}\int \frac{d^4k^E}{(2\pi)^4}\frac{(-1)^{n+1}}{2n}\left(\frac{\frac{1}{2}\lambda\varphi^2}{(k^E)^2+m^2}\right)^n,\end{aligned}$$

where we skipped the $i\epsilon$ in the denominator for convenience. Now we use the formula

$$\log(1+x) = \sum_{n=1}^{\infty}\frac{(-1)^{n+1}}{n}x^n,$$

and obtain

$$\delta V_{\mathrm{CW}} = \frac{1}{2}\int \frac{d^4k}{(2\pi)^4}\log\left(1+\frac{\frac{1}{2}\lambda\varphi^2}{k^2+m^2}\right), \tag{5.10}$$

where we skipped the superscript in k^E for brevity.

Let us rewrite $\delta V_{\rm CW}$ in a more useful way:

$$\begin{aligned}\delta V_{\rm CW} &= \frac{1}{2}\int \frac{d^4k}{(2\pi)^4}\log\left(\frac{k^2+m^2+\frac{1}{2}\lambda\varphi^2}{k^2+m^2}\right)\\ &= \frac{1}{2}\int \frac{d^4k}{(2\pi)^4}\left[\log\left(k^2+m^2+\frac{1}{2}\lambda\varphi^2\right)-\log\left(k^2+m^2\right)\right].\end{aligned} \tag{5.11}$$

This integral is UV-divergent and therefore has to be regularised. The procedure of dimensional regularisation of $\delta V_{\rm CW}$ is presented in detail in appendix C. The final result for the regularised one-loop contribution to the effective potential is given by

$$\delta V_{\rm CW} = \frac{m_{\rm eff}^4}{64\pi^2}\left[-\frac{2}{\epsilon}+\gamma_E-\frac{3}{2}+\log\left(\frac{m_{\rm eff}^2}{4\pi\mu^2}\right)\right]. \tag{5.12}$$

5.2.1.1 Renormalisation of $\delta V_{\rm CW}$

The result shown above, eq. (5.12), is clearly divergent as $\epsilon \to 0$. Therefore, we have to add counterterms to the potential which would cancel the divergences. Thus the one-loop effective potential will have the form

$$V_{\rm eff}^{(1)} = \frac{1}{2}m^2\varphi^2+\frac{\lambda}{4!}\varphi^4+\delta V_{\rm CW}+\frac{B}{2}\varphi^2+\frac{C}{4!}\varphi^4. \tag{5.13}$$

Different renormalisation conditions can be chosen to fix the counterterms. In the seminal paper by Coleman and Weinberg [168] the mass and coupling of the scalar particle were identified with the second and fourth derivative of the effective potential at $\varphi = 0$ (see also [169]),[3]

$$m^2 = \left.\frac{d^2V_{\rm eff}^{(1)}}{d\varphi^2}\right|_{\varphi=0}, \tag{5.14}$$

$$\lambda = \left.\frac{d^4V_{\rm eff}^{(1)}}{d\varphi^4}\right|_{\varphi=0}. \tag{5.15}$$

In this work we will use different renormalisation schemes — the on-shell (OS) scheme, in which masses of physical particles are not changed by the loop corrections, and the $\overline{\rm MS}$ scheme, where the counterterms simply cancel the divergencies of eq. (5.12). More details of the renormalisation procedure used in this work will be given in sections 6.2.1 and 6.3.2.

5.2.2 Case with $m^2 < 0$

In the case when the parameter m^2 in the potential (5.8) is negative, it cannot be interpreted as a mass term. We will therefore, treat it as a part of the interaction

[3] Special care should be taken when $m^2 = 0$ because then the conditions (5.14) and (5.15) lead to divergencies.

vertex, which is then equal to (see fig. 5.2)

$$-i\left(\frac{\lambda}{2}\varphi^2 + m^2\right),$$

and consequently the propagator is massless:

$$\frac{i}{k^2 + i\varepsilon}.$$

With this changes in the vertex and the propagator we can construct δV_{CW} analo-

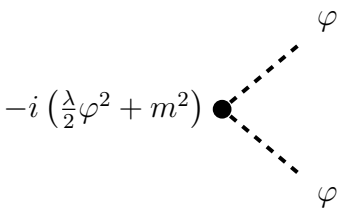

Figure 5.2: Field-dependent interaction vertex for $\lambda\phi^4$ theory with $m^2 < 0$.

gously to the case with $m^2 \geqslant 0$, however this time we sum diagrams with massless propagators, field-dependent interaction vertices, and no external legs, see fig. 5.3. The result reads (compare with eq. (5.9)):

$$\delta V_{\mathrm{CW}} = i\sum_{n=1}^{\infty}\int \frac{d^4k}{(2\pi)^4}\frac{1}{2n}\left(\frac{\frac{1}{2}\lambda\varphi^2 + m^2}{k^2 + i\varepsilon}\right)^n.$$

Performing the same steps as previously we arrive at the expression:

$$\delta V_{\mathrm{CW}} = \frac{1}{2}\int \frac{d^4k}{(2\pi)^4}\log\left(1 + \frac{\frac{1}{2}\lambda\varphi^2 + m^2}{k^2}\right). \tag{5.16}$$

Rewriting this expression as

$$\delta V_{\mathrm{CW}} = \frac{1}{2}\int \frac{d^4k}{(2\pi)^4}\log\left(k^2 + \frac{1}{2}\lambda\varphi^2 + m^2\right) - \frac{1}{2}\int \frac{d^4k}{(2\pi)^4}\log\left(k^2\right),$$

and comparing with eq. (5.11) we see that the two expressions differ only by the second, constant term. And even that one can be adjusted to the form of eq. (5.11) with a simple change of variables, $k'^2 + m^2 = k^2$. So the two approaches of treating m either as a mass, or as a contribution to the vertex are equivalent, and the final formula for δV_{CW} is given by eq. (5.12). We will frequently use the latter approach in the following parts of this chapter.

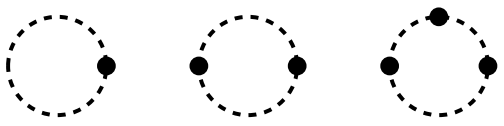

Figure 5.3: First three diagrams contributing to the one-loop effective potential of the $\lambda\varphi^4$ model with $m < 0$. The black dots denote the field-dependent interaction vertices, the scalar propagators are massless.

5.3 Effective potential in a model with a vector field

To learn how bosonic fields contribute to the effective potential, let us consider a model in which a scalar field interacts with a vector field. Then the lagrangian contains an interaction term of the form[4]

$$\mathcal{L} \supseteq e^2 A_\mu A^\mu \phi^2.$$

We are not be interested in purely scalar contributions to the effective potential, since these were already analyzed in the previous section. We only consider the scalar-vector interactions. The Feynman rules in the Landau gauge read:

- scalar–scalar–vector–vector vertex: $i2e^2 g_{\mu\nu}$,
- vector propagator: $-i\frac{g_{\mu\nu}-k_\mu k_\nu/k^2}{k^2+i\varepsilon}$,
- scalar propagator: $\frac{i}{k^2+i\varepsilon}$.

We have not included a mass term to the scalar propagator. If a mass term is present in the lagrangian, it can be included in the scalar self-interaction vertex, as described in the previous section.

To find the bosonic contribution to effective potential we have to sum the diagrams with even number of external scalar legs, the first three are presented in fig. 5.4. The symmetry factors for the diagrams will remain the same as in the scalar case, i.e., a diagram with n interaction vertices will be multiplied by $1/2n$.

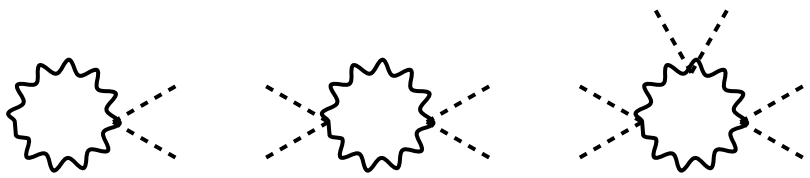

Figure 5.4: Diagrams with two, four, and six external scalar legs and bosonic internal lines contributing to the one-loop effective potential.

The diagram with one interaction vertex gives the contribution

$$\int \frac{d^4k}{(2\pi)^4}\frac{1}{2}\frac{\varphi^2 ie^2 g^{\mu\nu}(-i)(g_{\mu\nu}-k_\mu k_\nu/k^2)}{k^2+i\varepsilon} = \int \frac{d^4k}{(2\pi)^4}\frac{1}{2}\varphi^2 e^2 \frac{g^\mu{}_\mu - 1}{k^2+i\varepsilon},$$

[4]Of course a field to interact with a photon has to be charged so the model has to contain a complex scalar field. Here we are not interested in the details of the toy model, our focus is to demonstrate how bosonic fields contribute to the effective potential, so we can simply think of ϕ as a real part of a complex scalar field.

where the factor of 2 from the interaction vertex was cancelled by $\frac{1}{2}$ accounting for the exchange of the scalar fields. If we want to go to D dimensions to compute this integral we have to be careful, since $g^{\mu}{}_{\mu}$ depends on D. It also depends on whether dimensional regularisation or dimensional reduction is used. In the following we will use dimensional regularisation, and later on we will comment on the case of dimensional reduction. In D dimensions, with $D = 4 - \epsilon$ we have

$$\int \frac{d^D k}{(2\pi)^D} \mu^\epsilon \frac{1}{2} \varphi^2 e^2 \frac{g^{\mu}{}_{\mu} - 1}{k^2 + i\varepsilon} = (D-1) \int \frac{d^D k}{(2\pi)^D} \mu^\epsilon \frac{1}{2} \frac{\varphi^2 e^2}{k^2 + i\varepsilon}.$$

The diagram with two vertices will contribute as

$$\begin{aligned}
&\int \frac{d^D k}{(2\pi)^D} \mu^\epsilon \frac{1}{4} \frac{(\varphi^2 i e^2)^2 g^{\mu\nu} (-i)^2 (g_{\nu\rho} - k_\nu k_\rho / k^2) g^{\rho\sigma} (g_{\sigma\mu} - k_\sigma k_\mu / k^2)}{(k^2 + i\varepsilon)^2} \\
&= \int \frac{d^D k}{(2\pi)^D} \mu^\epsilon \frac{1}{4} (\varphi e)^4 \frac{g^{\mu}{}_{\rho} g^{\rho}{}_{\mu} - 2k^\mu k_\mu / k^2 + k^\mu k_\mu k^\rho k_\rho / k^4}{(k^2 + i\varepsilon)^2} \\
&= (D-1) \int \frac{d^D k}{(2\pi)^D} \frac{1}{4} \frac{(\varphi e)^4}{(k^2 + i\varepsilon)^2}.
\end{aligned}$$

The contributions from next diagrams are computed analogously. Finally, the sum of all 1-loop diagrams with vectorial internal lines gives

$$i \int \frac{d^D k}{(2\pi)^D} \mu^\epsilon (D-1) \sum_{n=1}^{\infty} \frac{1}{2n} \left[\frac{(\varphi e)^2}{k^2 + i\varepsilon} \right]^n.$$

Using the same tricks as described in section 5.2.1 (Wick rotation, summing the series) we get the result

$$\delta V_{\mathrm{CW}} = \int \frac{d^D k}{(2\pi)^D} \frac{1}{2} (D-1) \log \left(1 + \frac{e^2 \varphi^2}{k^2} \right).$$

The integral can be performed along the lines of section 5.2.1, however at the stage of expanding around $D = 4$ one has to remember about the factor $D - 1 = 3 - \epsilon$. It will modify the result slightly, namely

$$\delta V_{\mathrm{CW}} = \frac{3 m_{\mathrm{eff}}^4}{64\pi^2} \left[-\frac{2}{\epsilon} + \gamma_E - \frac{5}{6} + \log \left(\frac{m_{\mathrm{eff}}^2}{4\pi\mu^2} \right) \right], \tag{5.17}$$

where $m_{\mathrm{eff}}^2 = e^2 \varphi^2$. In general, m_{eff}^2 will always be replaced by a field-dependent mass of the considered particle, i.e. a mass acquired by the particle from the mass terms present in the lagrangian, and from the interaction with the φ field. The important difference between the scalar and the vector contributions is the factor of 3 in front of the expression. Moreover, the factor of $\frac{3}{2}$ in the bracket is replaced by $\frac{5}{6}$.

If dimensional reduction was used, the factor $D - 1$ coming from construction of bosonic propagators would give 3 instead of $3 - \epsilon$, and thus in eq. (5.17) $\frac{3}{2}$ instead of $\frac{5}{6}$ would be present.

5.4 Effective potential in a model with a fermionic field

Let as now consider a theory with a scalar and a fermionic field. The lagrangian includes a kinetic term for the fermionic field and a term describing interaction between the fermion and the scalar. The relevant part of the Lagrangian looks as follows

$$\mathcal{L} \supseteq \overline{\Psi} \not{\partial} \Psi + g \overline{\Psi} \phi \Psi.$$

As in the case of the scalar theory with $m < 0$, section 5.2.2, we will treat the classical field φ as a part of the interaction vertex. Therefore the Feynman rules will read:

- fermion-fermion-scalar vertex: $ig\varphi \equiv im_{\text{eff}}$,
- (massless) fermionic propagator: $\frac{i}{\not{p}+i\varepsilon}$.

If a mass term for the fermionic field is present it can be included in the fermion-fermion-scalar vertex, m_{eff}. In this theory only diagrams with an even number of fermionic propagators will contribute to the effective potential, since with every propagator one Dirac matrix is introduced, and a trace of an odd number of Dirac matrices is zero.

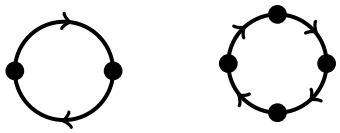

Figure 5.5: First two diagrams contributing to the one-loop effective potential of a model containing a scalar and a fermionic field. The black dots denote the field-dependent interaction vertices, the fermionic propagators are massless.

The simplest diagram, which contributes to the effective potential has two fermionic propagators, see fig. 5.5 (left). Its contribution reads

$$(-1) \int \frac{d^4k}{(2\pi)^4} \text{Tr} \left[im_{\text{eff}} \frac{i}{\not{k} + i\varepsilon} im_{\text{eff}} \frac{i}{\not{k} + i\varepsilon} \right],$$

where an overall factor of -1 for a fermionic loop should be noted. Simplifying this expression we get

$$- \int \frac{d^4k}{(2\pi)^4} \text{Tr} \left[\frac{m_{\text{eff}}^2}{(\not{k} + i\varepsilon)^2} \right] = -4 \int \frac{d^4k}{(2\pi)^4} \frac{m_{\text{eff}}^2}{k^2 + i\varepsilon}.$$

The factor of 4 comes from the trace over Dirac indices. The contribution from a diagram with four fermionic propagators is computed in an analogous way

$$\begin{aligned}&(-1)\int\frac{d^4k}{(2\pi)^4}\mathrm{Tr}\left[im_{\mathrm{eff}}\frac{i}{\not{k}+i\varepsilon}im_{\mathrm{eff}}\frac{i}{\not{k}+i\varepsilon}im_{\mathrm{eff}}\frac{i}{\not{k}+i\varepsilon}im_{\mathrm{eff}}\frac{i}{\not{k}+i\varepsilon}\right]\\&=-4\int\frac{d^4k}{(2\pi)^4}\left(\frac{m_{\mathrm{eff}}^2}{k^2+i\varepsilon}\right)^2.\end{aligned}$$

The symmetry factors for the diagrams are the same as previously, so the sum of all 1-loop diagrams can be performed straightforwardly

$$\delta V_{\mathrm{CW}}=-i\sum_{n=1}^{\infty}\frac{1}{2n}4\int\frac{d^4k}{(2\pi)^4}\left(\frac{m_{\mathrm{eff}}^2}{k^2+i\varepsilon}\right)^n=-4\left[\frac{1}{2}\int\frac{d^4k}{(2\pi)^4}\log\left(1+\frac{m_{\mathrm{eff}}^2}{k^2}\right)\right].\tag{5.18}$$

The result differs from the result for the scalar field by a factor of 4 coming from the trace over Dirac indices, and the overall factor of -1 (the $i\varepsilon$ term in the denominator was omitted in the last equality for convenience).

5.5 Effective potential in a model with k scalar fields

Let us consider a model with k types of scalar fields. The scalar interactions are described by the scalar potential which is a quartic polynomial of the fields ϕ_i $(i=1,\ldots,k)$. If it is to be renormalisable, it cannot contain terms of order three in the fields. So the one-loop contribution to the effective potential will amount to a sum of all one-loop diagrams with an even number of external legs. To compute this quantity we will need the quartic vertices. If we again employ the field-dependent vertices (as discusses in section 5.2.2), a general vertex will read as follows (see fig. 5.6)

$$-iW_{ab}(\varphi_i)=-i\frac{\partial^2V}{\partial\varphi_a\partial\varphi_b},$$

where the tree-level potential is treated as a function of the classical fields φ_i, corresponding to quantum fields ϕ_i (so V is the tree-level effective potential). W_{ab} is a quadratic function of φ_i and is symmetric in the a,b indices. With this kind of interactions, the type of particle propagating in the loop will change at the interaction point. The mass terms are of course included in the interaction vertices.

The simplest diagram, see fig. 5.7, will contain only one interaction vertex. Summing contributions from all types of fields that can propagate in the loop we will get

$$\sum_{a=1}^{k}\int\frac{d^4k}{(2\pi)^4}\frac{1}{2}(-iW_{aa})\frac{i}{k^2+i\varepsilon}=\sum_{a=1}^{k}\int\frac{d^4k}{(2\pi)^4}\frac{1}{2}\frac{W_{aa}}{k^2+i\varepsilon}.$$

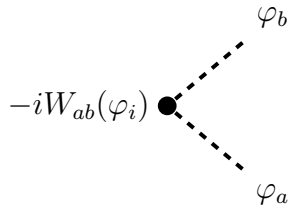

Figure 5.6: Field-dependent interaction vertex, $W_{ab}(\varphi_i)$. At the interaction point a field of type a is exchanged to a field of type b.

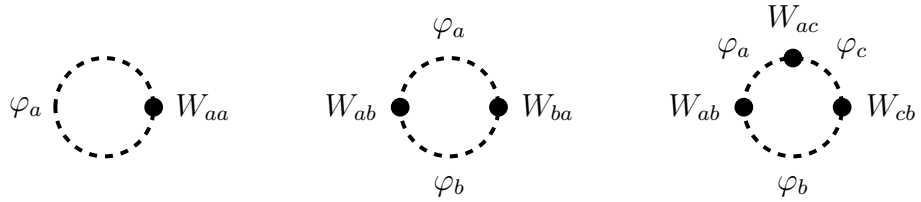

Figure 5.7: First three diagrams contributing to the one-loop effective potential of the model with k scalar fields. The black dots denote the field-dependent interaction vertices, the scalar propagators are massless.

In the case of two interaction vertices the contribution reads

$$\sum_{a=1}^{k}\sum_{b=1}^{k}\int\frac{d^4k}{(2\pi)^4}\frac{1}{4}\frac{W_{ab}W_{ba}}{(k^2+i\varepsilon)^2}.$$

In the case with n interaction vertices we have the contribution

$$\begin{aligned}&\sum_{a_1=1}^{k}\sum_{a_2=1}^{k}\cdots\sum_{a_n=1}^{k}\int\frac{d^4k}{(2\pi)^4}\frac{1}{2n}\frac{W_{a_1a_2}W_{a_2a_3}\ldots W_{a_{n-1}a_n}W_{a_na_1}}{(k^2+i\varepsilon)^n}\\&=\sum_{a_1=1}^{k}\int\frac{d^4k}{(2\pi)^4}\frac{1}{2n}\frac{(W^n)_{a_1a_1}}{(k^2+i\varepsilon)^n}.\end{aligned}$$

Of course, the numerator could be reduced to the trace of W^n, but we do not want to perform this simplification before summing the contributions from all diagrams.[5] Since W is symmetric we can diagonalise it, and in the eigenbasis $(W^n)_{a_1a_1} = (W_{a_1a_1})^n$. Hence, the full one-loop contribution to the effective potential, which is a sum of all one-loop diagrams, amounts to (in the eigenbasis of W)

$$\delta V_{\mathrm{CW}} = i\sum_{n=1}^{\infty}\sum_{a_1=1}^{k}\int\frac{d^4k}{(2\pi)^4}\frac{1}{2n}\frac{(W_{a_1a_1})^n}{(k^2+i\varepsilon)^n} = i\sum_{a_1=1}^{k}\left[\sum_{n=1}^{\infty}\int\frac{d^4k}{(2\pi)^4}\frac{1}{2n}\frac{(W_{a_1a_1})^n}{(k^2+i\varepsilon)^n}\right].$$

[5]Here W stands for W_{ab} with indices suppressed for the sake of clarity. It should not be confused with the generating functional W.

Now, inside the bracket we can perform usual tricks, i.e., Wick rotation and summation of the series, and we arrive at

$$\delta V_{\mathrm{CW}} = i \sum_{a_1=1}^{k} \int \frac{d^4k}{(2\pi)^4} \log\left(1 + \frac{W_{a_1a_1}}{k^2}\right).$$

Apart from the sum over a_1, it is the same as the result for the case with one scalar field, with $m < 0$ and m^2_{eff} replaced by $W_{a_1a_1}$. Therefore, the regularisation procedure will work the same, and δV_{CW} will read:

$$\delta V_{\mathrm{CW}} = \frac{1}{64\pi^2} \sum_{a_1=1}^{k} (W_{a_1a_1})^2 \left[\log\left(\frac{W_{a_1a_1}}{4\pi\mu^2}\right) - \frac{2}{\epsilon} + \gamma_E - \frac{3}{2}\right]. \tag{5.19}$$

Remembering that W is the matrix of second derivatives of the scalar potential so the mass matrix of the scalar sector, we see that a contribution to the effective potential in a model with k scalars is just a sum of the contributions of the scalars. However, one should note that the masses present in this formula are field-dependent, and in general each mass depend on k scalar fields.

The result can be written also in a basis independent form as

$$\delta V_{\mathrm{CW}} = \frac{1}{64\pi^2} \left\{ \mathrm{Tr}\left[W^2 \log\left(\frac{W}{4\pi\mu^2}\right)\right] + \mathrm{Tr}(W^2)\left[-\frac{2}{\epsilon} + \gamma_E - \frac{3}{2}\right]\right\}. \tag{5.20}$$

Since trace is independent of the basis in which it is computed, the formula will hold also for basis different than the eigenbasis of W.

5.6 Effective potential in a model with k vector fields

Let us now consider a model with k vector fields. We define the couplings between the classical scalar field and the bosonic fields as $\mathbf{M}^2(\varphi_i)$

$$\frac{1}{2} \sum_{a,b} \mathbf{M}^2_{ab} A_{\mu a} A^{\mu}_{b}.$$

$\mathbf{M}^2$, which is a field-dependent mass matrix of the bosonic sector, is a quadratic polynomial of φ_i and is symmetric in the a, b indices.

If we use the propagators in the Landau gauge, they will be of the form discusses in section 5.3. Once more, while computing contributions from 1-loop diagrams with different numbers of external legs, from the contraction of the numerators of propagators a factor of $D - 1$ (or 3, depending on the scheme used) will arise for each diagram. Further, the analysis goes along the same lines as above, in

the case of multiple scalar fields. Therefore we can simply write down the result for the contribution to the effective potential

$$\delta V_{\mathrm{CW}} = \frac{3}{64\pi^2}\left\{\mathrm{Tr}\left[\mathbf{M}^2\log\left(\frac{\mathbf{M}}{4\pi\mu^2}\right)\right] + \mathrm{Tr}(\mathbf{M}^2)\left[-\frac{2}{\epsilon}+\gamma_E - C\right]\right\}, \tag{5.21}$$

where $C = \frac{5}{6}$ or $\frac{3}{2}$ for dimensional regularisation or dimensional reduction, respectively. If we work in an mass-eigenbasis the result can be written in a simpler form

$$\delta V_{\mathrm{CW}} = \frac{3}{64\pi^2}\sum_{i=1}^{k} M_i^4\left[\log\left(\frac{M_i^2}{4\pi\mu^2}\right) - \frac{2}{\epsilon}+\gamma_E - C\right], \tag{5.22}$$

where the sum runs over all bosonic mass-eigenstates.

5.7 Effective potential in a model with k fermionic fields

Similar reasoning may be applied in the case of multiple fermionic fields. If the interactions with the classical scalar fields are of the form

$$-\sum_{ab}\overline{\Psi}_a\mathbf{m}(\varphi_i)_{ab}\Psi_b,$$

then the matrix $\mathbf{m}$ is a matrix in the internal space of the fermionic fields, and in the Dirac space

$$\mathbf{m}_{ab} = A_{ab} + iB_{ab}\gamma_5,$$

where A and B are Hermitian matrices and linear functions of φ_i.

Only the diagrams with an even number of internal fermionic lines will give non-vanishing contributions, as a trace of an odd number of Dirac matrices is equal zero. The contributions from 1-loop graphs will be similar as in the case of a single fermion, see section 5.4. However, now for m_{eff} we have to substitute $\mathbf{m}$, which is a matrix and it does not necessarily commute with the propagator. The contribution from a diagram with n external legs (and n fermionic propagators) will include

$$\mathrm{Tr}\left[\ldots\mathbf{m}\frac{1}{\not k}\mathbf{m}\frac{1}{\not k}\ldots\right] = \mathrm{Tr}\left[\ldots\mathbf{m}\frac{\not k}{k^2}\mathbf{m}\frac{\not k}{k^2}\ldots\right],$$

where we skipped $i\varepsilon$ in the denominators for convenience. Since $\{\gamma_\mu,\ \gamma_5\} = 0$, then

$$\mathbf{m}\not k = (A + iB\gamma_5)\not k = \not k(A - iB\gamma 5) = \not k\mathbf{m}^\dagger.$$

Therefore,

$$\mathrm{Tr}\left[\ldots\mathbf{m}\frac{\not k}{k^2}\mathbf{m}\frac{\not k}{k^2}\ldots\right] = \mathrm{Tr}\left[\ldots\mathbf{m}\mathbf{m}^\dagger\frac{1}{k^2}\ldots\right].$$

The number of $\mathbf{m}\not{k}$ sequences in all of the contributions is even, so they can be combined in pairs. And then the method from previous sections can be applied and the result is obtained in a straightforward way in the form

$$\delta V_{\mathrm{CW}} = -\frac{1}{64\pi^2}\left\{\mathrm{Tr}\left[\left(\mathbf{m}\mathbf{m}^\dagger\right)^2 \log\left(\frac{\mathbf{m}\mathbf{m}^\dagger}{4\pi\mu^2}\right)\right] + \mathrm{Tr}\left[\left(\mathbf{m}\mathbf{m}^\dagger\right)^2\right]\left[-\frac{2}{\epsilon}+\gamma_E-\frac{3}{2}\right]\right\}, \tag{5.23}$$

where the trace is taken over the Dirac indices and over the internal space (because we sum over different kinds of fermions). In the mass-eigenstate basis the result reads

$$\delta V_{\mathrm{CW}} = \frac{4}{64\pi^2}\sum_{i=1}^{k} M_i^4\left[\log\left(\frac{M_i^2}{4\pi\mu^2}\right)-\frac{2}{\epsilon}+\gamma_E-\frac{3}{2}\right], \tag{5.24}$$

where the sum runs over mass-eigenstates, and M_i are field-dependent masses of the fermions.

One has to remember that if the fermions have colour charge, an overall factor accounting for the number of colours should be added.

5.8 General one-loop correction to the effective potential

Summing up the results obtained in the preceding sections we can conclude that in a model containing scalars, bosons and fermions the one-loop CW contribution to the effective potential reads

$$\delta V_{\mathrm{CW}} = \frac{1}{64\pi^2}\sum_a n_a M_a(\varphi_i)^4\left[\log\left(\frac{M_a(\varphi_i)^2}{4\pi\mu^2}\right)-\frac{2}{\epsilon}+\gamma_E-C_a\right], \tag{5.25}$$

where the sum runs over all particles present in the theory. $M_a(\varphi_i)$ are the field-dependent mass-eigenvalues of the respective particles, in general they can depend on all the scalar fields present in the theory. The constant $C_a = \frac{5}{6}$ for bosons when dimensional regularisation is used and $C_a = \frac{3}{2}$ for boson when dimensional reduction is used, and for other particles independently of the regularisation method applied. The factor n_a counts the degrees of freedom corresponding to each particle, namely

$$n_a = (-1)^{2s_a} Q_a K_a (2s_a+1), \tag{5.26}$$

where s_a is the spin of the particle a, Q_a is equal 1 or 2 for neutral or charged particles, respectively, and K_a counts the number of colours of particle a.

Formula (5.25) is written in the mass-eigenbasis. If this basis is inconvenient, the general formulas, eq. (5.20), (5.21) and (5.23) should be used.

CHAPTER 6

VACUUM STABILITY

With the recent discovery of a Higgs boson and the measurement of its mass [18, 19, 92], the issue of vacuum stability gained a lot of attention. State of the art computations show that the SM vacuum is metastable — it is not a global minimum of the SM effective potential but its lifetime is extremely long [28–31], see fig. 6.1 (from ref. [29]). However, this is not the final answer to the question of vacuum stability because new BSM interactions can modify vacuum structure of the potential and change the lifetime of the EWSB vacuum [172–176].

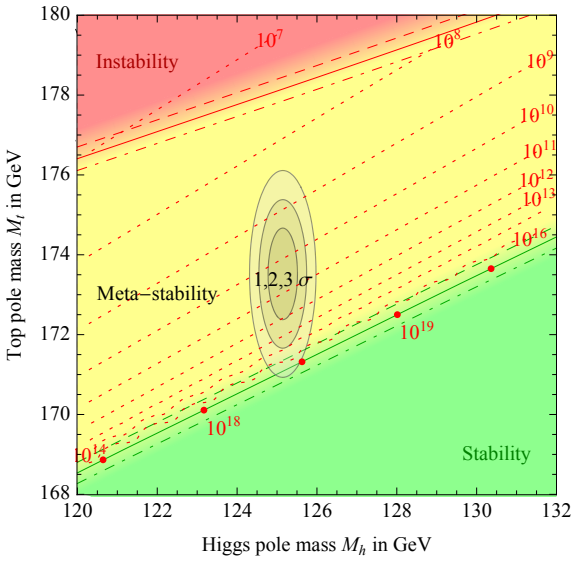

Figure 6.1: Phase diagram of the SM. The SM vacuum is in the metastability region. Plot taken from ref. [29].

To study stability of a vacuum state one normally starts from requiring the (effective) potential to be bounded from below (positivity conditions). The common way of achieving this at the one-loop level is to check the tree-level positivity conditions with running couplings inserted. The destabilising factor is the contribution from the fermions, in particular the top quark, because with fermionic loops a minus sign is associated (see the derivation of the contribution from a fermion to the effective potential, section 5.4). On the other hand, scalar fields contribute positively both to the running and to the effective potential (see section 5.2) so in presence of additional scalars the running Higgs self-coupling receives additional positive contribution, which helps to stabilise the potential. It has been shown that indeed in the IDM the potential is stable up to higher energy scales than the SM potential [139, 177, 178].

One has to remember that analysing the tree-level positivity conditions with running coupling constants inserted may not give an accurate answer to the question of boundedness from below of the one-loop effective potential [179, 180]. It is because the one-loop potential, besides the tree-level component, contains also the one-loop contribution. Of course, as long as we are within the perturbativity range, the one-loop correction should be small, and thus a tree-level potential with tree-level couplings replaced by the running ones should be a good approximation of the one-loop potential. However, if the the "running" positivity conditions are evolved through many different energy scales, it might happen that a scale is reached where the perturbative expansion breaks, and the tree-level conditions are no longer valid. Thus, this criterion should be used with an appropriate care.

Moreover, positivity of the effective potential is not enough for stability of the EWSB vacuum since the loop corrections can modify the structure of the effective potential introducing new minima, potentially deeper than the EWSB minimum. As was explained in the preceding section, to find the real vacuum state of the theory one has to minimise the effective potential. This is in general not an easy task, and the problem is even more complicated in models with additional scalar fields, because then the effective potential is a multivariable function, and can have extrema along various directions in the scalar-field space.

The aim of this chapter is to analyse the issue of the stability of the inert vacuum state. Since it is a complicated task, we will approach it from different perspectives. Starting from an effective, simplified approach, we will move to a more complete description of the problem. In the end, we will comment on remaining open questions and possible further developments.

6.1 Stability of a vacuum state

6.1.1 Stable, metastable and unstable vacua

Let us start from defining the notions that will be used throughout this chapter. A vacuum state is a ground state of a theory, i.e. a state of the lowest energy. Thus it should correspond to a global minimum of the (effective) potential. If a theory is built around a state which is not stable, it will be faulty since with the decay of the ground state it will no longer describe reality. This is a reason why a potential should be bounded from below — if it tends to minus infinity, no state can be really stable.

A state corresponding to a global minimum of a potential will be referred to as a stable vacuum or a true vacuum. A state which corresponds to only a local minimum of a potential can tunnel (decay) to the true vacuum. Nonetheless, it can play a role of the ground state of a theory, given that its lifetime is sufficiently long. If the lifetime of such a state was shorter than the age of the Universe it would have already decay and certainly it would not be an appropriate ground state for a theory describing present world. Thus, an acceptable ground state must have lifetime longer than the age of the Universe. Such states will be referred to as metastable vacua. If a state minimising a potential is short-lived (with respect to the Universe), then it is not an acceptable vacuum state and will be called an unstable or a false vacuum.

6.1.2 Tunnelling

A conservative approach leads to accepting as ground states only stable vacua. However, from the practical point of view, metastable vacua are also acceptable, and to distinguish them from the unstable ones, one needs to compute the lifetime of a given vacuum.

The tunnelling process between vacua is described semi-clasically. In the computation of the vacuum lifetime we follow the seminal papers [181, 182], and the more recent ones [172–175]. A good extended introduction to this topic can be found in the textbook by Rubakov [183].

To determine the lifetime of vacuum we have to find a classical trajectory, the so-called bounce solution, φ_B, which satisfies the following equation (in thecase when the problem is $O(4)$-symmetric it depends only on one variable $s = \sqrt{\vec{x}^2 + x_4^2}$):

$$\ddot{\varphi} + \frac{3}{s}\dot{\varphi} = \frac{\partial V_{\text{eff}}^{(1)}(\varphi)}{\partial \varphi}, \tag{6.1}$$

where the dot denotes a derivative with respect to s. The boundary conditions are: $\dot{\varphi}_B(0) = 0$, and $\varphi_B(\infty) = v$. Having this solution, an approximate relative lifetime

of the vacuum τ is given by (in the units of the age of the Universe T_U)

$$\tau = \frac{e^{S_E}}{\varphi_0^4 T_U^4}. \tag{6.2}$$

The formula above is an approximation, since quantum fluctuations around the bounce solution in the exponential prefactor have been replaced by another dimensionful quantity, $\varphi_0 = \varphi_B(0)$, see refs. [174, 175]. This approximation has been shown [174] to give a good estimation of the tunnelling time. The quantity S_E, the Euclidean action on the bounce solution φ_B, is given by

$$S_E = 2\pi^2 \int ds s^3 \left[\frac{1}{2}\dot{\varphi}_B^2(s) + V_{\text{eff}}^{(1)}(\varphi_B(s))\right]. \tag{6.3}$$

The effective potential is in general a complicated function of the classical field so it is not possible to solve eq. (6.1) analytically. Therefore, we solve it using the undershoot-overshoot method.

Equation (6.1) can be viewed as an equation describing movement of a body in the potential $-V_{\text{eff}}^{(1)}$, in the presence of a friction force (second term of eq. (6.1)), and time denoted by s; see figure 6.2 for an exemplary shape of $-V_{\text{eff}}^{(1)}(\varphi)$. A bounce solution corresponds to a classical trajectory of a body sliding down from the slope of the higher hill (corresponding to the deeper minimum of $V_{\text{eff}}^{(1)}$) with initial velocity $\dot{\varphi}$ equal zero, and stopping at the lower hill at infinite time s.[1] The task is to find appropriate starting point: if we start to close to the peak of the bigger hill we will overshoot and the body will not stop on the other hill. If we start too far, it will not reach the top. Somewhere in between lies the correct starting point. Knowing that, we look for it using the bisection method, and solve eq. (6.1) numerically.

The procedure presented above works for effective potentials being functions of one scalar field. Full effective potential of a multi-scalar model is a function of multiple classical fields, thus the computation of the tunneling time is more complicated. Even finding all the stationary points of such a potential may be very difficult. There exist computer programs, `CosmoTransitions` [184] and `Vevacious` [185] (the latter using the former), devised to deal with such problems. However, they are subject to certain limitations. Therefore, to avoid the complexities of multi-scalar approach but at the same time be able to understand the impact of additional scalars on the problem of vacuum stability, in the proceeding section we use an effective approach. This way only one scalar field will be considered as dynamical and we will be able to use the procedure of computation of the tunnelling time described above.

[1] For the computation of the tunnelling time we shift the potential such that it is equal zero at $\varphi = v$, not at $\varphi = 0$. Thanks to that the integrand in eq. (6.3) converges to zero for $s \to \infty$.

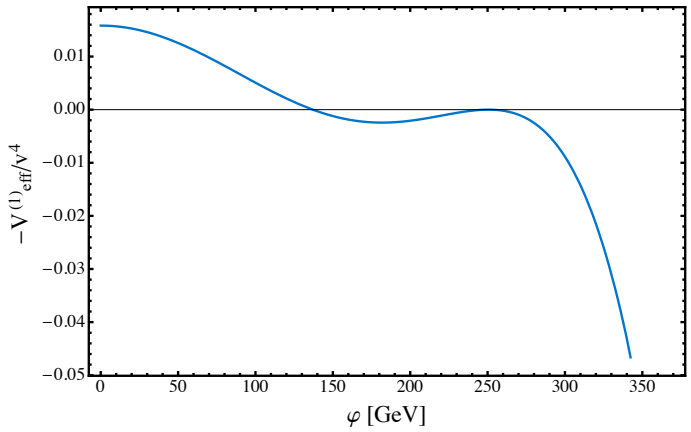

Figure 6.2: Minus effective potential as a function of the classical field φ. The bounce solution corresponds to a classical trajectory of a body sliding (in presence of a friction force) from the slope on the left with zero initial velocity and stopping on the top of the lower hill on the right at infinite time s.

6.2 Vacuum stability in the IDM with heavy inert scalars

Below we will analyse stability of the vacuum state in the IDM. As was already explained, in order to examine the vacuum structure of a model we need to analyse the effective potential [168]. Study of vacuum stability in models with extended scalar sector is a complex task as the effective potential becomes a function of multiple variables, and new minima can appear along various directions (see e.g. analysis in refs. [149, 186]). As was explained in section 2.2.2 in the IDM even at tree level minima with different vacuum expectation values can coexist [41]. Similarly, in the general 2HDM simultaneous tree-level minima can occur [187, 188]. Since the tree-level structure of 2HDMs is well studied [39, 41, 43–45, 188–191], here we focus on the loop effects. We follow the approach presented in refs. [2, 7].

To avoid the complexities of multi-variable potential, but still study the impact of the presence of additional scalars on vacuum stability in the IDM, we employ a simplified approach. Our assumption is that the inert scalars cannot be observed in the final/initial states, i.e. they are integrated out. Because of this approach, we focus on the heavy DM regime, where $M_H \gtrsim 500\,\text{GeV}$. In this way, in the effective potential computation we only consider one classical field on external legs of the diagrams, and the effective potential is a function of only one variable. Nonetheless, loop corrections from the inert scalars are included in the one-loop renormalisation process, and their contributions to the Coleman–Weinberg (CW) [168] potential (see eq. (5.25)) are taken into account. We will show that the impact of the new heavy scalars on

vacuum structure can be significant.

The procedure is as follows. We start from the tree-level potential and renormalise it on-shell. Then we add the CW terms. Infinities present in both components cancel, and we end up with a usable, one-loop effective potential. There is one subtlety here: since we allow the additional scalars only in the loop processes (or, equivalently we assume that the additional doublet does not develop a non-zero VEV) the tree-level potential will be just the SM potential. But to compute the loops (tadpoles and Higgs self-energy) we will need the couplings of the new scalars, so the full tree-level potential of the IDM will be used.

The one-loop effective potential is thus given by

$$V_{\text{eff}}^{(1)} = V_{\text{eff}}^{(0)} + \delta V_{\text{CW}} + \delta V + const. \tag{6.4}$$

$V_{\text{eff}}^{(0)}$ denotes the tree-level effective potential (in agreement with the convention of eq. (2.1))

$$V_{\text{eff}}^{(0)} = -\frac{1}{4} m_{11}^2 \varphi^2 + \frac{1}{8}\lambda_1 \varphi^4, \tag{6.5}$$

where φ is a real classical field. δV_{CW} stands for the one-loop CW potential, and δV is the counterterm potential. A constant that shifts the potential to get $\lim_{\varphi\to 0} V(\varphi) = 0$ is explicitly singled out.

In the following sections we will explain the procedure of computing different parts of the effective potential.

6.2.1 Renormalisation of the effective potential

We need to renormalise the potential (2.1), so we should shift the constants in the potential as $\lambda \to \lambda + \delta\lambda$, and compute the counterterms. However, as we are interested in an effective potential of a single classical field, we will finally substitute

$$\phi_S = \frac{1}{\sqrt{2}} \begin{pmatrix} 0 \\ \varphi \end{pmatrix}, \quad \phi_D = \begin{pmatrix} 0 \\ 0 \end{pmatrix} \tag{6.6}$$

to the renormalised potential. In this way all the terms with ϕ_D will vanish so we can get rid of them from the very beginning. Thus, the tree-level potential is given by eq. (6.5). We shift the constants as follows $m_{11}^2 \to m_{11}^2 + \delta m_{11}^2$, $\lambda_1 \to \lambda_1 + \delta\lambda_1$, $\varphi^2 \to (1+\delta Z)\varphi^2$. This gives us the renormalised potential

$$V_{\text{eff}}^{(0)} + \delta V = V_{\text{eff}}^{(0)} - \frac{1}{4}\left(m_{11}^2 \delta Z + \delta m_{11}^2\right)\varphi^2 + \frac{1}{4}\left(\lambda_1 \delta Z + \frac{1}{2}\delta\lambda_1\right)\varphi^4. \tag{6.7}$$

To find these renormalisation constants we use the on-shell conditions (we follow the method of ref. [149]), and demand that the tadpole of the Higgs boson vanishes,

i.e.,

$$\mathcal{T} + \delta\mathcal{T} = 0, \tag{6.8}$$

$$\Sigma_R(p^2)\big|_{p^2=M_h^2} = 0, \tag{6.9}$$

$$\left.\frac{d\Sigma_R(p^2)}{dp^2}\right|_{p^2=M_h^2} = 0, \tag{6.10}$$

where $\mathcal{T}$ is the Higgs tadpole, $\delta\mathcal{T}$ is the tadpole counterterm, and $\Sigma_R(p^2)$ is the renormalised Higgs self-energy, i.e., it is a sum of the loop corrections to the self-energy, Σ, and the counterterms, $\delta\Sigma$,

$$\Sigma_R = \Sigma + \delta\Sigma.$$

Condition (6.8) guarantees that the effective potential has an extremum at $\varphi = v$.

To compute the counterterms we perform the shift of the constants in the lagrangian as described above (at the level of quantum fields, not the classical fields). The relevant terms (proportional to h or h^2, where h denotes the Higgs field) in the renormalised lagrangian $\mathcal{L}_r$ read

$$\begin{aligned}\mathcal{L}_r \supseteq \frac{1}{2}\delta Z \partial_\mu h \partial^\mu h + h\left[\frac{1}{2}\left(m_{11}^2\delta Z + \delta m_{11}^2\right) - \left(\lambda_1\delta Z + \frac{1}{2}\delta\lambda_1\right)v^2\right]v \\ + \frac{1}{2}h^2\left[\frac{1}{2}\left(m_{11}^2\delta Z + \delta m_{11}^2\right) - 3\left(\lambda_1\delta Z + \frac{1}{2}\delta\lambda_1\right)v^2\right],\end{aligned}$$

This gives the expressions for the tadpole counterterm (the term proportional to h) and the self-energy counterterm (the term proportional to $\frac{1}{2}h^2$). Having that, we can make use of the renormalisation conditions (6.8)–(6.10). Since the renormalised lagrangian depends on three combinations of the counterterms: δZ, $(m_{11}^2\delta Z + \delta m_{11}^2)$, $\left(\lambda_1\delta Z + \frac{1}{2}\delta\lambda_1\right)$, we will try to use the renormalisation conditions, eqs. (6.8)–(6.10), in such a way as to get conditions for these combinations.

As was already mentioned, the tadpole counterterm consists of the terms linear in the field h, so it is equal to

$$-i\delta\mathcal{T} = -i\left[\frac{1}{2}\left(m_{11}^2\delta Z + \delta m_{11}^2\right) - \left(\lambda_1\delta Z + \frac{1}{2}\delta\lambda_1\right)v^2\right]v. \tag{6.11}$$

From our first renormalisation condition, eq. (6.8), we get

$$\mathcal{T} = -\delta\mathcal{T}. \tag{6.12}$$

The self-energy counterterm, $\delta\Sigma$, can be read off from the part of the counterterm Lagrangian which is quadratic in the field h

$$-i\delta\Sigma = -i\left[-p^2\delta Z + \frac{1}{2}\left(m_{11}^2\delta Z + \delta m_{11}^2\right) - 3\left(\lambda_1\delta Z + \frac{1}{2}\delta\lambda_1\right)v^2\right]. \tag{6.13}$$

Now, using expressions (6.11)–(6.13) we can obtain conditions for the combinations of the renormalisation constants which we need. We get

$$-i\delta\Sigma = -i\left[-p^2\delta Z - \frac{\mathcal{T}}{v} + 2\left(\lambda_1\delta Z + \frac{1}{2}\delta\lambda_1\right)v^2\right]. \tag{6.14}$$

Using the second renormalisation condition, eq. (6.9), we can write

$$\Sigma_R = \Sigma - p^2\delta Z - \frac{\mathcal{T}}{v} + 2\left(\lambda_1\delta Z + \frac{1}{2}\delta\lambda_1\right)v^2. \tag{6.15}$$

This gives a condition for the combination $\left(\lambda_1\delta Z + \frac{1}{2}\delta\lambda_1\right)$. To get a condition for the other combination, we proceed similarly, starting also from eq. (6.13) and adding and subtracting terms that we need. As a result we get

$$-i\delta\Sigma = -i\left[-p^2\delta Z - \frac{3\mathcal{T}}{v} + \left(m_{11}^2\delta Z + \delta m_{11}^2\right)\right], \tag{6.16}$$

and

$$\Sigma_R = \Sigma - p^2\delta Z - \frac{3\mathcal{T}}{v} + \left(m_{11}^2\delta Z + \delta m_{11}^2\right). \tag{6.17}$$

Now applying the renormalisation conditions we get

$$\begin{aligned}
\lambda_1\delta Z + \frac{1}{2}\delta\lambda_1 &= -\frac{1}{2v^2}\left[\Sigma(M_h^2) - M_h^2\Sigma'(M_h^2) - \frac{\mathcal{T}}{v}\right], \\
m_{11}^2\delta Z + \delta m_{11}^2 &= -\left[\Sigma(M_h^2) - M_h^2\Sigma'(M_h^2) - \frac{3\mathcal{T}}{v}\right], \\
\delta Z &= \Sigma'(M_h^2),
\end{aligned} \tag{6.18}$$

where $\Sigma'(M_h^2) := \left.\frac{d\Sigma(p^2)}{dp^2}\right|_{p^2=M_h^2}$. This is sufficient to renormalise the potential.

The only remaining components to be computed are Σ, Σ' and $\mathcal{T}$. This requires computation of a number of loop integrals. A complete calculation is presented in appendix D.

In the counterterms there is a source of imaginary part of the effective potential — the loops containing the b quark. This complexity signals instability of the Higgs boson, and we can simply take into account only the real part of the potential [192].

6.2.2 One-loop Coleman–Weinberg terms

To get a full one-loop effective potential we need to add to the renormalised tree-level potential the CW contributions coming from the Higgs boson, the Goldstone bosons, the fermions (we include top and bottom quarks as the heaviest ones), the gauge bosons, and the additional scalars. Such a contribution computed in dimensional regularisation ($D = 4 - \epsilon$) reads (see eq. (5.25))

$$\delta V_{\mathrm{CW}} = \sum_a \frac{n_a}{64\pi^2} M_a(\varphi)^4 \left[\log\left(\frac{M_a(\varphi)^2}{4\pi\mu^2}\right) - \frac{2}{\epsilon} + \gamma_E - C_i\right],$$

where n_a depends on the spin, charge, and color charge of a particle as given in eq. (5.26) ($n_h = n_H = n_G = n_A = 1$, $n_{G^\pm} = n_{H^\pm} = 2$, $n_t = n_b = 12$, $n_{W^\pm} = 6$, $n_Z = 3$), and $C_i = \frac{3}{2}$ for all of the particles, except the gauge bosons, for which $C_{W^\pm} = C_Z = \frac{5}{6}$.[2]

For the physical particles the field dependent masses $M_a(\varphi)$ are obtained by substituting φ instead of v in the tree-level masses. The tree-level masses of the scalars are given in eq. (2.13), the tree-level masses for the gauge bosons and fermions read

$$M_W = \frac{gv}{2}, \quad M_Z^2 = \frac{\sqrt{g^2+g'^2}}{2}v, \quad M_f = \frac{y_f v}{\sqrt{2}}. \tag{6.19}$$

For $\varphi = v$ the field-dependent masses of the Goldstone bosons of course vanish, however, for $\varphi < v$ they become negative, and the effective potential acquires an imaginary part. Recently it has been shown that the problematic Goldstone contributions can be consistently resummed, and this way the imaginary part can be removed [193, 194]. Furthermore, it has been demonstrated that this resummation procedure has little numerical impact on the results, thus we simply ignore the imaginary contributions from the Goldstones.

The infinities present in δV exactly cancel the $\frac{2}{\epsilon}$ terms in $\delta V_{\rm CW}$, together with $\gamma_E - \log(4\pi\mu^2)$. Thus the final potential is finite and μ-independent.

6.2.3 One-loop effective potential in the on-shell scheme

We can collect the contributions computed before to get the full 1-loop effective potential of the form

$$\begin{aligned}
V_{\rm eff}^{(1)} &= V_{\rm eff}^{(0)} + \delta V + \delta V_{\rm CW} \\
&= -\frac{1}{4}\left\{m_{11}^2 - \left[\Sigma(M_h^2) - M_h^2\Sigma'(M_h^2) - \frac{3\mathcal{T}}{v}\right]\right\}\varphi^2 \\
&+ \frac{1}{8}\left\{\lambda_1 - \frac{1}{v^2}\left[\Sigma(M_h^2) - M_h^2\Sigma'(M_h^2) - \frac{\mathcal{T}}{v}\right]\right\}\varphi^4 \\
&+ \frac{1}{64\pi^2}\left\{\frac{1}{4}\left(-m_{22}^2 + \lambda_{345}\phi^2\right)^2\left[-\frac{2}{\epsilon} + \gamma_E - \frac{3}{2} + \log\left(\frac{1}{2}\left(\frac{-m_{22}^2+\lambda_{345}\phi^2}{4\pi\mu^2}\right)\right)\right]\right. \\
&\left. + \frac{1}{4}\left(-m_{22}^2 + \lambda_{345}^-\phi^2\right)^2\left[-\frac{2}{\epsilon} + \gamma_E - \frac{3}{2} + \log\left(\frac{1}{2}\left(\frac{-m_{22}^2+\lambda_{345}^-\phi^2}{4\pi\mu^2}\right)\right)\right]\right.
\end{aligned} \tag{6.20}$$

[2]The value of $C_{W^\pm}$ and C_Z depends on the regularisation method used. If, instead of dimensional regularisation, dimensional reduction was used, then $C_{W^\pm}$ and C_Z would be equal $\frac{3}{2}$, as for the remaining particles, see section 5.3. This approach will be adopted in section 6.3.

$$+\frac{1}{2}\left(-m_{22}^2+\lambda_3\phi^2\right)^2\left[-\frac{2}{\epsilon}+\gamma_E-\frac{3}{2}+\log\left(\frac{1}{2}\left(\frac{-m_{22}^2+\lambda_3\phi^2}{4\pi\mu^2}\right)\right)\right]$$
$$+m_{22}^4\left[\frac{2}{\epsilon}-\gamma_E+\frac{3}{2}+\log\left(4\pi\mu^2\right)\right]-m_{22}^4\log\left(-\frac{1}{2}m_{22}^2\right)\Bigg\}+\delta V_{\mathrm{CW,SM}},$$

where the non-SM contribution is singled out, and the SM CW terms are symbolised by $\delta V_{\mathrm{CW,SM}}$. $V_{\mathrm{eff}}^{(0)}$ denotes the tree level effective potential (see eq. (6.5)), δV is the counterterm potential (see eq. (6.7)), with the renormalisation constants taken from eq. (6.18). In the last line constants are added for convenience: the first term cancels the constant infinity and some irrelevant constants, and the second one shifts the potential in such a way as to get $\lim_{\varphi\to 0} V(\varphi) = 0$.

From this form it is clear, that new, with respect to SM, contributions are present.

6.2.4 Electroweak vacuum stability with heavy inert scalars

To evaluate the impact of the heavy inert scalars on vacuum stability we analyse the structure of the effective potential, eq. (6.20) around the EW scale. In the literature, vacuum stability is often analysed in terms of the running tree-level positivity conditions. The behaviour of the effective potential is studied at large field values, see e.g. [139, 177, 178]. However, as was discussed in the introductory part of this chapter, this is not enough for the absolute stability of the vacuum. Thus, we will study the structure of minima of the effective potential focusing at the EW scale.

For this general discussion we fix the mass of the DM candidate to 550 GeV and $\lambda_{345} = -0.1$, as suggested by DM data (see e.g. ref. [3]). The A and $H^\pm$ particles are assumed to be degenerate, with common mass M. In figure 6.3 the OS effective potential for the IDM with different values of M is shown. The solid line represents the SM case (similar results were presented in ref. [149]).

A side remark is needed here. It can be viewed from fig. 6.3 that the value of the Higgs VEV used here is $v = 250.6\,\mathrm{GeV}$. A common way to compute v is to use its relation to the Fermi constant $v^2 = \frac{1}{\sqrt{2}G_F}$, which gives the value $v = 246.2\,\mathrm{GeV}$ (and this value is used in the remaining parts of this work). However, in the computations presented in this section we needed exact cancelation between terms coming from the CW potential, and from the OS renormalisation procedure (see section 6.2.2). In the latter, the tree-level masses of W and Z appear, and thus taking their measured values from Particle Data Group [195] ($M_W = 80.385\,\mathrm{GeV}$, $M_Z = 91.1876\,\mathrm{GeV}$), and the fine structure constant $\alpha = 1/137$ as input we have to compute v using the

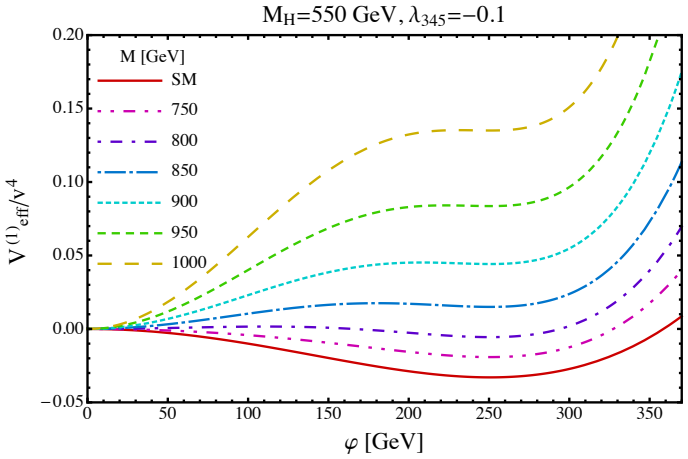

Figure 6.3: The one-loop OS effective potential for the IDM with heavy inert scalars integrated out given by eq. (6.20). In this plot $M_H = 550\,\text{GeV}, \lambda_{345} = -0.1$, and A and $H^\pm$ are assumed to be degenerate, with mass M.

tree-level relation with these quantities, namely

$$v = \frac{2M_W}{\sqrt{4\pi\alpha}}\sqrt{1-\left(\frac{M_W}{M_Z}\right)^2} \approx 250.6\,\text{GeV}.$$

Going back to the main topic, fig. 6.3 shows that for lighter inert scalars the effective potential of the IDM is very close to the SM one. While the common mass M of A and $H^\pm$ is increased (while M_H is fixed), the maximum at $\varphi = 0$ turns to a minimum, and a maximum for $0 < \varphi < v$ appears. Then, the minimum at $\varphi = v$ becomes a local minimum of the potential, and thus to constitute a metastable vacuum state for our model it must have long enough lifetime.

It might be surprising that the heavier the A and $H^\pm$ scalars are, the bigger the deviation from the SM scenario is. This is because the mass of H is fixed here, and increasing the splitting between M and M_H, we increase the couplings. For M and M_H being close (and heavy) we are in the decoupling regime, and no significant deviation from the SM is observed.

To check whether the local minima can constitute metastable vacuum states we computed their lifetimes according to the procedure described in section 6.1.2. We underline that we are interested here in lifetimes with respect to the tunnelling to the EW symmetric minimum, we do not consider tunnelling to a possible minimum at very high field values. In the cases with $M = 750,\ 800\,\text{GeV}$ the EWSB minima are stable, their energy is lower than the energy of the EW symmetric minimum. For $M = 850\,\text{GeV}$ the tunnelling can occur but the lifetime of the EWSB vacuum is very long, $\log_{10}\tau \approx 434$ (where τ is the lifetime of the vacuum with respect to the age of the Universe given by eq. (6.2)). For the cases with

$M = 900,\ 950,\ 1000\,\text{GeV}$ the EWSB minima are highly unstable, their lifetimes are given by $\log_{10}\tau \approx -129, -164, -171$, respectively. Thus they cannot be considered as ground states of the IDM.

This shows that additional scalars can have a striking impact on the stability of vacuum. Although the additional heavy scalars may improve the behaviour of running Higgs self-coupling at large field values [139, 177, 178], they can destabilise the vacuum due to EW-scale effects. We demonstrated this effect for the IDM with heavy inert scalars, but one can expect similar behaviour in other models with extra scalar fields.

As was mentioned above, the interesting case of unstable EWSB minimum corresponds to relatively large splitting between M and M_H. This suggests that "large" values of the λ_i parameters are required. How large? For the presented cases we checked the perturbative unitarity conditions, which constrain the parameters λ_i. In the scenarios with M up to 900 GeV the conditions are fulfilled, and starting from $M = 950\,\text{GeV}$ they are violated. So parameters λ_i required for the meta- or unstable scenarios are rather big but still within the allowed region. In section 6.2.6 we confront the bounds coming from the requirement of stability with other theoretical and experimental constraints in more detail to check whether meta- or instability scenarios can occur within viable parameter space of the IDM. But before that, in section 6.2.5 we study validity of the perturbative expansion of the effective potential.

6.2.5 Validity of the perturbative expansion

One may ask whether the one-loop approximation of the effective potential used in this work is valid. In the OS scheme the terms of the form $\log\mu$, where μ is the renormalisation scale, cancel out between the counterterm potential and the CW contribution. As a consequence, the logarithmic terms are of the form $\log\frac{M^2(\varphi)}{M^2}$, where M^2 is the physical mass of a particle, and $M^2(\varphi)$ is its field dependent mass. Therefore there is no freedom of adjusting μ to make the logarithms small.

The behaviour of the logarithms $\log\frac{M^2(\varphi)}{M^2}$ for the cases analysed above ($M_H = 550\,\text{GeV}$, $\lambda_{345} = -0.1$, $M_A = M_{H^\pm} = M$) is shown in figure 6.4. Different styles of the curves correspond to different values of M (the colour coding is the same as in figure 6.3). The horizontal black line corresponds to $\log\frac{M_H^2(\varphi)}{M_H^2}$.

It can be seen from the plot that $\log\frac{M_H^2(\varphi)}{M_H^2}$ is small for the whole range of φ. The absolute value of the other logarithm, $\log\frac{M^2(\varphi)}{M^2}$, for $M \leqslant 900\,\text{GeV}$ is less then 1 which is required for the perturbative expansion of the effective potential to be valid. For the cases with $M = 950, 1000\,\text{GeV}$ the logarithm becomes larger around

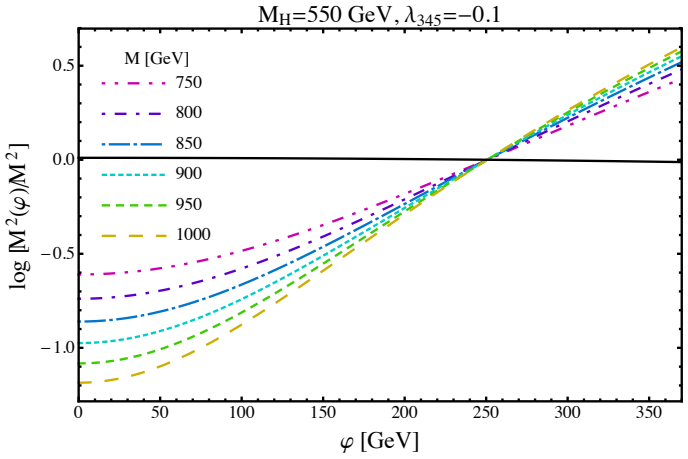

Figure 6.4: The logarithm $\log \frac{M^2(\varphi)}{M^2}$ as a function of φ for $M_H = 550\,\text{GeV}$, $\lambda_{345} = -0.1$. Different styles of the curves correspond to different values of the common mass of A and $H^\pm$, M. The horizontal black line corresponds to $\log \frac{M_H^2(\varphi)}{M_H^2}$.

$\varphi = 0$. This could suggest breakdown of perturbative expansion, however these two cases are already excluded by perturbative unitarity, as was shown above.

One should note, that the most important point, from the perspective of this analysis, is the point $\varphi = v$. And at this point all the logarithms vanish, and are small around. This means that the perturbative expansion of the effective potential should be trustworthy around the EWSB minimum. Since the CW contribution vanishes around $\varphi = v$, the shift in the value of the potential at this point that can be seen in figure 6.3, is due to the counterterms, and the shift fixing $V_{\text{eff}}^{(1)}(0) = 0$.

Another thing that should be taken into account is that the expansion of the effective potential is not in terms of the logarithms only, but rather in some coupling α times the logarithm. So the quantity $\frac{\alpha}{4\pi} \log \frac{M^2(\varphi)}{M^2}$ should be small (see e.g. [185, 186]). It is, however, not straightforward in the case of scalars to define α, since the scalar contributions to the CW potential are not linear in φ^4 (in contrast to the fermionic or gauge-boson contributions). Therefore we consider separately perturbativity of the couplings in section 6.2.6 (in terms of perturbative unitarity). Admittedly, the couplings get rather large (within the allowed region) in the interesting cases, but as explained above, it is hard to draw final conclusions from that fact.

The standard way of improving the validity of the effective potential is using the RGEs to resum the large logarithms. However, here the source of rather big logarithms is the splitting of the scales related to masses of different particles, and therefore RGEs should not improve the situation. Thus, only a two-loop calculation could definitely show whether the one-loop potential can be trusted in the range

where the logarithms become large. However, the two-loop computation is beyond the scope of this work.

6.2.6 Vacuum instability in the light of parameter space constraints

We will start from analysing the case with degenerate A and $H^{\pm}$, as was described in the preceding sections. We will examine the regions in the $(M_H,\ M)$ plane where the EWSB minimum is stable/metastable/unstable (phase diagram of the IDM), and confront them with other constraints. We underline that we do not consider the behaviour of the potential at large field values here, we are only interested in the stability around the EW scale.

The results can be seen in figure 6.5 (left panel), the solid line represents the region where $V_{\text{eff}}^{(1)}(v) = 0$, i.e. the boundary between stability and metastability region. Along the dashed line $\tau = 1$ (in the units of T_U) so it is the boundary between the metastable and unstable vacua. The shaded region is excluded by perturbative unitarity. Since $M_A = M_{H^{\pm}}$ the oblique parameter T is equal to zero and hence EWPT do not introduce new constraints. The parameter λ_{345} is fixed to -0.2. We checked that changing λ_{345} within the range that is favoured by the relic density constraints ($-0.3 \lesssim \lambda_{345} \lesssim 0.3$) [196] changes the picture only slightly.

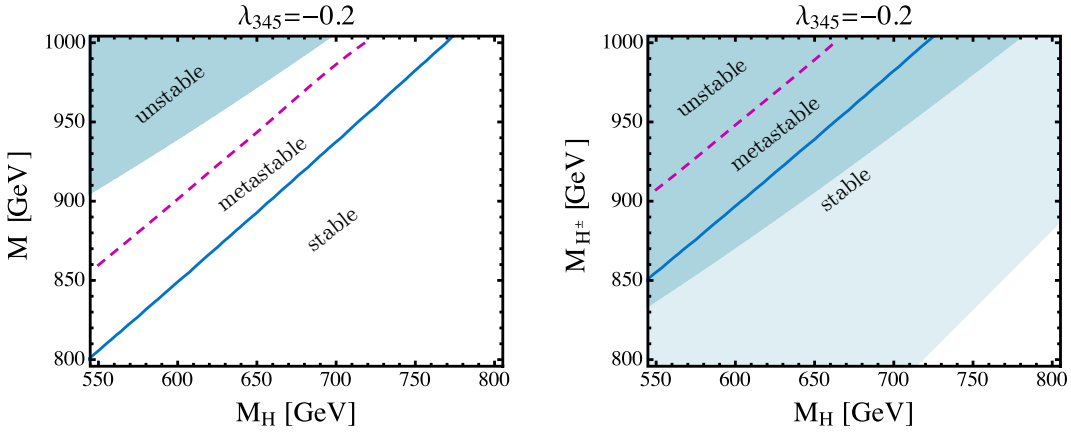

Figure 6.5: Stability/metastability/instability regions in the (M_H, M) plane (left panel) and $(M_H, M_{H^{\pm}})$ plane (right panel) for the case with $\lambda_{345} = -0.2$, and $M_A = M_{H^{\pm}} = M$ (left panel) or $M_A = M_H + 1\,\text{GeV}$ (right panel). The solid line denotes the boundary between stable and metastable vacua, the dashed line is the boundary between the metastability and instability region. The dark shaded region is excluded by unitarity, and the light shaded region is excluded by EWPT. EWPT do not constrain the case with $M_A = M_{H^{\pm}}$.

It is clear from figure 6.5 that in the degenerate case with $M_A = M_{H^{\pm}}$ meta- and

unstable scenarios are in agreement with unitarity constraints[3] and EWPT, as was discussed before. However, for an unstable vacuum to appear, the splitting between M_H and M has to be large, at the level of 300 GeV. This cannot be reconciled with the relic density constraints — the heavy DM needs coannihilation with other scalars to develop the correct relic density and the mass splitting among inert scalars must be small [162].

Let us then consider a case where H and A are quasi-degenerate (we assume $M_A = M_H + 1\,\text{GeV}$) to allow for coannihilation processes. Figure 6.5 (right panel) shows the boundaries between regions with vacua of different properties, the colour coding is the same as in the left panel. Once more we fix $\lambda_{345} = -0.2$, and small changes in λ_{345} do not alter the picture significantly. In this case we have to take into account the EWPT constraints. The light shaded region is excluded by constraints on S and T (it overlaps with the region excluded by unitarity). In this case unitarity and EWPT exclude the scenarios where metastability or instability can occur.

Therefore we conclude that the metastability or instability scenarios within the IDM with heavy scalars cannot be reconciled with theoretical and experimental constraints.

6.2.7 Summary

We showed that the new scalars can have a striking effect on the effective potential. They can turn the maximum of the effective potential at $\varphi = 0$ into a minimum, and moreover change the energy of the EWSB minimum in such a way that it becomes only a local one. This gives rise to unstable or metastable EWSB minimum, and the source of instability is around the EW scale. Our analysis was performed for the IDM but similar effects may be observed in other extensions of the SM. This shows that it is not enough to consider the behaviour of the effective potential or running coupling constants at large field values. Introduction of new fields can modify the effective potential at low energies and one has to check what effect such modifications have on vacuum stability.

For the particular case of the IDM we checked that the metastability/instability scenario is not a threat since the region where it is realised cannot be reconciled with perturbative unitarity, EWPT and the DM relic abundance measurements by the Planck experiment.

[3] If rather big values of λ_2 were considered, the meta- and unstable scenarios could be excluded by unitarity.

6.3 Coexistence of minima at one-loop level

In the preceding section we discussed the issue of the stability of the inert vacuum using an effective approach, in which the inert scalars were heavy and decoupled, and only the Higgs field was considered dynamical. This approach gave us some insight about the impact of the additional scalars on the stability of the inert vacuum.

However, in multi-scalar models, in principle, all the scalar fields can acquire a VEV, and thus the vacuum structure of the scalar potential can be complicated. As was already mentioned, the tree-level vacuum structure of 2HDMs is well studied [39, 41, 43–45, 188–191], and also many results for N-Higgs-doublet models are available [197–201]. Therefore, we are interested to study the loop effects. Since the IDM is of main interest for the work presented in this thesis, we will focus on the inert vacuum. In contrast to the previous section, here we will focus on the relation between the inert minimum, and other possible minima. At tree level an inert minimum can coexist with an inert-like minimum, and we will study what is the relation between these two minima at loop level. Can the inert-like minimum become a global minimum at loop level, if at tree level it was only a local one? In other words, can the inert vacuum be destabilised by the loop corrections? How much the picture differs from the tree-level one? These are the questions that are addressed in this section. The analysis described in this section is based on ref. [1] (see also ref. [8]).

6.3.1 Coexistence of inert and inert-like minima at tree level

Different types of minima which the $\mathbb{Z}_2$-symmetric potential of eq. (2.1) can develop have been described in section 2.2.2. Among them, the inert and inert-like extrema can be developed simultaneously (i.e. for one choice of the parameters' values the potential can have two minima of different types) [41], whereas if a mixed (normal) minimum exists for some choice of parameters, then no other can be developed.

As was discussed in section 3.1.2 (see eq. (3.3)) for the inert minimum to exist it is necessary that $m_{11}^2 > 0$. By analogy, for the inert-like state to be a minimum it is necessary that $m_{22}^2 > 0$. Thus a necessary condition for the coexistence of the two minima reads[4]

$$m_{11}^2 > 0 \quad \text{and} \quad m_{22}^2 > 0. \tag{6.21}$$

[4]Of course, this is not the only possible necessary condition. For an existence of the inert minimum it is also necessary that the scalar squared masses are positive. If one looks at eq. (2.13), and assumes that eq. (6.21) holds, than it is obvious that for M_H^2 to be positive, also λ_{345} has to be positive. Similar reasoning works for the inert-like minimum, thus $\lambda_{345} > 0$ is also a necessary condition for the coexistence of minima.

If the two minima coexist, one has to one has to make sure that the inert one is deeper, since in the inert-like minimum unphysical effects, such as massless fermions, appear.[5] The criterion (3.5) for the inert minimum being a global one, discussed in section 3.1.2, is based on comparison of the depths of inert and inert-like minima [41]. The difference in depths can be expressed in terms of the parameters of the potential or masses of scalar particles. In particular, we will use the following expressions

$$V_I - V_{IL} = -\frac{m_{11}^4}{8\lambda_1} + \frac{m_{22}^4}{8\lambda_2} \tag{6.22}$$

$$= \frac{1}{4}\left[\left(\frac{M_{H^\pm}^2}{v_D^2}\right)_{IL} - \left(\frac{M_{H^\pm}^2}{v_S^2}\right)_I\right] v_S^2 v_D^2, \tag{6.23}$$

where the subscript I refers to quantities computed in the inert minimum, i.e. V_I is the value of the potential at the inert minimum, and $\left(M_{H^\pm}^2\right)_I$ is the value of the charged scalar mass at the inert minimum (given in eq. (2.13)). Analogously, the subscript IL refers to the inert-like minimum (see eq. (2.16)).[6] The VEV of the neutral component of the ϕ_S doublet in the inert minimum is denoted by v_S (and in fact $v_S = v = 246\,\mathrm{GeV}$), and v_D is the corresponding value for the ϕ_D doublet in the inert-like minimum. It should be underlined that the value of v_D is, in principle, different that v.

Which of the minima is the global one is decided by the sign of the value of the expression above. This is, however, only a tree-level result. The question that we want to address in this section, is whether loop corrections can influence the tree-level vacuum structure. We will check whether they can modify the depths of the two minima in such a way that they are inverted — that the global one becomes local and vice versa. To answer this question an effective potential at one-loop level is needed.

6.3.2 Effective potential

For the computation of the one-loop effective potential we use the same formula as previously, eq. (5.25), however this time a different (than in section 6.2.1) renormalisation approach is adopted. First of all, dimensional reduction (DRED) is used instead of dimensional regularisation (DREG), which means that all the C_a factors in eq. (5.25) are equal to $\frac{3}{2}$. The renormalisation scheme is the minimal subtraction one ($\overline{\mathrm{MS}}/\overline{\mathrm{DR}}$), which means that the counterterms are adjusted in such a way, as

[5] A local inert minimum could also play a role of the ground state of the model if the tunnelling time to the inert-like global minimum was long enough. However, we will not discuss the issue of metastability in depth in this section.

[6] Notice that, as explained in section 2.5, in the inert-like minimum the $H^\pm$ particle originates from the ϕ_S doublet, and not the ϕ_D.

to cancel the terms proportional to $-\frac{2}{\epsilon} + \gamma_E - \log 4\pi$ in the CW contribution (see eq. (5.25)). This leaves us with the one-loop correction to the effective potential given by the following formula (which is a sum of the one-loop CW contribution δV_{CW} and the counterterm potential δV)

$$V_1(\varphi_i) = \frac{1}{64\pi^2} \sum_a n_a M_a^4(\varphi_i) \left[\log\left(\frac{M_a^2(\varphi_i)}{\mu^2} \right) - \frac{3}{2} \right]. \tag{6.24}$$

where $M_a^2(\varphi_i)$ are the field-dependend eigenvalues of the mass-squared matrix. In principle they depend on eight real (classical) scalar fields, which are labelled by the subscript i (see section 5.5). To identify these fields we will use the following decomposition (analogous to the one in eq. (6.25))

$$\phi_S = \frac{1}{\sqrt{2}} \begin{pmatrix} \eta_S + i\zeta_S \\ \rho_S + i\chi_S \end{pmatrix}, \quad \phi_D = \frac{1}{\sqrt{2}} \begin{pmatrix} \eta_D + i\zeta_D \\ \rho_D + i\chi_D \end{pmatrix}, \tag{6.25}$$

Written this way, the fields η_j, ζ_j, ρ_j, χ_j ($j = S, D$) are quantum fields. However, for the sake of simplicity we will use the same symbols to denote the classical fields, appearing as φ_i in the effective potential, eq. (6.24).

The eigenvalues M_a^2 are rather complicated for arbitrary values of the fields. However, in the inert and inert-like minima they are simple. The masses of the scalar particles in the inert minimum are given by eq. (2.13), while the masses of gauge bosons and fermions by eq. (6.19), with v replaced by ρ_1. In the case of the inert-like minimum also the field-dependent masses are given by the expressions for the tree-level masses, eq. (2.16), with v_2 replaced by ρ_2, however, one has to remember that the fermions are massless, since the ϕ_D doublet does not couple to fermions at tree level.

The full one-loop effective potential is thus given by

$$V_{\mathrm{eff}}^{(1)}(\varphi_i) = V_{\mathrm{eff}}^{(0)}(\varphi_i) + V_1(\varphi_i), \tag{6.26}$$

where $V_{\mathrm{eff}}^{(0)}(\varphi_i)$ is the tree-level potential of eq. (2.1) with the quantum fields replaced with respective classical fields.

In contrast to the case from the previous section, where the OS renormalisation scheme was used, the renormalisation scale parameter μ does not explicitly vanish from the effective potential computed in the $\overline{\mathrm{MS}}$ scheme. However, up to two-loop effects, the results for the masses or VEVs should not depend on the choice of this scale, as long as it is such that the loop corrections are small and the perturbative expansion holds.[7] To render the logarithms present in the one-loop correction to

[7] In fact, to guarantee independence of μ of the effective potential, we should add to it a φ_i-independent, μ-dependent parameter. However, since we are interested in differences in the depth of the effective potential at different minima, this parameter would cancel.

the effective potential small, μ should be of the order of the masses present in the theory [179]. Moreover, it is crucial to use the same renormalisation scale for computation of the effective potential at both of the minima [202, 203]. Thus, we adopted the value $\mu = 200\,\mathrm{GeV}$, as it is close enough to the values of the masses acquired by the particles at both of the studied minima.

6.3.3 Inert and inert-like minima at loop level

6.3.3.1 One-loop extremum conditions

To verify the existence of a given type of a stationary point at loop level one has to compute the first derivatives of the effective potential, eq. (6.26), and check whether they vanish. Simple calculation leads to the following formula

$$\frac{\partial V^{(1)}_{\text{eff}}}{\partial \varphi_i} = \frac{\partial V}{\partial \varphi_i} + \frac{1}{32\pi^2}\sum_a n_a m_a^2 \frac{\partial m_a^2}{\partial \varphi_i}\left[\log\left(\frac{m_a^2}{\mu^2}\right) - 1\right]. \tag{6.27}$$

To obtain numerical values of the derivatives, one has to compute the derivatives of the field-dependent mass-squared eigenvalues, which in general is a nontrivial task. Fortunately, in the inert and inert-like minima all derivatives of m_a^2, apart from the ones with respect to ρ_1 (in the case of the inert minimum) and ρ_2 (in the case of the inert-like minimum) vanish. Moreover, the derivatives of mass-squared eigenvalues evaluated at the inert (inert-like) minimum are equal to the derivatives of the eigenvalues at the inert (inert-like) minimum.[8] Therefore, the the only non-vanishing first derivative of the effective potential in the inert minimum reads

$$\begin{aligned}
\frac{1}{v_S}\left(\left.\frac{\partial V^{(1)}_{\text{eff}}}{\partial \rho_1}\right|_I\right) = &-\frac{1}{2}m_{11}^2 + \frac{1}{2}\lambda_1 v_S^2 \\
&+ \frac{1}{32\pi^2}\left\{\lambda_1 m_G^2\left[\log\left(\frac{m_G^2}{\mu^2}\right) - 1\right] + 3\lambda_1 m_h^2\left[\log\left(\frac{m_h^2}{\mu^2}\right) - 1\right]\right. \\
&+ \lambda_{345} m_H^2\left[\log\left(\frac{m_H^2}{\mu^2}\right) - 1\right] + \lambda_{345}^- m_A^2\left[\log\left(\frac{m_A^2}{\mu^2}\right) - 1\right] \\
&+ 2\lambda_3 m_{H^\pm}^2\left[\log\left(\frac{m_{H^\pm}^2}{\mu^2}\right) - 1\right] + 2\lambda_1 m_{G^\pm}^2\left[\log\left(\frac{m_{G^\pm}^2}{\mu^2}\right) - 1\right] \\
&- 6\lambda_t^2 m_t^2\left[\log\left(\frac{m_t^2}{\mu^2}\right) - 1\right] - 6\lambda_b^2 m_b^2\left[\log\left(\frac{m_b^2}{\mu^2}\right) - 1\right] \\
&- 2\lambda_\tau^2 m_\tau^2\left[\log\left(\frac{m_\tau^2}{\mu^2}\right) - 1\right] \\
&\left.+ 3\frac{g^2 + g'^2}{2} m_Z^2\left[\log\left(\frac{m_Z^2}{\mu^2}\right) - 1\right] + 3g^2 m_W^2\left[\log\left(\frac{m_W^2}{\mu^2}\right) - 1\right]\right\}
\end{aligned} \tag{6.28}$$

[8] This is not an obvious fact. It was checked with an explicit calculation with the use of Mathematica.

and it has to be equal zero for the inert state to be a stationary point at loop level. The masses in the equation above are the tree-level masses computed at the inert minimum. The non-vanishing derivative in the inert-like state is almost identical, and reads

$$\begin{aligned}\frac{1}{v_D}\left(\left.\frac{\partial V_{\text{eff}}^{(1)}}{\partial \rho_2}\right|_{IL}\right) = &-\frac{1}{2}m_{22}^2 + \frac{1}{2}\lambda_2 v_D^2 \\ &+ \frac{1}{32\pi^2}\left\{\lambda_2 m_G^2\left[\log\left(\frac{m_G^2}{\mu^2}\right)-1\right] + 3\lambda_2 m_h^2\left[\log\left(\frac{m_h^2}{\mu^2}\right)-1\right]\right. \\ &+ \lambda_{345} m_H^2\left[\log\left(\frac{m_H^2}{\mu^2}\right)-1\right] + \lambda_{345}^- m_A^2\left[\log\left(\frac{m_A^2}{\mu^2}\right)-1\right] \\ &+ 2\lambda_3 m_{H^\pm}^2\left[\log\left(\frac{m_{H^\pm}^2}{\mu^2}\right)-1\right] + 2\lambda_2 m_{G^\pm}^2\left[\log\left(\frac{m_{G^\pm}^2}{\mu^2}\right)-1\right] \\ &\left.+ 3\frac{g^2+g'^2}{2}m_Z^2\left[\log\left(\frac{m_Z^2}{\mu^2}\right)-1\right] + 3g^2 m_W^2\left[\log\left(\frac{m_W^2}{\mu^2}\right)-1\right]\right\},\end{aligned} \tag{6.29}$$

where the masses are the tree-level masses evaluated at the inert-like minimum. Notice, that in this case there are no contributions from fermions, since fermions are massless in the inert-like state.

6.3.3.2 One-loop minimum conditions

To check whether the stationary states are indeed minima of the potential, one has to compute the second derivatives of the effective potential. If we wanted to differentiate the formula of eq. (6.27) second time, and make use of the result in the explicit computations, we would encounter certain practical problems. Namely, we would need to compute the second derivatives of the field-dependent mass-squared eigenvalues, which is of course possible but rather cumbersome.

To avoid these problems an alternative approach can be adopted. We will use the fact that the second derivatives of the effective potential correspond to the one-loop masses of the scalar particles computed at zero external momentum. The one-loop mass of a particle, $\mathcal{M}$, is given by the formula

$$\mathcal{M}^2(p) = M^2 + \text{Re}\Sigma(p), \tag{6.30}$$

where M^2 is the tree-level mass, and $\Sigma(p)$ is the one-loop self-energy of the particle.[9] The physical mass is defined at momentum corresponding to this physical mass, i.e.

$$M_{\text{phys}}^2 = M^2 + \text{Re}\Sigma(M_{\text{phys}}). \tag{6.31}$$

[9]In the case when the discussed particle is unstable, its self-energy Σ acquires an imaginary part. That is why only the real part of the self-energy contributes to its mass, the imaginary part corresponds to the decay width [204].

The detailed computation of and formulas for the self-energies of the scalar particles in the inert minimum can be found in appendix D. For the sake of cross-check the obtained results were compared with formulas obtained by an adaptation of the general expressions derived by Martin [205, 206]. We have also verified that the one-loop Goldstone masses at zero momentum are zero, which means that the Goldstone bosons are massless also at loop level. Analogous formulas for the one-loop self-energies in the inert-like minimum can be easily obtained from the ones for the inert state, remembering about the following points

- fermions are massless in the inert-like state,
- fermions do couple to the fields from the Φ_S doublet, with the same couplings as in the inert state (the Yukawa couplings are defined by the Yukawa lagrangian, independently of the vacuum state),
- in all the scalar and VEV indices an exchange $1 \leftrightarrow 2$ should be performed,
- the Goldstone bosons of the inert-like state follow from the ϕ_D doublet so the expression for the self-energy of the χ_D field will be obtained from the G self-energy, etc. The Higgs boson in the inert-like minimum corresponds to the ρ_D field so its self-energy can be obtained from the one of h. However, the components of the ϕ_D doublets do not couple to fermions so the fermionic contributions will not appear,
- the massive scalars of the inert-like state follow from the ϕ_S doublet so their self-energies will be obtained from the A, H and $H^\pm$ self-energies. However, they do couple to fermions so an additional fermionic contribution will be present in the form of

$$(3y_t^2 + 3y_b^2 + y_\tau^2)p^2 B(p^2, 0, 0). \tag{6.32}$$

  It is equal for all of these scalars in the limit of massless fermions.

6.3.3.3 Numerical procedure

In order to find a region in the parameter space where at loop level an inert minimum and an inert-like one coexist we employed the following numerical procedure.

1. A solution of one-loop minimisation conditions (the first derivatives of the effective potential are given in eqs. (6.28) and (6.29)) is searched for numerically starting from a randomly generated initial point. It is required that $v_S = v = 246\,\mathrm{GeV}$, and that the physical mass of the h boson in the inert

minimum is close to 125 GeV (1 GeV deviation is allowed). The solution gives a set of the values of m_{11}^2, m_{22}^2, $\lambda_1, \ldots, \lambda_5$ and v_D.

2. To verify whether the stationary inert and inert-like points corresponding to the previously obtained set of parameters are minima, the one-loop scalar masses are computed. We check whether the masses are positive — if yes, the set of parameters is saved. It should be noted that also the Goldstone bosons' masses are also checked. Due to numerical accuracy they do not exactly vanish, and the obtained values (typically less than 10^{-6} GeV, while masses of the other scalars are of the order of hundreds of GeV) should be positive. A small but negative value would imply that the analysed set of parameters corresponds to a saddle point.[10]

3. Basic theoretical constraints are checked: perturbative unitarity, perturbativity (all the quartic couplings have their absolute values below 4π), and boundedness from below (eq. (3.1)).[11]

4. We take a conservative approach and only allow the values of parameters for which all the tree-level masses are positive. This corresponds to looking for the one-loop minima around the tree-level ones, and prevents an occurrence of a imaginary part in the effective potential.

5. After verifying all of the conditions, the values of the one-loop potential at the two minima are computed and stored. Subsequently, the scan starts again from the beginning.

6.3.4 Results

In this section the effect of the loop corrections on the vacuum structure of the IDM potential is studied and we present the results of the procedure described above. Since at the loop level not only scalar fields affect the potential, but also contributions from gauge bosons and fermions are present, we divide the analysis into parts, switching on respective contributions sequentially. This allows to study the impact of each part on the final result, and understand which sector introduces the biggest modifications. We will start from analysing a model containing scalar fields only, then the gauge

[10]The physical masses are computed, i.e. masses at the value of the momentum corresponding to the physical mass, and not at zero momentum. This, however, should not influence the result, since the masses computed with the effective potential approximation (i.e. at zero momentum) are normally very close to the physical masses [207–209].

[11]The positivity constraints of eq. (3.1) are tree-level conditions. They do not necessarily apply to the one-loop potential. However, we work at a fixed renormalisation scale for which the loop corrections are small. Thus, the use of the tree-level positivity constraints is a fair approximation.

bosons will be taken into account, and finally the full IDM with scalars, bosons and fermions will be analysed.

6.3.4.1 Scalar contributions only

We start from a toy model containing only scalar fields. Thus, in the computations only the contributions from the scalar particles are taken into account, and the fermionic and gauge terms are set to zero.

The question that we study is what is the difference in the relative depth of the inert and inert-like minima between the tree and the loop level. In particular, we are interested whether a tree-level global minimum may turn to a local one at loop level. To answer this question we compared the relative depth computed using the full one-loop effective potential, according to the procedure described in the previous section, and the tree-level expectations computed from the formulas of eqs. (6.22) and (6.23). We will refer to the result obtained from formula (6.22) as $\Delta V_0^{(1)}$, whereas to the one obtained from eq. (6.23) as $\Delta V_0^{(2)}$.[12] Since they were derived at tree level, we may expect that they are no longer equivalent at one-loop level.

The comparison of the exact one-loop result $(V_I - V_{IL})$, where $V_I = V_{\text{eff}}^{(1)}\Big|_I$ and $V_{IL} = V_{\text{eff}}^{(1)}\Big|_{IL}$, with the tree-level results $\Delta V_0^{(1)}$, $\Delta V_0^{(2)}$ is shown in fig. 6.6. Notice, that in the plot in the right panel the region around zero is presented, while in the left panel the range of the plot is wider.

In general, it can be noted that most of the points are located along the diagonal, which means that the tree-level computation is a fair approximation to the full result. Nonetheless, one immediately notices points in the lower part of the plot in the left panel which deviate significantly from the diagonal. The one-loop relative depth of the inert and inert-like minima for these points is around $-10^8\,\text{GeV}$, while the tree-level value for this quantity is mostly positive, which means that an inversion of the two minima occurs, i.e. the tree-level global minimum becomes a local one and vice versa. A closer examination of these points revealed that they correspond to $m_{22}^2 < 0$. As stated in eq. (6.21), at tree level the inert and inert-like minima cannot coexist in this part of the parameter space. This shows that at loop level the parameter space where coexistence of minima can occur is wider than at tree level. Moreover, this explains why the tree-level expectations differ so much from the loop results in this region. Simply, this region was excluded at tree level so it is hard to compare it with the loop results. A question may arise why these points are not present in the plot in the right panel. The answer is in the fact, that the quantities

[12] They are obtained with the use of the one-loop values of the parameters.

$\Delta V_0^{(1)}$ and $\Delta V_0^{(2)}$ are computed with the one-loop values of the parameters, and somehow the one-loop masses and VEVs incorporate the loop corrections better than the potential parameters.

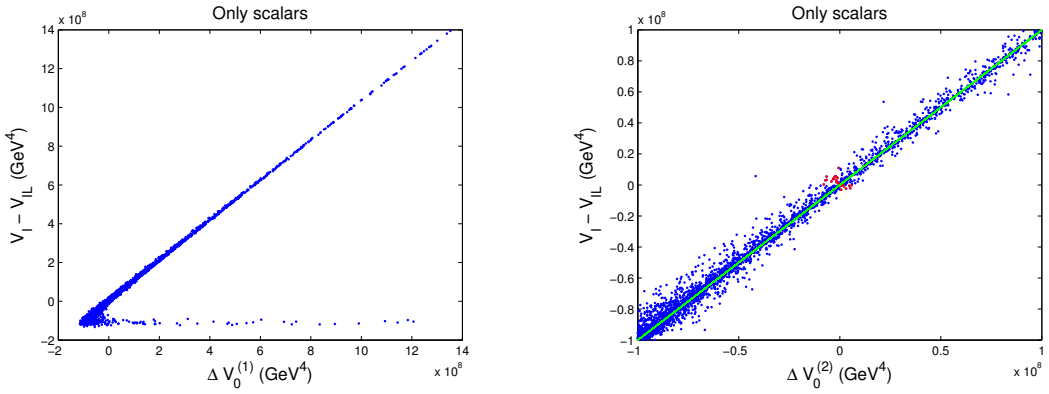

Figure 6.6: One-loop relative depth between the inert and inert-like minima, $V_I - V_{IL}$, in a toy model with scalars only versus the tree-level expectation $\Delta V_0^{(1)}$ computed from eq. (6.22) (left panel) or versus $\Delta V_0^{(2)}$ computed from eq. (6.23) (right panel). In the right panel the green line shows the diagonal, i.e. the line along which the tree-level results coincide with the loop-level result, the red points indicate the region where inversion of the minima, with respect to tree level, occurs.

There is another region where inversion of minima occurs — it is located around the point $(0, 0)$, and is displayed in red in the right panel of fig. 6.6. In this region the two minima are very close in energies — they are almost degenerate, so it is not strange that small loop corrections can reverse their hierarchy. Nonetheless, it is an important conclusion of this study — in the case of coexisting minima which are close in energies it is crucial to go beyond the tree-level potential to ascertain which of them is the global one.

6.3.4.2 Scalar and gauge contributions

We showed that even with scalar contributions to the effective potential only, the one-loop results may be significantly different than the tree-level ones. Now we will turn on the gauge contributions to see what difference they introduce.

The gauge contributions in both minima are qualitatively the same — the gauge bosons couple to both of the doublets in the same way, with the SM couplings. The only difference between the two minima is the value of the VEVs, which results in different masses of the gauge bosons.

A more detailed numerical analysis reveals that indeed inclusion of the gauge contributions does not change the picture significantly. The plots showing the comparison of the one-loop and tree-level relative depths of the minima look very similar

to the plots presented in fig. 6.6 so we do not show them here. Also, as previously, the allowed parameter space for coexistence of the minima is wider than at tree-level, with $m_{22}^2 < 0$ not excluded, and and inversion of minima is possible.

6.3.4.3 Full results

In this section we present the result for the full model, with scalars, gauge bosons, and fermions included. We can expect that the fermionic contributions will introduce certain discrimination between the inert and inert-like minima, since in the IDM fermions couple only to the ϕ_S doublet and do not to the ϕ_D, and thus they are massless in the inert-like minimum.

A technical difference that can be noticed while performing the numerical analysis is that it is more difficult to solve the minimisation conditions and find parameter points for which the two minima coexist. This may be caused by the differences between the fermionic properties of the two minima briefly discussed above.

Let us start the presentation of the results from an analog of the plot in the right panel of fig. 6.6, where the tree-level formula, $\Delta V_0^{(2)}$, is compared with the one-loop result $V_I - V_{IL}$, see fig. 6.7. It can be seen that now the tree-level results are a worse approximation of the one-loop ones. Nonetheless, still some points where inversion of minima occurs persist.

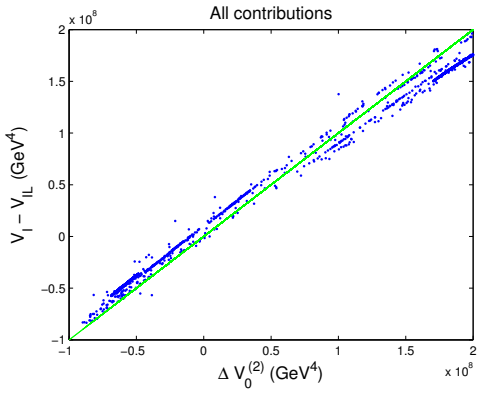

Figure 6.7: One-loop relative depth between the inert and inert-like minima, $V_I - V_{IL}$, in the full IDM versus the tree-level expectation $\Delta V_0^{(2)}$ computed from eq. (6.23), in the range around the $(0, 0)$ point, where inversion of minima can occur. The green line is the diagonal.

To compare the two tree-level formulas, $\Delta V_0^{(1)}$ and $\Delta V_0^{(2)}$, in fig. 6.8 we present also analogous plots for these two cases, with the same range of the plots. It can be noted that, in general, the formula $\Delta V_0^{(1)}$ underestimates the difference in depths between the inert and inert-like minima, whereas $\Delta V_0^{(2)}$ overestimates this difference. To sum up, even though the fermions distinguish the two minima, and make the tree-

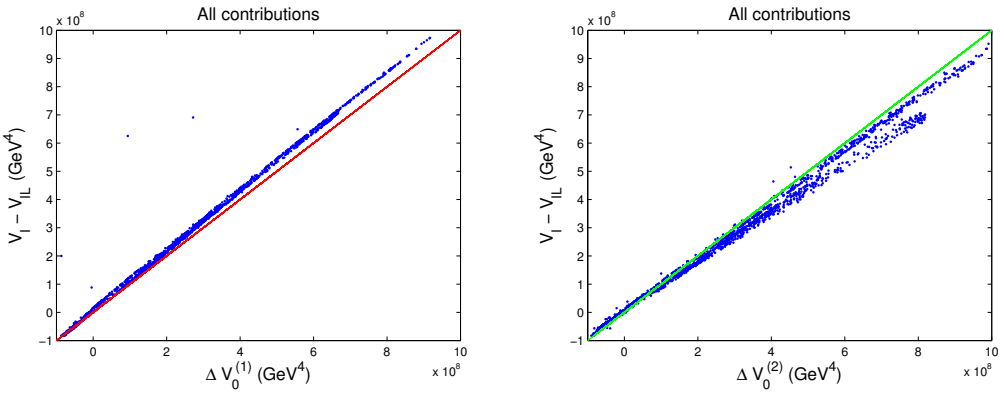

Figure 6.8: One-loop relative depth between the inert and inert-like minima, $V_I - V_{IL}$, in the full IDM versus the tree-level expectation $\Delta V_0^{(1)}$ computed from eq. (6.22) (left panel) or versus $\Delta V_0^{(2)}$ computed from eq. (6.23) (right panel). The red (left panel) and green (right panel) lines correspond to diagonals.

level predictions less accurate, the key conclusions remain the same as in the case with scalar contributions only: the hierarchy of the minima can be inverted by the loop corrections and the coexistence of the two minima can be realised in a region that was forbidden at tree level.

The one-loop effective potential of the IDM was thoroughly analysed in ref. [149]. The main purpose of this paper was the study of possibility of first-order phase transition in the course of the evolution of the Universe, for which a temperature-dependent effective potential was used. Nonetheless, the authors also studied the zero-temperature potential. Although the renormalisation scheme was chosen differently than in the present work (the on-shell scheme in place of the $\overline{\text{MS}}$), some of the results can be compared. It can be inferred from fig. 2 of ref. [149] that the inert and inert-like minima can coexist in a region that was forbidden at tree level — namely for $\lambda_{345} < 0$, which confirms our finding that the region of coexistence of the minima is extended at the one-loop level. However, in ref. [149] the problem of inversion of minima was not studied. The existence of the inert minimum at loop level was guaranteed by one of the renormalisation conditions, however it is not enforced that the inert minimum is global at tree level. Thus, it cannot be inferred whether or not the loop corrections change the nature of the tree-level minimum. Therefore, a full comparison of the two approaches is not possible, but certainly the conclusion about enlarging the parameter space where the inert and inert-like minima can coexist is common to our work and the results presented in ref. [149].

6.3.5 Discussion

The conclusions of the present work, about the possibility of inversion of minima and enlarged parameter space where coexistence is allowed, may have important meaning for the studies of the IDM. First of all, they show that the loop corrections may indeed qualitatively change the tree-level predictions. In particular, the vacuum state, which is a fundamental of the theoretical description, may be misidentified when tree-level potential is used. Fortunately, this risk comes into play only when the coexisting inert and inert-like minima are close in the energies, and in these cases the one-loop potential should be used.

What is probably even more important, is that these results point towards a more general problem — a problem of the vacuum structure of other 2HDMs beyond tree level. The tree-level vacuum structure has been well studied [39, 41, 43–45, 188–191], and possible types of minima were identified. The geometric analysis of ref. [44] showed that only minima which break the same symmetries of the scalar potential can coexist. For example normal (mixed) minima cannot coexist with inert ones. A question that arises is whether these conclusions hold beyond tree-level. Our analysis showed that some of the tree-level predictions can be altered by loop corrections which suggests that the same may happen in other cases. This problem is still to be studied.

6.4 Towards a complete description

In the two preceding sections we discussed some approaches to the issue of vacuum stability in the IDM. We used an effective approach, where only one field is dynamical, and analysed the impact of the loop effects from the additional scalars on the stability of the SM vacuum. Further on, we moved to a more general approach in which all the fields are dynamical, and we studied the coexistence of inert and inert-like minima. However, as was mentioned in the previous section, the study of the vacuum structure in 2HDMs beyond tree level in full generality remains an open question. One of the biggest obstacles in this task are the problems with the consistent use of the effective potential being a function of many scalar fields, in particular, the appearance of different energy scales associated to these fields.

In section 6.3 we used the full one-loop effective potential in the $\overline{\text{MS}}$ scheme. However, since we were only interested in the coexistence of two minima, we were able to control the energy scale of φ_i and adjust the renormalisation scale which would render all the logarithms in eq. (6.24) fairly small. If one wants to examine the general vacuum structure of a 2HDM, one has to allow VEVs along any direction in the φ_i

space. In this case, some of φ_i can be big, and some small, introducing various energy scales under the logarithms in the effective potential. This may potentially lead to breakdown of the perturbative expansion, since it may be impossible to choose one scale that would simultaneously make all the logarithms small.

A possible solution to this problem may be introduction of the formalism of ref. [210], which was originally devised mainly to cope with the problems arising due to the presence of many mass scales in supersymmetric models, even if only one scalar field is present (see also [211, 212] for earlier attempts to deal with similar issues). In brief, the main idea is to decouple each particle species at an energy corresponding to its field-dependent mass, $M_i(\varphi)$. This means that each component in the sum over a in eq. (6.24) would be multiplied by $\theta_a = \theta(\mu_a - M_a(\varphi))$, where $\mu_a^2 = e^{C_a}\mu^2$. C_a, as previously is equal $\frac{3}{2}$ for all the particles if DRED is used, and $\frac{5}{6}$ for vector bosons when DREG is employed. This way, all the particles contributing to the effective potential at a given scale are lighter that this energy scale, and thus effectively behave as massless and there is no problem with big logarithms (they are resummed).

This procedure is very useful because for each choice of φ there exists a boundary scale equal to $\min\{M_a(\varphi)\}$, below which the effective potential is just the tree-level one, with running coupling constants. This way it is easy to use and moreover the perturbative expansion is well applicable, because for any scale $\mu^* \leqslant \min\{M_a(\varphi)\}$ both the loop corrections and the explicit μ dependence of the effective potential vanish. Therefore it is always possible to use the tree-level potential with running couplings, however the running has to be studied carefully. One has to remember that the running of the couplings is also affected by the decoupling procedure, and that the β functions also contain the θ functions. Moreover, for each value of φ the running will be different, because the field-dependent masses will take different values, and thus the decoupling scales will change. Therefore, with this approach it is only possible to study the effective potential for fixed values of φ. To get the low energy values of the parameters one has to fix them at a scale high enough so that none of the fields is decoupled (these values are φ independent), and then run them down to the selected energy scale, remembering about the θ functions which depend on the value of φ. Doing this for different values of φ, the low-scale effective potential can be reconstructed point by point.

The approach described very briefly above can be extrapolated to the case of a model containing many scalar fields. In this situation, the field-dependent masses depend on all the scalar fields, and thus their decoupling scales do as well. Thus fixing high-scale values of parameters, one has to evolve them to the optimal μ^* scale separately for each point in the field space. This way the effective potential at μ^*

can be numerically reconstructed. However, to study the vacuum structure of such a potential, it should be carefully reconstructed, not to miss some of the minima. This is a complex task, requiring development of well-suited numerical algorithms.

This approach presumably gives a chance to study the effective potential of a general 2HDM (or any other model with an extended scalar sector), being a function of many classical fields, in a consistent way, staying within the scope of perturbation theory. However, the numerical complexity of this task has impeded obtention of final results. Thus this issue remains an open question to be studied in the future.

Chapter 7

Summary

7.1 Summary and conclusions

This dissertation is aimed at the study of 2HDMs with the Higgs boson serving as a guideline. The Higgs boson is treated as a probe of new physics — by studying its properties within 2HDMs we draw conclusions about the properties of the new scalar particles. Moreover, it is also a portal to DM — we showed that combing the results of the Higgs-related experiments and the DM data provides new important insight to the nature of the DM particle. Last but not least, the discovery of the Higgs boson and the measurement of its mass leads us to the question of the stability of the vacuum state, and the influence the new physics can exert on it.

The main focus of this dissertation is on the IDM which is a special kind of 2HDM containing a SM-like Higgs boson and a DM candidate. There are three main parts of the thesis: first we study the parameter space of 2HDMs (IDM and the 2HDM with a normal (mixed) vacuum state) in the light of theoretical and experimental constraints; then we analyse the properties of the Higgs boson of the IDM using the LHC results and the DM data; in the end we study the stability of the SM-like inert vacuum state from different perspectives. The main results of the dissertation are summarised below.

Parameter space of 2HDMs. We studied the allowed parameter space under the following constraints: positivity of the scalar potential, tree-level stability of the vacuum state, perturbative unitarity, EWPT and the LEP constraints. We also used the fact that a SM-like Higgs particle with mass around 125 GeV was discovered.

For the IDM we gave constraints on the values of the parameters of the scalar potential, as well as on the couplings between the physical scalar particles. They appeared to be, in some cases, more stringent than the traditional perturbativity bounds. Moreover, we presented correlations between the couplings, showing that they are not independent, one of another. We also gave constraints on masses of the scalar particles, depending on the value of the mass parameter of the potential, m_{22}^2. We showed that the value of this parameter is also bounded — we derived an upper bound from the condition for the inert minimum and perturbative unitarity. This constraint had not been studied in the literature before and considering the diphoton Higgs decay we proved that it excludes some interesting region in the parameter space.

For the 2HDM (mixed) we provided similar constraints on the scalar parameters and masses, which are in this case absolute since they do not depend on m_{22}^2 as it was in the IDM. Moreover, we obtained a new interesting strong bound on the $\tan\beta$ parameter, that is independent of the Yukawa interactions, and follows from perturbative unitarity and the value of the Higgs boson mass. We also pointed out an interesting fact that the bound is only valid if the lighter of the two CP even scalars of the 2HDM (mixed) plays the role of the SM-like Higgs boson and explained this situation.

Higgs boson in the light of the LHC and DM data. We started from analysing the signal strength of the diphoton decay of the Higgs boson, $R_{\gamma\gamma}$ within the IDM. We studied the possibility of modifying this parameter with respect to the SM expectation. In particular, following the experimental hints, we were interested in the possibility of enhancing the signal. We showed that there are two factors modifying the signal strength: the invisible decays of the Higgs boson to the inert particles, and a new loop effect due to the exchange of the charged scalar. The invisible decays, if kinematically allowed, decrease the signal strength, while the charged scalar loop can interfere with the SM part either constructively or destructively.

Analysing analytically the formula for the diphoton signal strength, and performing a numerical scan of the parameter space we showed that an enhanced signal strength can be obtained only if the neutral inert scalars are heavier than half of the mass of the Higgs boson, i.e. when the invisible decay channels are closed. At the same time $R_{\gamma\gamma}$ can be grater than one for any value of the charged scalar (remembering about the lower bound from LEP, $M_{H^\pm} \geqslant 70\,\mathrm{GeV}$). However, for very heavy charged scalar its contribution decouples and $R_{\gamma\gamma} \approx 1$. If the diphoton signal strength is greater than (and not equal to) 1, upper

bounds on $M_{H^\pm}$ arise. Since the DM candidate is the lightest of the inert scalars, its mass is also constrained from above. In particular, we showed that if $R_{\gamma\gamma} > 1.2$, then $62.5\,\text{GeV} < M_H \lesssim 154\,\text{GeV}$, $70\,\text{GeV} < M_{H^\pm} \lesssim 154\,\text{GeV}$, which would mean that the H and $H^\pm$ particles are within the reach of the current experiments.

In the next step we analysed the possibility of suppressing the diphoton signal strength. We showed that an important parameter, λ_{345} proportional the coupling between the Higgs boson and a pair of DM particles, influences both the diphoton signal strength and the DM relic density. Thus, we combined the DM data from the Planck experiment with constraints obtained by assuming some lower limit on $R_{\gamma\gamma}$. We proved that if $R_{\gamma\gamma} > 0.7$ light inert DM, with masses below 10 GeV, is excluded. In the intermediate mass region, we showed that the same assumption leads to a lower bound on DM mass, $M_H \gtrsim 53\,\text{GeV}$. In the heavy DM regime, the diphoton signal strength is always very close to one, due to decoupling, and the DM relic density can be accounted for by the inert candidate.

Moreover, we studied the correlation between the signal strength of the $h \to Z\gamma$ and $h \to \gamma\gamma$ decays. We showed that the correlation is positive, providing an experimental test of the validity of the IDM, to be checked by the future experiments.

Apart from that, also the measurements of the total decay width and invisible branching ratios of the Higgs boson were analysed by us. We provided constraints on the DM coupling to the Higgs boson as a function of the DM mass.

Vacuum stability. We studied the issue of the vacuum stability in the IDM from two perspectives. The first approach was to look at the influence of additional heavy inert scalars on the SM-like inert vacuum state. The new scalars were assumed to be heavy so that they could only influence the potential through loop effects. The common knowledge is that additional scalars stabilise the vacuum state, contributing positively to the effective potential and to the running of the Higgs self-coupling. This reasoning is normally applied to high energy scales. In this work, we focused on the influence that the additional scalars exert on the effective potential around the EW scale. Moreover, we were interested in the structure of the potential, i.e. the types of possible minima, rather than the running of the couplings. Adopting this new approach we showed, contrary to what is normally assumed, that additional scalars may

have a striking effect on the effective potential, destabilising the SM EWSB vacuum by introducing a new EW symmetric minimum which is deeper than the EWSB one. This proved that it is not enough to consider the effect of the new scalars at large field values, and that it is crucial to study the structure of the effective potential, rather than just the running of the coupling constants. Further on, we demonstrated that the instability (or metastability) scenarios are excluded within the IDM by the perturbative unitarity, EWPT and DM relic abundance. Nonetheless, it is expected that similar effect can occur in other models with additional scalars.

Another approach we took was more general as all of the scalar fields appeared in the effective potential. We were interested to study the stability of the inert vacuum with respect to the inert-like state. These two types of minima can coexist at tree level and we analysed what influence on this coexistence and energy hierarchy between them have the one-loop corrections. Our results show that the coexistence at one-loop level can be realised in a wider parameter space than at tree level. Moreover, we demonstrated that the two minima can be inverted by loop corrections, i.e. a global inert minimum can be turned to a local one, leading to an unstable or a metastable state. This situation can take place only if the two minima are very close in energies but it shows important limitations of the common tree-level approach to the study of vacuum stability in models with extended scalar sector.

7.2 Open questions

Vacuum stability in a general 2HDM beyond tree level. A question that naturally follows the results presented in this thesis is about a general answer to the question of vacuum stability in a generic 2HDM beyond tree level. In this dissertation we assumed two approaches which allowed us to study different aspects of this problem within the IDM. Nonetheless, obtaining a general classification of all possible minima of the one-loop effective potential of a generic 2HDM would be very interesting. As was described in section 6.4 the main difficulty in studying this problem is the consistent use of the effective potential being a function of several scalar fields. Since with each of the scalar fields an independent energy scale can be associated, large logarithms of the ratios of these scales may easily appear rendering the perturbative description of the problem inappropriate. We discussed a possible approach to cope with

the effective potential which assures that the perturbative expansion of the effective potential remains valid. Still, its practical implication requires involved and nontrivial numerical algorithms. Thus this problems remains as a matter of further studies.

New LHC results. The LHC has started a new run at an energy higher than before and certainly will provide new data which 2HDMs will need to be confronted with.

A first example of an intriguing experimental hint is a diphoton excess around 750 GeV reported in December 2015 by the CMS [26] and ATLAS [25] collaborations. Even though the statistical significance of the signal is not yet great, and it can be still interpreted as a fluctuation, it remains puzzling and many authors attempted to explain it within new physics models. In particular, several authors interpreted the excess within the framework of a 2HDM or its extensions [213–223]. In general, it is concluded that in a pure 2HDM it is not possible to account for the observed signal strength in the $gg \to H \to \gamma\gamma$ or $gg \to A \to \gamma\gamma$ channels. The most common solution is to propose additional new particles, vector-like quarks and leptons or scalars. This shows that with the new data the 2HDM will have to be thoroughly tested, and there is a chance it will be proven wrong, or will require certain modifications.

Appendix A

The range of the mixing angle α in the 2HDM (mixed)

The mixing angle α originates from diagonalisation of the mass-matrix of the neutral, CP-even scalar fields in the 2HDM (mixed). As mentioned in section 2.3, in the literature one may encounter different conventions for the range of this angle, some of them being in contradiction with one another. To clarify this issue, below we present a derivation of the expression for $\sin\alpha$, and explain which ranges can be chosen for α.

A.1 Condition for diagonalisation of a symmetric matrix

Let us consider an arbitrary symmetric 2×2 matrix M:

$$M = \begin{pmatrix} a & b \\ b & c \end{pmatrix},$$

and assume that it is diagonalised by a rotation of an angle α. Then the new basis (f_1, f_2), which diagonalises M, is obtained from the old basis (η_1, η_2) by means of a transformation R defined as follows

$$R = \begin{pmatrix} \cos\alpha & \sin\alpha \\ -\sin\alpha & \cos\alpha \end{pmatrix}, \quad R^{-1} = \begin{pmatrix} \cos\alpha & -\sin\alpha \\ \sin\alpha & \cos\alpha \end{pmatrix}. \tag{A.1}$$

The matrix M is diagonalised in the following way

$$\Delta = RMR^{-1},$$

where Δ is diagonal. By performing explicitly the multiplication RMR^{-1} and requiring that the off-diagonal terms of Δ vanish, we obtain a condition that has to be fulfilled by α in order to diagonalise M. It reads

$$(c-a)\sin\alpha\cos\alpha + b(\cos^2\alpha - \sin^2\alpha) = 0, \tag{A.2}$$

and is equivalent to $\tan 2\alpha = \frac{2b}{a-c}$.

Using basic trigonometric identities and eq. (A.2), it can be verified that if α diagonalises M, than also $\alpha - \pi/2$, $\alpha - \pi$, $\alpha + \pi/2$, etc. do. This shows that for a symmetric matrix M, in any quadrant there exists an angle that diagonalises it.

A.2 Relation between different angles diagonalising M

Let us assume, as described above, that α diagonalises M, i.e. in the diagonalising basis (f_1, f_2) this operator reads:

$$\Delta = \begin{pmatrix} \lambda_+ & 0 \\ 0 & \lambda_- \end{pmatrix}.$$

Let us also assume that $\lambda_+ \geqslant \lambda_-$.

We now know that $\alpha + \pi/2$ also diagonalises M, so if we rotate the basis $(f_1,\ f_2)$ by $\pi/2$, the operator M should be also diagonal in the new basis. Let us call the new basis $(g_1,\ g_2)$ and the operator in this basis Δ_1. We have

$$\Delta_1 = R_1 \Delta R_1^{-1},$$

where

$$R_1 = \begin{pmatrix} \cos\frac{\pi}{2} & \sin\frac{\pi}{2} \\ -\sin\frac{\pi}{2} & \cos\frac{\pi}{2} \end{pmatrix} = \begin{pmatrix} 0 & 1 \\ -1 & 0 \end{pmatrix}, \quad R_1^{-1} = \begin{pmatrix} 0 & -1 \\ 1 & 0 \end{pmatrix}.$$

Therefore Δ_1 reads

$$\Delta_1 = \begin{pmatrix} 0 & 1 \\ -1 & 0 \end{pmatrix} \begin{pmatrix} \lambda_+ & 0 \\ 0 & \lambda_- \end{pmatrix} \begin{pmatrix} 0 & -1 \\ 1 & 0 \end{pmatrix} = \begin{pmatrix} \lambda_- & 0 \\ 0 & \lambda_+ \end{pmatrix},$$

and $g_1 = f_2$, $g_2 = -f_1$.

Thus although both α and $\alpha + \pi/2$ diagonalise M, the orderings of the eigenvalues associated with these angles are different. Therefore, if we want to diagonalise M in such a way that the first eigenvalue is bigger, it is not sufficient to look for α only in one quadrant.

A.3 The range of α

We will now perform the diagonalisation of the mass matrix M for the CP even sector explicitly. With M given by

$$M = \begin{pmatrix} a & b \\ b & c \end{pmatrix}, \quad a = \lambda_1 \cos^2\beta v^2, \quad b = \lambda_{345} \cos\beta \sin\beta v^2, \quad c = \lambda_2 \sin^2\beta v^2.$$

the eigenvalues read

$$\lambda_\pm = \frac{1}{2}\left(a + c \pm \sqrt{(a-c)^2 + 4b^2}\right),$$

where $\lambda_+ > \lambda_-$.

Denoting $S = \sqrt{(a-c)^2 + 4b^2}$ and remembering that the eigenvector associated to the eigenvalue λ_+, $v_+ = (v_{+1}, v_{+2})$, must fulfil the condition $(M - \lambda_+ \mathbb{I})\, v_+ = 0$ we obtain the following equation

$$\frac{1}{2}(a - c - S)\, v_{+1} + b v_{+2} = 0.$$

Thus

$$v_+ = \gamma_+ \begin{pmatrix} 1 \\ \frac{c-a+S}{2b} \end{pmatrix},$$

where γ_+ is a normalisation constant. Requiring that v_+ is normalised to 1, $|v_+|^2 = 1$, we get:

$$v_+ = \pm \frac{|2b|}{\sqrt{4b^2 + (c-a+S)^2}} \begin{pmatrix} 1 \\ \frac{c-a+S}{2b} \end{pmatrix}. \tag{A.3}$$

The same procedure can be conducted for λ_-. This brings us to the result:

$$v_- = \pm \frac{|2b|}{\sqrt{4b^2 + (c-a+S)^2}} \begin{pmatrix} \frac{a-c-S}{2b} \\ 1 \end{pmatrix}. \tag{A.4}$$

It can be easily checked that $v_+ \cdot v_- = 0$.

Now we would like to match the eigenvectors $v_\pm$ with the mass eigenstates H and h. We want H to be heavier than h, so it must correspond to v_+. We adopt the following convention for the angle α (as defined by the R matrix, eq. (A.1)),

$$v_+ = H = \cos\alpha\eta_1 + \sin\alpha\eta_2 = \begin{pmatrix} \cos\alpha \\ \sin\alpha \end{pmatrix}, \tag{A.5}$$

$$v_- = h = -\sin\alpha\eta_1 + \cos\alpha\eta_2 = \begin{pmatrix} -\sin\alpha \\ \cos\alpha \end{pmatrix}. \tag{A.6}$$

It can be now seen that if eqs. (A.5) and (A.6) are to be in agreement with eqs. (A.3) and (A.4), the overall signs in eqs. (A.3) and (A.4) should be the same. By comparing eqs. (A.5) and (A.6) with eqs. (A.3) and (A.4) we get:

$$\cos\alpha = \pm\frac{|2b|}{\sqrt{4b^2+(c-a+S)^2}},$$
$$\sin\alpha = \pm\frac{|2b|(c-a+S)}{2b\sqrt{4b^2+(c-a+S)^2}}.$$

Thus, if we pick the plus sign in both of the equations presented above, then $\cos\alpha$ has to be always positive, so the correct range for α is $(-\pi/2,\, \pi/2)$. If we pick the minus sign, then $\cos\alpha < 0$ and $\alpha \in (-3\pi/2,\, -\pi/2)$. Since the choice of the overall sign is arbitrary, we will choose the positive sign for convenience. Then, $\sin\alpha$ can be either positive or negative, the sign depending on the sign of $\frac{|2b|(c-a+S)}{2b\sqrt{4b^2+(c-a+S)^2}}$. Therefore

$$\mathrm{sgn}(\sin\alpha) = \mathrm{sgn}\left(\frac{|2b|(c-a+S)}{2b\sqrt{4b^2+(c-a+S)^2}}\right) = \mathrm{sgn}(b)\mathrm{sgn}(c-a+S),$$

since $\sqrt{4b^2+(c-a+S)^2} > 0$. Moreover, $c-a+S = c-a+\sqrt{(a-c)^2+4b^2} \geqslant c-a+\sqrt{(a-c)^2} = c-a+|c-a| \geqslant 0$, so $\mathrm{sgn}(\sin\alpha) = \mathrm{sgn}(b)$. Remembering the definition of b, $b = \lambda_{345}\cos\beta\sin\beta v^2$, and assuming that $\beta \in (0,\, \pi/2)$, we conclude that:

$$\mathrm{sgn}(\sin\alpha) = \mathrm{sgn}(\lambda_{345}).$$

And we see that indeed, both positive and negative α have to be taken into account if we want to keep the first eigenvalue greater than the other one. So the proper range of α, with the conventions we have adopted, is $(-\pi/2,\, \pi/2)$.

APPENDIX B

Decay widths of the Higgs boson

Below we summarize the decay widths of the Higgs boson following Refs. [47, 63, 146, 151–155, 157]. Some of the formulas (for the decays $h \to \gamma\gamma$, $h \to Z\gamma$, $h \to HH$,$h \to AA$) appear in the main text of the dissertation, however they are also repeated here for the sake of completeness. These formulas were used in the analysis of chapter 4 for the computation of the total decay width of the Higgs boson.

B.1 $h \to q\bar{q}$

$$\Gamma(h \to q\bar{q}) = \frac{3G_F}{4\sqrt{2}\pi} M_h \overline{m}_q^2(M_h) \Bigg\{ 1 + 5.67 \frac{\overline{\alpha}_s(M_h)}{\pi} + \left[37.51 - 1.36 N_f - \frac{2}{3} \log \frac{M_h^2}{m_t^2} + \left(\frac{1}{3} \log \frac{\overline{m}_q^2(M_h)}{M_h^2} \right)^2 \right] \frac{\overline{\alpha}_s^2(M_h)}{\pi^2} \Bigg\}.$$

$N_f = 5$ is the number of active light-quark flavors. The running quark mass defined at the scale M_h is [153]

$$\overline{m}_q(M_h) = \overline{m}_q(m_q) \left(\frac{\overline{\alpha}_s(M_h)}{\overline{\alpha}_s(m_q)} \right)^{12/(33-2N_f)} \frac{1 + c_{1q}\overline{\alpha}_s(M_h)/\pi + c_{2q}\overline{\alpha}_s^2(M_h)/\pi^2}{1 + c_{1q}\overline{\alpha}_s(m_q)/\pi + c_{2q}\overline{\alpha}_s^2(m_q)/\pi^2},$$

where for the bottom quark $c_{1b} = 1.17$, $c_{2b} = 1.50$ and for the charm quark $c_{1c} = 1.01$, $c_{2c} = 1.39$. The running strong coupling constant is approximated at the one-loop level (for energy scales around M_h, where the number of active light quarks can be taken to be constant) [154]

$$\overline{\alpha}_s(M_h) = \frac{\overline{\alpha}_s(M_Z)}{1 + \frac{33-2N_f}{12\pi} \overline{\alpha}_s(M_Z) \log \frac{M_h^2}{M_Z^2}}.$$

The values of quark masses and of the strong coupling are taken from the Particle Data Group [154]: $\overline{m}_b(m_b) = 4.18\,\text{GeV}$, $\overline{m}_c(m_c) = 1.273\,\text{GeV}$, $\overline{\alpha}_s(M_Z) = 0.118$, $\overline{\alpha}_s(m_b) = 0.223$, and $\overline{\alpha}_s(m_c) = 0.38$.

B.2 $h \to \tau^+\tau^-$

$$\Gamma(h \to \tau^+\tau^-) = \frac{G_F N_c}{4\sqrt{2}\pi} M_h m_\tau^2 \left(1 - \frac{4m_\tau^2}{M_h^2}\right)^{3/2}.$$

B.3 $h \to VV^*$

$$\Gamma(h \to VV^*) = \frac{3G_F^2}{16\pi^3} M_V^4 M_h \delta_V R_T(x),$$

where $\delta_W = 1$, $\delta_Z = \frac{7}{12} - \frac{10}{9}\sin^2\theta_W + \frac{40}{9}\sin^4\theta_W$,

$$\begin{aligned} R_T(x) = {} & \frac{3(1 - 8x + 20x^2)}{\sqrt{4x-1}} \arccos\left(\frac{3x-1}{2x^{3/2}}\right) - \frac{1-x}{2x}\left(2 - 13x + 47x^2\right) \\ & - \frac{3}{2}(1 - 6x + 4x^2)\log x \end{aligned}$$

and $x = \frac{M_V^2}{M_h^2}$.

B.4 $h \to gg$

$$\Gamma(h \to gg) = \frac{G_F \alpha_s^2 M_h^3}{36\sqrt{2}\pi^3} \left|\frac{3}{4} A_{1/2}\left(\frac{4m_t^2}{M_h^2}\right)\right|^2.$$

B.5 $h \to \varphi\varphi$ $(\varphi = H, A)$

$$\Gamma(h \to \varphi\varphi) = \frac{\lambda_{h\varphi\varphi}^2 v^2}{32\pi M_h} \sqrt{1 - \frac{4M_\varphi^2}{M_h^2}}, \tag{B.1}$$

where $\lambda_{hHH} = \lambda_{345}$ and $\lambda_{hAA} = \lambda_{345}^-$.

B.6 $h \to \gamma\gamma$

$$\begin{aligned} \Gamma(h \to \gamma\gamma)^{\text{IDM}} = \frac{G_F \alpha^2 M_h^3}{128\sqrt{2}\pi^3} \Bigg| & \frac{4}{3} A_{1/2}\left(\frac{4M_t^2}{M_h^2}\right) + A_1\left(\frac{4M_W^2}{M_h^2}\right) \\ & + \frac{2M_{H^\pm}^2 + m_{22}^2}{2M_{H^\pm}^2} A_0\left(\frac{4M_{H^\pm}^2}{M_h^2}\right)\Bigg|^2, \end{aligned} \tag{B.2}$$

where

$$\begin{aligned} A_0(\tau) &= -\tau[1 - \tau f(\tau)], \\ A_{1/2}(\tau) &= 2\tau[1 + (1-\tau) f(\tau)], \\ A_1(\tau) &= -[2 + 3\tau + 3\tau(2-\tau) f(\tau)] \end{aligned}$$

and

$$f(\tau) = \begin{cases} \arcsin^2\left(\frac{1}{\sqrt{\tau}}\right) & \text{for } \tau \geqslant 1, \\ -\frac{1}{4}\left[\log\left(\frac{1+\sqrt{1-\tau}}{1-\sqrt{1-\tau}}\right) - i\pi\right]^2 & \text{for } \tau < 1. \end{cases}$$

B.7 $h \to Z\gamma$

$$\begin{aligned} \Gamma(h \to Z\gamma) = \frac{G_F^2 \alpha}{64\pi^4} M_W^2 M_h^3 \left(1 - \frac{M_Z^2}{M_h^2}\right)^3 \Bigg| & 2 \frac{1 - \frac{8}{3}\sin^2\theta_W}{\cos\theta_W} A_{1/2}^h\left(\frac{4m_t^2}{M_h^2}, \frac{4m_t^2}{M_Z^2}\right) \\ & + A_1^h\left(\frac{4M_W^2}{M_h^2}, \frac{4M_W^2}{M_Z^2}\right) \\ & - \frac{2M_{H^\pm}^2 + m_{22}^2}{2M_{H^\pm}^2} \frac{(1 - 2\sin^2\theta_W)}{\cos\theta_W} I_1\left(\frac{4M_{H^\pm}^2}{M_h^2}, \frac{4M_{H^\pm}^2}{M_Z^2}\right) \Bigg|^2, \end{aligned} \tag{B.3}$$

where

$$\begin{aligned} A_{1/2}^h(\tau,\lambda) &= I_1(\tau,\lambda) - I_2(\tau,\lambda), \\ A_1^h(\tau,\lambda) &= \cos\theta_W \left\{ 4\left(3 - \frac{\sin^2\theta_W}{\cos^2\theta_W}\right) I_2(\tau,\lambda) + \left[\left(1 + \frac{2}{\tau}\right)\frac{\sin^2\theta_W}{\cos^2\theta_W} - \left(5 + \frac{2}{\tau}\right)\right] I_1(\tau,\lambda) \right\}, \\ I_1(\tau,\lambda) &= \frac{\tau\lambda}{2(\tau-\lambda)} + \frac{\tau^2\lambda^2}{2(\tau-\lambda)^2}\big[f(\tau) - f(\lambda)\big] + \frac{\tau^2\lambda}{(\tau-\lambda)^2}\big[g(\tau^{-1}) - g(\lambda^{-1})\big], \\ I_2(\tau,\lambda) &= -\frac{\tau\lambda}{2(\tau-\lambda)}\big[f(\tau) - f(\lambda)\big], \end{aligned}$$

$$g(\tau) = \begin{cases} \sqrt{\frac{1}{\tau} - 1}\arcsin\sqrt{\tau} & \text{for } \tau \leqslant 1, \\ \frac{\sqrt{1-\frac{1}{\tau}}}{2}\left(\log\frac{1+\sqrt{1-\frac{1}{\tau}}}{1-\sqrt{1-\frac{1}{\tau}}} - i\pi\right) & \text{for } \tau > 1. \end{cases}$$

Note the minus sign of the charged scalar contribution [155], which is different than the result in ref. [151].

APPENDIX C

Dimensional regularisation of the one-loop contribution to the effective potential

In this appendix we present the details of the procedure of dimensional regularisation of the one-loop contribution to the effective potential, δV_{CW}. Our starting point is the expression of eq. (5.11), which is UV divergent and requires regularisation.

In the following we will use the abbreviation

$$m_{\mathrm{eff}}^2 = m^2 + \frac{1}{2}\lambda\varphi^2.$$

of course m_{eff}^2 depends on φ but we will not write it explicitly to make the formulas shorter. We will work with the first part of the integral from eq. (5.11):

$$I = \int \frac{d^4k}{(2\pi)^4} \log\left(k^2 + m_{\mathrm{eff}}^2\right).$$

This integral is divergent in 4 dimensions so let us use dimensional regularisation and consider I in D dimensions, so we have to introduce the energy scale μ, for the dimensions to agree, $I_D = \int \frac{d^Dk}{(2\pi)^D}\mu^{4-D}\log\left(k^2 + m_{\mathrm{eff}}^2\right)$. We will perform a trick first differentiating I_D with respect to φ, next integrating over momentum k, then expanding it around $D = 4$, and finally integrating over φ.

$$\begin{aligned}\frac{\partial}{\partial\varphi} I_D &= \frac{\partial}{\partial\varphi}\int \frac{d^Dk}{(2\pi)^D}\mu^{4-D}\log\left(k^2 + m_{\mathrm{eff}}^2\right) = \mu^{4-D}\int \frac{d^Dk}{(2\pi)^D}\frac{1}{k^2 + m_{\mathrm{eff}}^2}\frac{\partial}{\partial\varphi}\left(m_{\mathrm{eff}}^2\right) \\ &= \mu^{4-D}\frac{\partial m_{\mathrm{eff}}^2}{\partial\varphi}\int \frac{d^Dk}{(2\pi)^D}\frac{1}{k^2 + m_{\mathrm{eff}}^2}.\end{aligned}$$

A formula for the integral in the equation above is known, it reads

$$\int \frac{d^D k}{(2\pi)^D} \frac{1}{(k^2+a)^n} = \frac{1}{(4\pi)^{D/2}} \frac{\Gamma\left(n-\frac{D}{2}\right)}{\Gamma(n)} a^{D/2-n}.$$

Remembering that $\Gamma(1)=1$, setting $D=4-\epsilon$, and using the fact that $x\Gamma(x)=\Gamma(x+1)$ (so $\left(\frac{\epsilon}{2}-1\right)\Gamma\left(\frac{\epsilon}{2}-1\right)=\Gamma\left(\frac{\epsilon}{2}\right)$) we get

$$\frac{\partial}{\partial\varphi} I_D = \mu^\epsilon \frac{\partial m_{\text{eff}}^2}{\partial\varphi} \frac{1}{(4\pi)^{2-\epsilon/2}} \frac{\Gamma\left(\frac{\epsilon}{2}\right)}{\frac{\epsilon}{2}-1} \left(m_{\text{eff}}^2\right)^{1-\epsilon/2}.$$

Now we are ready to expand this expression in terms of ϵ. We will use the following facts:

$$\begin{aligned} \Gamma\left(\frac{\epsilon}{2}\right) &\approx \frac{2}{\epsilon} - \gamma_E, \\ a^\epsilon = e^{\log a^\epsilon} &= e^{\epsilon \log a} \approx 1 + \epsilon \log a, \\ \frac{1}{1-x} &\approx 1 + x, \end{aligned}$$

where γ_E denotes the Euler gamma, $\gamma_E \approx 0.5772$. Therefore

$$\left(\frac{4\pi\mu^2}{m_{\text{eff}}^2}\right)^{\epsilon/2} \approx 1 + \frac{\epsilon}{2} \log\left(\frac{4\pi\mu^2}{m_{\text{eff}}^2}\right),$$

and

$$\frac{\partial}{\partial\varphi} I_D = -\frac{m_{\text{eff}}^2}{(4\pi)^2} \frac{\partial m_{\text{eff}}^2}{\partial\varphi} \left[1 + \frac{\epsilon}{2} \log\left(\frac{4\pi\mu^2}{m_{\text{eff}}^2}\right)\right] \left(1+\frac{\epsilon}{2}\right) \left(\frac{2}{\epsilon} - \gamma_E\right).$$

Now we neglect the terms which tend to zero as ϵ goes to zero (so the terms that vanish in $D=4$),

$$\frac{\partial}{\partial\varphi} I_D = \frac{m_{\text{eff}}^2}{(4\pi)^2} \frac{\partial m_{\text{eff}}^2}{\partial\varphi} \left[-1 - \frac{2}{\epsilon} - \log\left(\frac{4\pi\mu^2}{m_{\text{eff}}^2}\right) + \gamma_E\right].$$

In the next step we have to integrate $\frac{\partial}{\partial\varphi} I_D$ over φ,

$$I_D = \int d\varphi \frac{\partial}{\partial\varphi} I_D = \int d\varphi \frac{m_{\text{eff}}^2}{(4\pi)^2} \frac{\partial m_{\text{eff}}^2}{\partial\varphi} \left[-1 - \frac{2}{\epsilon} + \log\left(\frac{m_{\text{eff}}^2}{4\pi\mu^2}\right) + \gamma_E\right].$$

Let us change variables in this integral substituting $x = \frac{m_{\text{eff}}^2}{4\pi\mu^2}$ and consequently $dx = \frac{\partial m_{\text{eff}}^2}{\partial\varphi} d\varphi$. Then our integral takes the form

$$I_D = \left(\frac{4\pi\mu^2}{4\pi}\right)^2 \int dx x \left[-\frac{2}{\epsilon} + \gamma_E - 1 + \log x\right].$$

So the following formula is needed

$$\int dx x(a + \log x) = x^2 \left(\frac{1}{2}a \ - \frac{1}{4} + \frac{1}{2}\log x\right).$$

Applying it to I_D we get

$$I_D = \frac{1}{2}\frac{m_{\text{eff}}^4}{(4\pi)^2}\left[-\frac{2}{\epsilon} + \gamma_E - \frac{3}{2} + \log\left(\frac{m_{\text{eff}}^2}{4\pi\mu^2}\right)\right].$$

Substituting this result to eq. (5.11) we finally obtain (the second term in (5.11) is computed in the same way as the first one):

$$\delta V_{\text{CW}} = \frac{m_{\text{eff}}^4}{64\pi^2}\left[-\frac{2}{\epsilon} + \gamma_E - \frac{3}{2} + \log\left(\frac{m_{\text{eff}}^2}{4\pi\mu^2}\right)\right] - \frac{m^4}{64\pi^2}\left[-\frac{2}{\epsilon} + \gamma_E - \frac{3}{2} + \log\left(\frac{m^2}{4\pi\mu^2}\right)\right].$$

The second term above is a constant so it can be removed from the effective potential without loss of generality.[1] This gives the well known result quoted also in chapter 5 in eq. (5.12)

$$\delta V_{\text{CW}} = \frac{m_{\text{eff}}^4}{64\pi^2}\left[-\frac{2}{\epsilon} + \gamma_E - \frac{3}{2} + \log\left(\frac{m_{\text{eff}}^2}{4\pi\mu^2}\right)\right].$$

[1] It should be noted that the constant term depends on the renormalisation scale μ so its can be omitted if values of the potential at a fixed scale are considered. If the effective potential at different scales is analysed, the running of the vacuum energy should also be taken into account [202, 203].

APPENDIX D

Self-energies of the scalar particles in the IDM

In this appendix we present a complete computation of the self-energies of the scalar particles and the Goldstone bosons within the IDM. The results derived here were used in the analyses of chapter 6. The final results were cross-checked with the results obtained from the general prescriptions given by Martin in refs. [205, 206].

D.1 Definitions of the loop functions

In the following we will compute loop corrections to the tadpoles and to the self-energy of the Higgs boson and other scalar particles. To make the computations cleaner, we will reduce all the integrals to the basic Passarino–Veltman functions [224] (note, however, that various definitions of these functions exist, differing by overall factors). These are the scalar vacuum integrals. We will need only the two simplest of them, namely

$$a(m^2) = \int \frac{d^D k}{(2\pi)^D} \frac{i\mu^\epsilon}{k^2 - m^2 + i\epsilon}, \tag{D.1}$$

$$b_0(p^2, m_1, m_2) = \int \frac{d^D k}{(2\pi)^D} \frac{i\mu^\epsilon}{(k^2 - m_1^2 + i\epsilon)\left[(p-k)^2 - m_2^2 + i\epsilon\right]}. \tag{D.2}$$

It is important to note that the b_0 function is symmetric under the exchange of the second and third argument.

Using the standard Feynman parametrization, and expansion in ϵ, the functions

can be evaluated, up to terms vanishing for $\epsilon \to 0$

$$a(m^2) = -\frac{m^2}{(4\pi)^2}\left(\frac{2}{\epsilon} - \gamma_E + \log(4\pi\mu^2) - \log m^2 + 1\right), \tag{D.3}$$

$$b_0(p^2, m_1, m_2) = -\frac{1}{(4\pi)^2}\left(\frac{2}{\epsilon} - \gamma_E + \log(4\pi\mu^2) - \int_0^1 dx \log\Delta\right), \tag{D.4}$$

where $\Delta = -x(1-x)p^2 + xm_1^2 + (1-x)m_2^2$. For the sake of performing cross-checks of intermediate results it is helpful to note that the divergent parts of a and b_0 differ only by a factor of m^2. It is also useful to know that

$$a(0) = 0.$$

We also introduce a non-standard a^b and b_0^b functions, which will be useful for the bosonic loops

$$3a^b(m^2) = (D-1)a(m^2) = -\frac{3m^2}{(4\pi)^2}\left(\frac{2}{\epsilon} - \gamma_E + \log(4\pi\mu^2) - \log m^2 + \frac{1}{3}\right), \tag{D.5}$$

$$\begin{aligned} 4b_0^b(p^2, m_1^2, m_2^2) &= Db_0(p^2, m_1^2, m_2^2) \\ &= -\frac{4}{(4\pi)^2}\left(\frac{2}{\epsilon} - \gamma_E + \log(4\pi\mu^2) - \int_0^1 dx \log\Delta - \frac{1}{2}\right). \end{aligned} \tag{D.6}$$

They differ from the original ones only by the finite part.[1]

D.2 Higgs self-energy and tadpoles in the SM

We will start our computations from a case of a single Higgs boson within the SM. Not much more computations will be needed to give the self-energy expressions for the scalars in the IDM. To conform with the conventions used within this thesis the SM potential we use if of the form of eq. (2.1) with ϕ_D set to zero.

D.2.1 Tadpoles

We start by computing the tadpole diagrams for the Higgs field. In the loop the $W^\pm, Z, t, b, G^\pm$ and G can propagate. Respective diagrams are shown in fig. D.1, and the relevant couplings in fig. D.2. For the couplings we follow Ref. [225], with $\xi = 0$, since we work in the Landau gauge.

The scalar tadpoles are easy to compute, because they are just equal to the a or a^b functions, with appropriate coefficients. Therefore, since $G^\pm$ and G are massless,

[1] These functions would not appear if we used DRED instead of DREG.

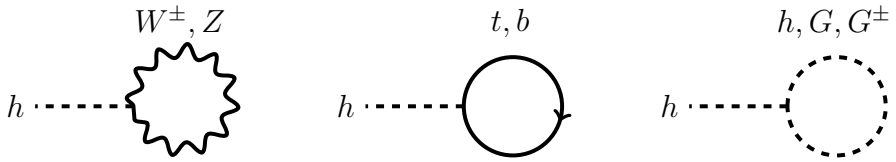

Figure D.1: The Higgs tadpole diagrams.

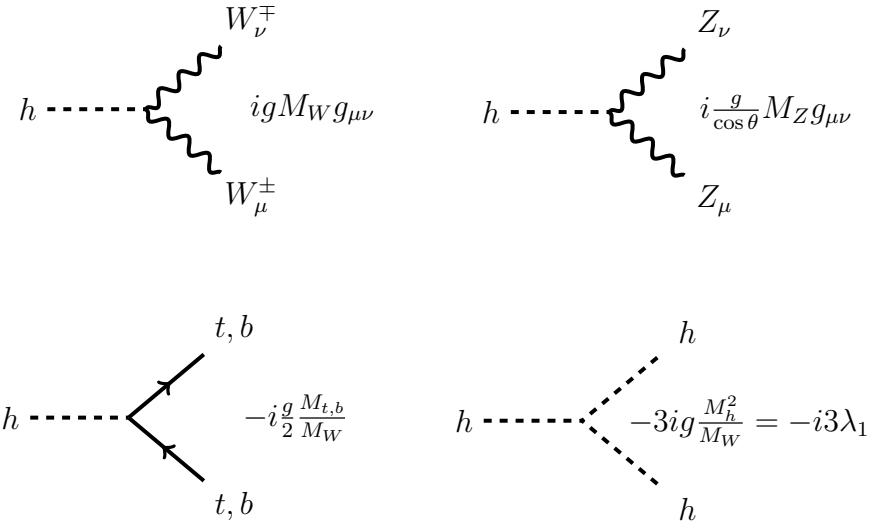

Figure D.2: The couplings relevant for the computation of the Higgs tadpole diagrams.

their contribution will vanish. We only have to take care of the $\frac{1}{2}$ symmetry factor for the Higgs loop, and will express the coupling as

$$3g\frac{M_h^2}{M_W} = 3\lambda_1 v^2 \frac{2}{gv} = 3\lambda_1 v.$$

The W loop yields the following expression

$$gM_W \int \frac{d^D k}{(2\pi)^D}\mu^\epsilon \frac{g_{\mu\nu}\left(g^{\mu\nu} - \frac{k^\mu k^\nu}{k^2}\right)}{k^2 - M_W^2} = -i\frac{g^2 v(D-1)}{2}\int \frac{d^D k}{(2\pi)^D} i\mu^\epsilon \frac{1}{k^2 - M_W^2}$$
$$= -i\frac{3g^2 v}{2}a^b(M_W).$$

The Z loop differs only by a symmetry factor $\frac{1}{2}$, and by the coupling, and gives the result

$$-i\frac{3}{2}\sqrt{g^2 + g'^2}M_Z a^b(M_Z) = -i\frac{3}{4}(g^2 + g'^2)v a^b(M_Z).$$

The fermionic loops will give similar contributions (below M_f is the mass of the fermion and the color factor of 3 is taken into account)

$$\frac{3g}{2}\frac{M_f}{M_W}\int \frac{d^D k}{(2\pi)^D}\mu^\epsilon \mathrm{Tr}\left(\frac{1}{\not{k} - m}\right) = \frac{3g}{2}\frac{M_f}{M_W}\int \frac{d^D k}{(2\pi)^D}\mu^\epsilon \mathrm{Tr}\left(\frac{\not{k} + m}{k^2 - m^2}\right)$$
$$= -i6g\frac{M_f^2}{M_W}\int \frac{d^D k}{(2\pi)^D} i\mu^\epsilon \frac{1}{k^2 - m^2} = -6ig\frac{M_f^2}{M_W}a(M_f) = -6iy_f^2 v a(M_f).$$

These contributions can be summarised as follows

$$-i\mathcal{T} = -i\Big[\frac{3}{2}\lambda a(M_h) + \frac{3}{2}g^2 a^b(M_W) + \frac{3}{4}(g^2+g'^2)a^b(M_Z) - 6y_t^2 a(M_t) - 6y_b^2 a\ (M_b)\Big]v. \tag{D.7}$$

D.2.2 Higgs self-energy

The next step towards renormalizing the effective potential of the SM amounts to the computation of the self-energy of the Higgs boson. To this end numerous diagrams have to be computed. They are depicted in fig. D.3, and the relevant couplings are listed in fig. D.4.

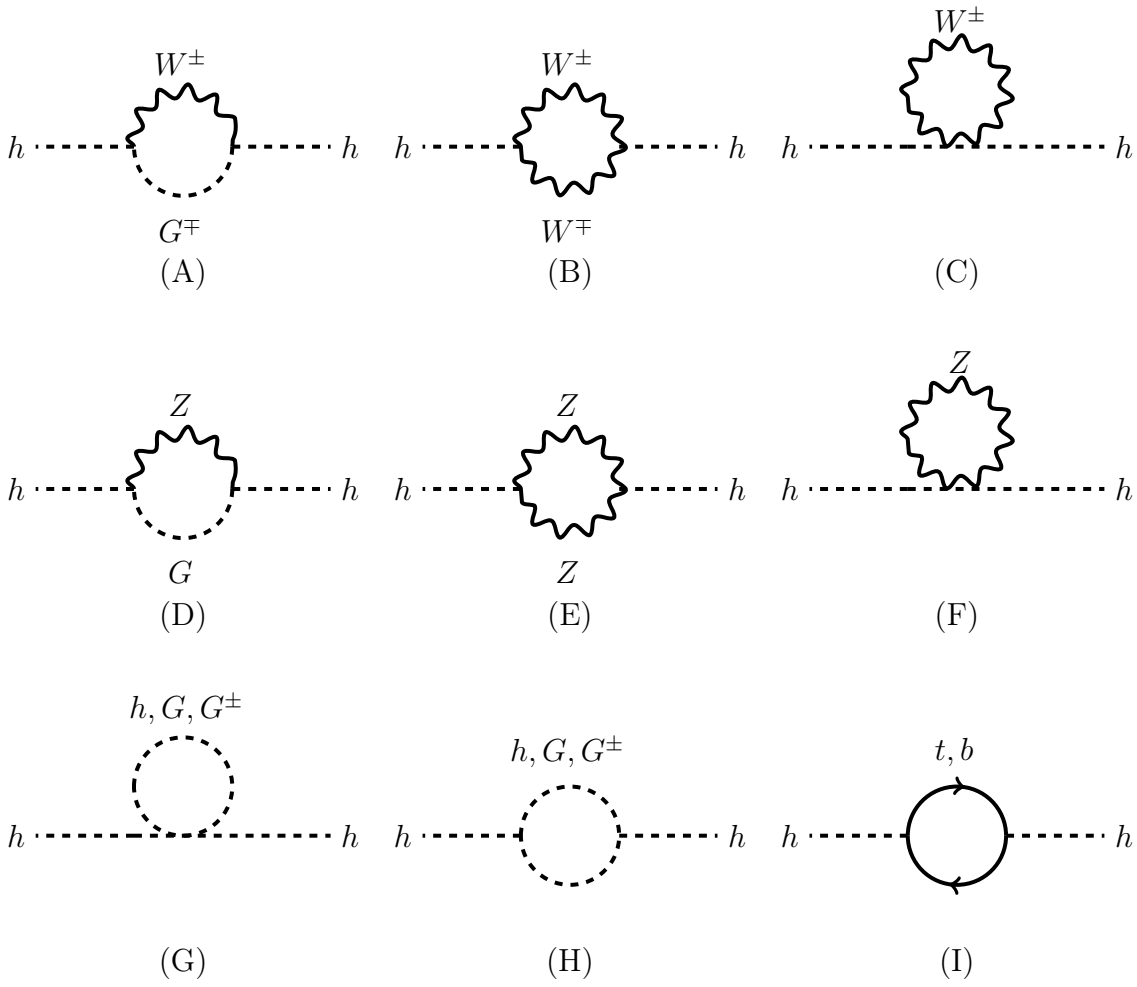

Figure D.3: Diagrams contributing to the Higgs self-energy.

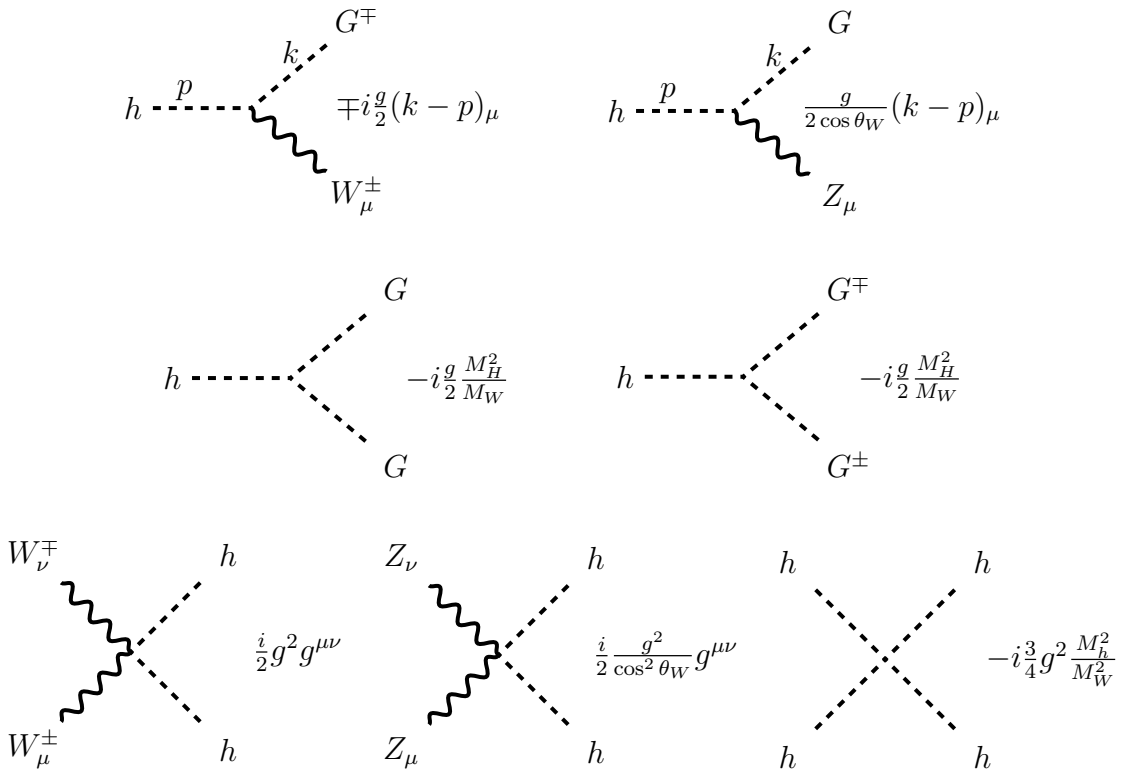

Figure D.4: Couplings relevant for the computation of the Higgs self-energy. The couplings are defined for all the momenta incoming. We omit the ones that are listed in fig. D.2.

D.2.2.1 Diagrams (A) and (D)

Let us start the computation from the diagram (A) of fig. D.3. For the beginning we will express the $W^\pm$ propagator in a more useful way (below we skip the $i\varepsilon$ term in the denominator).

$$-i\left[\frac{g_{\mu\nu}-(1-\xi)\frac{k^\mu k^\nu}{k^2-\xi M_W^2}}{k^2-M_W^2}\right]=-i\left[\frac{g^{\mu\nu}}{k^2-M_W^2}+\frac{k^\mu k^\nu}{M_W^2}\left(\frac{1}{k^2-\xi M_W^2}-\frac{1}{k^2-M_W^2}\right)\right]. \tag{D.8}$$

It is true, because of the following simple identity

$$\frac{1}{k^2-\xi M_W^2}-\frac{1}{k^2-M_W^2}=-\frac{(1-\xi)M_W^2}{(k^2-M_W^2)(k^2-\xi M_W^2)}.$$

We will set $\xi=0$ only at the end of the computation. Now we are ready to write down the expression corresponding to this diagram. For concreteness let us assume that the W^+ boson is propagating in the loop (the contribution from the diagram with W^- will be the same, so in the end we will multiply the result by 2). Assigning momentum p to the Higgs boson, momentum k to the W boson, and (due to

momentum conservation) $p-k$ to the G, we arrive at the following integral[2]

$$\frac{g^2}{4}\int\frac{d^Dk}{(2\pi)^D}(k-2p)_\mu\left[\frac{g^{\mu\nu}}{k^2-M_W^2}+\frac{k^\mu k^\nu}{M_W^2}\left(\frac{1}{k^2-\xi M_W^2}-\frac{1}{k^2-M_W^2}\right)\right]\times(2p-k)_\nu\frac{1}{(p-k)^2}\mu^\epsilon. \tag{D.9}$$

We will treat the part containing $g^{\mu\nu}$, and the one containing $k^\mu k^\nu$ separately. Let us start with the $g^{\mu\nu}$ part.

$$\text{numerator}=(k-2p)_\mu g^{\mu\nu}(2p-k)_\nu=-(2p-k)^2=-4p^2+4pk-k^2.$$

Substituting

$$pk=\frac{1}{2}\left[p^2+k^2-(p-k)^2\right], \tag{D.10}$$

we can continue

$$\text{numerator}=-4p^2-k^2+2p^2+2k^2-2(p-k)^2=k^2-2p^2-2(p-k)^2.$$

Adding the denominator we get the following expression (below the trick is to modify the numerator in such a way, as to cancel the denominator)

$$\begin{aligned}\int\frac{d^Dk}{(2\pi)^D}\mu^\epsilon\frac{k^2-2p^2-2(p-k)^2}{(k^2-M_W^2)(p-k)^2}&=\int\frac{d^Dk}{(2\pi)^D}\frac{k^2-M_W^2-2(p-k)^2-2p^2+M_W^2}{(k^2-M_W^2)(p-k)^2}\\&=-i\Bigg[\int\frac{d^Dk}{(2\pi)^D}\frac{i\mu^\epsilon}{(p-k)^2}-2\int\frac{d^Dk}{(2\pi)^D}\frac{i\mu^\epsilon}{k^2-M_W^2}\\&\quad+(-2p^2+M_W^2)\int\frac{d^Dk}{(2\pi)^D}\frac{i\mu^\epsilon}{(k^2-M_W^2)(p-k)^2}\Bigg]\\&=-i\left[a(0)-2a(M_W)+(-2p^2+M_W^2)b_0(p^2,M_W,0)\right]\\&=-i\left[-2a(M_W)+(-2p^2+M_W^2)b_0(p^2,M_W,0)\right],\end{aligned} \tag{D.11}$$

where in the last equality we used the fact that $a(0)=0$.

Let us now move to the second part, containing $k^\mu k^\nu$. Looking first at the numerator, we get

$$\text{numerator}=(k-2p)_\mu k^\mu k^\nu(2p-k)_\nu=-\left[(k-2p)k\right]^2=-\left(k^2-2pk\right)^2.$$

Using the same expression for $2pk$ as above, and arrive at

$$\text{numerator}=-\left[-p^2+(p-k)^2\right]^2=-\left[p^4-2p^2(p-k)^2+(p-k)^4\right].$$

[2]Note that when constructing this expression one has to take the coupling hG^-W^+ once with the "+" sign, and once with the "-" sign, because an incoming W^+ is equivalent to an outgoing W^-.

Now we want to add the denominator and use the same strategy as previously, to reduce the integral to the Passarino–Veltman functions. In the expression (D.9) a sum of two terms with different denominators is present. They differ by the ξ coefficient multiplying the W mass. To reduce the length of the calculations, we will perform it only for one "generic" denominator wit an arbitrary ξ. Then, adding in the final result two terms – one with $\xi = 0$ (it corresponds to the denominator with ξ, and in the Landau gauge $\xi = 0$), and the other with $\xi = 1$ (it reproduces a denominator with no ξ), we will recover the correct result in the Landau gauge.

$$\begin{aligned}
&-\int \frac{d^Dk}{(2\pi)^D}\mu^\epsilon \frac{[p^4 - 2p^2(p-k)^2 + (p-k)^4]}{(k^2 - \xi M_W^2)(p-k)^2} \\
&\quad = -i\Bigg[- p^4 \int \frac{d^Dk}{(2\pi)^D} \frac{i\mu^\epsilon}{(k^2 - \xi M_W^2)(p-k)^2} + 2p^2 \int \frac{d^Dk}{(2\pi)^D} \frac{i\mu^\epsilon}{k^2 - \xi M_W^2} \\
&\qquad - \int \frac{d^Dk}{(2\pi)^D} i\mu^\epsilon \frac{(p-k)^2}{k^2 - \xi M_W^2} \Bigg] \\
&\quad = -i\left[-p^4 b_0(p^2, \xi M_W, 0) + 2p^2 a(\xi M_W) - \int \frac{d^Dk}{(2\pi)^D} i\mu^\epsilon \frac{(p-k)^2}{k^2 - \xi M_W^2} \right]. \qquad \text{(D.12)}
\end{aligned}$$

Above the notation $a(\xi M_W)$ should be treated rather symbolically. $\sqrt{\xi}$ would be more correct than ξ, however as we consider only $\xi = 0, 1$, it does not matter, as $\sqrt{\xi} = \xi$. Let us elaborate a bit more on the last integral

$$\begin{aligned}
&\int \frac{d^Dk}{(2\pi)^D} i\mu^\epsilon \frac{(p-k)^2}{k^2 - \xi M_W^2} = \int \frac{d^Dk}{(2\pi)^D} i\mu^\epsilon \frac{p^2 - 2pk + k^2}{k^2 - \xi M_W^2} \\
&\quad = p^2 \int \frac{d^Dk}{(2\pi)^D} \frac{i\mu^\epsilon}{k^2 - \xi M_W^2} + \int \frac{d^Dk}{(2\pi)^D} i\mu^\epsilon + \xi M_W^2 \int \frac{d^Dk}{(2\pi)^D} \frac{i\mu^\epsilon}{k^2 - \xi M_W^2} \\
&\quad = (p^2 + \xi M_W^2) a\ (\xi M_W) + \int \frac{d^Dk}{(2\pi)^D} i\mu^\epsilon, \qquad \text{(D.13)}
\end{aligned}$$

where the integral over kp in the first line is zero, because it is an odd function, while the denominator is even under the change $k \to -k$.

Now, collecting the results of Eq. (D.12) and (D.13) we get the result for a generic denominator

$$-i\left[-p^4 b_0(p^2, \xi M_W, 0) + (p^2 - \xi M_W^2) a\ (\xi M_W) - \int \frac{d^Dk}{(2\pi)^D} i\mu^\epsilon \right].$$

So when we subtract the two terms with $\xi = 0$ and $\xi = 1$, we get

$$(\xi = 0) - (\xi = 1) = -i\left\{ -p^4 [b_0(p^2, 0, 0) - b_0(p^2, M_W, 0)] - (p^2 - M_W^2) a(M_W) \right\}, \qquad \text{(D.14)}$$

where the fact that $a(0) = 0$ was taken into account.

Finally, adding the terms with $k^\mu k^\nu$, Eq. (D.14) (remembering that it should be divided by M_W^2), and $g^{\mu\nu}$, Eq. (D.11), we end up with the following result

$$\begin{aligned}
&-i\frac{g^2}{4}\Big\{-2a(M_W)+\left(-2p^2+M_W^2\right)b_0(p^2,M_W,0)\\
&\quad-\frac{p^4}{M_W^2}\left[b_0(p^2,0,0)-b_0(p^2,M_W,0)\right]+\left(-\frac{p^2}{M_W^2}+1\right)a(M_W)\Big\}\\
&=-i\frac{g^2}{4}\Bigg[-\left(\frac{p^2}{M_W^2}+1\right)a(M_W)+\left(\frac{p^4}{M_W^2}-2p^2+M_W^2\right)b_0(p^2,M_W,0)\\
&\quad-\frac{p^4}{M_W^2}b_0(p^2,0,0)\Bigg]\\
&=-i\frac{g^2}{4M_W^2}\left[-\left(p^2+M_W^2\right)a(M_W)+\left(p^2-M_W^2\right)^2b_0(p^2,M_W,0)-p^4b_0(p^2,0,0)\right].
\end{aligned}\tag{D.15}$$

To get the final result for the diagram (A) of fig. D.3 we should multiply Eq. (D.15) by a factor of 2 since in fact it represents two diagrams with either W^+ or W^- propagating in the loop. The final contribution reads

$$\begin{aligned}
(\mathrm{A})=-i\frac{g^2}{2M_W^2}\Big[&M_W^2a\left(M_{G^\pm}\right)+\left(-p^2-M_W^2+M_{G^\pm}^2\right)a(M_W)\\
&-(p^2-M_{G^\pm}^2)^2b_0\left(p^2,0,M_{G^\pm}\right)\\
&+\left(p^4+M_{G^\pm}^4+M_W^4-2p^2M_W^2-2M_{G^\pm}^2M_W^2-2p^2M_{G^\pm}^2\right)b_0(p^2,M_W,M_{G^\pm})\Big].
\end{aligned}\tag{D.16}$$

Above we have explicitly included the masses of the Goldstone bosons. It these particles are on-shell, these masses of course vanish, and the expression simplifies. However, for certain computations it is needed to allow for non-zero Goldstone masses.

The diagram (D) differs from (A) only by: the value of the coupling, the mass of the propagating boson (M_W has to be changed to M_Z) and the overall factor of 2, which is not present in this case. The coupling can be expressed as follows

$$\frac{g^2}{4\cos^2\theta_W}=\frac{g^2+g'^2}{4}.$$

Having that, we can just write down the final result:

$$\begin{aligned}
(\mathrm{D})=-i\frac{g^2+g'^2}{4M_Z^2}\Big[&M_Z^2a\left(M_G\right)+\left(-p^2-M_Z^2+M_G^2\right)a(M_Z)\\
&-(p^2+M_G^2)^2b_0\left(p^2,0,M_G\right)+\left(p^2+M_G^2-M_Z^2\right)^2b_0(p^2,M_Z,M_G)\Big].
\end{aligned}\tag{D.17}$$

D.2.2.2 Diagrams (B) and (E)

Diagrams (B) and (E) will be computed in absolutely analogous manner. Let us start with the diagram (B). It is the one that requires the longest calculations.

Using the propagator from Eq. (D.8), assigning momentum p to the external Higgs fields, momentum k and $p-k$ to the W bosons, and using the couplings from fig. D.2 we can write down the integral corresponding to the diagram (B)

$$(B) = g^2 M_W^2 \int \frac{d^D k}{(2\pi)^D} \mu^\epsilon \underbrace{g_{\mu\rho} g_{\nu\sigma}}_{\bigstar} \left[\underbrace{\frac{g^{\mu\nu}}{k^2 - M_W^2}}_{\heartsuit} + \underbrace{\frac{k^\mu k^\nu}{M_W^2} \left(\frac{1}{k^2 - \xi M_W^2} - \frac{1}{k^2 - M_W^2} \right)}_{\spadesuit} \right]$$
$$\times \left[\underbrace{\frac{g^{\rho\sigma}}{(p-k)^2 - M_W^2}}_{\diamondsuit} + \underbrace{\frac{(p-k)^\rho (p-k)^\sigma}{M_W^2} \left(\frac{1}{(p-k)^2 - \xi M_W^2} - \frac{1}{(p-k)^2 - M_W^2} \right)}_{\clubsuit} \right].$$

The expression is rather lengthy and requires multiplying various terms. Because of that we labelled different terms with symbols, and will treat their products separately.

$\underline{\bigstar \cdot \heartsuit \cdot \diamondsuit}$

$$\begin{aligned} \int \frac{d^D k}{(2\pi)^D} \mu^\epsilon (\bigstar \cdot \heartsuit \cdot \diamondsuit) &= \int \frac{d^D k}{(2\pi)^D} \mu^\epsilon g_{\mu\rho} g_{\nu\sigma} g^{\mu\nu} g^{\rho\sigma} \frac{1}{k^2 - M_W^2} \frac{1}{(p-k)^2 - M_W^2} \\ &= \int \frac{d^D k}{(2\pi)^D} \mu^\epsilon g^\rho{}_\rho \frac{1}{k^2 - M_W^2} \frac{1}{(p-k)^2 - M_W^2} = -iDb_0(p^2, M_W, M_W) \\ &= -4ib_0^b(p^2, M_W, M_W). \end{aligned} \tag{D.18}$$

$\underline{\bigstar \cdot \spadesuit \cdot \diamondsuit}$

Let us start from the numerator

$$\text{numerator} = g_{\mu\rho} g_{\nu\sigma} g^{\mu\nu} k^\rho k^\sigma = k^\mu k^\nu g^{\mu\nu} = k^2.$$

Now let us proceed with a term, which has a generic denominator, with $\xi \in \{0, 1\}$ (as above in section D.2.2.1). As previously, we add and subtract mass terms in the numerator in such a way as to cancel some of the terms in the denominator.

$$\begin{aligned} &\frac{1}{M_W^2} \int \frac{d^D k}{(2\pi)^D} i\mu^\epsilon \frac{k^2}{(k^2 - \xi M_W^2)\left[(p-k)^2 - M_W^2\right]} \\ &= \frac{1}{M_W^2} \int \frac{d^D k}{(2\pi)^D} i\mu^\epsilon \frac{k^2 - \xi M_W^2}{(k^2 - \xi M_W^2)\left[(p-k)^2 - M_W^2\right]} \\ &\quad + \frac{\xi M_W^2}{M_W^2} \int \frac{d^D k}{(2\pi)^D} i\mu^\epsilon \frac{1}{(k^2 - \xi M_W^2)\left[(p-k)^2 - M_W^2\right]} \\ &= -i \left[\frac{1}{M_W^2} a(M_W) + \xi b_0(p^2, \xi M_W, M_W) \right]. \end{aligned}$$

Now the full result of this part will be obtained by subtracting the term with $\xi = 1$ from the term with $\xi = 0$.

$$\int \frac{d^D k}{(2\pi)^D} \mu^\epsilon (\bigstar \cdot \spadesuit \cdot \diamondsuit) = -i \left[\frac{1}{M_W^2} a(M_W) - \frac{1}{M_W^2} a(M_W) - b_0(p^2, M_W, M_W) \right] = -i \left[-b_0(p^2, M_W, M_W) \right]. \quad \text{(D.19)}$$

$\underline{\bigstar \cdot \heartsuit \cdot \clubsuit}$

If we change the variables in this expression, such as $k' = k - p$ we recover precisely the expression $\bigstar \cdot \spadesuit \cdot \diamondsuit$, so the result of this part will be exactly the same as above.

$\underline{\bigstar \cdot \spadesuit \cdot \clubsuit}$

Let us start from simplifying the numerator

$$\text{numerator} = g_{\mu\rho} g_{\nu\sigma} k^\mu k^\nu (p-k)^\rho (p-k)^\sigma = k_\rho k_\sigma (p-k)^\rho (p-k)^\sigma = \left[k(p-k) \right]^2.$$

We use the familiar expression $pk = \frac{1}{2}\left[p^2 + k^2 - (p-k)^2\right]$ and continue

$$\text{numerator} = \left[\frac{1}{2} p^2 + \frac{1}{2} k^2 - \frac{1}{2} (p-k)^2 - k^2 \right]^2 = \frac{1}{4} \left[p^2 - k^2 - (p-k)^2 \right]^2$$
$$= \frac{1}{4} \left[\underbrace{p^4}_{(a)} + \underbrace{k^4}_{(b)} + \underbrace{(p-k)^4}_{(c)} - 2\underbrace{p^2 k^2}_{(d)} - 2\underbrace{p^2 (p-k)^2}_{(e)} + 2\underbrace{k^2 (p-k)^2}_{(f)} \right]. \quad \text{(D.20)}$$

To keep track of all the terms we will consider them separately. We will analyze each term with a generic denominator, and then choosing appropriate values for ξ and ξ' write down the full result. In the following we add a factor of i in the numerators, to comply with the definitions of a and b_0 functions, so we need to remember to add a $-i$ compensating factor in the final result.

(a)

$$p^4 \int \frac{d^D k}{(2\pi)^D} \frac{i\mu^\epsilon}{(k^2 - \xi M_W^2)\left[(p-k)^2 - \xi' M_W^2\right]} = p^4 b_0(p^2, \xi M_W, \xi' M_W). \quad \text{(D.21)}$$

(b)

$$\int \frac{d^D k}{(2\pi)^D} i\mu^\epsilon \frac{k^4}{(k^2 - \xi M_W^2)\left[(p-k)^2 - \xi' M_W^2\right]}$$
$$= \int \frac{d^D k}{(2\pi)^D} i\mu^\epsilon \frac{k^2 \left(k^2 - \xi M_W^2\right) + k^2 \xi M_W^2}{(k^2 - \xi M_W^2)\left[(p-k)^2 - \xi' M_W^2\right]}$$

$$= \int \frac{d^Dk}{(2\pi)^D} i\mu^\epsilon \frac{k^2}{[(p-k)^2 - \xi' M_W^2]} + \xi M_W^2 \int \frac{d^Dk}{(2\pi)^D} i\mu^\epsilon \frac{k^2}{(k^2 - \xi M_W^2)\,[(p-k)^2 - \xi' M_W^2]}.$$

In the first integral we change variables $l = k - p$, and proceed.

$$\begin{aligned}
&\int \frac{d^Dk}{(2\pi)^D} i\mu^\epsilon \frac{(l+p)^2}{l^2 - \xi' M_W^2} + \xi M_W^2 \int \frac{d^Dk}{(2\pi)^D} i\mu^\epsilon \frac{1}{[(p-k)^2 - \xi' M_W^2]} \\
&\quad + \xi^2 M_W^4 \int \frac{d^Dk}{(2\pi)^D} i\mu^\epsilon \frac{1}{(k^2 - \xi M_W^2)\,[(p-k)^2 - \xi' M_W^2]} \\
&= \int \frac{d^Dk}{(2\pi)^D} i\mu^\epsilon \frac{l^2 + lp + p^2}{l^2 - \xi' M_W^2} + \xi M_W^2 a(\xi' M_W) + \xi^2 M_W^4 b_0(p^2, \xi M_W, \xi' M_W).
\end{aligned} \tag{D.22}$$

The integral over lp vanishes, because it is an odd function of l, while the denominator is even. Continuing we get

$$\begin{aligned}
&\int \frac{d^Dk}{(2\pi)^D} i\mu^\epsilon + \left(p^2 + \xi' M_W^2\right) a(\xi' M_W) + \xi M_W^2 a(\xi' M_W) + \xi^2 M_W^4 b_0(p^2, \xi M_W, \xi' M_W) \\
&= \int \frac{d^Dk}{(2\pi)^D} i\mu^\epsilon + \left[p^2 + (\xi + \xi') M_W^2\right] a(\xi' M_W) + \xi^2 M_W^4 b_0(p^2, \xi M_W, \xi' M_W).
\end{aligned} \tag{D.23}$$

(c) It is easy to check, by changing the variables so that $l = k - p$, that the result of this part is the same as of the part above with the exchange $\xi \leftrightarrow \xi'$.

$$\begin{aligned}
&\int \frac{d^Dk}{(2\pi)^D} i\mu^\epsilon \frac{(p-k)^4}{(k^2 - \xi M_W^2)\,[(p-k)^2 - \xi' M_W^2]} \\
&= \int \frac{d^Dk}{(2\pi)^D} i\mu^\epsilon \frac{l^4}{[(p-l)^2 - \xi M_W^2]\,(l^2 - \xi' M_W^2)} \\
&= \int \frac{d^Dk}{(2\pi)^D} i\mu^\epsilon + \left[p^2 + (\xi + \xi') M_W^2\right] a(\xi M_W) + \xi'^2 M_W^4 b_0(p^2, \xi M_W, \xi' M_W).
\end{aligned} \tag{D.24}$$

(d)

$$\begin{aligned}
&p^2 \int \frac{d^Dk}{(2\pi)^D} i\mu^\epsilon \frac{k^2}{(k^2 - \xi M_W^2)\,[(p-k)^2 - \xi' M_W^2]} \\
&= p^2 \int \frac{d^Dk}{(2\pi)^D} i\mu^\epsilon \frac{k^2 - \xi M_W^2}{(k^2 - \xi M_W^2)\,[(p-k)^2 - \xi' M_W^2]} \\
&\quad + p^2 \xi M_W^2 \int \frac{d^Dk}{(2\pi)^D} i\mu^\epsilon \frac{1}{(k^2 - \xi M_W^2)\,[(p-k)^2 - \xi' M_W^2]} \\
&= p^2 \left[a(\xi' M_W) + \xi M_W^2 b_0(p^2, \xi M_W, \xi' M_W)\right].
\end{aligned} \tag{D.25}$$

(e) In the same way as in the point (c), it can be shown that the result of this point is the same as the result of (d) with the exchange $\xi \leftrightarrow \xi'$, namely

$$p^2 \int \frac{d^D k}{(2\pi)^D} i\mu^\epsilon \frac{(p-k)^2}{(k^2-\xi M_W^2)\left[(p-k)^2-\xi' M_W^2\right]} = p^2 \left[a(\xi M_W) + \xi' M_W^2 b_0(p^2, \xi M_W, \xi' M_W)\right]. \tag{D.26}$$

(f)

$$\begin{aligned}\int \frac{d^D k}{(2\pi)^D} i\mu^\epsilon \frac{k^2(p-k)^2}{(k^2-\xi M_W^2)\left[(p-k)^2-\xi' M_W^2\right]} &= \int \frac{d^D k}{(2\pi)^D} i\mu^\epsilon \frac{k^2\left[(p-k)^2-\xi' M_W^2\right]}{(k^2-\xi M_W^2)\left[(p-k)^2-\xi' M_W^2\right]} \\ &+ \xi' M_W^2 \int \frac{d^D k}{(2\pi)^D} i\mu^\epsilon \frac{k^2}{(k^2-\xi M_W^2)\left[(p-k)^2-\xi' M_W^2\right]}.\end{aligned}$$

The result for the second term can be obtained from the point (d). Thus we get

$$\begin{aligned}&\int \frac{d^D k}{(2\pi)^D} i\mu^\epsilon \frac{k^2-\xi M_W^2}{(k^2-\xi M_W^2)} + \xi M_W^2 \int \frac{d^D k}{(2\pi)^D} i\mu^\epsilon \frac{1}{(k^2-\xi M_W^2)} \\ &\quad + \xi' M_W^2 \left[a(\xi' M_W) + \xi M_W^2 b_0(p^2, \xi M_W, \xi' M_W)\right] \\ &= \int \frac{d^D k}{(2\pi)^D} i\mu^\epsilon + M_W^2 \left[\xi a(\xi M_W) + \xi' a(\xi' M_W) + \xi\xi' M_W^2 b_0(p^2, \xi M_W, \xi' M_W)\right].\end{aligned} \tag{D.27}$$

Now we can collect the contributions of the points (a)–(f) (Eqs. (D.21)–(D.27)).

$$\begin{aligned}&(a)+(b)+(c)-2(d)-2(e)+2(f) \\ &= p^4 b_0(p^2, \xi M_W, \xi' M_W) \\ &\quad + \int \frac{d^D k}{(2\pi)^D} i\mu^\epsilon + \left[p^2 + (\xi+\xi') M_W^2\right] a(\xi' M_W) + \xi^2 M_W^4 b_0(p^2, \xi M_W, \xi' M_W) \\ &\quad + \int \frac{d^D k}{(2\pi)^D} i\mu^\epsilon + \left[p^2 + (\xi+\xi') M_W^2\right] a(\xi M_W) + \xi'^2 M_W^4 b_0(p^2, \xi M_W, \xi' M_W) \\ &\quad - 2p^2 \left[a(\xi' M_W) + \xi M_W^2 b_0(p^2, \xi M_W, \xi' M_W)\right] \\ &\quad - 2p^2 \left[a(\xi M_W) + \xi' M_W^2 b_0(p^2, \xi M_W, \xi' M_W)\right] \\ &\quad + 2 \int \frac{d^D k}{(2\pi)^D} i\mu^\epsilon + 2M_W^2 \left[\xi a(\xi M_W) + \xi' a(\xi' M_W) + \xi\xi' M_W^2 b_0(p^2, \xi M_W, \xi' M_W)\right]\end{aligned}$$

$$
\begin{aligned}
&= 4\int \frac{d^Dk}{(2\pi)^D} i\mu^\epsilon + \left[-p^2 + (3\xi+\xi')M_W^2\right] a(\xi M_W) + \left[-p^2 + (3\xi'+\xi)M_W^2\right] a(\xi' M_W) \\
&\quad + \left[p^4 + M_W^4\left(\xi^2 + \xi'^2 + 2\xi\xi'\right) - 2p^2M_W^2(\xi+\xi')\right] b_0(p^2, \xi M_W, \xi' M_W) \\
&= 4\int \frac{d^Dk}{(2\pi)^D} i\mu^\epsilon + \left[-p^2 + (3\xi+\xi')M_W^2\right] a(\xi M_W) + \left[-p^2 + (3\xi'+\xi)M_W^2\right] a(\xi' M_W) \\
&\quad + \left[p^2 - M_W^2(\xi+\xi')\right]^2 b_0(p^2, \xi M_W, \xi' M_W).
\end{aligned}
$$

Therefore our integral with a generic denominator reads

$$
\begin{aligned}
&\frac{1}{4M_W^4}\int \frac{d^Dk}{(2\pi)^D} i\mu^\epsilon \frac{\left[p^2 - k^2 - (p-k)^2\right]^2}{(k^2 - \xi M_W^2)\left[(p-k)^2 - \xi' M_W^2\right]} \\
&\quad = \frac{1}{M_W^4}\int \frac{d^Dk}{(2\pi)^D} i\mu^\epsilon + \frac{1}{4M_W^4}\Big\{ \left[-p^2 + (3\xi+\xi')M_W^2\right] a(\xi M_W) \\
&\qquad + \left[-p^2 + (3\xi'+\xi)M_W^2\right] a(\xi' M_W) + \left[p^2 - M_W^2(\xi+\xi')\right]^2 b_0(p^2, \xi M_W, \xi' M_W)\Big\} \\
&\quad \equiv \mathcal{I}(\xi, \xi').
\end{aligned}
$$

To get the final result for $\int(\bigstar \cdot \spadesuit \cdot \clubsuit)$ we have to add terms with different values of ξ, ξ'. It is easy to see that $\mathcal{I}(\xi, \xi') = \mathcal{I}(\xi', \xi)$. Hence

$$
\begin{aligned}
&\int \frac{d^Dk}{(2\pi)^D} i\mu^\epsilon (\bigstar \cdot \spadesuit \cdot \clubsuit) = \mathcal{I}(0,0) + \mathcal{I}(1,1) - 2\mathcal{I}(1,0) \\
&\quad = \frac{1}{M_W^4}\int \frac{d^Dk}{(2\pi)^D} i\mu^\epsilon + \frac{p^4}{4M_W^4} b_0(p^2, 0, 0) \\
&\qquad + \frac{1}{M_W^4}\int \frac{d^Dk}{(2\pi)^D} i\mu^\epsilon + \frac{1}{4M_W^4}\left[2\left(-p^2 + 4M_W^2\right) a(M_W) + \left(p^2 - 2M_W^2\right)^2 b_0(p^2, M_W, M_W)\right] \\
&\qquad - \frac{2}{M_W^4}\int \frac{d^Dk}{(2\pi)^D} i\mu^\epsilon - \frac{1}{4M_W^4}\left[2(-p^2 + 3M_W^2) a(M_W) + 2\left(p^2 - M_W^2\right)^2 b_0(p^2, M_W, 0)\right].
\end{aligned}
$$

After simplifying we get

$$
\begin{aligned}
\int \frac{d^Dk}{(2\pi)^D} i\mu^\epsilon (\bigstar \cdot \spadesuit \cdot \clubsuit) = \frac{1}{4M_W^4}\Big[&2M_W^2 a(M_W) + p^4 b_0(p^2, 0, 0) \\
&+ \left(p^2 - 2M_W^2\right)^2 b_0(p^2, M_W, M_W) - 2\left(p^2 - M_W^2\right)^2 b_0(p^2, M_W, 0)\Big].
\end{aligned}
\tag{D.28}
$$

Eventually, we can collect all the contributions, Eqs. (D.18), (D.19), (D.28), and write down the final result for the (B) diagram.

$$
\begin{aligned}
(B) = &- ig^2\Big\{4M_W^2 b_0^b(p^2, M_W, M_W) - 2M_W^2 b_0(p^2, M_W, M_W) \\
&+ \frac{1}{4M_W^2}\Big[2M_W^2 a(M_W) + p^4 b_0(p^2, 0, 0) + \left(p^2 - 2M_W^2\right)^2 b_0(p^2, M_W, M_W) \\
&- 2\left(p^2 - M_W^2\right)^2 b_0(p^2, M_W, 0)\Big]\Big\}
\end{aligned}
$$

$$= -\frac{ig^2}{4M_W^2}\Big[2M_W^2 a(M_W) + p^4 b_0(p^2,0,0) - 2\left(p^2 - M_W^2\right)^2 b_0(p^2,M_W,0) + 16M_W^4 b_0^b(p^2,M_W,M_W) + \left(p^4 - 4p^2M_W^2 - 4M_W^4\right) b_0(p^2,M_W,M_W)\Big]. \tag{D.29}$$

The result for the diagram (E) will differ from the one above only by the coupling (see fig. D.2) and a symmetry factor of $\frac{1}{2}$. Therefore

$$(E) = -\frac{i\left(g^2+g'^2\right)}{8M_Z^2}\Big[2M_Z^2 a(M_Z) + p^4 b_0(p^2,0,0) - 2\left(p^2 - M_Z^2\right)^2 b_0(p^2,M_Z,0) + 16M_Z^4 b_0^b(p^2,M_Z,M_Z) + \left(p^4 - 4p^2M_Z^2 - 4M_Z^4\right) b_0(p^2,M_Z,M_Z)\Big]. \tag{D.30}$$

D.2.2.3 Diagrams (C) and (F)

The diagram (C) is easy to compute. If we assign a momentum k to the W circulating in the loop, and use the coupling from fig. D.4, we get the following expression

$$(C) = \frac{g^2}{2}\int \frac{d^Dk}{(2\pi)^D}\mu^\epsilon \frac{g_{\mu\nu}\left(g^{\mu\nu} - \frac{k^\mu k^\nu}{k^2}\right)}{k^2 - M_W^2} = -i\frac{g^2(D-1)}{2}\int \frac{d^Dk}{(2\pi)^D} i\mu^\epsilon \frac{1}{k^2 - M_W^2} = -i\frac{3g^2}{2}a^b(M_W). \tag{D.31}$$

The computation for the diagram (F) works exactly the same, up to the value of the coupling constant and the symmetry factor. The result reads

$$(F) = -i\frac{3\left(g^2+g'^2\right)}{4}a^b(M_Z). \tag{D.32}$$

D.2.2.4 Diagrams (G)

The diagrams (G) are proportional to the a function. The result for the h loop reads (with k being the momentum of h inside the loop)

$$-i\frac{3}{8}g^2\frac{M_h^2}{M_W^2}\int \frac{d^Dk}{(2\pi)^D} i\mu^\epsilon \frac{1}{k^2 - M_h^2} = -i\frac{3}{8}g^2\frac{M_h^2}{M_W^2}a(M_h).$$

The remaining diagrams are computed analogously, and the result reads

$$(G) = -i\left[\frac{3}{8}g^2\frac{M_h^2}{M_W^2}a(M_h) + \frac{g^2}{4}\frac{M_h^2}{M_W^2}a(M_{G^\pm}) + \frac{g^2}{8}\frac{M_h^2}{M_W^2}a(M_G)\right]. \tag{D.33}$$

D.2.2.5 Diagrams (H)

The contributions from the diagrams (H) are also very easy to compute since only scalar integrals are involved. The contributions from different scalars differ only by

the coupling constants and symmetry factors. The result reads

$$(H) = -i\left[\frac{g^2}{4}\frac{M_h^4}{M_W^2}b_0(p^2, M_{G^\pm}, M_{G^\pm}) + \frac{g^2}{8}\frac{M_h^4}{M_W^2}b_0(p^2, M_G, M_G) + \frac{9}{8}g^2\frac{M_h^4}{M_W^2}b_0(p^2, M_h, M_h)\right]. \tag{D.34}$$

D.2.2.6 Diagrams (I)

The contribution from fermions reads as follows (M_f is the mass of the fermion, and a color factor equal 3 is added)

$$\begin{aligned}
&\frac{3g^2}{4}\frac{M_f^2}{M_W^2}\int\frac{d^Dk}{(2\pi)^D}\mu^\epsilon(-1)\mathrm{Tr}\left[\frac{1}{\not k - M_f}\frac{1}{(\not k - \not p) - M_f^2}\right]\\
&= -\frac{3g^2}{4}\frac{M_f^2}{M_W^2}\int\frac{d^Dk}{(2\pi)^D}\mu^\epsilon\mathrm{Tr}\left\{\frac{k^2 - kp + m^2}{(k^2 - M_f^2)[(k-p)^2 - M_f^2]}\right\}.
\end{aligned}$$

Using Eq. (D.10) for pk, and taking $\mathrm{Tr}(\mathbb{I}) = 4$ we get

$$\begin{aligned}
&-3g^2\frac{M_f^2}{M_W^2}\int\frac{d^Dk}{(2\pi)^D}\mu^\epsilon\frac{k^2 - \frac{1}{2}k^2 - \frac{1}{2}p^2 + \frac{1}{2}(p-k)^2 + m^2}{(k^2 - M_f^2)[(k-p)^2 - M_f^2]}\\
&= -\frac{3g^2}{2}\frac{M_f^2}{M_W^2}\int\frac{d^Dk}{(2\pi)^D}\mu^\epsilon\frac{k^2 - p^2 + (p-k)^2 + 2m^2}{(k^2 - M_f^2)[(k-p)^2 - M_f^2]}\\
&= i\frac{3g^2}{2}\frac{M_f^2}{M_W^2}\int\frac{d^Dk}{(2\pi)^D}i\mu^\epsilon\frac{k^2 - M_f^2 + (p-k)^2 - M_f^2 - p^2 + 4m^2}{(k^2 - M_f^2)[(k-p)^2 - M_f^2]}\\
&= i\frac{3g^2}{2}\frac{M_f^2}{M_W^2}\left[2a(M_f) + (-p^2 + 4M_f^2)b_0(p^2, M_f, M_f)\right].
\end{aligned}$$

The final contribution is a sum of the expressions for t and b quarks (we neglect the light quarks)

$$\begin{aligned}
(I) = i\frac{3g^2}{2M_W^2}\big\{&M_t^2\left[2a(M_t) + (-p^2 + 4M_t^2)b_0(p^2, M_t, M_t)\right]\\
&+ M_b^2\left[2a(M_b) + (-p^2 + 4M_b^2)b_0(p^2, M_b, M_b)\right]\big\}.
\end{aligned} \tag{D.35}$$

D.2.2.7 Higgs self-energy

Now we can collect all the contributions computed in the previous sections. The computation is rather lengthy but we display it for the sake of completeness.

$$\begin{aligned}
\Sigma(p^2) = \frac{g^2}{2M_W^2}\Big[&M_W^2 a\left(M_{G^\pm}\right) + \left(-p^2 - M_W^2 + M_{G^\pm}^2\right)a(M_W)\\
&- (p^2 + M_{G^\pm}^2)^2 b_0\left(p^2, 0, M_{G^\pm}\right) + \left(p^2 + M_{G^\pm}^2 - M_W^2\right)^2 b_0(p^2, M_W, M_{G^\pm})\Big]
\end{aligned}$$

$$
\begin{aligned}
&+\frac{g^2+g'^2}{4M_Z^2}\Big[M_Z^2 a\left(M_G\right)+\left(-p^2-M_Z^2+M_G^2\right)a(M_Z)\\
&\quad-(p^2+M_G^2)^2 b_0\left(p^2,0,M_G\right)+\left(p^2+M_G^2-M_Z^2\right)^2 b_0(p^2,M_Z,M_G)\Big]\\
&+\frac{g^2}{4M_W^2}\Big[2M_W^2 a(M_W)+p^4 b_0(p^2,0,0)-2\left(p^2-M_W^2\right)^2 b_0(p^2,M_W,0)\\
&\quad+16M_W^4 b_0^b(p^2,M_W,M_W)+\left(p^4-4p^2M_W^2-4M_W^4\right)b_0(p^2,M_W,M_W)\Big]\\
&+\frac{(g^2+g'^2)}{8M_Z^2}\Big[2M_Z^2 a(M_Z)+p^4 b_0(p^2,0,0)-2\left(p^2-M_Z^2\right)^2 b_0(p^2,M_Z,0)\\
&\quad+16M_Z^4 b_0^b(p^2,M_Z,M_Z)+\left(p^4-4p^2M_Z^2-4M_Z^4\right)b_0(p^2,M_Z,M_Z)\Big]\\
&+\frac{3g^2}{2}a^b(M_W)\\
&+\frac{3\left(g^2+g'^2\right)}{4}a^b(M_Z)\\
&+\frac{3}{8}g^2\frac{M_h^2}{M_W^2}a(M_h)+\frac{g^2}{4}\frac{M_h^2}{M_W^2}a(M_{G^\pm})+\frac{g^2}{8}\frac{M_h^2}{M_W^2}a(M_G)\\
&+\frac{9}{8}g^2\frac{M_h^4}{M_W^2}b_0(p^2,M_h,M_h)+\frac{g^2}{4}\frac{M_h^4}{M_W^2}b_0(p^2,M_{G^\pm},M_{G^\pm})+\frac{g^2}{8}\frac{M_h^4}{M_W^2}b_0(p^2,M_G,M_G)\\
&-\frac{3g^2}{2M_W^2}M_t^2\left[2a(M_t)+(-p^2+4M_t^2)b_0(p^2,M_t,M_t)\right]\\
&-\frac{3g^2}{2M_W^2}M_b^2\left[2a(M_b)+(-p^2+4M_b^2)b_0(p^2,M_b,M_b)\right]\\
=&\frac{g^2}{2M_W^2}\Big[M_W^2 a\left(M_{G^\pm}\right)+\left(-p^2+M_{G^\pm}^2\right)a(M_W)\\
&\quad-(p^2+M_{G^\pm}^2)^2 b_0\left(p^2,0,M_{G^\pm}\right)+\left(p^2+M_{G^\pm}^2-M_W^2\right)^2 b_0(p^2,M_W,M_{G^\pm})\Big]\\
&+\frac{g^2+g'^2}{4M_Z^2}\Big[M_Z^2 a\left(M_G\right)+\left(-p^2+M_G^2\right)a(M_Z)\\
&\quad-(p^2+M_G^2)^2 b_0\left(p^2,0,M_G\right)+\left(p^2+M_G^2-M_Z^2\right)^2 b_0(p^2,M_Z,M_G)\Big]\\
&+\frac{g^2}{4M_W^2}\Big[p^4 b_0(p^2,0,0)-2\left(p^2-M_W^2\right)^2 b_0(p^2,M_W,0)\\
&\quad+16M_W^4 b_0^b(p^2,M_W,M_W)+\left(p^4-4p^2M_W^2-4M_W^4\right)b_0(p^2,M_W,M_W)\Big]\\
&+\frac{(g^2+g'^2)}{8M_Z^2}\Big[p^4 b_0(p^2,0,0)-2\left(p^2-M_Z^2\right)^2 b_0(p^2,M_Z,0)\\
&\quad+16M_Z^4 b_0^b(p^2,M_Z,M_Z)+\left(p^4-4p^2M_Z^2-4M_Z^4\right)b_0(p^2,M_Z,M_Z)\Big]\\
&+\frac{3g^2}{2}a^b(M_W)
\end{aligned}
$$

$$
\begin{aligned}
&+\frac{3\left(g^2+g'^2\right)}{4}a^b(M_Z)\\
&+\frac{3}{2}\lambda_1 a(M_h)+\lambda_1 a(M_{G^\pm})+\frac{1}{2}\lambda_1 a(M_G)\\
&+\frac{9}{2}\lambda_1^2 v^2 b_0(p^2,M_h,M_h)+\lambda_1^2 v^2 b_0(p^2,M_{G^\pm},M_{G^\pm})+\frac{1}{2}\lambda_1^2 v^2 b_0(p^2,M_G,M_G)\\
&-\frac{3g^2}{2M_W^2}M_t^2\left[2a(M_t)+(-p^2+4M_t^2)b_0(p^2,M_t,M_t)\right]\\
&-\frac{3g^2}{2M_W^2}M_b^2\left[2a(M_b)+(-p^2+4M_b^2)b_0(p^2,M_b,M_b)\right].
\end{aligned}
$$

D.3 Higgs self-energy and tadpoles in the IDM

Now we turn to the computations of one-loop tadpoles and self-energy of the Higgs boson within the IDM. All the diagrams that were present in the SM case will be also present here. The only new contributions that have to be taken into account are purely scalar loops, no other new couplings are present.

From the potential (2.1) couplings between the scalar particles can be read off after a symmetry breaking VEV is introduced. The quartic and trilinear scalar couplings are listed below, in tables D.1 and D.2.

$G^+G^+G^-G^-$	$2\lambda_1$,	H^+H^-HH	λ_2,	G^-H^+Ah	$\frac{i}{2}(-\lambda_4+\lambda_5)$,
$hhGG$	λ_1,	G^+G^-HH	λ_3,	H^-G^+hA	$\frac{i}{2}(\lambda_4-\lambda_5)$,
$GGGG$	$3\lambda_1$,	hhH^+H^-	λ_3,	H^-G^+GH	$\frac{i}{2}(-\lambda_4+\lambda_5)$,
G^+G^-GG	λ_1,	GGH^+H^-	λ_3,	G^-H^+GH	$\frac{i}{2}(\lambda_4-\lambda_5)$,
$hhhh$	$3\lambda_1$,	G^+G^-AA	λ_3,	H^-G^+hH	$\frac{1}{2}(\lambda_4+\lambda_5)$,
G^+G^-hh	λ_1,	$H^-H^-G^+G^+$	$2\lambda_5$,	H^-G^+GA	$\frac{1}{2}(\lambda_4+\lambda_5)$,
$H^+H^+H^-H^-$	$2\lambda_2$,	$G^-G^-H^+H^+$	$2\lambda_5$,	$hhHH$	$\lambda_3+\lambda_4+\lambda_5$,
$HHAA$	λ_2,	$hGAH$	λ_5,	$AAGG$	$\lambda_3+\lambda_4+\lambda_5$,
$HHHH$	$3\lambda_2$,	$G^+G^-H^+H^-$	$\lambda_3+\lambda_4$,	$GGHH$	$\lambda_3+\lambda_4-\lambda_5$,
$AAAA$	$3\lambda_2$,	G^-H^+AG	$\frac{1}{2}(\lambda_4+\lambda_5)$,	$hhAA$	$\lambda_3+\lambda_4-\lambda_5$.
H^+H^-AA	λ_2,	G^-H^+hH	$\frac{1}{2}(\lambda_4+\lambda_5)$,		

Table D.1: Quartic couplings between the scalars. All should be multiplied by a factor $-i$.

hGG	$\lambda_1 v$	hhh	$3\lambda_1 v$	G^+G^-h	$\lambda_1 v$
GAH	$\lambda_5 v$	hH^+H^-	$\lambda_3 v$	G^-H^+H	$\frac{1}{2}(\lambda_4+\lambda_5)v$
G^-H^+A	$\frac{i}{2}(-\lambda_4+\lambda_5)v$	$H-G+A$	$\frac{i}{2}(\lambda_4-\lambda_5)v$	H^-G^+H	$\frac{1}{2}(\lambda_4+\lambda_5)v$
hHH	$(\lambda_3+\lambda_4+\lambda_5)v$	hAA	$(\lambda_3+\lambda_4-\lambda_5)v$		

Table D.2: Trilinear couplings between the scalars. All should be multiplied by a factor $-i$.

D.3.1 Higgs tadpole

The only new contribution to the Higgs tadpole will be the scalar loops depicted in fig. D.5. They are easily computable, and the result reads

$$-i\mathcal{T}_{\text{IDM}} = -i\left[\lambda_3 a(M_{H^\pm}) + \frac{1}{2}\lambda_{345} a(M_H) + \frac{1}{2}\lambda_{345}^- a(M_A)\right] v.$$

The total tadpole is a sum of SM and IDM contributions

$$\mathcal{T} = \mathcal{T}_{\text{SM}} + \mathcal{T}_{\text{IDM}}.$$

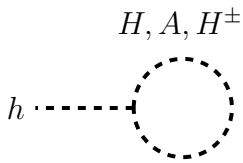

Figure D.5: The Higgs tadpole diagrams in the IDM. In addition there are the diagrams present also in the SM, see fig. D.1

D.3.2 Higgs self-energy

The non-SM contributions to the Higgs self-energy are presented in fig. D.6. There are two types of diagrams, but since only scalar particles are present, they are all easy to compute.

The contribution of the (A)-type diagrams reads

$$(A) = -i\left[\lambda_3 a(M_{H^\pm}) + \frac{1}{2}\lambda_{345} a(M_H) + \frac{1}{2}\lambda_{345}^- a(M_A)\right],$$

and the contributions of the (B)-type diagrams give

$$\begin{aligned}(B) = -i\Bigg[&(\lambda_3 v)^2 b_0\left(p^2, M_{H^\pm}, M_{H^\pm}\right) + \frac{1}{2}(\lambda_{345} v)^2 b_0\left(p^2, M_H, M_H\right) \\ &+ \frac{1}{2}(\lambda_{345}^- v)^2 b_0\left(p^2, M_A, M_A\right)\Bigg].\end{aligned} \tag{D.36}$$

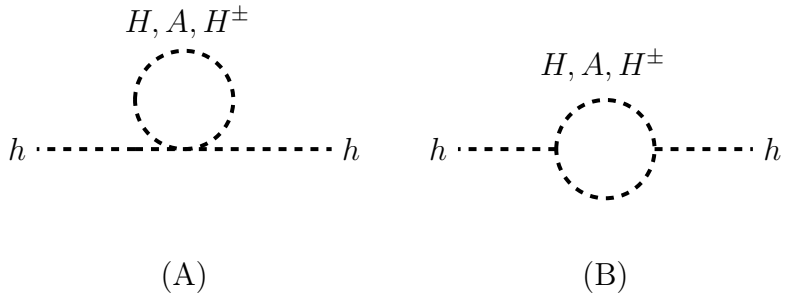

Figure D.6: Non-SM contributions to the Higgs self-energy in the IDM.

Once more, the Higgs self-energy is the sum of the SM and the IDM terms

$$\Sigma = \Sigma_{\text{SM}} + \Sigma_{\text{IDM}} = \Sigma_{\text{SM}} + i(A) + i(B).$$

D.4 Self-energies of the inert scalars and the Goldstone bosons

For the computation of the self-energies of the remaining scalars we will need to know the couplings between them and the gauge bosons. These couplings are listed in figs. D.7 and D.8 (all the following figures can be found in the end of this appendix). All the momenta should be assumed to be incoming. The results for the dark scalars can be written down with the use of the computations done for the Higgs self-energy, and knowing the list of couplings. Additional complications will appear for the Goldstone bosons.

D.4.1 H

The diagrams contributing to the self-energy of H are listed in fig. D.9. The letters are assigned to different types of diagrams such that diagrams of the same type present in the Higgs self-energy have the same label. There are no fermionic contributions, nor diagrams with two gauge propagators. The result reads

$$\begin{aligned}
-i\Sigma_H = -i\Bigg\{ & \frac{g^2}{2M_W^2}\left[M_W^2 a\left(M_{H^\pm}\right) + \left(-p^2 - M_W^2 + M_{H^\pm}^2\right) a(M_W)\right. \\
& - (p^2 - M_{H^\pm}^2)^2 b_0\left(p^2, 0, M_{H^\pm}\right) \\
& \left. + \left(p^4 + M_{H^\pm}^4 + M_W^4 - 2p^2 M_W^2 - 2p^2 M_{H^\pm}^2 - 2M_{H^\pm}^2 M_W^2\right) b_0\left(p^2, M_W, M_{H^\pm}\right)\right] \\
& + \frac{3g^2}{2} a^b(M_W)
\end{aligned}$$

$$
\begin{aligned}
&+\frac{g^2+g'^2}{4M_Z^2}\left[M_Z^2 a\left(M_A\right)+\left(-p^2-M_Z^2+M_A^2\right)a(M_Z)\right.\\
&\quad-(p^2-M_A^2)^2 b_0\left(p^2,0,M_A\right)\\
&\quad\left.+\left(p^4+M_A^4+M_Z^4-2p^2M_A^2-2p^2M_Z^2-2M_A^2M_Z^2\right)b_0\left(p^2,M_Z,M_A\right)\right]\\
&+\frac{3}{4}\frac{g^2}{\cos^2\theta_W}a^b(M_Z)\\
&+\frac{3}{2}\lambda_2 a(M_H)+\frac{1}{2}\lambda_2 a(M_A)+\lambda_2 a(M_{H^\pm})\\
&+\lambda_3 a(M_{G^\pm})+\frac{1}{2}\lambda_{345}a(M_h)+\frac{1}{2}\lambda_{345}^- a\ (M_G)\\
&\left.+\lambda_5^2 v^2 b_0(p^2,M_A,M_G)+\lambda_{345}^2 v^2 b_0(p^2,M_H,M_h)+\frac{1}{2}\lambda_{45}^2 v^2 b_0(p^2,M_{H^\pm},M_{G^\pm})\right\}.
\end{aligned}
$$

D.4.2 A

The results are very similar for the A scalar. The diagrams contributing to the self-energy of A are shown in fig. D.10, and the result for the self-energy reads

$$
\begin{aligned}
-i\Sigma_A=-i\Big\{&\frac{g^2}{2M_W^2}\left[M_W^2 a\left(M_{H^\pm}\right)+\left(-p^2-M_W^2+M_{H^\pm}^2\right)a(M_W)\right.\\
&\quad-(p^2-M_{H^\pm}^2)^2 b_0\left(p^2,0,M_{H^\pm}\right)\\
&\quad\left.+\left(p^4+M_{H^\pm}^4+M_W^4-2p^2M_{H^\pm}^2-2p^2M_W^2-2M_{H^\pm}^2M_W^2\right)b_0(p^2,M_W,M_{H^\pm})\right]\\
&+\frac{3g^2}{2}a^b(M_W)\\
&+\frac{g^2+g'^2}{4M_Z^2}\left[M_Z^2 a\left(M_H\right)+\left(-p^2-M_Z^2+M_H^2\right)a(M_Z)\right.\\
&\quad-(p^2-M_H^2)^2 b_0\left(p^2,0,M_H\right)\\
&\quad\left.+\left(p^4+M_H^4+M_Z^4-2p^2M_H^2-2p^2M_Z^2-2M_H^2M_Z^2\right)b_0(p^2,M_Z,M_H)\right]\\
&+\frac{3}{4}\frac{g^2}{\cos^2\theta_W}a^b(M_Z)\\
&+\frac{1}{2}\lambda_2 a(M_H)+\frac{3}{2}\lambda_2 a(M_A)+\lambda_2 a(M_{H^\pm})\\
&+\lambda_3 a\ (M_{G^\pm})+\frac{1}{2}\lambda_{345}a(M_G)+\frac{1}{2}\lambda_{345}^- a(M_h)\\
&+\lambda_5^2 v^2 b_0(p^2,M_G,M_H)+\frac{1}{2}(\lambda_5-\lambda_4)^2 v^2 b_0(p^2,M_{G^\pm},M_{H^\pm})\\
&+(\lambda_{345}^-)^2 v^2 b_0(p^2,M_h,M_A)\Big\}.
\end{aligned}
$$

D.4.3 $H^\pm$

The $H^\pm$ scalar has more contributions to the self-energy than the neutral inert scalars since it couples to the photon. The relevant diagrams are shown in fig. D.11.

The contribution of the (C') diagram is 0, since $a(0) = 0$. The diagram with one photonic internal line is computed with a regulator mass M_γ, which is then taken to zero. The limit $M_\gamma = 0$ needs to be taken with care. We use a similar strategy to the one used in ref. [205, 206], and this way no infrared singularities arise.

$$
\begin{aligned}
-i\Sigma_{H^\pm} = -i\Big\{ & e^2 \left[3a(M_{H^\pm}) - 3(p^2 + M_{H^\pm}^2) b_0(p^2, M_{H^\pm}, 0) - 2p^2\right] \\
& + \frac{g^2}{4M_W^2} \left[M_W^2 a\left(M_H\right) + \left(-p^2 - M_W^2 + M_H^2\right) a(M_W)\right. \\
& \quad - (p^2 - M_H^2)^2 b_0\left(p^2, 0, M_H\right) \\
& \quad \left. + \left(p^4 + M_H^4 + 2M_W^4 - 2p^2 M_H^2 - 2p^2 M_W^2 - 2M_H^2 M_W^2\right) b_0(p^2, M_W, M_H)\right] \\
& + \frac{g^2}{4M_W^2} \left[M_W^2 a\left(M_A\right) + \left(-p^2 - M_W^2 + M_A^2\right) a(M_W)\right. \\
& \quad - (p^2 - M_A^2)^2 b_0\left(p^2, 0, M_A\right) \\
& \quad \left. + \left(p^4 + M_A^4 + M_W^4 - 2p^2 M_A^2 - 2p^2 M_W^2 - 2M_A^2 M_W^2\right) b_0(p^2, M_W, M_A)\right] \\
& + \frac{3g^2}{2} a^b(M_W) \\
& + \frac{e^2 \cot^2 2\theta_W}{M_Z^2} \left[M_Z^2 a\left(M_{H^\pm}\right) + \left(-p^2 - M_Z^2 + M_{H^\pm}^2\right) a(M_Z)\right. \\
& \quad - (p^2 - M_{H^\pm}^2)^2 b_0\left(p^2, 0, M_{H^\pm}\right) \\
& \quad \left. + \left(p^4 + M_{H^\pm}^4 + M_Z^4 - 2p^2 M_{H^\pm}^2 - 2p^2 M_Z^2 - 2M_{H^\pm}^2 M_Z^2\right) b_0(p^2, M_Z, M_{H^\pm})\right] \\
& + \frac{3}{4} \frac{g^2 \cos^2 2\theta_W}{\cos^2 \theta_W} a^b(M_Z) \\
& + 2\lambda_2 a(M_{H^\pm}) + \frac{1}{2}\lambda_2 a(M_A) + \frac{1}{2}\lambda_2 a(M_H) \\
& + \frac{1}{2}\lambda_3 a(M_h) + \frac{1}{2}\lambda_3 a(M_G) + \lambda_{34} a(M_{G^\pm}) \\
& + \frac{1}{4}(\lambda_5 - \lambda_4)^2 v^2 b_0(p^2, M_G^\pm, M_A) + \lambda_3^2 v^2 b_0(p^2, M_h, M_{H^\pm}) \\
& + \frac{1}{4}\lambda_{45}^2 v^2 b_0(p^2, M_{G^\pm}, M_H)\Big\}.
\end{aligned}
$$

D.4.4 G

The diagrams contributing to G self-energy are listed in fig. D.12. G couples to fermions, contrary to the inert scalars (the coupling to fermions is taken from Ref. [225]). The result for the self-energy reads

$$
\begin{aligned}
-i\Sigma_G = -i\Big\{ & \frac{g^2}{2M_W^2} \left[M_W^2 a(M_{G^\pm}) + \left(-p^2 - M_W^2 + M_{G^\pm}^2\right) a(M_W)\right. \\
& \quad - (p^2 - M_{G^\pm}^2)^2 b_0(p^2, 0, M_{G^\pm}) \\
& \quad \left. + \left(p^4 + M_{G^\pm}^4 + M_W^4 - 2p^2 M_{G^\pm}^2 - 2p^2 M_W^2 - 2M_{G^\pm} M_W^2\right) b_0(p^2, M_W, M_{G^\pm})\right]
\end{aligned}
$$

$$
\begin{aligned}
&+ \frac{3g^2}{2} a^b(M_W) \\
&+ \frac{g^2+g'^2}{4M_Z^2}\left[M_Z^2 a\left(M_h\right) + \left(-p^2 - M_Z^2 + M_h^2\right) a(M_Z) - (p^2 - M_h^2)^2 b_0\left(p^2, 0, M_h\right)\right. \\
&\quad \left. + \left(p^4 + M_h^4 + M_Z^4 - 2p^2 M_h^2 - 2p^2 M_Z^2 - 2M_h^2 M_Z^2\right) b_0(p^2, M_Z, M_h)\right] \\
&+ \frac{3}{4}\frac{g^2}{\cos^2\theta_W} a^b(M_Z) \\
&+ \frac{1}{2}\lambda_1 a(M_h) + \frac{3}{2}\lambda_1 a(M_G) + \lambda_1 a(M_{G^\pm}) \\
&+ \frac{1}{2}\lambda_{345} a(M_A) + \frac{1}{2}\lambda_{345}^- a(M_H) + \lambda_3 a(M_{H^\pm}) \\
&+ \lambda_1^2 v^2 b_0(p^2, M_G, M_h) + \lambda_5^2 v^2 b_0(p^2, M_H, M_A) \\
&+ 3y_f^2\left[-2a(m_f) + p^2 b_0(p^2, m_f, m_f)\right] \Bigg\}.
\end{aligned}
$$

D.4.5 $G^\pm$

The diagrams relevant for the $G^\pm$ self-energy are shown in figs. D.13 and D.14. There appear the (B)-type diagrams with two distinct bosonic lines in the loop. Thus, the computation is more involved than in the SM case, where the bosons in the loop were of the same kind. However, we do not present the full derivation here because it goes along the same lines as in the SM case. The (B") diagram has to be computed with a regulator mass of the photon, and then the limit $M_\gamma \to 0$ must be taken [205, 206]. The result reads (the contribution from the diagram (C') vanishes, the coupling to fermions is taken from Ref. [225])

$$
\begin{aligned}
-i\Sigma_{G^\pm} = -i\Bigg\{ & e^2\left[3a(M_{G^\pm}) - 3(p^2 + M_{G^\pm}^2) b_0(p^2, M_{G^\pm}, 0) - 2p^2\right] \\
&+ \frac{g^2}{4M_W^2}\left[M_W^2 a\left(M_h\right) + \left(-p^2 - M_W^2 + M_h^2\right) a(M_W)\right. \\
&\quad - (p^2 - M_h^2)^2 b_0\left(p^2, 0, M_h\right) \\
&\quad \left. + \left(p^4 + M_h^4 + M_W^4 - 2p^2 M_h^2 - 2p^2 M_W^2 - 2M_h^2 M_W^2\right) b_0(p^2, M_W, M_h)\right] \\
&+ \frac{g^2}{4M_W^2}\left[M_W^2 a\left(M_G\right) + \left(-p^2 - M_W^2 + M_G^2\right) a(M_W)\right. \\
&\quad - (p^2 - M_G^2)^2 b_0\left(p^2, 0, M_G\right) \\
&\quad \left. + \left(p^4 + M_G^4 + M_W^4 - 2p^2 M_G^2 - 2p^2 M_W^2 - 2M_G^2 M_W^2\right) b_0(p^2, M_W, M_G)\right] \\
&+ \frac{3g^2}{2} a^b(M_W)
\end{aligned}
$$

$$
\begin{aligned}
&+\frac{g^2\sin^4\theta_W}{4M_W^2}\left[16M_Z^2M_W^2b_0^b(p^2,M_Z,M_W)\right.\\
&\quad+(-8M_W^2M_Z^2+(p^2-M_Z^2-M_W^2)^2)b_0(p^2,M_Z,M_W)\\
&\quad-(p^2-M_W^2)^2b_0(p^2,0,M_W)-(p^2-M_Z^2)^2b_0(p^2,M_Z,0)+p^4b_0(p^2,0,0)\\
&\quad\left.+M_Z^2a(M_W)+M_W^2a(M_Z)\right]\\
&+\frac{e^2}{4}\left[16M_W^2b_0^b(p^2,0,M_W)+3p^2b_0(p^2,0,0)\right.\\
&\quad\left.-(3p^2+7M_W^2)b_0(p^2,0,M_W)+3a(M_W)\right]\\
&+\frac{g^2}{4M_Z^2}\frac{\cos^2 2\theta_W}{\cos^2\theta_W}\left[M_Z^2a\left(M_{G^\pm}\right)+\left(-p^2-M_Z^2+M_{G^\pm}^2\right)a(M_Z)\right.\\
&\quad-(p^2-M_{G^\pm}^2)^2b_0\left(p^2,0,M_{G^\pm}\right)\\
&\quad\left.+\left(p^4+M_{G^\pm}^4+M_Z^4-2p^2M_{G^\pm}^2-2p^2M_Z^2-2M_{G^\pm}^2M_Z^2\right)b_0(p^2,M_Z,M_{G^\pm})\right]\\
&+\frac{3}{4}\frac{g^2\cos^2 2\theta_W}{\cos^2\theta_W}a^b(M_Z)\\
&+2\lambda_1a(M_{G^\pm})+\frac{1}{2}\lambda_1a(M_G)+\frac{1}{2}\lambda_1a(M_h)\\
&+\frac{1}{2}\lambda_3a(M_H)+\frac{1}{2}\lambda_3a(M_A)+(\lambda_3+\lambda_4)a(M_{H^\pm})\\
&+\frac{1}{4}(\lambda_5-\lambda_4)^2v^2b_0(p^2,M_{H^\pm},M_A)+\lambda_1^2v^2b_0(p^2,M_{G^\pm},M_h)\\
&+\frac{1}{4}(\lambda_4+\lambda_5)^2v^2b_0(p^2,M_{H^\pm},M_H)\\
&+\frac{3g^2}{2M_W^2}\left[\left((m_t^2+m_b^2)p^2-(m_t^2-m_b^2)^2\right)b_0(p^2,m_t,m_b)\right.\\
&\quad\left.\left.-(m_t^2+m_b^2)\left(a(m_t)+a(m_b)\right)\right]\right\}.
\end{aligned}
$$

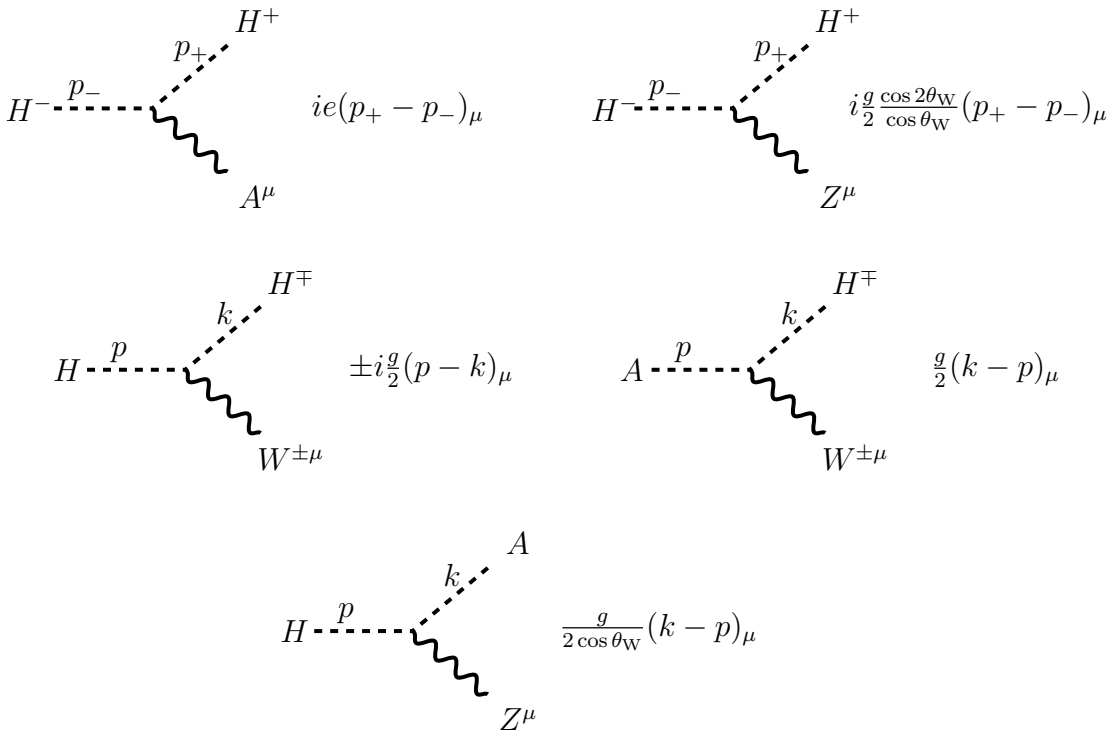

Figure D.7: Triple scalar-gauge coulings in the IDM. All momenta are incoming.

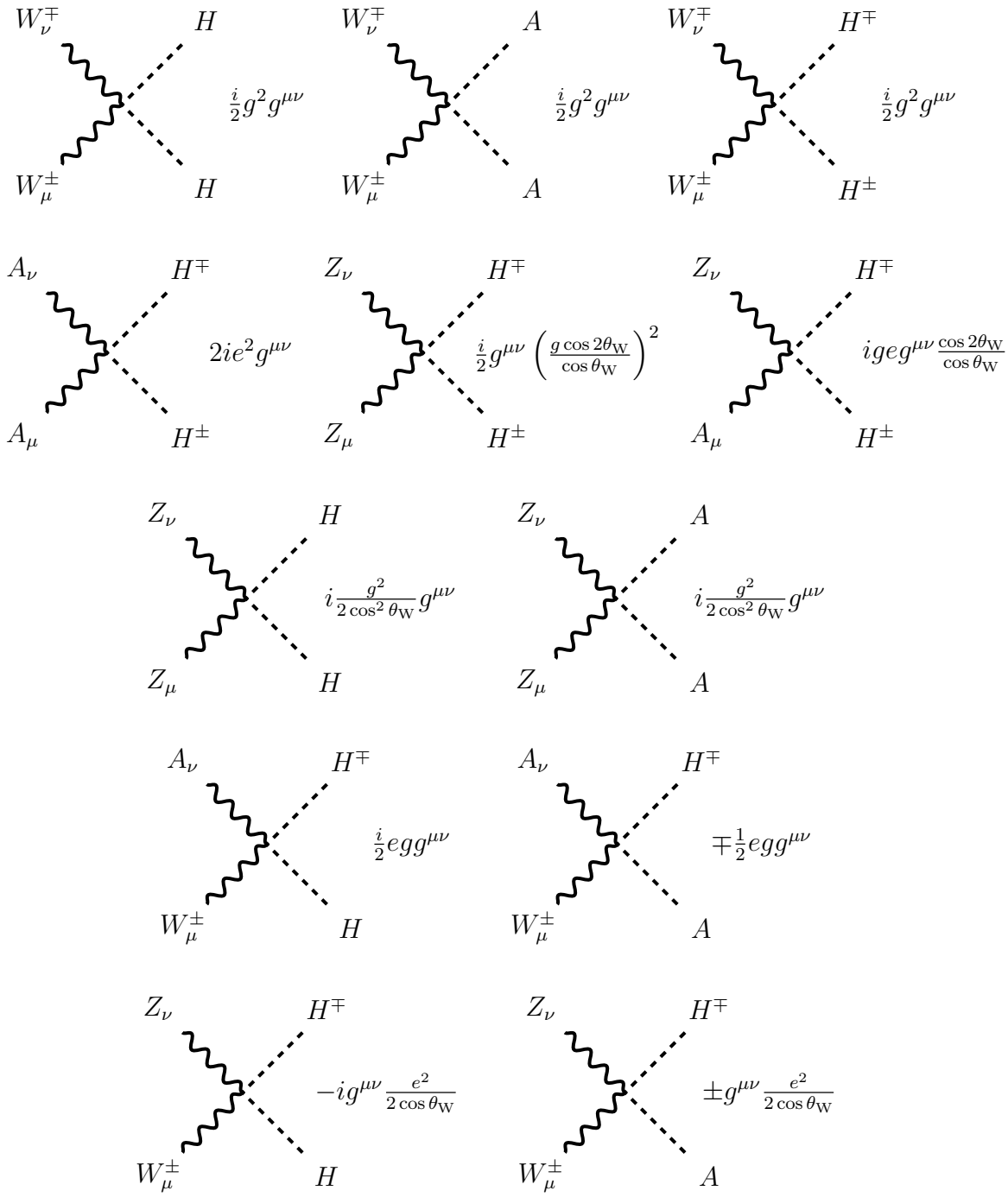

Figure D.8: Quartic scalar-gauge couplings in the IDM.

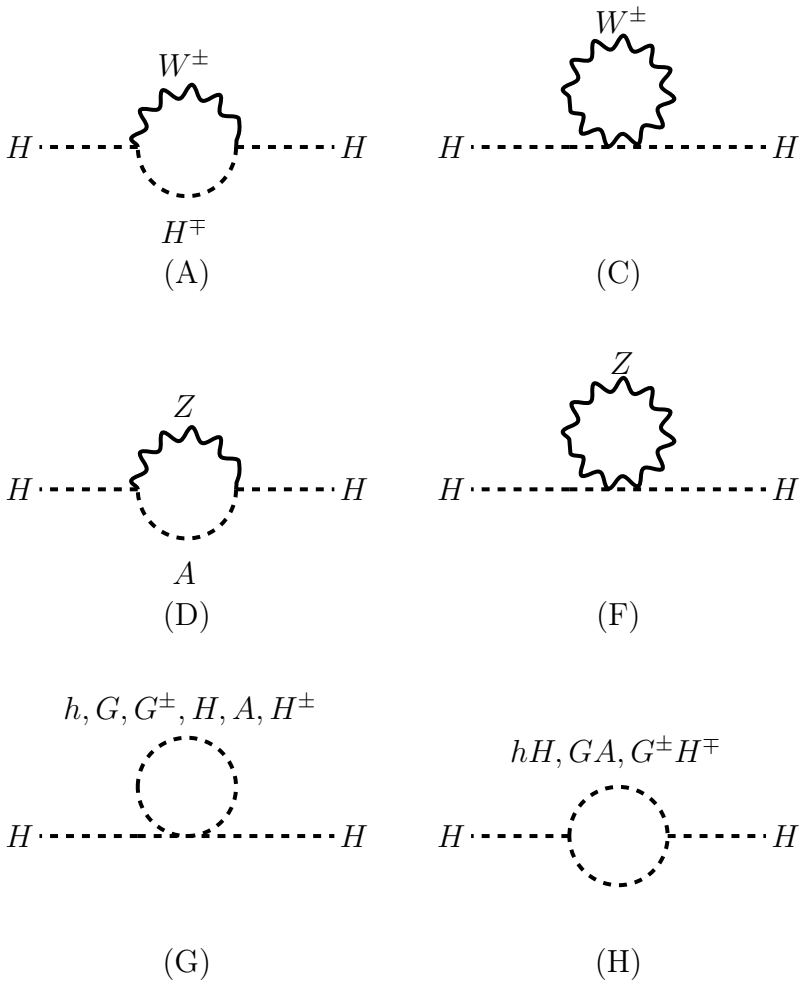

Figure D.9: Diagrams contributing to the self-energy of H.

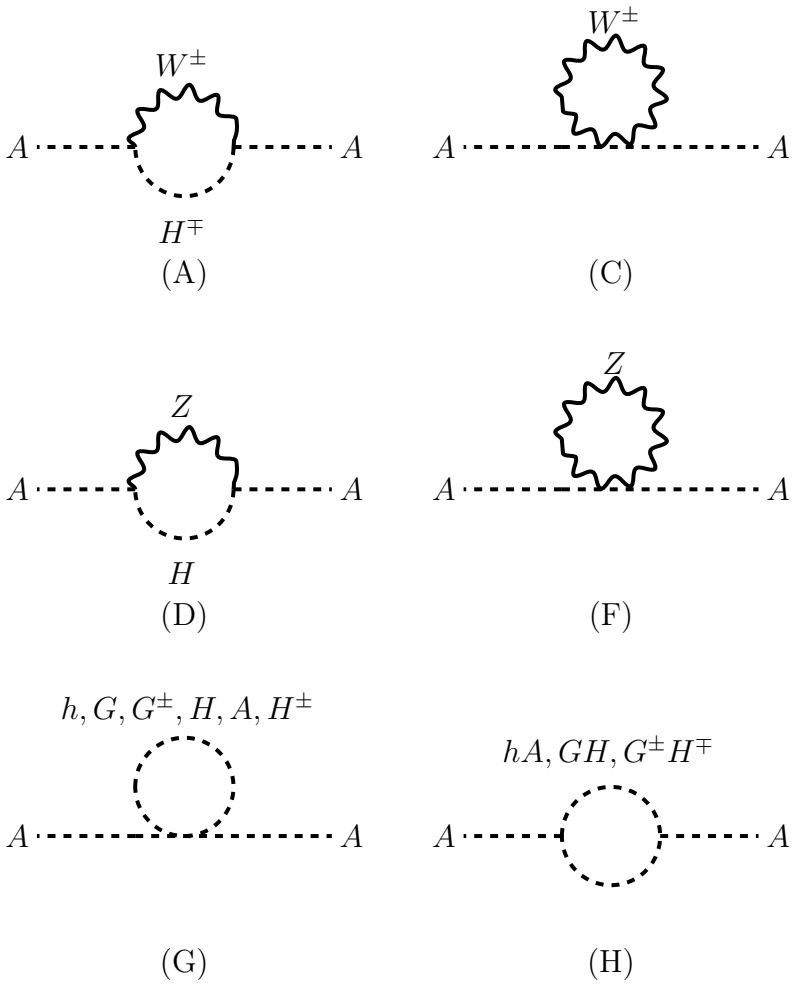

Figure D.10: Diagrams contributing to the self-energy of A.

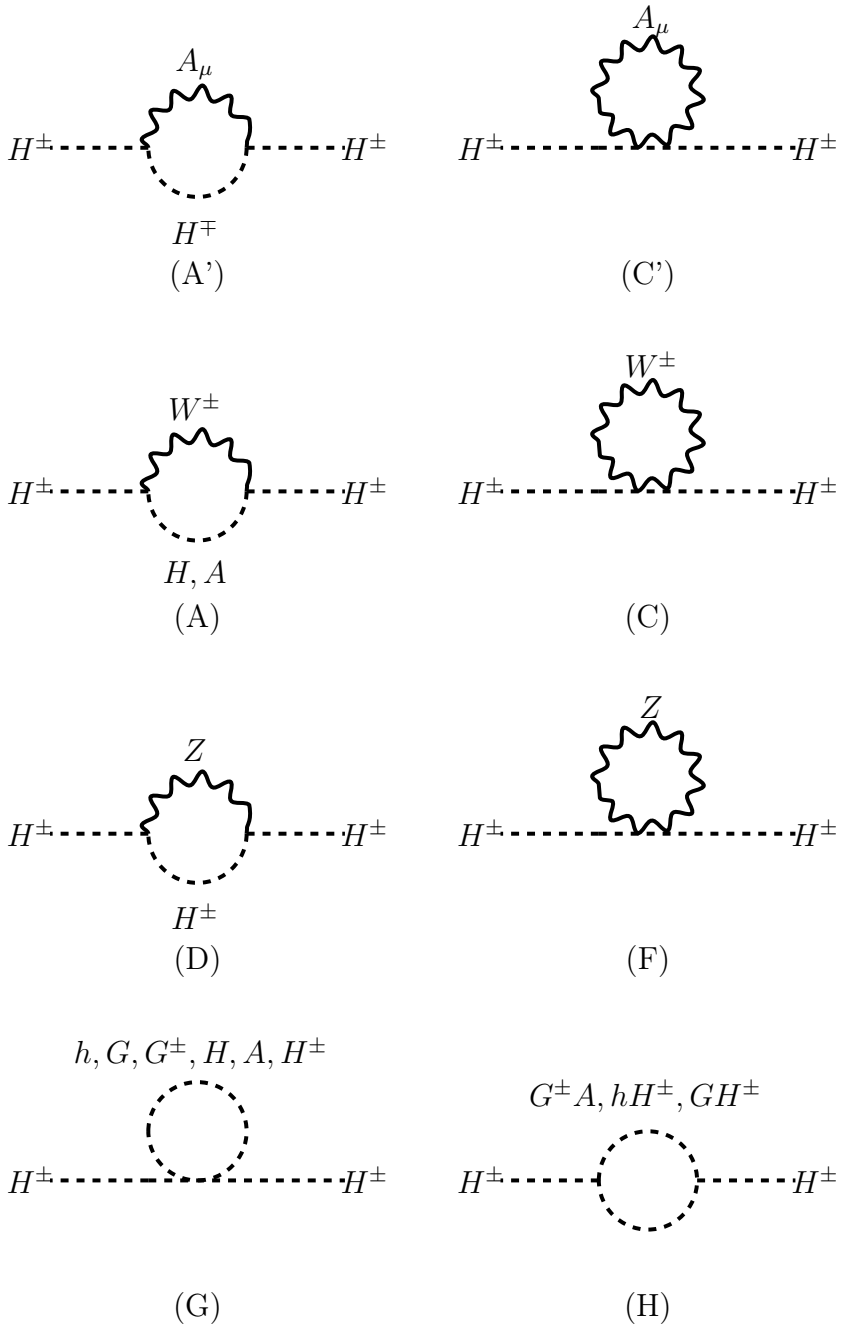

Figure D.11: Diagrams contributing to the self-energy of $H^\pm$.

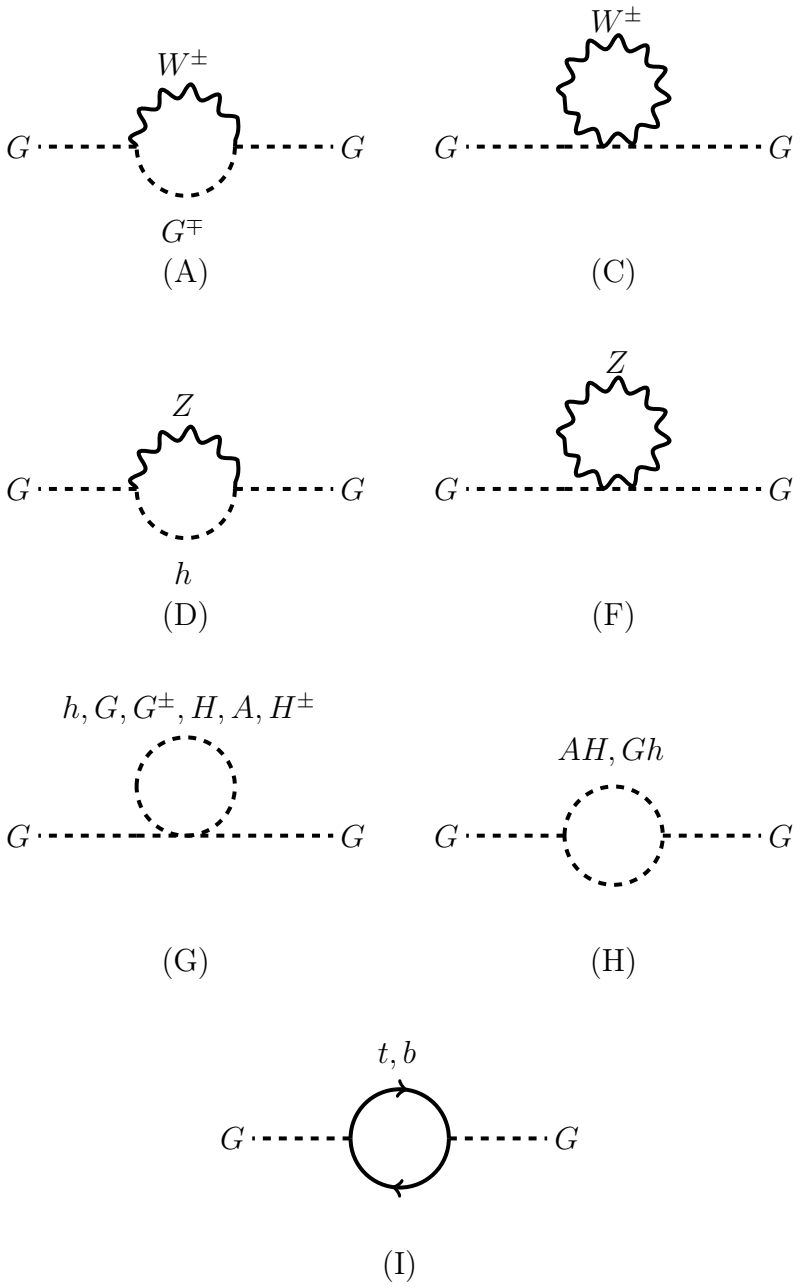

Figure D.12: Diagrams contributing to the self-energy of G.

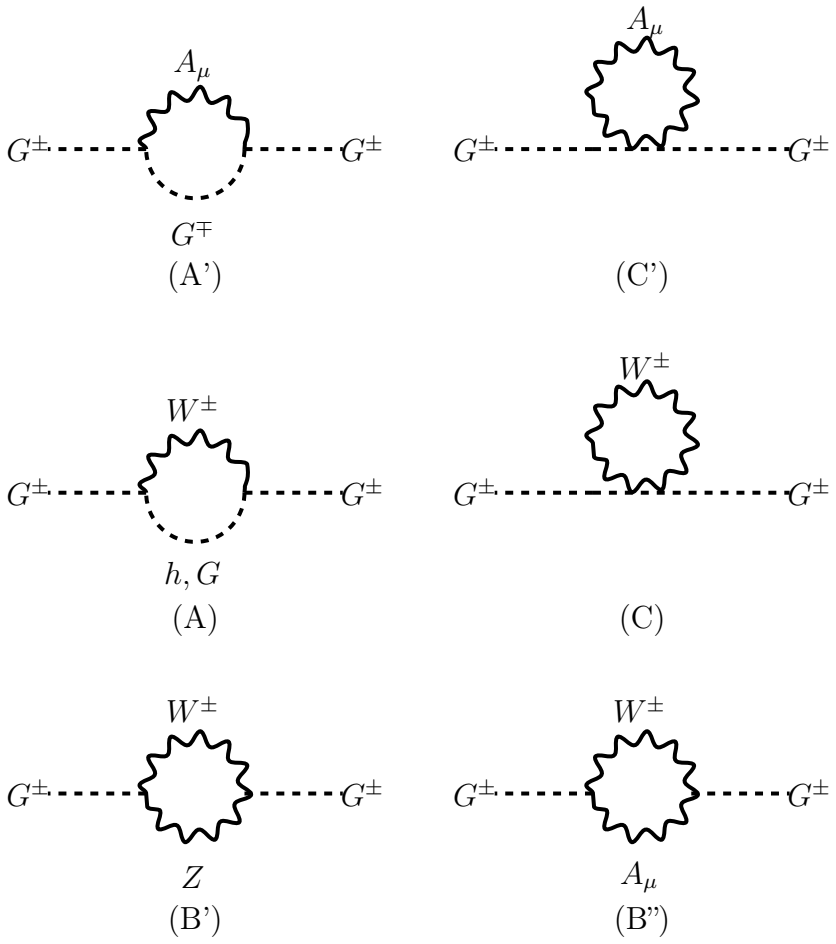

Figure D.13: Diagrams contributing to the self-energy of $G^\pm$ (part 1).

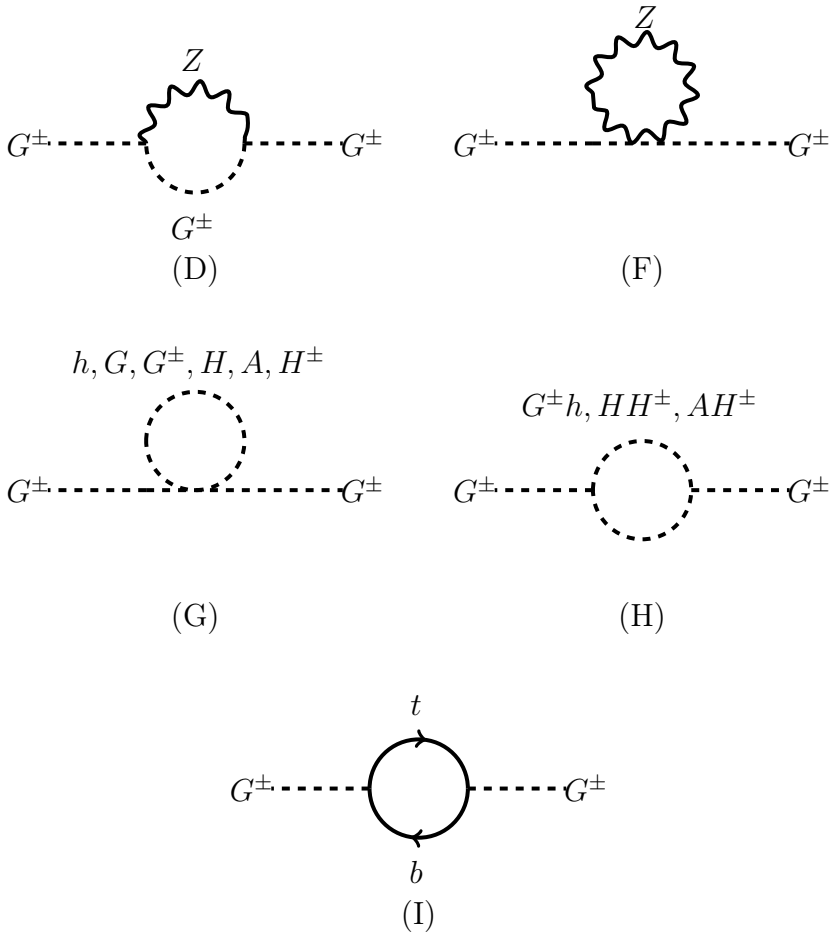

Figure D.14: Diagrams contributing to the self-energy of $G^\pm$ (part 2).

Bibliography

[1] P. M. Ferreira and B. Świeżewska. "One-loop contributions to neutral minima in the inert doublet model". In: (2015). arXiv: 1511.02879 [hep-ph].

[2] B. Świeżewska. "Inert scalars and vacuum metastability around the electroweak scale". In: *JHEP* 07 (2015), p. 118. DOI: 10.1007/JHEP07(2015)118. arXiv: 1503.07078 [hep-ph].

[3] M. Krawczyk, D. Sokołowska, P. Swaczyna, and B. Świeżewska. "Constraining Inert Dark Matter by $R_{\gamma\gamma}$ and WMAP data". In: *JHEP* 1309 (2013), p. 055. DOI: 10.1007/JHEP09(2013)055. arXiv: 1305.6266 [hep-ph].

[4] B. Świeżewska and M. Krawczyk. "Diphoton rate in the inert doublet model with a 125 GeV Higgs boson". In: *Phys.Rev.* D88.3 (2013), p. 035019. DOI: 10.1103/PhysRevD.88.035019. arXiv: 1212.4100 [hep-ph].

[5] B. Świeżewska. "Yukawa independent constraints for two-Higgs-doublet models with a 125 GeV Higgs boson". In: *Phys.Rev.* D88.5 (2013). Erratum-ibid. D88 (2013) 11, 119903, p. 055027. DOI: 10.1103/PhysRevD.88.119903. arXiv: 1209.5725 [hep-ph].

[6] B. Gorczyca and M. Krawczyk. "Tree-Level Unitarity Constraints for the SM-like 2HDM". In: (2011). arXiv: 1112.5086 [hep-ph].

[7] B. Świeżewska. "Inert scalars and vacuum stability". In: *2nd Toyama International Workshop on Higgs as a Probe of New Physics (HPNP2015) Toyama, Japan, February 11-15, 2015.* 2015.

[8] P. M. Ferreira and B. Świeżewska. "One-loop inert and pseudo-inert minima". In: *2nd Toyama International Workshop on Higgs as a Probe of New Physics (HPNP2015) Toyama, Japan, February 11-15, 2015.* 2015. arXiv: 1506.00585 [hep-ph]. URL: http://inspirehep.net/record/1373947/files/arXiv:1506.00585.pdf.

[9] M. Krawczyk, M. Matej, D. Sokołowska, and B. Świeżewska. "The Universe in the Light of LHC". In: *Acta Phys. Polon.* B46.1 (2015), pp. 169–179. DOI: 10.5506/APhysPolB.46.169. arXiv: 1501.04529 [hep-ph].

[10] B. Świeżewska, M. Krawczyk, D. Sokołowska, and P. Swaczyna. "Implications of the 125 GeV Higgs for the inert Dark Matter". In: *Proceedings, 49th Rencontres de Moriond on QCD and High Energy Interactions*. 2014, pp. 229–232. URL: http://moriond.in2p3.fr/Proceedings/2014/Moriond_QCD_2014.pdf.

[11] B. Świeżewska. "Decay rates of the Higgs boson to two photons and Z plus photon in Z_2-symmetric Two Higgs Doublet Models". In: *PoS* EPS-HEP2013 (2013), p. 066. arXiv: 1309.7343 [hep-ph].

[12] M. Krawczyk, D. Sokołowska, P. Swaczyna, and B. Świeżewska. "Higgs $\to \gamma\gamma$, $Z\gamma$ in the Inert Doublet Model". In: *Acta Phys. Polon.* B44.11 (2013), pp. 2163–2170. DOI: 10.5506/APhysPolB.44.2163. arXiv: 1309.7880 [hep-ph].

[13] B. Świeżewska and M. Krawczyk. "Two photon decay rate of the Higgs boson in the Inert Doublet Model". In: *PoS* Photon2013 (2013), p. 078.

[14] B. Świeżewska and M. Krawczyk. "2-photon decay rate of the scalar boson in the Inert Doublet Model". In: *Proceedings, 48th Rencontres de Moriond on Electroweak Interactions and Unified Theories*. 2013, pp. 563–566. arXiv: 1305.7356 [hep-ph]. URL: http://inspirehep.net/record/1236372/files/arXiv:1305.7356.pdf.

[15] M. Krawczyk, D. Sokołowska, and B. Świeżewska. "Inert Doublet Model with a 125 GeV Higgs". In: *1st Toyama International Workshop on Higgs as a Probe of New Physics 2013 (HPNP2013) Toyama, Japan, February 13-16, 2013*. 2013. arXiv: 1304.7757 [hep-ph]. URL: http://inspirehep.net/record/1230966/files/arXiv:1304.7757.pdf.

[16] M. Krawczyk, D. Sokołowska, and B. Świeżewska. "2HDM with Z_2 symmetry in light of new LHC data". In: *J. Phys. Conf. Ser.* 447 (2013), p. 012050. DOI: 10.1088/1742-6596/447/1/012050. arXiv: 1303.7102 [hep-ph].

[17] B. Gorczyca and M. Krawczyk. "New Results for the Inert Doublet Model". In: *Acta Phys. Polon.* B42 (2011). [Erratum: Acta Phys. Polon.B43,481(2012)], pp. 2229–2236. DOI: 10.5506/APhysPolB.43.481,10.5506/APhysPolB.42.2229. arXiv: 1112.4356 [hep-ph].

[18] G. Aad et al. "Observation of a new particle in the search for the Standard Model Higgs boson with the ATLAS detector at the LHC". In: *Phys.Lett.* B716 (2012), pp. 1–29. DOI: 10.1016/j.physletb.2012.08.020. arXiv: 1207.7214 [hep-ex].

[19] S. Chatrchyan et al. "Observation of a new boson at a mass of 125 GeV with the CMS experiment at the LHC". In: *Phys.Lett.* B716 (2012), pp. 30–61. DOI: 10.1016/j.physletb.2012.08.021. arXiv: 1207.7235 [hep-ex].

[20] F. Englert and R. Brout. "Broken Symmetry and the Mass of Gauge Vector Mesons". In: *Phys. Rev. Lett.* 13 (1964), pp. 321–323. DOI: 10.1103/PhysRevLett.13.321.

[21] P. W. Higgs. "Broken Symmetries and the Masses of Gauge Bosons". In: *Phys. Rev. Lett.* 13 (1964), pp. 508–509. DOI: 10.1103/PhysRevLett.13.508.

[22] P. W. Higgs. "Broken symmetries, massless particles and gauge fields". In: *Phys. Lett.* 12 (1964), pp. 132–133. DOI: 10.1016/0031-9163(64)91136-9.

[23] P. W. Higgs. "Spontaneous Symmetry Breakdown without Massless Bosons". In: *Phys. Rev.* 145 (1966), pp. 1156–1163. DOI: 10.1103/PhysRev.145.1156.

[24] S. Chatrchyan et al. *Measurements of the Higgs boson production and decay rates and constraints on its couplings from a combined ATLAS and CMS analysis of the LHC pp collision data at $\sqrt{s}$ = 7 and 8 TeV*. CMS-PAS-HIG-15-002. 2015.

[25] G. Aad et al. *Search for resonances decaying to photon pairs in 3.2 fb^{-1} of pp collisions at $\sqrt{s}$ = 13 TeV with the ATLAS detector*. ATLAS-CONF-2015-081. 2015.

[26] S. Chatrchyan et al. *Search for new physics in high mass diphoton events in proton-proton collisions at 13TeV*. CMS-PAS-EXO-15-004. 2015.

[27] T. D. Lee. "A Theory of Spontaneous T Violation". In: *Phys. Rev.* D8 (1973), pp. 1226–1239. DOI: 10.1103/PhysRevD.8.1226.

[28] G. Degrassi, S. Di Vita, J. Elias-Miro, J. R. Espinosa, G. F. Giudice, et al. "Higgs mass and vacuum stability in the Standard Model at NNLO". In: *JHEP* 1208 (2012), p. 098. DOI: 10.1007/JHEP08(2012)098. arXiv: 1205.6497 [hep-ph].

[29] D. Buttazzo, G. Degrassi, P. P. Giardino, G. F. Giudice, F. Sala, et al. "Investigating the near-criticality of the Higgs boson". In: *JHEP* 1312 (2013), p. 089. DOI: 10.1007/JHEP12(2013)089. arXiv: 1307.3536 [hep-ph].

[30] A. Spencer-Smith. "Higgs Vacuum Stability in a Mass-Dependent Renormalisation Scheme". In: (2014). arXiv: 1405.1975 [hep-ph].

[31] A. Kobakhidze and A. Spencer-Smith. "The Higgs vacuum is unstable". In: (2014). arXiv: 1404.4709 [hep-ph].

[32] G. C. Branco, P. M. Ferreira, L. Lavoura, M. N. Rebelo, M. Sher, and J. P. Silva. "Theory and phenomenology of two-Higgs-doublet models". In: *Phys. Rept.* 516 (2012), pp. 1–102. DOI: 10.1016/j.physrep.2012.02.002. arXiv: 1106.0034 [hep-ph].

[33] S. L. Glashow and S. Weinberg. "Natural Conservation Laws for Neutral Currents". In: *Phys. Rev.* D15 (1977), p. 1958. DOI: 10.1103/PhysRevD.15.1958.

[34] E. A. Paschos. "Diagonal Neutral Currents". In: *Phys. Rev.* D15 (1977), p. 1966. DOI: 10.1103/PhysRevD.15.1966.

[35] J. F. Gunion, H. Haber, G. Kane, and S. Dawson. *The Higgs Hunter's Guide*. Westview Press, 2000. ISBN: 9780738203058.

[36] G. C. Branco, L. Lavoura, and J. P. Silva. *CP violation*. Vol. 103. International Series on Monographs on Physics. Oxford University Press, 1999. ISBN: 0198503997.

[37] J. F. Gunion and H. E. Haber. "The CP conserving two Higgs doublet model: The Approach to the decoupling limit". In: *Phys. Rev.* D67 (2003), p. 075019. DOI: 10.1103/PhysRevD.67.075019. arXiv: hep-ph/0207010 [hep-ph].

[38] I. F. Ginzburg and M. Krawczyk. "Symmetries of two Higgs doublet model and CP violation". In: *Phys. Rev.* D72 (2005), p. 115013. DOI: 10.1103/PhysRevD.72.115013. arXiv: hep-ph/0408011 [hep-ph].

[39] N. G. Deshpande and E. Ma. "Pattern of Symmetry Breaking with Two Higgs Doublets". In: *Phys.Rev.* D18 (1978), p. 2574. DOI: 10.1103/PhysRevD.18.2574.

[40] I. F. Ginzburg and K. A. Kanishev. "Different vacua in 2HDM". In: *Phys. Rev.* D76 (2007), p. 095013. DOI: 10.1103/PhysRevD.76.095013. arXiv: 0704.3664 [hep-ph].

[41] I. Ginzburg, K. Kanishev, M. Krawczyk, and D. Sokołowska. "Evolution of Universe to the present inert phase". In: *Phys.Rev.* D82 (2010), p. 123533. DOI: 10.1103/PhysRevD.82.123533. arXiv: 1009.4593 [hep-ph].

[42] D. Sokołowska. "Ewolucja Wszechświata w modelu z dwoma dubletami pól Higgsa". (In Polish.) PhD thesis. University of Warsaw, 2012.

[43] I. P. Ivanov. "Minkowski space structure of the Higgs potential in 2HDM". In: *Phys. Rev.* D75 (2007). [Erratum: Phys. Rev.D76,039902(2007)], p. 035001. DOI: 10.1103/PhysRevD.76.039902, 10.1103/PhysRevD.75.035001. arXiv: hep-ph/0609018 [hep-ph].

[44] I. P. Ivanov. "Minkowski space structure of the Higgs potential in 2HDM. II. Minima, symmetries, and topology". In: *Phys. Rev.* D77 (2008), p. 015017. DOI: 10.1103/PhysRevD.77.015017. arXiv: 0710.3490 [hep-ph].

[45] A. Barroso, P. M. Ferreira, and R. Santos. "Neutral minima in two-Higgs doublet models". In: *Phys. Lett.* B652 (2007), pp. 181–193. DOI: 10.1016/j.physletb.2007.07.010. arXiv: hep-ph/0702098 [HEP-PH].

[46] R. Barbieri, L. J. Hall, and V. S. Rychkov. "Improved naturalness with a heavy Higgs: An Alternative road to LHC physics". In: *Phys.Rev.* D74 (2006), p. 015007. DOI: 10.1103/PhysRevD.74.015007. arXiv: hep-ph/0603188 [hep-ph].

[47] Q.-H. Cao, E. Ma, and G. Rajasekaran. "Observing the Dark Scalar Doublet and its Impact on the Standard-Model Higgs Boson at Colliders". In: *Phys.Rev.* D76 (2007), p. 095011. DOI: 10.1103/PhysRevD.76.095011. arXiv: 0708.2939 [hep-ph].

[48] B. Gorczyca. "Unitarity constraints for the Inert Doublet Model". In Polish. M.Sc. Thesis. University of Warsaw, 2011.

[49] H. A. Weldon. "The effects of multiple Higgs bosons on tree unitarity". In: *Phys.Rev.* D30 (1984), p. 1547. DOI: 10.1103/PhysRevD.30.1547.

[50] H. Huffel and G. Pocsik. "Unitarity bounds on Higgs boson masses in the Weinberg-Salam model with two Higgs doublets". In: *Z.Phys.* C8 (1981), p. 13. DOI: 10.1007/BF01429824.

[51] R. Casalbuoni, D. Dominici, R. Gatto, and C. Giunti. "Strong interacting two doublet and doublet singlet Higgs models". In: *Phys.Lett.* B178 (1986), p. 235. DOI: 10.1016/0370-2693(86)91502-9.

[52] R. Casalbuoni, D. Dominici, F. Feruglio, and R. Gatto. "Tree level unitarity violation for large scalar mass in multi-Higgs extensions of the Standard Model". In: *Nucl.Phys.* B299 (1988), p. 117. DOI: 10.1016/0550-3213(88)90469-5.

[53] J. Maalampi, J. Sirkka, and I. Vilja. "Tree level unitarity and triviality bounds for two Higgs models". In: *Phys.Lett.* B265 (1991), pp. 371–376. DOI: 10.1016/0370-2693(91)90068-2.

[54] S. Kanemura, T. Kubota, and E. Takasugi. "Lee-Quigg-Thacker bounds for Higgs boson masses in a two doublet model". In: *Phys.Lett.* B313 (1993), pp. 155–160. DOI: 10.1016/0370-2693(93)91205-2. arXiv: hep-ph/9303263 [hep-ph].

[55] A. G. Akeroyd, A. Arhrib, and E.-M. Naimi. "Note on tree level unitarity in the general two Higgs doublet model". In: *Phys.Lett.* B490 (2000), pp. 119–124. DOI: 10.1016/S0370-2693(00)00962-X. arXiv: hep-ph/0006035 [hep-ph].

[56] A. Arhrib. "Unitarity constraints on scalar parameters of the standard and two Higgs doublets model". In: (2000). arXiv: hep-ph/0012353 [hep-ph].

[57] I. Ginzburg and I. Ivanov. "Tree level unitarity constraints in the 2HDM with CP violation". In: (2003). arXiv: hep-ph/0312374 [hep-ph].

[58] I. Ginzburg and I. Ivanov. "Tree-level unitarity constraints in the most general 2HDM". In: *Phys.Rev.* D72 (2005), p. 115010. DOI: 10.1103/PhysRevD.72.115010. arXiv: hep-ph/0508020 [hep-ph].

[59] J. Hořejší and M. Kladiva. "Tree-unitarity bounds for THDM Higgs masses revisited". In: *Eur.Phys.J.* C46 (2006), pp. 81–91. DOI: 10.1140/epjc/s2006-02472-3. arXiv: hep-ph/0510154 [hep-ph].

[60] S. Kanemura, Y. Okada, H. Taniguchi, and K. Tsumura. "Indirect bounds on heavy scalar masses of the two-Higgs-doublet model in light of recent Higgs boson searches". In: *Phys.Lett.* B704 (2011), pp. 303–307. DOI: 10.1016/j.physletb.2011.09.035. arXiv: 1108.3297 [hep-ph].

[61] H. Cheon and S. K. Kang. "Constraining parameter space in type-II two-Higgs doublet model in light of a 126 GeV Higgs boson". In: *JHEP* 1309 (2013), p. 085. DOI: 10.1007/JHEP09(2013)085. arXiv: 1207.1083 [hep-ph].

[62] G. Funk, D. O'Neil, and R. M. Winters. "What the Oblique Parameters S, T, and U and Their Extensions Reveal About the 2HDM: A Numerical Analysis". In: *Int.J.Mod.Phys.* A27 (2012), p. 1250021. DOI: 10.1142/S0217751X12500212. arXiv: 1110.3812 [hep-ph].

[63] A. Arhrib, R. Benbrik, and N. Gaur. "$H \to \gamma\gamma$ in Inert Higgs Doublet Model". In: *Phys. Rev.* D85 (2012), p. 095021. DOI: 10.1103/PhysRevD.85.095021. arXiv: 1201.2644 [hep-ph].

[64] M. Gustafsson, S. Rydbeck, L. Lopez-Honorez, and E. Lundstrom. "Status of the Inert Doublet Model and the Role of multileptons at the LHC". In: (2012). arXiv: 1206.6316 [hep-ph].

[65] E. M. Dolle and S. Su. "The Inert Dark Matter". In: *Phys.Rev.* D80 (2009), p. 055012. DOI: 10.1103/PhysRevD.80.055012. arXiv: 0906.1609 [hep-ph].

[66] M. Maniatis, A. von Manteuffel, O. Nachtmann, and F. Nagel. "Stability and symmetry breaking in the general two-Higgs-doublet model". In: *Eur. Phys. J.* C48 (2006), pp. 805–823. DOI: 10.1140/epjc/s10052-006-0016-6. arXiv: hep-ph/0605184 [hep-ph].

[67] M. Gustafsson. "The Inert Doublet Model and Its Phenomenology". In: *PoS* CHARGED2010 (2010), p. 030. arXiv: 1106.1719 [hep-ph].

[68] B. W. Lee, C. Quigg, and H. Thacker. "The Strength of Weak Interactions at Very High-Energies and the Higgs Boson Mass". In: *Phys.Rev.Lett.* 38 (1977), pp. 883–885. DOI: 10.1103/PhysRevLett.38.883.

[69] B. W. Lee, C. Quigg, and H. Thacker. "Weak Interactions at Very High-Energies: The Role of the Higgs Boson Mass". In: *Phys.Rev.* D16 (1977), p. 1519. DOI: 10.1103/PhysRevD.16.1519.

[70] J. M. Cornwall, D. N. Levin, and G. Tiktopoulos. "Derivation of Gauge Invariance from High-Energy Unitarity Bounds on the s Matrix". In: *Phys.Rev.* D10 (1974), p. 1145. DOI: 10.1103/PhysRevD.10.1145,10.1103/PhysRevD.11.972.

[71] M. E. Peskin and T. Takeuchi. "Estimation of oblique electroweak corrections". In: *Phys. Rev.* D46 (1992), pp. 381–409. DOI: 10.1103/PhysRevD.46.381.

[72] W. Grimus, L. Lavoura, O. Ogreid, and P. Osland. "The Oblique parameters in multi-Higgs-doublet models". In: *Nucl.Phys.* B801 (2008), pp. 81–96. DOI: 10.1016/j.nuclphysb.2008.04.019. arXiv: 0802.4353 [hep-ph].

[73] W. Grimus, L. Lavoura, O. Ogreid, and P. Osland. "A Precision constraint on multi-Higgs-doublet models". In: *J.Phys.G* G35 (2008), p. 075001. DOI: 10.1088/0954-3899/35/7/075001. arXiv: 0711.4022 [hep-ph].

[74] M. Baak et al. "The global electroweak fit at NNLO and prospects for the LHC and ILC". In: *Eur.Phys.J.* C74 (2014), p. 3046. DOI: 10.1140/epjc/s10052-014-3046-5. arXiv: 1407.3792 [hep-ph].

[75] K. Nakamura et al. "Review of particle physics". In: *J. Phys.* G37 (2010), p. 075021. DOI: 10.1088/0954-3899/37/7A/075021.

[76] D. Eriksson, J. Rathsman, and O. Stål. "2HDMC: Two-Higgs-Doublet Model Calculator Physics and Manual". In: *Comput. Phys. Commun.* 181 (2010), pp. 189–205. DOI: 10.1016/j.cpc.2009.09.011. arXiv: 0902.0851 [hep-ph].

[77] E. Lundstrom, M. Gustafsson, and J. Edsjo. "The Inert Doublet Model and LEP II Limits". In: *Phys. Rev.* D79 (2009), p. 035013. DOI: 10.1103/PhysRevD.79.035013. arXiv: 0810.3924 [hep-ph].

[78] A. Pierce and J. Thaler. "Natural Dark Matter from an Unnatural Higgs Boson and New Colored Particles at the TeV Scale". In: *JHEP* 08 (2007), p. 026. DOI: 10.1088/1126-6708/2007/08/026. arXiv: hep-ph/0703056 [HEP-PH].

[79] G. Abbiendi et al. "Search for Charged Higgs bosons: Combined Results Using LEP Data". In: *Eur. Phys. J.* C73 (2013), p. 2463. DOI: 10.1140/epjc/s10052-013-2463-1. arXiv: 1301.6065 [hep-ex].

[80] T. Enomoto and R. Watanabe. "Flavor constraints on the Two Higgs Doublet Models of Z_2 symmetric and aligned types". In: (2015). arXiv: 1511.05066 [hep-ph].

[81] A. Wahab El Kaffas, P. Osland, and O. M. Ogreid. "Constraining the Two-Higgs-Doublet-Model parameter space". In: *Phys. Rev.* D76 (2007), p. 095001. DOI: 10.1103/PhysRevD.76.095001. arXiv: 0706.2997 [hep-ph].

[82] M. Jung, A. Pich, and P. Tuzon. "Charged-Higgs phenomenology in the Aligned two-Higgs-doublet model". In: *JHEP* 11 (2010), p. 003. DOI: 10.1007/JHEP11(2010)003. arXiv: 1006.0470 [hep-ph].

[83] X.-D. Cheng, Y.-D. Yang, and X.-B. Yuan. "Phenomenological discriminations of the Yukawa interactions in two-Higgs doublet models with Z_2 symmetry". In: *Eur. Phys. J.* C74.10 (2014), p. 3081. DOI: 10.1140/epjc/s10052-014-3081-2. arXiv: 1401.6657 [hep-ph].

[84] A. Matyja et al. "Observation of $B^0 \to D^{*-}\tau^+\nu_\tau$ decay at Belle". In: *Phys. Rev. Lett.* 99 (2007), p. 191807. DOI: 10.1103/PhysRevLett.99.191807. arXiv: 0706.4429 [hep-ex].

[85] A. Bozek et al. "Observation of $B^+ \to \bar{D}^{*0}\tau^+\nu_\tau$ and Evidence for $B^+ \to \bar{D}^0\tau^+\nu_\tau$ at Belle". In: *Phys. Rev.* D82 (2010), p. 072005. DOI: 10.1103/PhysRevD.82.072005. arXiv: 1005.2302 [hep-ex].

[86] M. Huschle et al. "Measurement of the branching ratio of $\bar{B} \to D^{(*)}\tau^-\bar{\nu}_\tau$ relative to $\bar{B} \to D^{(*)}\ell^-\bar{\nu}_\ell$ decays with hadronic tagging at Belle". In: *Phys. Rev.* D92.7 (2015), p. 072014. DOI: 10.1103/PhysRevD.92.072014. arXiv: 1507.03233 [hep-ex].

[87] B. Aubert et al. "Observation of the semileptonic decays $B \to D^* \tau^- \bar{\nu}(\ \tau^)$ and evidence for $B \to D \tau^- \bar{\nu}(\ \tau^)$". In: *Phys. Rev. Lett.* 100 (2008), p. 021801. DOI: 10.1103/PhysRevLett.100.021801. arXiv: 0709.1698 [hep-ex].

[88] J. P. Lees et al. "Measurement of an Excess of $\bar{B} \to D^{(*)} \tau^- \bar{\nu}_\tau$ Decays and Implications for Charged Higgs Bosons". In: *Phys. Rev.* D88.7 (2013), p. 072012. DOI: 10.1103/PhysRevD.88.072012. arXiv: 1303.0571 [hep-ex].

[89] R. Aaij et al. "Measurement of the ratio of branching fractions $\mathcal{B}(\bar{B}^0 \to D^{*+} \tau^- \bar{\nu}_\tau)/\mathcal{B}(\bar{B}^0 \to D^{*+} \mu^- \bar{\nu}_\mu)$". In: *Phys. Rev. Lett.* 115.11 (2015). [Addendum: Phys. Rev. Lett.115,no.15,159901(2015)], p. 111803. DOI: 10.1103/PhysRevLett.115.159901,10.1103/PhysRevLett.115.111803. arXiv: 1506.08614 [hep-ex].

[90] M. Freytsis, Z. Ligeti, and J. T. Ruderman. "Flavor models for $\bar{B} \to D^{(*)} \tau \bar{\nu}$". In: *Phys. Rev.* D92.5 (2015), p. 054018. DOI: 10.1103/PhysRevD.92.054018. arXiv: 1506.08896 [hep-ph].

[91] M. Misiak et al. "Updated NNLO QCD predictions for the weak radiative B-meson decays". In: *Phys. Rev. Lett.* 114.22 (2015), p. 221801. DOI: 10.1103/PhysRevLett.114.221801. arXiv: 1503.01789 [hep-ph].

[92] G. Aad et al. "Combined Measurement of the Higgs Boson Mass in pp Collisions at $\sqrt{s} = 7$ and 8 TeV with the ATLAS and CMS Experiments". In: *Phys. Rev. Lett.* 114 (2015), p. 191803. DOI: 10.1103/PhysRevLett.114.191803. arXiv: 1503.07589 [hep-ex].

[93] V. Khachatryan et al. "Constraints on the Higgs boson width from off-shell production and decay to Z-boson pairs". In: *Phys. Lett.* B736 (2014), p. 64. DOI: 10.1016/j.physletb.2014.06.077. arXiv: 1405.3455 [hep-ex].

[94] G. Aad et al. "Constraints on the off-shell Higgs boson signal strength in the high-mass ZZ and WW final states with the ATLAS detector". In: *Eur. Phys. J.* C75.7 (2015), p. 335. DOI: 10.1140/epjc/s10052-015-3542-2. arXiv: 1503.01060 [hep-ex].

[95] G. Aad et al. "Constraints on new phenomena via Higgs boson couplings and invisible decays with the ATLAS detector". In: (2015). arXiv: 1509.00672 [hep-ex].

[96] G. Belanger, B. Dumont, U. Ellwanger, J. F. Gunion, and S. Kraml. "Status of invisible Higgs decays". In: *Phys. Lett.* B723 (2013), pp. 340–347. DOI: 10.1016/j.physletb.2013.05.024. arXiv: 1302.5694 [hep-ph].

[97] L. Bergström. "Nonbaryonic dark matter: Observational evidence and detection methods". In: *Rept. Prog. Phys.* 63 (2000), p. 793. DOI: 10.1088/0034-4885/63/5/2r3. arXiv: hep-ph/0002126 [hep-ph].

[98] G. Bertone, D. Hooper, and J. Silk. "Particle dark matter: Evidence, candidates and constraints". In: *Phys. Rept.* 405 (2005), pp. 279–390. DOI: 10.1016/j.physrep.2004.08.031. arXiv: hep-ph/0404175 [hep-ph].

[99] L. Bergström. "Dark Matter Evidence, Particle Physics Candidates and Detection Methods". In: *Annalen Phys.* 524 (2012), pp. 479–496. DOI: 10.1002/andp.201200116. arXiv: 1205.4882 [astro-ph.HE].

[100] K. G. Begeman, A. H. Broeils, and R. H. Sanders. "Extended rotation curves of spiral galaxies: Dark haloes and modified dynamics". In: *Mon. Not. Roy. Astron. Soc.* 249 (1991), p. 523.

[101] M. Markevitch, A. H. Gonzalez, D. Clowe, A. Vikhlinin, L. David, W. Forman, C. Jones, S. Murray, and W. Tucker. "Direct constraints on the dark matter self-interaction cross-section from the merging galaxy cluster 1E0657-56". In: *Astrophys. J.* 606 (2004), pp. 819–824. DOI: 10.1086/383178. arXiv: astro-ph/0309303 [astro-ph].

[102] D. Clowe, M. Bradac, A. H. Gonzalez, M. Markevitch, S. W. Randall, C. Jones, and D. Zaritsky. "A direct empirical proof of the existence of dark matter". In: *Astrophys. J.* 648 (2006), pp. L109–L113. DOI: 10.1086/508162. arXiv: astro-ph/0608407 [astro-ph].

[103] G. Hinshaw et al. "Nine-Year Wilkinson Microwave Anisotropy Probe (WMAP) Observations: Cosmological Parameter Results". In: *Astrophys. J. Suppl.* 208 (2013), p. 19. DOI: 10.1088/0067-0049/208/2/19. arXiv: 1212.5226 [astro-ph.CO].

[104] P. Ade et al. "Planck 2013 results. XVI. Cosmological parameters". In: *Astron.Astrophys.* 571 (2014), A16. DOI: 10.1051/0004-6361/201321591. arXiv: 1303.5076 [astro-ph.CO].

[105] R. Bernabei et al. "Final model independent result of DAMA/LIBRA-phase1". In: *Eur. Phys. J.* C73 (2013), p. 2648. DOI: 10.1140/epjc/s10052-013-2648-7. arXiv: 1308.5109 [astro-ph.GA].

[106] C. E. Aalseth et al. "Results from a Search for Light-Mass Dark Matter with a P-type Point Contact Germanium Detector". In: *Phys. Rev. Lett.* 106 (2011), p. 131301. DOI: 10.1103/PhysRevLett.106.131301. arXiv: 1002.4703 [astro-ph.CO].

[107] G. Angloher et al. "Results from 730 kg days of the CRESST-II Dark Matter Search". In: *Eur. Phys. J.* C72 (2012), p. 1971. DOI: 10.1140/epjc/s10052-012-1971-8. arXiv: 1109.0702 [astro-ph.CO].

[108] E. Aprile et al. "Dark Matter Results from 225 Live Days of XENON100 Data". In: *Phys. Rev. Lett.* 109 (2012), p. 181301. DOI: 10.1103/PhysRevLett.109.181301. arXiv: 1207.5988 [astro-ph.CO].

[109] D. S. Akerib et al. "First results from the LUX dark matter experiment at the Sanford Underground Research Facility". In: *Phys. Rev. Lett.* 112 (2014), p. 091303. DOI: 10.1103/PhysRevLett.112.091303. arXiv: 1310.8214 [astro-ph.CO].

[110] D. S. Akerib et al. "Improved WIMP scattering limits from the LUX experiment". In: (2015). arXiv: 1512.03506 [astro-ph.CO].

[111] G. Angloher et al. "Results on low mass WIMPs using an upgraded CRESST-II detector". In: *Eur. Phys. J.* C74.12 (2014), p. 3184. DOI: 10.1140/epjc/s10052-014-3184-9. arXiv: 1407.3146 [astro-ph.CO].

[112] G. Angloher et al. "Results on light dark matter particles with a low-threshold CRESST-II detector". In: (2015). arXiv: 1509.01515 [astro-ph.CO].

[113] M. Cirelli. "Indirect Searches for Dark Matter: a status review". In: *Pramana* 79 (2012), pp. 1021–1043. DOI: 10.1007/s12043-012-0419-x. arXiv: 1202.1454 [hep-ph].

[114] O. Adriani et al. "An anomalous positron abundance in cosmic rays with energies 1.5-100 GeV". In: *Nature* 458 (2009), pp. 607–609. DOI: 10.1038/nature07942. arXiv: 0810.4995 [astro-ph].

[115] M. Aguilar et al. "Talks at the "AMS Days at CERN", 15–17 April, 2015". In: (2015).

[116] G. Giesen, M. Boudaud, Y. Génolini, V. Poulin, M. Cirelli, P. Salati, and P. D. Serpico. "AMS-02 antiprotons, at last! Secondary astrophysical component and immediate implications for Dark Matter". In: *JCAP* 1509.09 (2015), p. 023. DOI: 10.1088/1475-7516/2015/09/023,10.1088/1475-7516/2015/9/023. arXiv: 1504.04276 [astro-ph.HE].

[117] M. Ackermann et al. "Measurement of separate cosmic-ray electron and positron spectra with the Fermi Large Area Telescope". In: *Phys. Rev. Lett.* 108 (2012), p. 011103. DOI: 10.1103/PhysRevLett.108.011103. arXiv: 1109.0521 [astro-ph.HE].

[118] A. Hektor, M. Raidal, and E. Tempel. "Evidence for indirect detection of dark matter from galaxy clusters in Fermi γ-Ray data". In: *Astrophys. J.* 762 (2013), p. L22. DOI: 10.1088/2041-8205/762/2/L22. arXiv: 1207.4466 [astro-ph.HE].

[119] J. M. Cline. "130 GeV dark matter and the Fermi gamma-ray line". In: *Phys. Rev.* D86 (2012), p. 015016. DOI: 10.1103/PhysRevD.86.015016. arXiv: 1205.2688 [hep-ph].

[120] M. Persic. "CTA: the future of ground-based gamma-ray astrophysics". In: *Nucl. Phys. Proc. Suppl.* 239-240 (2013), pp. 210–215. DOI: 10.1016/j.nuclphysbps.2013.05.048. arXiv: 1303.2346 [astro-ph.HE].

[121] B. S. Acharya et al. "Introducing the CTA concept". In: *Astropart. Phys.* 43 (2013), pp. 3–18. DOI: 10.1016/j.astropartphys.2013.01.007.

[122] F. S. Queiroz and C. E. Yaguna. "The CTA aims at the Inert Doublet Model". In: (2015). arXiv: 1511.05967 [hep-ph].

[123] C. Garcia-Cely, M. Gustafsson, and A. Ibarra. "Probing the Inert Doublet Dark Matter Model with Cherenkov Telescopes". In: (2015). arXiv: 1512.02801 [hep-ph].

[124] P. J. Fox, R. Harnik, J. Kopp, and Y. Tsai. "Missing Energy Signatures of Dark Matter at the LHC". In: *Phys. Rev.* D85 (2012), p. 056011. DOI: 10.1103/PhysRevD.85.056011. arXiv: 1109.4398 [hep-ph].

[125] E. Dolle, X. Miao, S. Su, and B. Thomas. "Dilepton Signals in the Inert Doublet Model". In: *Phys.Rev.* D81 (2010), p. 035003. DOI: 10.1103/PhysRevD.81.035003. arXiv: 0909.3094 [hep-ph].

[126] P. Swaczyna. "Dark Matter effects in the Inert Doublet Model in the light of the newest LHC data". In Polish. M.Sc. Thesis. University of Warsaw, 2013.

[127] G. Belanger, B. Dumont, A. Goudelis, B. Herrmann, S. Kraml, and D. Sengupta. "Dilepton constraints in the Inert Doublet Model from Run 1 of the LHC". In: *Phys. Rev.* D91.11 (2015), p. 115011. DOI: 10.1103/PhysRevD.91.115011. arXiv: 1503.07367 [hep-ph].

[128] X. Miao, S. Su, and B. Thomas. "Trilepton Signals in the Inert Doublet Model". In: *Phys. Rev.* D82 (2010), p. 035009. DOI: 10.1103/PhysRevD.82.035009. arXiv: 1005.0090 [hep-ph].

[129] A. Arhrib, Y.-L. S. Tsai, Q. Yuan, and T.-C. Yuan. "An Updated Analysis of Inert Higgs Doublet Model in light of the Recent Results from LUX, PLANCK, AMS-02 and LHC". In: *JCAP* 1406 (2014), p. 030. DOI: 10.1088/1475-7516/2014/06/030. arXiv: 1310.0358 [hep-ph].

[130] G. Belanger, F. Boudjema, A. Pukhov, and A. Semenov. "MicrOMEGAs 2.0: A Program to calculate the relic density of dark matter in a generic model". In: *Comput. Phys. Commun.* 176 (2007), pp. 367–382. DOI: 10.1016/j.cpc.2006.11.008. arXiv: hep-ph/0607059 [hep-ph].

[131] G. Belanger, F. Boudjema, A. Pukhov, and A. Semenov. "Dark matter direct detection rate in a generic model with micrOMEGAs 2.2". In: *Comput. Phys. Commun.* 180 (2009), pp. 747–767. DOI: 10.1016/j.cpc.2008.11.019. arXiv: 0803.2360 [hep-ph].

[132] G. Belanger, F. Boudjema, P. Brun, A. Pukhov, S. Rosier-Lees, P. Salati, and A. Semenov. "Indirect search for dark matter with micrOMEGAs2.4". In: *Comput. Phys. Commun.* 182 (2011), pp. 842–856. DOI: 10.1016/j.cpc.2010.11.033. arXiv: 1004.1092 [hep-ph].

[133] L. Lopez Honorez, E. Nezri, J. F. Oliver, and M. H. Tytgat. "The Inert Doublet Model: An Archetype for Dark Matter". In: *JCAP* 0702 (2007), p. 028. DOI: 10.1088/1475-7516/2007/02/028. arXiv: hep-ph/0612275 [hep-ph].

[134] C. Arina, F.-S. Ling, and M. H. Tytgat. "IDM and iDM or The Inert Doublet Model and Inelastic Dark Matter". In: *JCAP* 0910 (2009), p. 018. DOI: 10.1088/1475-7516/2009/10/018. arXiv: 0907.0430 [hep-ph].

[135] M. H. G. Tytgat. "The Inert Doublet Model: A New archetype of WIMP dark matter?" In: *J. Phys. Conf. Ser.* 120 (2008), p. 042026. DOI: 10.1088/1742-6596/120/4/042026. arXiv: 0712.4206 [hep-ph].

[136] L. Lopez Honorez and C. E. Yaguna. "The inert doublet model of dark matter revisited". In: *JHEP* 1009 (2010), p. 046. DOI: 10.1007/JHEP09(2010)046. arXiv: 1003.3125 [hep-ph].

[137] D. Sokołowska. "Dark Matter Data and Constraints on Quartic Couplings in IDM". In: (2011). arXiv: 1107.1991 [hep-ph].

[138] D. Sokołowska. "Dark Matter Data and Quartic Self-Couplings in Inert Doublet Model". In: *Acta Phys. Polon.* B42 (2011), p. 2237. DOI: 10.5506/APhysPolB.42.2237. arXiv: 1112.2953 [hep-ph].

[139] A. Goudelis, B. Herrmann, and O. Stål. "Dark matter in the Inert Doublet Model after the discovery of a Higgs-like boson at the LHC". In: *JHEP* 1309 (2013), p. 106. DOI: 10.1007/JHEP09(2013)106. arXiv: 1303.3010 [hep-ph].

[140] T. Abe, R. Kitano, and R. Sato. "Discrimination of dark matter models in future experiments". In: (2014). arXiv: 1411.1335 [hep-ph].

[141] P. Bechtle, O. Brein, S. Heinemeyer, G. Weiglein, and K. E. Williams. "HiggsBounds: Confronting Arbitrary Higgs Sectors with Exclusion Bounds from LEP and the Tevatron". In: *Comput. Phys. Commun.* 181 (2010), pp. 138–167. DOI: 10.1016/j.cpc.2009.09.003. arXiv: 0811.4169 [hep-ph].

[142] P. Bechtle, O. Brein, S. Heinemeyer, G. Weiglein, and K. E. Williams. "HiggsBounds 2.0.0: Confronting Neutral and Charged Higgs Sector Predictions with Exclusion Bounds from LEP and the Tevatron". In: *Comput. Phys. Commun.* 182 (2011), pp. 2605–2631. DOI: 10.1016/j.cpc.2011.07.015. arXiv: 1102.1898 [hep-ph].

[143] P. Bechtle, O. Brein, S. Heinemeyer, O. Stål, T. Stefaniak, G. Weiglein, and K. E. Williams. "HiggsBounds – 4: Improved Tests of Extended Higgs Sectors against Exclusion Bounds from LEP, the Tevatron and the LHC". In: *Eur. Phys. J.* C74.3 (2014), p. 2693. DOI: 10.1140/epjc/s10052-013-2693-2. arXiv: 1311.0055 [hep-ph].

[144] P. Bechtle, S. Heinemeyer, O. Stål, T. Stefaniak, and G. Weiglein. "*HiggsSignals*: Confronting arbitrary Higgs sectors with measurements at the Tevatron and the LHC". In: *Eur. Phys. J.* C74.2 (2014), p. 2711. DOI: 10.1140/epjc/s10052-013-2711-4. arXiv: 1305.1933 [hep-ph].

[145] A. Ilnicka, M. Krawczyk, and T. Robens. "The Inert Doublet Model in the light of LHC and astrophysical data – An Update –". In: (2015). arXiv: 1508.01671 [hep-ph].

[146] P. Posch. "Enhancement of $h \to \gamma\gamma$ in the Two Higgs Doublet Model Type I". In: *Phys.Lett.* B696 (2011), pp. 447–453. DOI: 10.1016/j.physletb.2011.01.003. arXiv: 1001.1759 [hep-ph].

[147] J. Chang, K. Cheung, P.-Y. Tseng, and T.-C. Yuan. "Various Models Mimicking the SM Higgs Boson". In: *Int.J.Mod.Phys.* A27 (2012), p. 1230030. DOI: 10.1142/S0217751X1230030X. arXiv: 1211.6823 [hep-ph].

[148] D. Borah and J. M. Cline. "Inert Doublet Dark Matter with Strong Electroweak Phase Transition". In: *Phys.Rev.* D86 (2012), p. 055001. DOI: 10.1103/PhysRevD.86.055001. arXiv: 1204.4722 [hep-ph].

[149] G. Gil, P. Chankowski, and M. Krawczyk. "Inert Dark Matter and Strong Electroweak Phase Transition". In: *Phys.Lett.* B717 (2012), pp. 396–402. DOI: 10.1016/j.physletb.2012.09.052. arXiv: 1207.0084 [hep-ph].

[150] N. Chakrabarty, D. K. Ghosh, B. Mukhopadhyaya, and I. Saha. "Dark matter, neutrino masses and high scale validity of an inert Higgs doublet model". In: (2015). arXiv: 1501.03700 [hep-ph].

[151] A. Djouadi. "The Anatomy of electro-weak symmetry breaking. II. The Higgs bosons in the minimal supersymmetric model". In: *Phys.Rept.* 459 (2008), pp. 1–241. DOI: 10.1016/j.physrep.2007.10.005. arXiv: hep-ph/0503173 [hep-ph].

[152] A. Djouadi. "The Anatomy of electro-weak symmetry breaking. I: The Higgs boson in the standard model". In: *Phys.Rept.* 457 (2008), pp. 1–216. DOI: 10.1016/j.physrep.2007.10.004. arXiv: hep-ph/0503172 [hep-ph].

[153] A. Djouadi, J. Kalinowski, and P. Zerwas. "Two and three-body decay modes of SUSY Higgs particles". In: *Z.Phys.* C70 (1996), pp. 435–448. DOI: 10.1007/s002880050121. arXiv: hep-ph/9511342 [hep-ph].

[154] J. Beringer et al. "Review of Particle Physics". In: *Phys. Rev. D* 86 (1 2012), p. 010001. DOI: 10.1103/PhysRevD.86.010001. URL: http://link.aps.org/doi/10.1103/PhysRevD.86.010001.

[155] C.-S. Chen, C.-Q. Geng, D. Huang, and L.-H. Tsai. "New Scalar Contributions to $h \to Z\gamma$". In: *Phys. Rev. D87,* 075019 (2013). DOI: 10.1103/PhysRevD.87.075019. arXiv: 1301.4694 [hep-ph].

[156] B. Świeżewska and M. Krawczyk. "Two photon decay rate of the Higgs boson in the Inert Doublet Model". In: *PoS* Photon2013 (2013), p. 078.

[157] M. Spira. "QCD effects in Higgs physics". In: *Fortsch.Phys.* 46 (1998), pp. 203–284. arXiv: hep-ph/9705337 [hep-ph].

[158] S. Chatrchyan et al. "Search for a Higgs boson decaying into a Z and a photon in pp collisions at sqrt(s) = 7 and 8 TeV". In: *Phys. Lett.* B726 (2013), pp. 587–609. DOI: 10.1016/j.physletb.2013.09.057. arXiv: 1307.5515 [hep-ex].

[159] G. Aad et al. "Search for Higgs boson decays to a photon and a Z boson in pp collisions at $\sqrt{s}$=7 and 8 TeV with the ATLAS detector". In: *Phys. Lett.* B732 (2014), pp. 8–27. DOI: 10.1016/j.physletb.2014.03.015. arXiv: 1402.3051 [hep-ex].

[160] A. Arhrib, R. Benbrik, and T.-C. Yuan. "Associated Production of Higgs at Linear Collider in the Inert Higgs Doublet Model". In: *Eur. Phys. J.* C74 (2014), p. 2892. DOI: 10.1140/epjc/s10052-014-2892-5. arXiv: 1401.6698 [hep-ph].

[161] M. A. Díaz, B. Koch, and S. Urrutia-Quiroga. "Constraints to Dark Matter from Inert Higgs Doublet Model". In: (2015). arXiv: 1511.04429 [hep-ph].

[162] T. Hambye, F.-S. Ling, L. Lopez Honorez, and J. Rocher. "Scalar Multiplet Dark Matter". In: *JHEP* 0907 (2009). Erratum-ibid. 1005 (2010) 066, p. 090. DOI: 10.1007/JHEP05(2010)066,10.1088/1126-6708/2009/07/090. arXiv: 0903.4010 [hep-ph].

[163] M. Klasen, C. E. Yaguna, and J. D. Ruiz-Alvarez. "Electroweak corrections to the direct detection cross section of inert higgs dark matter". In: *Phys. Rev.* D87 (2013), p. 075025. DOI: 10.1103/PhysRevD.87.075025. arXiv: 1302.1657 [hep-ph].

[164] T. Abe and R. Sato. "Quantum corrections to the spin-independent cross section of the inert doublet dark matter". In: *JHEP* 03 (2015), p. 109. DOI: 10.1007/JHEP03(2015)109. arXiv: 1501.04161 [hep-ph].

[165] S. Andreas, T. Hambye, and M. H. G. Tytgat. "WIMP dark matter, Higgs exchange and DAMA". In: *JCAP* 0810 (2008), p. 034. DOI: 10.1088/1475-7516/2008/10/034. arXiv: 0808.0255 [hep-ph].

[166] S. Andreas, M. H. G. Tytgat, and Q. Swillens. "Neutrinos from Inert Doublet Dark Matter". In: *JCAP* 0904 (2009), p. 004. DOI: 10.1088/1475-7516/2009/04/004. arXiv: 0901.1750 [hep-ph].

[167] A. Crivellin, M. Hoferichter, and M. Procura. "Accurate evaluation of hadronic uncertainties in spin-independent WIMP-nucleon scattering: Disentangling two- and three-flavor effects". In: *Phys. Rev.* D89 (2014), p. 054021. DOI: 10.1103/PhysRevD.89.054021. arXiv: 1312.4951 [hep-ph].

[168] S. R. Coleman and E. J. Weinberg. "Radiative Corrections as the Origin of Spontaneous Symmetry Breaking". In: *Phys.Rev.* D7 (1973), pp. 1888–1910. DOI: 10.1103/PhysRevD.7.1888.

[169] T. P. Cheng and L. F. Li. *Gauge theory of elementary particle physics.* Oxford Science Publications, 1984.

[170] S. Coleman. *Aspects of Symmetry: Selected Erice Lectures.* Cambridge University Press, 1988.

[171] P. Chankowski. *Quantum Field Theory of Fundamental Interactions.*

[172] V. Branchina and E. Messina. "Stability, Higgs Boson Mass and New Physics". In: *Phys.Rev.Lett.* 111 (2013), p. 241801. DOI: 10.1103/PhysRevLett.111.241801. arXiv: 1307.5193 [hep-ph].

[173] V. Branchina, E. Messina, and A. Platania. "Top mass determination, Higgs inflation, and vacuum stability". In: *JHEP* 1409 (2014), p. 182. DOI: 10.1007/JHEP09(2014)182. arXiv: 1407.4112 [hep-ph].

[174] V. Branchina, E. Messina, and M. Sher. "The lifetime of the electroweak vacuum and sensitivity to Planck scale physics". In: (2014). arXiv: 1408.5302 [hep-ph].

[175] Z. Lalak, M. Lewicki, and P. Olszewski. "Higher-order scalar interactions and SM vacuum stability". In: *JHEP* 1405 (2014), p. 119. DOI: 10.1007/JHEP05(2014)119. arXiv: 1402.3826 [hep-ph].

[176] E. Greenwood, E. Halstead, R. Poltis, and D. Stojkovic. "Dark energy, the electroweak vacua and collider phenomenology". In: *Phys.Rev.* D79 (2009), p. 103003. DOI: 10.1103/PhysRevD.79.103003. arXiv: 0810.5343 [hep-ph].

[177] M. Kadastik, K. Kannike, A. Racioppi, and M. Raidal. "Implications of the 125 GeV Higgs boson for scalar dark matter and for the CMSSM phenomenology". In: *JHEP* 1205 (2012), p. 061. DOI: 10.1007/JHEP05(2012)061. arXiv: 1112.3647 [hep-ph].

[178] N. Khan and S. Rakshit. "Constraints on inert dark matter from metastability of electroweak vacuum". In: (2015). arXiv: 1503.03085 [hep-ph].

[179] G. Gamberini, G. Ridolfi, and F. Zwirner. "On Radiative Gauge Symmetry Breaking in the Minimal Supersymmetric Model". In: *Nucl. Phys.* B331 (1990), pp. 331–349. DOI: 10.1016/0550-3213(90)90211-U.

[180] J. A. Casas, A. Lleyda, and C. Munoz. "Strong constraints on the parameter space of the MSSM from charge and color breaking minima". In: *Nucl. Phys.* B471 (1996), pp. 3–58. DOI: 10.1016/0550-3213(96)00194-0. arXiv: hep-ph/9507294 [hep-ph].

[181] S. R. Coleman. "The Fate of the False Vacuum. 1. Semiclassical Theory". In: *Phys.Rev.* D15 (1977), pp. 2929–2936. DOI: 10.1103/PhysRevD.15.2929, 10.1103/PhysRevD.16.1248.

[182] J. Callan Curtis G. and S. R. Coleman. "The Fate of the False Vacuum. 2. First Quantum Corrections". In: *Phys.Rev.* D16 (1977), pp. 1762–1768. DOI: 10.1103/PhysRevD.16.1762.

[183] V. A. Rubakov. *Classical theory of gauge fields*. Princeton, NJ: Princeton Univ., 2002. URL: https://cds.cern.ch/record/639408.

[184] C. L. Wainwright. "CosmoTransitions: Computing Cosmological Phase Transition Temperatures and Bubble Profiles with Multiple Fields". In: *Comput. Phys. Commun.* 183 (2012), pp. 2006–2013. DOI: 10.1016/j.cpc.2012.04.004. arXiv: 1109.4189 [hep-ph].

[185] J. Camargo-Molina, B. O'Leary, W. Porod, and F. Staub. "**Vevacious**: A Tool For Finding The Global Minima Of One-Loop Effective Potentials With Many Scalars". In: *Eur.Phys.J.* C73.10 (2013), p. 2588. DOI: 10.1140/epjc/s10052-013-2588-2. arXiv: 1307.1477 [hep-ph].

[186] M. Sher. "Electroweak Higgs Potentials and Vacuum Stability". In: *Phys.Rept.* 179 (1989), pp. 273–418. DOI: 10.1016/0370-1573(89)90061-6.

[187] A. Barroso, P. Ferreira, I. Ivanov, R. Santos, and J. P. Silva. "Evading death by vacuum". In: *Eur.Phys.J.* C73 (2013), p. 2537. DOI: 10.1140/epjc/s10052-013-2537-0. arXiv: 1211.6119 [hep-ph].

[188] A. Barroso, P. Ferreira, I. Ivanov, and R. Santos. "Metastability bounds on the two Higgs doublet model". In: *JHEP* 1306 (2013), p. 045. DOI: 10.1007/JHEP06(2013)045. arXiv: 1303.5098 [hep-ph].

[189] P. M. Ferreira, R. Santos, and A. Barroso. "Stability of the tree-level vacuum in two Higgs doublet models against charge or CP spontaneous violation". In: *Phys. Lett.* B603 (2004). [Erratum: Phys. Lett.B629,114(2005)], pp. 219–229. DOI: 10.1016/j.physletb.2004.10.022. arXiv: hep-ph/0406231 [hep-ph].

[190] A. Barroso, P. M. Ferreira, and R. Santos. "Charge and CP symmetry breaking in two Higgs doublet models". In: *Phys. Lett.* B632 (2006), pp. 684–687. DOI: 10.1016/j.physletb.2005.11.031. arXiv: hep-ph/0507224 [hep-ph].

[191] I. P. Ivanov and J. P. Silva. "Tree-level metastability bounds for the most general two Higgs doublet model". In: (2015). arXiv: 1507.05100 [hep-ph].

[192] E. J. Weinberg and A.-q. Wu. "Understanding complex perturbative effective potentials". In: *Phys.Rev.* D36 (1987), p. 2474. DOI: 10.1103/PhysRevD.36.2474.

[193] S. P. Martin. "Taming the Goldstone contributions to the effective potential". In: *Phys.Rev.* D90.1 (2014), p. 016013. DOI: 10.1103/PhysRevD.90.016013. arXiv: 1406.2355 [hep-ph].

[194] J. Elias-Miro, J. Espinosa, and T. Konstandin. "Taming Infrared Divergences in the Effective Potential". In: *JHEP* 1408 (2014), p. 034. DOI: 10.1007/JHEP08(2014)034. arXiv: 1406.2652 [hep-ph].

[195] K. Olive et al. "Review of Particle Physics". In: *Chin.Phys.* C38 (2014), p. 090001. DOI: 10.1088/1674-1137/38/9/090001.

[196] M. Krawczyk, D. Sokołowska, P. Swaczyna, and B. Świeżewska. "Higgs $\to \gamma\gamma$, $Z\gamma$ in the Inert Doublet Model". In: *Acta Phys.Polon.* B44.11 (2013), pp. 2163–2170. DOI: 10.5506/APhysPolB.44.2163. arXiv: 1309.7880 [hep-ph].

[197] I. P. Ivanov and C. C. Nishi. "Symmetry breaking patterns in 3HDM". In: *JHEP* 01 (2015), p. 021. DOI: 10.1007/JHEP01(2015)021. arXiv: 1410.6139 [hep-ph].

[198] A. Degee, I. P. Ivanov, and V. Keus. "Geometric minimization of highly symmetric potentials". In: *JHEP* 02 (2013), p. 125. DOI: 10.1007/JHEP02(2013)125. arXiv: 1211.4989 [hep-ph].

[199] M. Maniatis and O. Nachtmann. "Stability and symmetry breaking in the general n-Higgs-doublet model". In: *Phys. Rev.* D92.7 (2015), p. 075017. DOI: 10.1103/PhysRevD.92.075017. arXiv: 1504.01736 [hep-ph].

[200] M. Maniatis and O. Nachtmann. "Stability and symmetry breaking in the general three-Higgs-doublet model". In: *JHEP* 02 (2015), p. 058. DOI: 10.1007/JHEP02(2015)058. arXiv: 1408.6833 [hep-ph].

[201] M. Maniatis and D. Mehta. "On exact minimization of Higgs potentials". In: *Eur. Phys. J. Plus* 129 (2014), p. 109. DOI: 10.1140/epjp/i2014-14109-0. arXiv: 1307.1703 [hep-ph].

[202] P. M. Ferreira. "A Full one loop charge and color breaking effective potential". In: *Phys. Lett.* B509 (2001). [Erratum: Phys. Lett.B518,333(2001)], pp. 120–130. DOI: 10.1016/S0370-2693(01)00552-4. arXiv: hep-ph/0008115 [hep-ph].

[203] P. M. Ferreira. "Minimization of a one loop charge breaking effective potential". In: *Phys. Lett.* B512 (2001). [Erratum: Phys. Lett.B518,334(2001)], pp. 379–391. DOI: 10.1016/S0370-2693(01)00716-X. arXiv: hep-ph/0102141 [hep-ph].

[204] M. E. Peskin and D. V. Schroeder. *An Introduction to quantum field theory*. Addison-Wesley Publishing Company, 1995. ISBN: 9780201503975, 0201503972. URL: http://www.slac.stanford.edu/spires/find/books/www?cl=QC174.45%3AP4.

[205] S. P. Martin. "Two loop scalar self energies in a general renormalizable theory at leading order in gauge couplings". In: *Phys. Rev.* D70 (2004), p. 016005. DOI: 10.1103/PhysRevD.70.016005. arXiv: hep-ph/0312092 [hep-ph].

[206] S. P. Martin. "Evaluation of two loop selfenergy basis integrals using differential equations". In: *Phys. Rev.* D68 (2003), p. 075002. DOI: 10.1103/PhysRevD.68.075002. arXiv: hep-ph/0307101 [hep-ph].

[207] J. R. Ellis, G. Ridolfi, and F. Zwirner. "Radiative corrections to the masses of supersymmetric Higgs bosons". In: *Phys. Lett.* B257 (1991), pp. 83–91. DOI: 10.1016/0370-2693(91)90863-L.

[208] J. R. Ellis, G. Ridolfi, and F. Zwirner. "On radiative corrections to supersymmetric Higgs boson masses and their implications for LEP searches". In: *Phys. Lett.* B262 (1991), pp. 477–484. DOI: 10.1016/0370-2693(91)90626-2.

[209] A. Brignole, J. R. Ellis, G. Ridolfi, and F. Zwirner. "The Supersymmetric charged Higgs boson mass and LEP phenomenology". In: *Phys. Lett.* B271 (1991), pp. 123–132. DOI: 10.1016/0370-2693(91)91287-6.

[210] J. A. Casas, V. Di Clemente, and M. Quiros. "The Effective potential in the presence of several mass scales". In: *Nucl. Phys.* B553 (1999), pp. 511–530. DOI: 10.1016/S0550-3213(99)00262-X. arXiv: hep-ph/9809275 [hep-ph].

[211] M. Bando, T. Kugo, N. Maekawa, and H. Nakano. "Improving the effective potential: Multimass scale case". In: *Prog. Theor. Phys.* 90 (1993), pp. 405–418. DOI: 10.1143/PTP.90.405. arXiv: hep-ph/9210229 [hep-ph].

[212] M. Bando, T. Kugo, N. Maekawa, and H. Nakano. "Improving the effective potential". In: *Phys. Lett.* B301 (1993), pp. 83–89. DOI: 10.1016/0370-2693(93)90725-W. arXiv: hep-ph/9210228 [hep-ph].

[213] M. Badziak. "Interpreting the 750 GeV diphoton excess in minimal extensions of Two-Higgs-Doublet models". In: (2015). arXiv: 1512.07497 [hep-ph].

[214] A. Angelescu, A. Djouadi, and G. Moreau. "Scenarii for interpretations of the LHC diphoton excess: two Higgs doublets and vector-like quarks and leptons". In: (2015). arXiv: 1512.04921 [hep-ph].

[215] D. Becirevic, E. Bertuzzo, O. Sumensari, and R. Z. Funchal. "Can the new resonance at LHC be a CP-Odd Higgs boson?" In: (2015). arXiv: 1512.05623 [hep-ph].

[216] X.-F. Han and L. Wang. "Implication of the 750 GeV diphoton resonance on two-Higgs-doublet model and its extensions with Higgs field". In: (2015). arXiv: 1512.06587 [hep-ph].

[217] X.-F. Han, L. Wang, L. Wu, J. M. Yang, and M. Zhang. "Explaining 750 GeV diphoton excess from top/bottom partner cascade decay in two-Higgs-doublet model extension". In: (2016). arXiv: 1601.00534 [hep-ph].

[218] S. K. Kang and J. Song. "Top-phobic heavy Higgs boson as the 750 GeV diphoton resonance". In: (2015). arXiv: 1512.08963 [hep-ph].

[219] S. Moretti and K. Yagyu. "The 750 GeV diphoton excess and its explanation in 2-Higgs Doublet Models with a real inert scalar multiplet". In: (2015). arXiv: 1512.07462 [hep-ph].

[220] A. E. C. Hernández, I. d. M. Varzielas, and E. Schumacher. "The 750 GeV diphoton resonance in the light of a 2HDM with S_3 flavour symmetry". In: (2016). arXiv: 1601.00661 [hep-ph].

[221] S. Di Chiara, L. Marzola, and M. Raidal. "First interpretation of the 750 GeV di-photon resonance at the LHC". In: (2015). arXiv: 1512.04939 [hep-ph].

[222] N. Bizot, S. Davidson, M. Frigerio, and J. L. Kneur. "Two Higgs doublets to explain the excesses $pp \to \gamma\gamma(750\ GeV)$ and $h \to \tau^{\pm}\mu^{\mp}$". In: (2015). arXiv: 1512.08508 [hep-ph].

[223] W.-C. Huang, Y.-L. S. Tsai, and T.-C. Yuan. "Gauged Two Higgs Doublet Model confronts the LHC 750 GeV di-photon anomaly". In: (2015). arXiv: 1512.07268 [hep-ph].

[224] G. Passarino and M. Veltman. "One Loop Corrections for e^+e^- Annihilation Into $\mu^+\mu^-$ in the Weinberg Model". In: *Nucl.Phys.* B160 (1979), p. 151. DOI: 10.1016/0550-3213(79)90234-7.

[225] J. C. Romão. *Advanced Quantum Field Theory.* Available from http://porthos.ist.utl.pt/ftp/textos/tca.pdf. 2015.